Modeling the SAC Microstructure Evolution under Thermal, Thermomechanical and Electrical Constraints

Von der
Fakultät für Elektrotechnik und Informatik
der Gottfried Wilhelm Leibniz Universität Hannover

und der

Ecole Doctorale des Physiques et de l’Ingénieur'
der Université de Bordeaux

zur Erlangung des akademischen Grades

Doktor-Ingenieur (abgekürzt: Dr.-Ing.)
Docteur en Electronique

genehmigte Dissertation

von

Dipl.-Ing. Lutz Meinshausen

geboren am 19. November 1983
in Göttingen

2014

1. Referent: Prof. Dr.-Ing. Ernst **Gockenbach**

2. Referentin: PD Dr.-Ing. Dipl.-Phys.**Kirsten Weide-Zaage**

Tag der Promotion: 25.03.2014 *)

*) Datum der mündlichen Doktorprüfung

Abstract

Key Words: Intermetallic Compound, Transient Liquid Phase Soldering, Electromigration,
Thermomigration

Modeling the SAC Microstructure Evolution under Thermal, Thermomechanical and Electrical Constraints

A further miniaturization of microelectronic components by three dimensional packaging, as well as the use of microelectronic devices under harsh environment conditions, requires the development of more robust alternatives to the existing Sn based solder joints. One promising technique is the diffusion and migration driven transformation of conventional solder bumps into intermetallic compound (IMC) connections. The related process is called transient liquid phase soldering (TLPS). The technical challenge regarding to TLPS, and the aim of this work, is the prediction of the IMC formation under consideration of the solder joints geometry and the chosen process parameters. Especially the use of electromigration (EM) and thermomigration (TM) for an acceleration of the IMC growth, without increasing the process test temperature, is of interest.

Against this background an investigation of the IMC formation under consideration of TM and EM will be performed. For the stress tests Package on Package structures are used. The final result is a general model for the IMC formation in solder joints. Combined with a Finite Element Analysis (FEA) this model is used to predict the IMC formation in solder joints for a broad range of boundary conditions. The model is approached in several intermediate steps:

As a first step of the investigation the atomic model of diffusion, being based on the conditions in fcc metals, is evaluated for the specific conditions in the crystal lattice of the IMCs Cu_3Sn and Cu_6Sn_5.

Long and short term temperature storage (TS) tests are performed. Knowing the long- and the short term behavior of the diffusion driven IMC formation the tests are combined with three other TS tests at different temperatures. The results of the short term tests are used to characterize the diffusion driven IMC formation.

EM and TM tests at three different test temperatures are performed. For the EM and TM stress tests TS is combined with a direct current and an alternating current. The EM and TM induced mass fluxes values are used to characterize the migration induced IMC formation by extracting temperature independent material parameters, being related to EM and TM.

The material values are inserted into an user routine for the calculation of the diffusion EM and TM induced mass fluxes. After the validation of the material values by comparing the simulation and the experimental results, the single migration phenomena are summarized to a total mass flux. The total mass flux is used to calculate the IMC growth speed. A dynamic simulation of the IMC growth becomes possible by dividing the test time into numerous time steps. The result is a FEA of the IMC growth under consideration of the chosen boundary conditions and the three dimensional form of the solder joints.

In future the model of the diffusion and migration driven IMC formation can be used to optimize a TLPS process under consideration of the chosen process parameters and the form of the solder joints.

Kurzfassung

Schlagworte: Intermetallische Phase, Diffusionslöten, Elektromigration, Thermomigration

Modeling the SAC Microstructure Evolution under Thermal, Thermomechanical and Electrical Constraints

Die aktuellen Lötkontakte für ICs basieren auf Löthöckern aus bleifreien Zinnloten. Für die weitere Miniaturisierung elektronischer Komponenten, oder die industrielle Anwendung von ICs unter extremen Umweltbedingungen werden jedoch robustere Lötkontakte benötigt. Ein vielversprechendes Verfahren ist in diesem Zusammenhang die Umwandlung einer bereits bestehenden Lötverbindung in eine intermetallische Phase (IMC). Das dazugehörige Verfahren heißt „Transient Liquid Phase Soldering“, kurz TLPS. Von zunehmendem Interesse für die zukünftige Anwendung von TLPS an Bauteilen ist die Beschleunigung der Phasenumwandelung bei gleicher Prozesstemperatur durch einen zusätzlichen Materialtransport in Folge von Elektromigration (EM) und Thermomigration (TM).

Vor diesem Hintergrund soll die Entstehung von IMCs unter dem Einfluss von EM und TM untersucht werden. Für die Belastungstests werden Package on Package (PoP) Strukturen verwendet. Das Ziel der Untersuchungen ist die Entwicklung eines allgemeinen Models zur IMC Entstehung in Lötpunkten. In Kombination mit einer Finiten Elemente Analyse (FEA) kann dieses Modell zur Vorhersage der Wachstumsgeschwindigkeit von IMC Schichten in Lötpunkten verwendet werden.

Zu Beginn der Untersuchung wird die atomistische Theorie zur Teilchenbewegung erläutert. Dieses Anhand einer idealisierten Kristallstruktur entworfene Modell wird dann and die besonderen Begebenheiten in den IMCs Cu_3Sn und Cu_6Sn_5 angepasst.

Durch eine mehrwöchige Temperaturlagerung der PoP Strukturen wird eine mögliche Verlangsamung des IMC Wachstums bei großen Schichtdicken ermittelt. Nachdem das Langzeitverhalten des IMC Wachstums bekannt ist, werden drei weitere Versuche bei unterschiedlichen Temperaturen durchgeführt. Aus den daraus folgenden Daten lassen sich die temperaturunabhängigen Materialparameter zur Beschreibung des diffusionsbedingen IMC Wachstums extrahieren.

Für die darauf folgenden EM und TM Belastungstests wird die Temperaturlagerung mit einem Gleichstrom und einem Wechselstrom kombiniert. Die Resultate ermöglichen eine Modellierung des IMC Schichtwachstums unter dem Einfluss von EM und TM auf Basis von temperaturunabhängigen Materialparametern.

Die ermittelten Materialparameter werden in selbstentwickelte Programme integriert um die Massenflüsse durch Diffusion, EM und TM zu berechnen. Durch den Vergleich der Simulationsergebnisse mit den Versuchsergebnissen werden die verwendeten Materialparameter überprüft. Anschließend werden die einzelnen Massenflüsse zu einem Gesamtmassenfluss addiert, aus dem sich auch die aktuelle Wachstumsgeschwindigkeit der IMC Schichten ergibt. Darauf Aufbauend erlaubt eine Aufteilung der simulierten Zeitspanne in viele Einzelschritte die dynamische Simulation des IMC Wachstums.

Die FEA erlaubt in diesem Zusammenhang die Vorhersage des IMC Schichtwachstums für eine breite Spanne möglicher Randbedingungen, so dass die Optimierung eines TLPS Prozesses unter Berücksichtigung der gewählten Prozessparameter und der dreidimensionalen Form der Lötpunkte möglich wird.

Résumé

Mots clés: composé intermétallique, brasage-diffusion, électromigration, thermomigration

Modeling the SAC Microstructure Evolution under Thermal, Thermomechanical and Electrical Constraints

La miniaturisation des circuits microélectroniques, leur assemblage tridimensionnel et leur utilisation dans des conditions environnementales extrêmement sévères nécessitent le développement d'alternatives plus robustes pour les contacts électriques. Une technique prometteuse est la transformation des contacts de brasure conventionnelle en composé intermétallique (IMC). Ce processus est appelé « Transient Liquid Phase Soldering « (TLPS). Le principal défi en ce qui concerne la TLPS est la prédiction de la formation de l'IMC, en fonction de la géométrie des joints de brasure, ou encore des conditions de fabrication. En particulier, on peut envisager d´accélérer la croissance des IMC par électromigration (EM) et thermomigration (TM), et ces ans augmenter la température des processus de fabrication.

Dans ce contexte, des tests accélérés permettant la formation d'IMC par TM et EM ont été effectués sur des structures « boîtier sur boîtier » (« *Package on Package* » ou PoP). L'objectif principal est le développement d'un modèle général permettant de décrire la formation des IMC dans les joints de brasure. Combiné avec une analyse par éléments finis (FEA) ce modèle pourra être utilisé pour prédire la formation des IMC dans les joints de brasure pour des structures et des profils de missions différents. Pour bâtir ce modèle, plusieurs étapes ont été nécessaires.

La première étape consiste à évaluer le modèle atomique de la diffusion dans les métaux de structure cubique à face centrée, pour les conditions spécifiques dans la structure cristalline de composés intermétalliques Cu_3Sn et Cu_6Sn_5.

Des tests de stockage à température élevée (TS) sont effectués sur de courtes durées et sur de longues durées, afin de déterminer les constantes de diffusion des deux phases de croissance des IMC. Trois autres tests à différentes températures sont effectués pour caractériser le comportement en température de la formation des IMC.

Pour évaluer et discriminer l'influence de l'électromigration, et de la thermomigration, les composants stockés à température élevée sont parcouru par un courant continuo un courant alternatif de forte densité. Les résultats permettent la modélisation de la croissance des intermétalliques sous l'influence de l'électromigration et de la thermomigration, sur la base de paramètres indépendants de la température.

Ces paramètres matériaux sont utilisés pour paramétrer le logiciel par élément finis, afin de calculer les flux de masse induits par la diffusion, l'électromigration et la thermomigration. La comparaison des résultats de simulation avec les résultats expérimentaux permet de valider ces paramètres. Finalement, les flux de masse individuels sont additionnés, et le flux total de masse est utilisé pour calculer le développement de couche d'IMC. Une simulation dynamique est possible en divisant le temps de test en plusieurs intervalles de temps. Ainsi, la simulation doit permettre de déterminer la croissance de la couche intermétallique, en fonction des conditions aux limites imposées, ou de la géométrie des joints de brasure. A l'avenir, le modèle de formation des IMC pourra être utilisé pour optimiser un processus TLPS.

Table of Contents

List of Abbreviations and Symbols

Abbreviations:

AC	**A**lternating **C**urrent
AF	**A**cceleration **F**actor
AF*	Acceleration factor with downtimes
AFT	**F**actor of **T**emperature **A**cceleration
APDL	**A**NSYS **P**arameter **D**esign **L**anguage
BGA	**B**all **G**rid **A**rray
BSE	**B**ack **S**cattered **E**lectron
C4	**C**ontrolled **C**ollapsed **C**hip **C**onnection
CAF	**C**onductive **A**nodic **F**ilaments
CME	**C**oefficient of **M**oisture **E**xpansion
CTE	Coefficient of thermal expansion
CoC	**C**hip-**o**n-**C**hip
CPU	**C**entral **P**rocessing **U**nit
CRT	**C**athode **R**ay **T**ube
CSP	**C**hip **S**cale **P**ackage
CTE	**C**oefficients of **T**hermal **E**xpansion
DC	**D**irect **C**urrent
DRAM	**D**ynamic **R**andom-**A**ccess **M**emory
DIP	**D**ual in **L**ine **P**ackage
ECM	**E**lectro**c**hemical **M**igration
EDS	**E**nergy-**D**ispersive X-Ray **S**pectroscopy
ECU	**E**ngine **C**ontrol **U**nit
EM	**E**lectro**m**igration
ENIG	**E**lectroless **Ni**ckel **G**old
Eq.	**Eq**uation
FEA	**F**inite **E**lement **A**nalysis
FEM	**F**inite **E**lement **M**ethod
fcc	**f**ace **c**entered **c**ubic
FR-4	**F**lame **R**etardant grade **4** (glass-reinforced epoxy laminate board)
GPU	**G**raphics **P**rocessing **U**nit
GWP	**G**rowth **W**orld **P**roduct
HTC	**H**eat **T**ransmission **C**oefficient
IC	**I**ntegrated **C**ircuit
I/O	**I**nput/**O**utput
IMC	**I**nter**m**etallic **C**ompounds
MEMS	**M**icro**e**lectro**m**echanical **S**ystems
MTTF	**M**ean **T**ime **T**o **F**ailure
NAND	**N**ot **And** gate
OSP	**O**rganic **S**olderability **P**reservative
PCB	**P**rinted **C**ircuit **B**oard
PoP	**P**ackage **o**n **P**ackage

ppm	**p**arts **p**er **m**illion
QFP	**Q**uad **F**lat **P**ackage
R&D	**R**esearch and **D**evelopment
SAB	**S**urface-**A**ctivated **B**onding
SD	**S**tandard **D**eviation
SE	**S**econdary **E**lectron
SEM	**S**canning **E**lectron **M**icroscope
SLID	**S**olid-**L**iquid **I**nterdiffusion **B**onding
SMB	**S**olid **M**etal **B**onding
SMD	**S**urface **M**ount **D**evices
SiP	**S**ystem **i**n **P**ackage
SoC	**S**ystem **o**n **C**hip
SSD	**S**olid **S**tate **D**isk
TE	**T**hermal **E**lectrical
TCT	**T**emperature **C**ycle **T**ests
TCR	**T**emperature **C**oefficient of the **R**esistance
TCU	**T**ransmission **C**ontrol **U**nit
TH	**T**emperature **H**umidity
TM	**T**hermo**m**igration
TL	**T**ime **L**imit to saturation
TLPS	**T**ransient **L**iquid **P**hase **S**oldering
TS	**T**emperature **S**torage
TSV	**T**hrough **S**ilicon **V**ia
TTF	**Time to failure**
UTS	**U**ltimate **T**ensile **S**trength
WLP	**W**afer **L**evel **P**ackaging

Symbols:

A	Contact surface
A_0	Pre exponential constant: moisture diffusion
a	Lattice constant
a_P	Pre exponential constant: power law
α	Linear temperature coefficient of Z**
α_T	Logarithmic growth rate: number of transistors per chip
B_0	Pre exponential constant: electrochemical migration
b	Logarithmic growth rate: IC package dimensions
β	Driving force for material accumulation
β_M	Exponential term: Moisture
β_{TM}	Reduction of H^M by crystal lattice/ion interactions
C	Number of Input/Output contacts per package
c	Exponential constant: temperature cycling tests
C_M	Moisture concentration
CME	Coefficient of moisture expansion
D	Diffusion coefficient
D_0	Diffusion constant

D_B	Bump diameter
D_C	Contact pad diameter
d	Contact diameter
δ	Logarithmic growth rate: costs per fab
E	Young’s Modulus
$\vec{E}$	Electric field
E_A	Activation energy
E_i	Energy
ΔE	Shift of the activation energy
e	Elementary charge
ε	Strain
ε_F	Fermi energy
ε_0	Vacuum permittivity
F	Force
f	Jumping frequency
G	Thermodynamic activity
g	Logarithmic growth rate: Input/Output contacts per package
g_n	Standard gravity
H	Drop Height
H_α	Energy transport by a crystal ion
H_C	Pre exponential constant: temperature cycling tests
H^M	Transport energy of the moving ion
H_m	Enthalpy change per activated complex
H_S	Heat of solution
H_V	Enthalpy change per vacancy
H_γ	Placement energy an ion in crystal lattice
h	IMC layer thickness (chapter 2 only)
h_B	PCB thickness
h_P	Planck constant
J	Mass flux density
j	Current density
K	Activity coefficient
K_C	Pre exponential constant: temperature cycling tests
k_B	Boltzmann constant
κ	Thermal conductivity
κ_e	Thermal conductivity by the electron gas
l	Length
M	Mass
M_O	Atomic mass
m	Mass fraction
m_C	Exponential constant: temperature cycling tests
m_e	Electron mass
m_e^*	Effective electron mass
N	Atomic density
N_C	Number of temperature cycles
N_D	Defect density

N_T	Number of transistors per chip
N_V	Vacancy density
n	Number of jumps
n_A	Atomic areal density
n_B	Exponential constant: Black equation
n_P	Exponential constant: power law
n_i	Number of atoms
η	Relative volume portion of the IMC layers
Ω	Atomic volume
P	Pressure
p	Logarithmic growth rate: growth world product
p_V	Probability of vacancy creation
ρ	Mass density
ρ_{el}	Specific resistance
Φ	Electrical potential
Q	Heat
Q^*	Heat of transport
Q^*_p	Phonon part of Q*
Q^*_e	Electron part of Q*
Q^{**}	Temperature dependent heat of transport value
R	Total distance
r	Passed distance per jump
r_H	Bohr radius
rh	Relative humidity
S	Entropy
S_D	Distance value
s_T	Thermoelectric voltage
σ	Mechanical stress
σ_e	Cross section for electron scattering
σ_H	Hydrostatic stress
σ_P	Cross section for phonon scattering
T	Temperature
t	Time
τ	Lifetime of the electrons
θ	Angle
U	Internal energy of a closed system
u	PCB deformation
μ	Chemical potential
V	Volume
v	Velocity
v_D	Debye frequency
v_p	Speed of sound
W	Work
w	Jumping frequency of an atom in one direction
$\ddot{\omega}$	Angular acceleration
X	Optional simulation result

Y	Constant: Deal Grove Model
Z	Valence number
Z_G	Constant: Deal Grove Model
Z*	Effective charge of the moving ion
Z**	Temperature dependent effective charge value

1 Introduction

1.1 Technical and Economic Background

For many years the miniaturization of transistors and the resulting increase of their performance and number per integrated circuit (IC) was the common way to create innovation. Moore's law predicted an exponential increase of the transistors number per IC and a permanent decrease of the costs per transistor. Unfortunately an exponential increase of costs goes along with the fulfillment of Moore's law and as a consequence the miniaturization on transistor level reaches its economic limits.
Against this background alternatives to the miniaturization on transistor level were needed. Alternative approaches for the exploration of new markets for microelectronic devices are the use of ultra large scaled logic devices under harsh environment conditions or the further miniaturization of microelectronic devices on package level by using three dimensional packaging solutions.
The melting point of conventional solders like SnAgCu is too low for the use under harsh environment applications. The low melting point of Sn based solders also has the consequence that they are easily affected by electromigration (EM). Reliability issues due to EM appear as a consequence of an increasing current density due to miniaturization. Hence alternative solders have to be used, and new connecting techniques are needed to create innovative microelectronic devices.

One promising technique for the development of future electronic devices is the diffusion driven transformation of Sn solders into intermetallic compounds (IMC) like Cu_6Sn_5 or Cu_3Sn. The related process is called transient liquid phase soldering (TLPS). The main benefit of Cu-Sn IMCs compared to common Sn based solders is the fact that their melting temperatures are a few hundred degrees higher than the melting point of SnAgCu. Hence the temperature resistivity of IMC joints is sufficient for harsh environment applications and they are not affected by EM induced reliability issues. IMC joints have also proven to be very resistant against corrosion or crack formation due to thermomechanical stress. Furthermore Cu-Sn IMCs were always present as interlayer between the contact pads and the solder bumps. As a side effect of miniaturization they will automatically become more and more important.

To enable the successful application of TLPS for the industrial fabrication of IMC contacts the characterization of the IMC formation in SnAgCu solder joints under consideration of the chosen process parameters and the form of the solder joints will be needed. Taking into account common packaging technologies, the characterization of the diffusion induced IMC formation should cover Cu-Sn IMCs being formed at direct Sn to Cu contacts, as well as Cu-Ni-Sn IMCs being formed in solder joints on Ni pads.

1.2 Previous Works and the Aims of this Investigation

In recent years several investigations of the diffusion driven IMC formation were performed. Based on temperature storage (TS) tests the formation of Cu-Sn and Cu-Ni-Sn IMCs in different solders, including SnAgCu, was investigated. Furthermore EM tests were performed. Unfortunately pure Sn joints, instead of common solders, were used for EM tests. For the formation of Cu-Ni-Sn IMCs only a few diffusion related parameters were available. Material values related to the TM induced IMC formation are completely missing for all Cu-Sn and Cu-Ni-Sn IMCs. Nevertheless for the use of TLPS the diffusion, EM and TM related material parameters are needed in a temperature independent form.

Hence the first aim of this investigation is the determination of the required material parameters for the description of the diffusion and migration driven Cu-Sn and Cu-Ni-Sn formations in SnAgCu solder joints. The second aim is the simulation of the IMC growth with the finite element method. The required material parameters are the activation energy for atomic motion (E_A), the diffusion constant of the single components in the IMCs (D_0), the effective charge of the moving ions Z* (EM parameter) and the heat of transport Q* (TM parameter) of every single component in the different IMC layers.

Against this background several TS, EM and TM stress tests will be performed on Package on Package (PoP) devices. The PoP devices include solder joints being directly placed on the Cu metal lines and solder joints being placed on Ni pads. After the stress tests, the IMC formation speed and the related mass fluxes in the IMCs will be calculated. Finally the atomic theory of diffusion enables the parameter extraction though the mass flux values.
Afterwards ANSYS®, user developed routines and the extracted material parameters will be used for a finite element analysis (FEA) of the IMC formation. In contrast with previous methods the FEA will enable the investigation of the IMC formation in three dimensional structures. In future the FEA of the IMC formation will support the development and the optimization of TLPS processes under consideration of the chosen process parameters and the shape of the solder joints.

1.3 Content

In the second chapter an overview of the economic and technical evolution of the microelectronics market will be given. It will be shown that new packaging concepts are needed for the development of new high-end electronics and the application of microelectronic devices under harsh environment conditions. Based on the consequences of further progress in miniaturization, and the use profile of harsh environment applications it will be shown that alternatives to the conventional Sn based solder contacts are necessary to fulfill the reliability requirements for future microelectronics devices.
The transformation of Sn based solder joints into IMC joints through TLPS will be introduced as a promising technique for the production of reliable electrical contacts for future microelectronic devices. The benefits of TLPS will be shown by comparing it to new techniques like sintering with Ag or Cu nano particles and by stating the promising results of previous reliability tests on IMC contacts.
In a detailed description of TLPS it will be explained why the prediction of the IMC formation speed dependence on the solder joints dimensions and the chosen process parameters is one of the main problems that have to be solved for an industrial application of TLPS.
Based on a principal description of the IMC formation under the influence of diffusion, EM and TM it will be shown which material parameter must be known to predict the IMC formation speed in solder joints. Knowing the required material parameters previous investigations will be evaluated and the available parameters will be summarized. A comparison between the required and the available material parameters will show which additional parameters will be needed to develop a general model for the EM and TM driven IMC formation in SnAgCu solder joints.

At the beginning of the third chapter the atomic theory of diffusion will be explained and the related Nernst-Einstein equation will be given. Afterwards the more specific equations of the diffusion, EM, TM induced mass fluxes will be stated. A physical interpretation of the relevant material parameters E_A, D_0, Z*, Q* will be given. Based on these interpretations it will be shown that the special conditions in the IMCs, like the high defect density and the temperature dependent solubility of the single components, have to be taken into account for a correct interpretation of the EM and TM induced IMC formation. In addition the Nernst-Einstein equation will be used to develop an empirical model of the Cu and Au accumulation due to local differences in solubility.

Based on this theoretical background the experimental procedure for the investigation of the diffusion and migration induced IMC growth and the following extraction of the material parameter will be explained. It will be shown that several temperature storage (TS), TM and EM tests at different temperatures have to be performed to get the D_0 and E_A, as well as temperature independent Z* and Q* values. Furthermore the TM induced IMC formation will be investigated by a separate stress test. For the EM stress tests TS will be combined with a direct current (DC), for the TM stress tests an alternating current (AC) will be used. The experimental setup will be shown, and Package on Package structures will be introduced as devices under test. The PoP structures include direct solder to Cu contacts and solder joints on Ni pads. The direct solder to Cu contacts allow the inflow of Cu from the metal line into the solder, while Ni pads act as diffusion barriers.

In the following, equations will be derived that enable the extraction of the mass flux values through the average IMC formation speed during the stress tests.

Diffusion, EM and TM are exponentially temperature dependent. Hence for the interpretation of the AC and the DC tests under consideration of Joule heating a FEA will be needed. Against this background the PoP will be measured through light microscopy and a FE model will be designed. Temperature measurements being performed during the DC and AC tests will be used as boundary conditions for thermal-electrical simulations. The simulation results will show the exact test temperature at the IMC layers under consideration of Joule heating.

In the first part of chapter four the average IMC dimensions in the top and bottom bumps before and after the TS will be documented. Furthermore the material composition of the IMC will be determined. In the following the mass flux values will be calculated through the average IMC formation speed. Knowing the diffusion driven mass fluxes at different test temperatures the E_A and D_0 of the single IMC components (e.g. Cu and Sn for the Cu-Sn IMCs Cu_3Sn and Cu_6Sn_5) can be extracted. If possible the resulting material parameters will be compared with literature values.

In the following, DC and AC tests will be performed and the mass flux values will be extracted. The mass flux due to EM will be determined by comparing the up- and the downstream tests. The mass flux due to TM will be extracted by subtracting the mass flux due diffusion from the average mass flux values during the AC and the DC tests. Afterwards temperature dependent "$Z^{**}_{(T)}$" and the "$Q^{**}_{(T)}$" values of the single IMC components can be calculated through the mass flux values. The final temperature independent Z* values become available by taking into account the influence of crystal defects on the electron flux. Taking into account the temperature dependent solubility of the single components in the IMCs, also temperature independent Q* values become available.

In the last regular chapter the extracted $E_{A,}$ $D_{0,}$ Z*, Q* values will be used to calculate the mass flux due to diffusion, EM, TM in the IMC layers. The compliance between test and simulation results will validate the extracted material parameters. Afterwards the single mass flux values will be added to a total mass flux. The total mass flux can be used to calculate the momentary IMC formation speed. A dynamic simulation of the IMC growth becomes possible by dividing the test time into numerous time steps, and by calculating the additional IMC formation for every time step. The main benefit of the FEA is its consideration of the three dimensional geometry of the solder joints. Finally the dynamic simulation of the IMC growth can used to predict the IMC formation during a TLPS process under consideration of the chosen process parameters (temperature, applied current, etc.) and the solder joint geometry.

2 Microelectronics Assembly and Packaging Trends

In this chapter the motivation for this work will be given by stating the main trends on the microelectronics market and their relation to new concepts of microelectronics packaging (sections 2.1-2).

By stating the side effects of miniaturization on package level (section2.3) and the conditions for the use of microelectronic products in the industry (section 2.4), the necessity of new techniques for the fabrication of electrical contacts will be shown. The benefits of IMC bumps and the related TLPS process will be shown by comparing TLPS to alternative techniques (section 2.4). Afterwards actual investigations on the reliability of IMC bumps will be stated (section 2.5).

In the last part of the second chapter the TLPS process will be explained in detail. The technical challenges being related to TLPS, as well as the available solutions in the literature will be shown. Based on the detailed description of TLPS the required material parameters for a process optimization will be stated. At least the experimental part of this work will be explained by comparing the required material parameters with the available ones in the literature.

2.1 Diffusion of Innovations on the Microelectronics Market

The aims of research and development (R&D) in microelectronics packaging are defined by marketing trends and consumer behavior. Following the concept “diffusion of innovations” described in [2.1] the main difference between a successful technical breakthrough, like personal computers or smart phones, and unsuccessful technical breakthroughs, like the unicycle, is the fact that successful concepts were adopted by a critical number of consumers and the further process became self-sustaining [2.1]. For new technologies their rate of diffusion in society depends on consumer resistance to innovations [2.2]. The power of consumer resistance is due to their free will, which simply allows the people to not buy a product even when no alternatives are available [2.3]. Furthermore, consumers are often able to create their own alternative, which was often seen in the information technology (IT) business [2.3]. The most radical way to enforce innovation is the elimination of the consumer’s free will. This can be done by using patents laws or by outlawing alternatives, like it was done with light bulbs in the European Union. Of course this way to enforce innovations has only a weak relation to R&D, because it is a more political one and it is not accessible for many products of the microelectronics industry. Hence the focus will be on alternative ways to enforce innovations.

Based on the time of adoption consumers are classified in five different groups [2.1]: Innovators, early adopters, early majority, late majority and laggards. While innovators are a small group being easy to convince and often being wealthy enough to carry high financial risks, the less flexible and more critical early and late majority define more than two-thirds of all possible customers. The number of users which have adopted a specific technology over time can be displayed by an S-curve (Fig. 2.1).

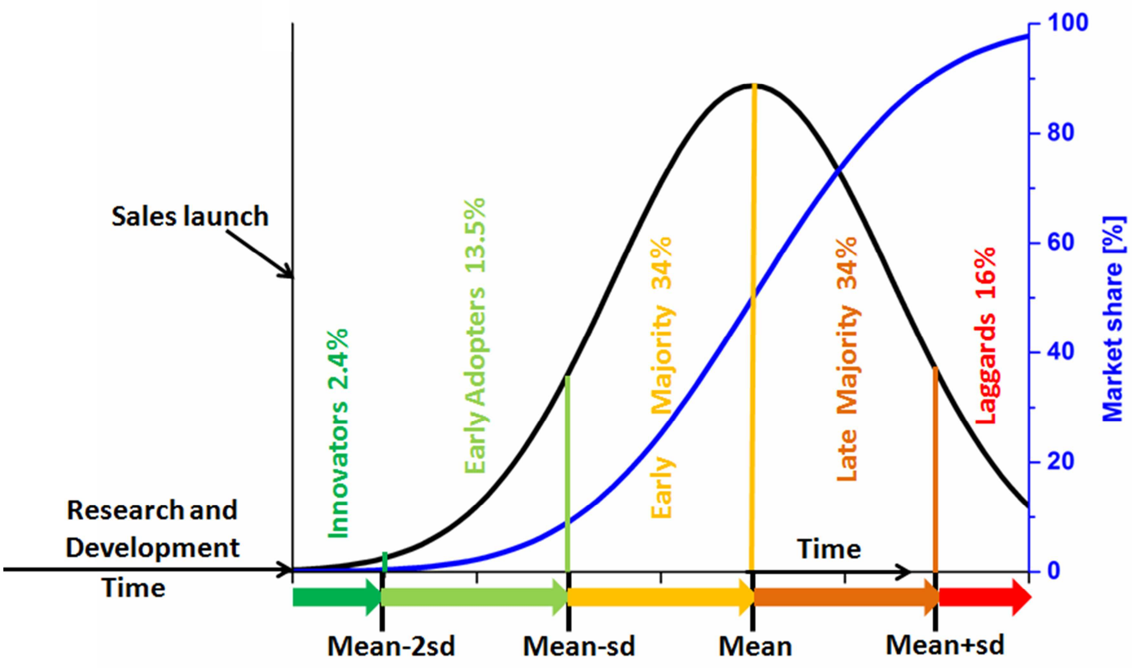

Figure 2.1: The five groups of possible consumers sorted by the time until adoption of an innovation (mean: mean time to adoption; sd: standard deviation)

Based on [2.3] and [2.4] ten possible reasons of private persons, companies or organizations, to avoid innovations can be stated:

- The **usage barrier** becomes relevant when private consumers or companies have to change their daily routine or their work flow: *for example long recharging times and a short driving range slowed down the dispersion of electric cars.*

- The **value barrier** means that, from the consumer point of view, the costs for a new product are not in relation with its benefits compared to previous ones.
  For a long time data storage devices based on integrated circuits like Solid State Disks (SSD) were too expensive and too limited in their storage capacity to replace the available ferromagnetic hard disks.

- **The risk barrier exists because** new products may include several risks, including financial risks like a high purchase price combined with a low quality, a short lifetime of the product, or a clear price decline when a new generation of the product appears. In addition many products, like medical drugs, include physical risks or they could damage previous investments because of compatibility risks.
  Often PC hardware is developed with a very short time to market. Consequently problems with compatibility and quality and a permanent price decline for new technologies appear and prevent investments.

- **Psychological barriers** appear when the innovation is in conflict with regional traditions and cultural values *(e. g. skirts for men)* or the responsible company/institution has image problems.

In addition companies have to face several economic risks during development [2.3-4].

- **Access to market barrier:** the company does not have a foot print on the relevant market or an infrastructure to sell the product. *For example software has to be compatible with a limited number of existing operating systems.*

- **Expertise barrier:** Companies often specialize in a specific field and they try to improve their efficiency instead of making experiments on new fields. As a consequence companies have problems to follow rapid innovations on the market or they have problems to reach new markets. For example during the change from cathode ray tube (CRT) monitors to flat screens most European companies in that field were replaced by competitors. The expertise barrier is more a management than a R&D problem. It can be overcome by joint ventures, with research alliances including other companies and universities, or by acquisition of innovators [2.3].

- **Operations barrier:** In many companies and especially in the semiconductor business the fabrication process is very complex and sensitive to changes. As a result the companies are very conservative when they adjust their processes.

- **Development barrier:** Difficulties to transform a prototype into an industrial product (*a permanent problem of carbon nanotubes).* Also pure physical problems like a high RC delay or increasing leakage current as consequence of miniaturization on transistor level are development barriers*.*

- **Resource barrier:** The costs for development are too high or the expected income is too low. This problem is often linked with the development barriers: *for example high k dielectrics by replacement gates or the use of FinFETs for commercial products. Furthermore the access to raw materials, like noble earths, can be difficult.*

- **Regulatory barrier:** governmental laws and regulation like safety standards or patents can lead to an economic failure of innovations. *Examples are the problems of nuclear or genetic engineering in Germany.*

An interesting point about [2.4], being written in the 1980s, is the fact that the development and the financial barrier were related to entrepreneurs, but today the costs for the fabrication of leading edge products in the semiconductor business are so high that these problems are relevant for larger companies too.

A reasonable number of consumers have to adopt an innovation before it becomes a fast selling item. The marketing concepts to pass this critical time are often directly connected to R&D and many solutions can be given with new IC packaging concepts:

- A conventional concept to overcome **the usage barrier** is the integration of an innovation in an existing product [2.2]. IC packaging is directly linked to this strategy by the "More Than Moore" concept. One example is the integration of GPS functions or miniaturized digital cameras in mobile phones.

- In the IT business a clear increase of the product performance is the favored solution to get over **the value barrier**. Especially in microelectronics a better performance is combined with new multimedia functions or additional ways to use the same product like the appearance of notebooks as portable PCs. A better performance of microelectronic devices can be realized by down scaling on transistor level (Moore's law [2.5-6]), but it is also possible to increase the performance by a further integration on package level ("More Than Moore"). For example the performance of Dynamic Random Access Memory –DRAM-, used for computer memory, and NAND memory, used for Solis State Disks (SSD), was improved by connecting stacked ICs with Through Silicon Vias (TSV) [2.7].

- The **risk barrier** is directly related to the reliability and the aging of microelectronic products. Strict quality rules for suppliers like "zero ppm" (failures) in the automotive area are an efficient way to reduce the financial risks for the producers and the customers. Also more robust and energy efficient technologies like SSDs can help to improve the reliability and usability of mobile electronic devices.

- In many cases **the psychological barriers** like regional traditions are very difficult to get over, or it is simply impossible. Nevertheless, in case of image problems, improved quality and reliability concepts can help to create a new image of a company or a brand, like it was done by the Japanese car manufacturers by solving their quality problems [2.3], or by the introduction of "zero ppm" to solve the teething problems that appear with the use of microelectronic devices in the automotive area.

- **Regulatory barriers** can also be used to increase the diffusion rate of an innovation [2.2] like the restriction for the use of SnPb solders led to the development of reliable lead free SnAgCu soldering processes [2.8].

- To overcome the **operations barrier** the fabrication process of a new product must be compatible to the existing production processes. For example Wafer Level Packaging (WLP) enables the fabrication of Ball Grid Arrays (BGAs) and testing of the ICs before dicing [2.9].

- **The development barrier** and the **resource barrier** are the main problems for innovations in microelectronics and they have excluded many fabricants from the semiconductor market [2.10]. The development of reliable three dimensional packaging concepts may help to reduce the cost for the integration of new functions in electronic devices. The integration of simulation based reliability investigation reduces the development costs by replacing physical experiments and expensive trial and error procedures.

Looking on the possible solution to overcome the customer resistance to innovation and to enable the economic success of innovations on the semiconductor market, the "More than Moore" philosophy is the relevant link between R&D in microelectronics packaging and the evolution of the consumer market. Furthermore R&D works can be supported by simulations to reduce the development and financial risks and to support the cost effective analysis of possible reliability problems, including a fast way to develop and benchmark alternative solutions.

2.2 “More Moore” and “More than Moore”

For a long time miniaturization on the transistor level was the main concept to drive innovations in microelectronics [2.3]. The critical parts of the transistors were scaled down with the electric field kept constant [2.6]. As a consequence a rising number of transistors was combined with a rising operating frequency and the resulting exponential increase in the IC performance was a efficient way to outperform the costumer’s resistance due to the value barrier. Nevertheless in the last years the miniaturization on the transistor level reached its physical and economic limits. Today transistors have a gate length of 22nm [2.11-12] while quantum mechanics (leakage current) and signal transmission delays (RC-Delay) limit the performance and the usability of the resulting devices [2.13-14]. Consequently scaling on the transistor level, often called “More Moore”, is very expensive (2-3 billion dollars per fab [2.10, 2.15]) and became a reason for the collapsing of semiconductor manufacturers on an unstable market [2.10]. Furthermore more complex ICs need more input/output terminals and interconnections on Printed Circuit Boards (PCB). Hence they lead to growing costs for the PCB fabrication [2.16].

Following Moore’s law the semiconductor industry doubled the number of transistors every two years. Unfortunately also the costs for semiconductor fabs are increasing by 14% per year and limit a further evolution [2.10, 2.15, 2.17]. Following a statement of Moore, that 1% of the Gross World Product (GWP) is spent for microelectronics [2.17] and expecting 15 new fabs per year, the whole income of the microelectronics industries would be reinvested in new fabs (no money for development or employees) in 2035 (Fig. 2, left). Of course this is impossible, and the number of transistors per chip is coupled to the growth of the GWP. Expecting constant costs per chip and no economic limitations, the number of transistors would be given by (2.1) with $N_{2010}=1x10^9$ transistors per chip since 2010 and a logarithmic growth factor $\alpha_T=0.34$ for Moore’s law [2.17]. The growth rate being coupled to the GWP would be given by (2.2). The additional logarithmic growth factor would be $\rho=0.04$ when the GWP growth is 4% per year [2.18] and $\delta=0.13$ represents the growing costs per fab. When Moore’s law is coupled with the economic boundary conditions the number of transistors is doubled every 3 years (Fig. 2, right).

$$N_{T,1(t)} = N_{T-2010} \cdot exp[\alpha_T \cdot (t-2010)] \quad (2.1)$$

$$N_{T,2(t)} = N_{T,1(t)} \cdot exp[(\rho-\delta) \cdot (t-2010)] \quad (2.2)$$

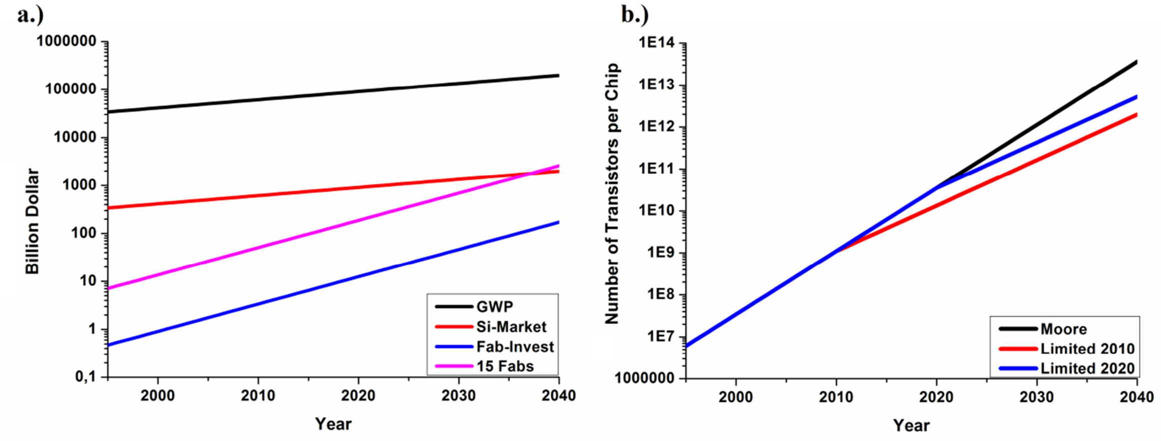

Figure 2.2: Evolution of the Growth World Product (black) and the microelectronic market (red) against the increasing costs for one (Fab-invest) and fifteen semiconductor fabs (a). Number of transistors per chip predicted by Moore (black) and limited by the economy from 2010 (red) or 2020 (blue)

Under these conditions, scaling at the transistor level cannot be the only source of innovation in microelectronics and two new concepts were created to bring innovations to the semiconductor market:

- The first concept is called “More Moore”, it is based on further downscaling of the existing transistor technology and alternatives to the existing transistor structures. The main areas of research are the integration of compound semiconductors (GaAs or InSb).
  On silicon wafers, the replacement of the transistor gate by nanowires or even the use of organic cells as information processors [2.19]. At the moment this is fundamental research which is not related to IC packaging.

- The second concept is called “More than Moore” and it is based on the fact that the barriers to innovations do not have to be passed by an increase of the single chip performance only. It is also possible to integrate new innovations in existing products. This can be done by combining digital components on one chip (“System on Chip” - SoC), e.g. today Central Processing Units (CPUs) for notebooks often include a Graphics Processing Unit (GPU). A further integration is also possible on the package level by combining non-digital with digital systems (“System in Package” – SiP) [2.20]. In this case a CPU can be combined with MEMS (“Microelectromechanical systems“), e.g. as a sensor for an energy harvesting device. Nevertheless “More Moore” can drive the evolution of More than Moore concepts [2.21] e.g. by increasing the performance of ICs being responsible for the data analysis in a SiP device with a complex sensor.

Following early concepts of a “More Than Moore” roadmap [2.20-21] its further evolution is based on three dimensional packaging. In addition the automotive industry uses integrated sensors for engine control [2.22] and the mining industry wants to place measurements-while-drilling systems closer to the drill bit [2.23]. In contrast with PCs or mobile electronics, the use of chips in cars or drill heads goes together with harsh environment conditions. In addition the presence of dozens of ICs in a car means an accumulation of their failure risks. To avoid high failure rates, the automotive industry is forced to reduce the failure rate of the used ICs under harsh environment conditions on a minimum (<0.1ppm) [2.24].
The “More than Moore” concept, driven by the “Diffusion of Innovations” on the microelectronics market and the economic limits of “More Moore”, has three relevant consequences from the reliability point of view:

1. The dimension of packages and their electrical contacts shrink as a consequence of three dimensional integration on the package level.
2. Chip packages are used more under harsh environment conditions (high temperature/ humidity or stress by mechanical shocks).
3. The strict reliability conditions for the industrial application (automotive, mining, aerospace) of ICs require a very good understanding of possible failure mechanism at the transistor and package levels.

In the following sections it will be shown how new soldering concepts could address the challenges of the different "More than Moore" concepts. Furthermore it will be shown that the further miniaturization on package level as well as the harsh environment application of microelectronics leads to growing importance of intermetallic compounds (IMCs) as soldering materials.

2.3 Three Dimensional Integration at the Package Level

The main purpose of three dimensional integration at the package level, like System in Package (SiP), is the placement of a growing number of ICs on the same foot print and a reduction of the signal propagation time between the components. A growing number of ICs on the same surface is reached by stacking and a reduced distance between the components can be realized by more local connections. In both cases the result is an increase in the product performance going together with a growing number of in and out contacts (I/Os) and the down scaling of the associated solder joints. Unlike the integration on the IC level, SiP allows the combination of different technologies in one package: like logic-devices on Si substrates and GaAs based high frequency devices [2.25].

In [2.26] the single package evolution is described in detail: the first two steps in the evolution were the through-hole technologies like Dual in Line Packages (DIP), with contact pins on two sides of the package (1970s) and Surface Mount Devices (SMD) with contact pins on all four sides (Quad Flat Package or QFP) in the 1980s. In the 1990s SMD was advanced by Ball Grid Arrays (BGA) which enable the use of the whole package surface for solder contacts. With BGAs it was possible to reduce the package foot print close to the IC dimensions (Chip Scale Package or CSP). Also the active side of the ICs can be used for the BGAs. The related technique was introduced by IBM and is called C4-Flip-Chip (controlled collapsed chip connection) [2.27].

Different packaging techniques from SMD to CoC are visualized in Fig. 2.3. Changing the packaging technology from DPI to QFP and from QFP to BGAs increased the number of available I/Os without changing the dimension of the solder contacts or a degradation of their reliability [2.27]. The through-hole or SMD techniques are very robust in mechanical loads and easy to assemble, so they are still in use for single passive components like single resistors or capacitors.

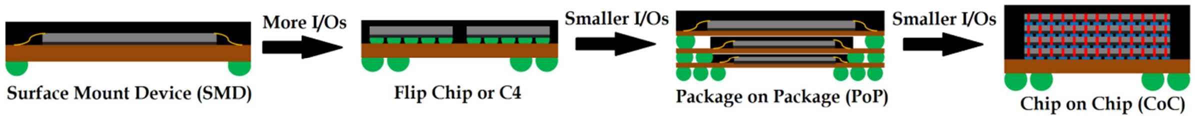

Figure 2.3: Important steps in the evolution of IC packaging from a relatively low device density applicable by SMD to a high device density applicable by CoC

The next steps of integration at the package level were three dimensional packaging concepts, like Package on Package (PoP). A PoP structure is built up by two or more packages being placed on top of each other. The packages are connected with BGAs. If a PoP consists of two packages the upper one is called "top" and the lower one is called "bottom". In the same manner the bumps of the BGAs are called "top- or bottom bumps".

PoP enabled the placement of several ICs on the same food print. Hence the device density could be rapidly increased. Nevertheless the stacking of packages also results in a growing number of required contacts from the upper to the lower packages, while the package surface keeps the same. Consequently the diameter of the solder balls is decreasing from the upper to the lower packages.

Over the last years vertical electrical interconnects called Through Silicon Vias (TSVs) appeared [2.28]. TSVs are directed through the Si substrate and they enabled the stacking of ICs to Chip-on-Chip (CoC) devices as shown in Fig 2.4. The benefits of CoC are the high number of stackable ICs and the minimum distance between the single chips [2.29]. Those benefits can be developed by wafer thinning, which also reduces the development barriers for TSV contacts. Problems with yield can appear, when a failure during the CoC process damages several ICs at once. Against this background it is possible to combine PoP with CoC to increase the number of available ICs per package while limiting risks to the yield [2.30].

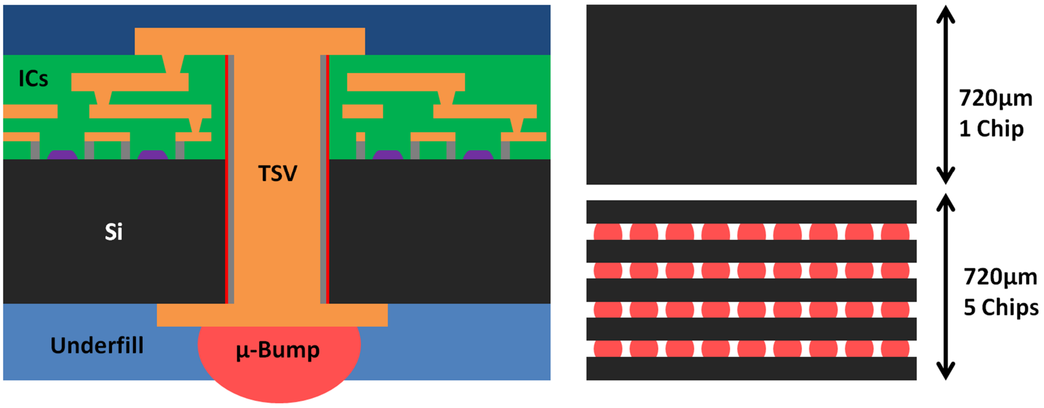

Figure 2.4: TSV on the active side of the wafer (left). In combination with wafer thinning, TSV can be used to increase the number of chips per volume (right)

In case of BGAs the processing of the contact pads and the solder joints can be done with lithography [2.29, 2.32] and like the number of transistors per chip also the number of contacts per package is increasing exponentially [2.26]. In [BGA-Trends] a growth rate of 1.1% per year is given for the number CSP contacts, while the package size decreases 6% per year. The main trend for the number of possible I/Os per package (C), for the contact diameter “d” and for the contact area (A) of single contacts can be described with (2.3-2.5). In this case the growth factors for the number of I/Os is g = ln (1.011) = 0.097 and the factor for the package dimension is b = ln (1.06) = 0.06.

$$C_{(t)} = C_{2001} \cdot exp[g \cdot (t - 2001)] \quad (2.3)$$

$$d_{(t)} = d_{2001} \cdot exp[-0.5 \cdot (g + 2b) \cdot (t - 2001)] \quad (2.4)$$

$$A_{(t)} = A_{2001} \cdot exp[-(g + 2b) \cdot (t - 2001)] \quad (2.5)$$

BGAs are connected with a reflow process (Fig 2.5). The reflow process begins with deposition of the solder on the contact pad area of the chip side. Afterwards the structure is heated to melt the solder. In case of SnPb this means a maximum temperature of more than 180°C and in case of lead free solders a maximum temperature of more than 200°C [2.33]. During the reflow the surface energy of the molten solder leads to the round shape of the final contacts. The molten solder is pressed on the contact pads of the board. The reflow process leads to an IMC formation between the contact pads and the solder joints [3.34].

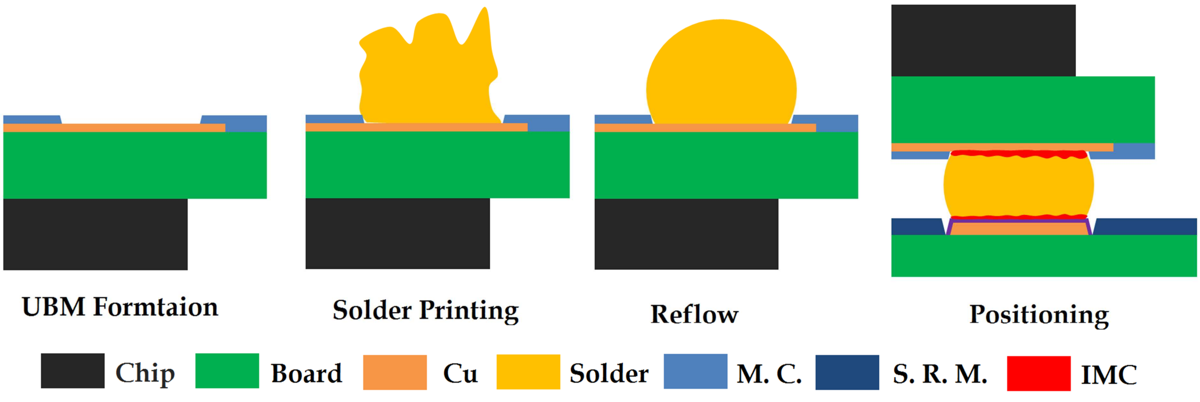

Figure 2.5: Visualization of BGA processing with solder printing and BGA contacting with reflow

The dimension of the IMCs (h) depends on the duration of the reflow process and the chosen process temperatures, but it is independent from the size of the solder contacts [2.34]. Hence the relative volume of the IMCs, compared to the total volume of the solder contacts, is growing. Based on (2.4) the trend of the solder volume is described by (2.6). Considering the IMC layers as ball sections (2.7) the relative volume of the IMCs (η) can be described by (2.8.) In Fig. 2.6 a scenario for CSP-BGAs solder bumps is shown. The starting diameter is 56µm [2.20] in 2010 and the IMC thickness after reflow was set to h=3.3µm [2.35].

$$V_{(t)} = V_{2010} \cdot exp[-1.5 \cdot (g + 2b) \cdot (t - 2010)] \quad (2.6)$$

$$V_{IMC(t)} = \frac{2h^2\pi}{3} \cdot \left(1.5 \cdot d_{(t)} - h\right) \quad D \geq 2h \quad (2.7)$$

$$\eta_{(t)} = \frac{V_{IMC(t)}}{V_{(t)}} \quad (2.8)$$

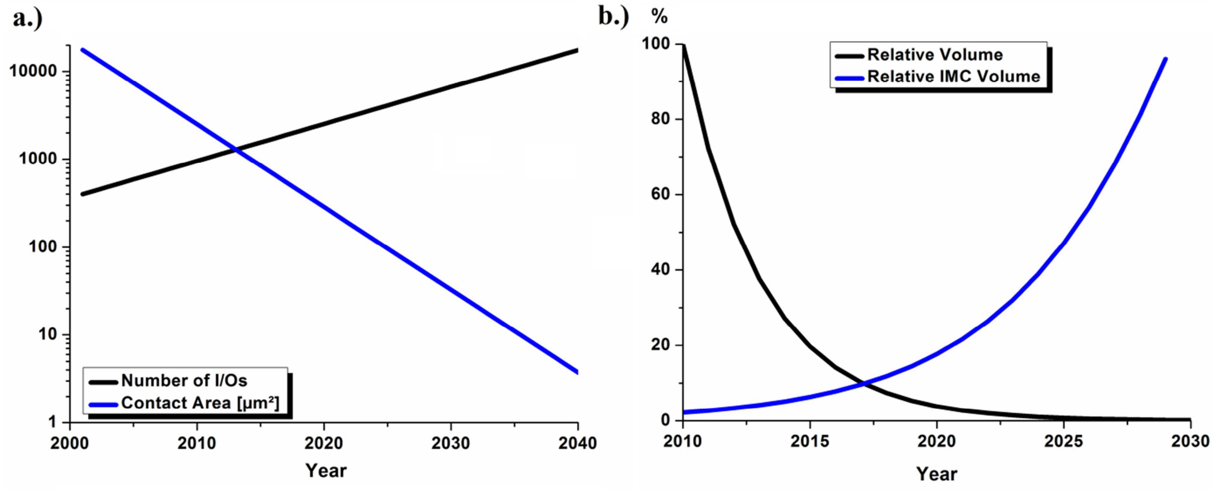

Figure 2.6: Trend of available I/Os per package and resulting contact surface of single contacts (a). Percentage of the remaining solder contact volume compared to 2010 and the relative portion of the IMC layers (b)

Following the scenario in Fig 2.6 it becomes clear, that the down scaling of the solder joints finally leads to pure IMC micro bumps which are formed during the reflow process. Such a transformation is normally called Solid-Liquid Interdiffusion Bonding (SLID). In addition the contact area of the solder joints is rapidly decreasing because the rising number of I/Os is combined with a shrinking package size.

2.4 Soldering Techniques for Harsh Environment Applications

In automobiles, public transport, airplanes or in the raw materials industry a rising number of ICs, being operated under harsh environment conditions, can be found. In cars certain number of ICs is used for comfort and entertainment and works normally under standard conditions (T_{max}<45°C) [2.22]. Beginning with new restrictions regarding fuel consumption, more effective engines were needed and as a consequence more powerful sensors based on microelectronic devices replaced pure mechanical systems [2.22]. In case of Engine or Transmission Control Units (ECUs & TCUs) the packaged ICs have to be placed close to the engine [2.22]. Unlike entertainment systems these sensors have to face harsh environment conditions and new solutions for packaging and soldering have to be developed.

As a first step TCUs or ECUs were placed at a relatively cold point of the engine and the maximum ambient temperatures were expected to be below 150°C [2.36]. If sensors will be integrated into the engine their maximum temperature goes up to 200°C [2.36]. Furthermore the use of sensors in the combustion chamber ($T \approx 500°C$) or in the exhaust system ($T \approx 800°C$) could be needed for future applications [2.22].

The melting point of soft, tin based solders, is 183°C for $Sn_{63}Pb_{37}$ and more than 200°C for lead free solders like SnAgCu (SAC) [2.38]. The diffusion of atoms in the crystal lattice becomes relevant at temperatures above 80% of the melting point [2.39]. The diffusion of atoms reduces the creep resistance of the solders. As a consequence reliable solder contacts can only be guaranteed, when the operation temperature is below 80% of the melting temperature [2.40-41]. Finally it is clear, that due to their relatively low melting point, soft solders are not of use for harsh environment applications.

2.4.1 Alternative Materials

A common alternative to soft solders are hard solders like AuSn, but those solders need high soldering temperatures which can exceed the temperature limit of conventional Si chips and their plastic packages ($T > 150°C$) [2.42]. Nevertheless for harsh environment applications the chips and their packages also have to survive high operation temperatures ($T > 300°C$) [2.42]. Hence instead of Si chips or plastic packages more temperature resistant materials have to be used. Known alternatives are semiconductors with a big band gap (SiC or GaN) as substrates and glass covers for IC packages [2.42-44]. High operation temperatures also enable increased soldering temperatures and the use of hard solders for microelectronic contacts. Unfortunately the maximum operation temperatures of hard solder contacts would not be sufficient for future harsh environment applications ($T > 500°C$). Consequently alternative soldering techniques have to be developed.

2.4.2 Direct Bonding

One alternative to conventional soldering is direct bonding. During direct bonding two surfaces are pressed on each other (10kN for a 200mm wafer [2.29, 2.45]), then two different bonding procedures can be executed [2.29]:

- **Thermocompression Bonding**: a high process temperature leads to diffusion and the resulting mass flux forms the interface. For thermocompression bonding no vacuum chamber and no surface preparation is necessary. Hence the technique is easy to handle and cost efficient, but the process time is exponentially temperature dependent which can lead to problems when sensible devices like MEMS have to be connected (high value barrier).

- **Surface-Activated Bonding (SAB)** is based on an electron transfer at the metal surface. The crystal structure of metals includes a free electron gas with very mobile non bonded electrons, which enables direct bonding at low process temperatures. Electrical insulators or semiconductors can be connected too, but due to their bonded electrons high process temperatures are needed. An illustration of SAB is given by Fig. 2.7. In the case of Cu the high electron mobility enables reliable Cu to Cu bonding at room temperature [2.46], when the metal surfaces are activated by cleaning. The cleaning step can be done with an ion beam (e.g. with Ar ions [2.46]). Surface-Activated bonding has to be done under ultra-high vacuum condition which increases the process complexity and costs (high resource and development barriers) [2.29].

In both cases the toughness of the Cu to Cu joints is clearly increased when the bonding process is followed by an annealing step which can be done at process temperatures between 100°C and 400°C [2.47]. The maximum operation temperature of the final contacts depends on the melting temperature of the used materials ($T_{use}<0.8T_{melt}$).

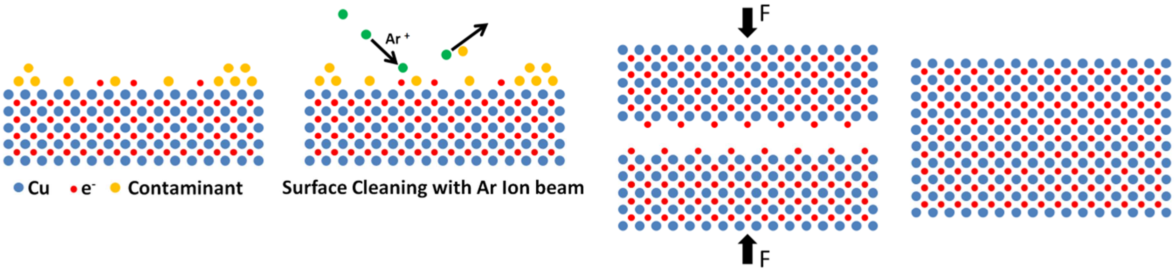

Figure 2.7: Principal illustration of surface activated bonding for metal contacts

2.4.3 Sintering with Nano Particles

Another alternative is the sintering of solder pastes with nano scaled particles solved in an organic binding material. This sintering technique takes advantage of the fact that the melting point of nano scaled grains is lower than the melting point of the bulk material and that the surface to volume ratio of the nano particles is very high [2.48]. During the sintering process a relatively high pressure is necessary (e.g. 20MPa) and the binding material between the nano particles has to be burnt out [2.49]. The possible process temperatures are going down to 100°C for nanosilver paste [2.50], while the maximum operation temperature is related to the melting temperature of the material ($T_{use}<0.8T_{melt}$).

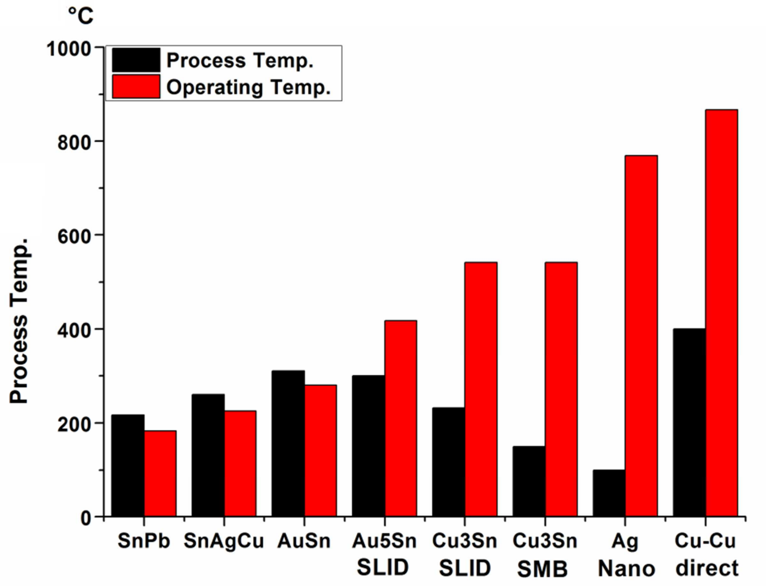

Figure 2.8: Process and operation temperatures for different soldering techniques including lead and lead free soft soldering, SLID, and non-diffusion soldering techniques like the sintering of Ag nano paste and Cu-to-Cu SAB

2.4.4 Comparison

In Fig. 2.8 a comparison of different soldering techniques is shown. Hard soldering techniques enable operating temperatures being in range of the actual harsh environment specifications, but they would not be sufficient for future applications. Furthermore their high process temperatures are often above the temperature tolerance of common packaging materials [2.42] and they lead to high stress values in the processed ICs [2.51].

The maximum operation temperature of direct bonding contacts is only limited by the melting point of the used materials while the bonding process can be performed at room temperature [2.46]. The maximum operation temperature of direct bonding contacts is in range of actual and future harsh environment applications, but low bonding temperatures are only accessible under ultra-high vacuum conditions. Furthermore Cu oxidation increases the contact resistance during bonding at atmosphere [2.29], but for microelectronics a low contact resistance is needed to limit the RC delay. Furthermore high pressure is needed to form the contact [2.29], but like the intrinsic thermal stress also an external mechanical stress can damage a chip. The use of pyramidal formed contacts instead of a flat surface is one approach to reduce the required pressure during the bonding process [2.52].

Sintering with Ag nano pastes enables similar operation temperatures like direct contacting and it does not need an annealing step, but it is also based on high pressure during the soldering process. Furthermore silver is several times more costly than tin or copper [2.38].

2.4.5 Transient Liquid Phase Soldering

As a consequence of various problems to contact high performance devices for harsh environment applications the industry is very interested in Transient Liquid Phase Soldering (TLPS). TLPS is a diffusion based soldering process which transforms a high melting material like Cu or Au and a low melting material like Sn into an IMC connection [2.53]. In principal TLPS can be performed by two different ways: by solid state interdiffusion without melting one of the components [2.54], or by melting the component with a low melting point (e.g. Sn) while the other component keeps in its solid state [2.53]. The first way is called Solid Metal Bonding (SMB) and has the benefit of a low process temperatures compared to the second way, but the process design needs a good understanding of diffusion in solids and the bonding pressure is relatively high [2.54]. The second way is more common and it is called Solid-Liquid Interdiffusion Bonding (SLID) [2.29] Compared to other soldering techniques for three dimensional integration or harsh environment applications the two different TLPS processes have several advantages from the industrial point of view:

- The process temperatures are below 300°C ($T_{melt,Sn}$=232°C), so the process is applicable for many microelectronic components (low usage barrier) [2.29].
- The resulting IMCs have high melting points (e.g. 676°C for Cu_3Sn= [2.55]) so they can be used for common and for future harsh environment or high power applications (low value barrier).
- In case of Cu-Sn TLPS the used materials are not expensive and readily available (low resource barrier) [2.38].
- The used materials have an extensive heritage in the microelectronics industry (low operations barrier) [2.29].

But there are also problems that have to be solved:

- The IMCs are brittle, which can lead to crack formation during drop or temperature cycle tests (high risk barrier). In case of a big mismatch in thermal expansion of the used package and chip materials the more expensive Au-Sn TLPS has to be used [2.29].
- During the formation of Cu_3Sn out of the previous Cu_6Sn_5 IMC voiding can appear due to imbalance in the Cu diffusion in both IMCs or as consequence of impurities in the previous metal layers [2.29] (high development barrier).
- During the Cu-Sn IMC growth long Cu_6Sn_5 whiskers are formed which could affect the mechanical strength of the IMC contacts (high risk barrier)[2.56].
- For bigger solder joints the formation of the IMC contact depends on the solid state diffusion rate in the IMCs and the bonding process needs a lot of time (high operation barrier) [2.53].

Overall TLPS is a very promising soldering technique and has the strong relation to the diffusion driven IMC formation in solder bumps. The process temperatures and the process duration can be decreased by combining SLID with SMB. In practice the IMC formation is an intrinsic effect of the reflow soldering process (SLID) and the SMB process step can be added by a following temperature storage episode. The temperature storage can be combined with an applied current to increase the total mass flux by adding electro- and thermomigration to the diffusion process [2.150]. In all cases the physics of diffusion have to be investigated to calculate the process time and to enable a reliable process management. In addition several forms of migration have to be combined to reach realistic process times at low process temperatures or for the creation of more thick IMC layers.

2.5 Influence of IMC Formation on Microelectronics Packaging Reliability

IMC and tin solders clearly differ in their material properties. Hence the formation of IMCs and their interaction with the remaining material affects the reliability of solder joints. Furthermore the lifetime of pure IMC joints, like the micro bumps for CoC stacks, clearly outperforms the test results of conventional solder joints.

In general four different effects can lead to defective solder joints: Moisture, thermal mismatch, external stress loads and electromigration.

2.5.1 Moisture

During use or storage IC packages and their PCBs are exposed to atmospheric moisture which diffuses into them. Especially plastic materials and the substrate/copper interfaces are diffusion paths for moisture [2.57]. When the presence of moisture in the package or the PCB is combined with heat (e.g. during the reflow process) vaporizations can lead to structural damage, like “popcorn cracking” of the packages, or the delamination of interconnects on the PCB [2.58-61]. In addition the metal lines and solder joints can be degraded by corrosion [2.62].

2.5.1.1 Popcorn cracking and delamination

During reflow the package temperature is above 200°C, and the moisture present becomes vaporized. The resulting vaporization stress is added to thermal stress due the thermal deformation of the materials and can lead to cracking at the internal interfaces of the package [2.63]. During the reflow process the stress in the materials and the delaminated regions depends on the moisture concentration before reflow (C), the Coefficient of Moisture Expansion (CME) and Young's modulus (E) of the affected materials (2.9) [2.64]. With an increasing temperature the Young's modulus of the relevant plastic materials decreases, while their CME increases until the glass transition temperature is reached [2.63].

$$\sigma_{(T,t)} = E_{(T)} \cdot CME_{(T)} \cdot C_{M(T,t)} \qquad (2.9)$$

The moisture concentration depends on the time of storage (t), the storage temperature (T_s) and the moisture diffusivity (D). The partial differential equation of the resulting moisture equation (2.10) is difficult to solve and the calculation of the moisture profile is often done with the Finite Element Method (FEM) [2.60, 2.65].

$$\frac{\partial C_M}{\partial t} = D \cdot \left(\frac{\partial^2 C_M}{\partial x^2} + \frac{\partial^2 C_M}{\partial y^2} + \frac{\partial^2 C_M}{\partial z^2} \right) \qquad (2.10)$$

Nevertheless a few general statements about the resulting moisture profile can be made:

- The moisture concentration grows continuously until the maximum concentration C_{sat} is reached.
- The time until the concentration is balanced out depends on the moisture diffusivity. That means the plastic materials and interface layers reach their maximum concentration faster than other parts of the package.
- The closer a surface is placed to the source of moisture the faster C_{sat} is reached.

As consequence the maximum moisture concentration C_{sat} can be found at the plastic interfaces close to the outer faces of the package or PCB (2.11). The maximum moisture concentration follows an Arrhenius relation (2.12). Hence there is an exponential relation between the storage temperature and the resulting stress at the interfaces.

$$\sigma_{(T,t)} = E_{(T)} \cdot CME_{(T)} \cdot C_{M,sat} \qquad (2.11)$$

$$C_{M,sat} = P_{ext} \cdot A_0 \cdot exp\left(\frac{E_A}{k_B \cdot T_S} \right) \qquad (2.12)$$

P_{ext}= exterior vapour pressure at T_S; A_0 = pre exponential constant, k_B = Boltzmann constant,
E_A= activation energy

Temperature Humidity (TH) tests are often performed to evaluate the resistivity against moisture induced stress. They are performed at high temperatures and a high relative humidity (rh). Typical test conditions to prove the moisture reliability of packages or PCBs are 85°C/85%rh [2.61]. The simulation results for moisture diffusion in the PoP devices and the resulting hydromechanical stress are shown in Fig. 2.9 [2.65].

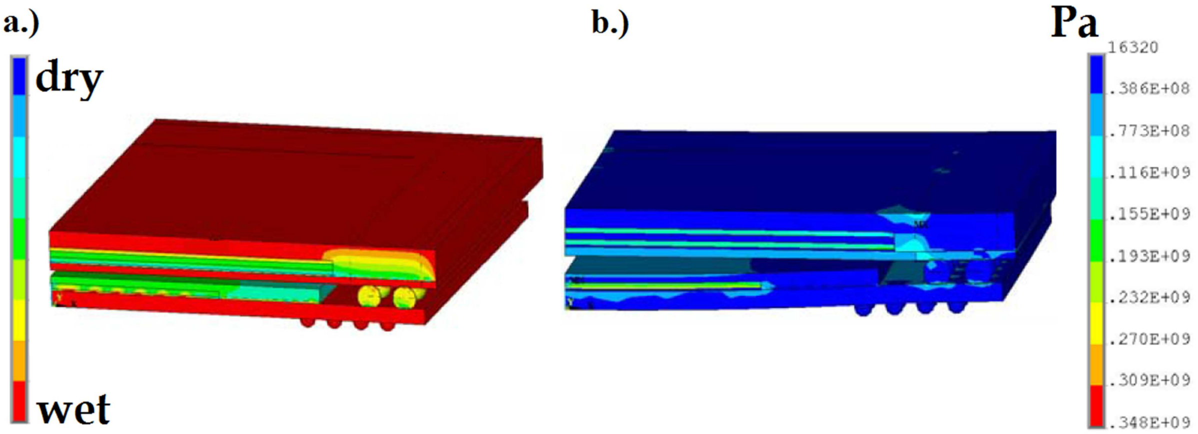

Figure 2.9: ANSYS® simulation of moisture concentration (a) and resulting hydromechanical stress in the PoP device after a TH test at 85°C/85% rh (b) [2.65]

Previous TH tests did not show any influence of moisture on the IMC formation speed [2.66]. When an organic solder ability preservative (SOP) is used as cover layer for the Cu pads, an oxidation of the organic materials leads to void formation at the contact surfaces. As a consequence the mechanical robustness of the solder joints is reduced [2.66]. In case of IMC micro-bumps only the used underfill materials seem to limit a further scaling down of the solder joints, because their high moisture solubility leads to leakage currents between the micro-bumps [2.67].

2.5.1.2 Corrosion

The presence of moisture also enforces corrosion phenomena. A relevant reliability issue of solder joints is the growth of Conductive Anodic Filaments (CAF) due electrochemical migration (ECM) [2.68-69]. ECM appears when a potential difference between two conducting lines, respectively solders joints, is combined with a thin moisture surface that enables the transport of metal ions across or through the substrate from the anode to the cathode [2.62]. The migration of metal ions, coming from the anode and following the electric field lines, leads to material deposition at the cathode. Recombination of the ions at the cathode forms a bridge between the anode and cathode. Finally both lines fail due to a short circuit [2.68]. A principal illustration of the CAF formation is shown by Fig. 2.10. In Fig 2.11 typical ECM failures of electrical contacts are shown.

The chemical process of ECM should not be mixed with the physical phenomena of electromigration, which describes a diffusion process of thermal activated ions in the metal lines, which is directed by an electron flux.

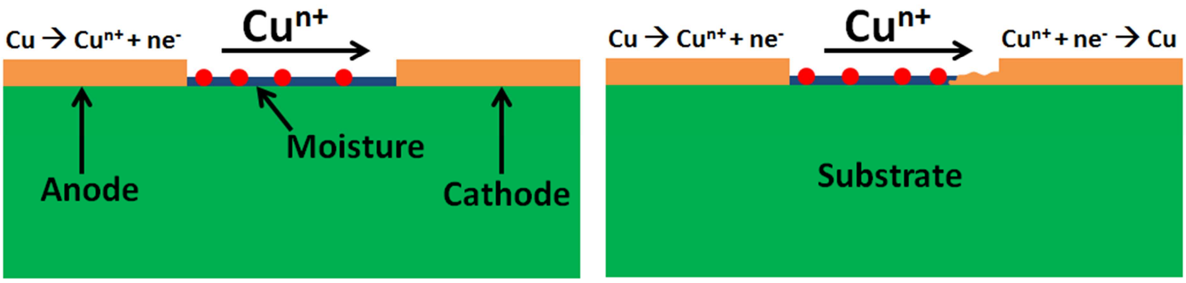

Figure 2.10: An Illustration of the Conductive Anodic Filament formation by Cu ion migration after moisture accumulation in the substrate

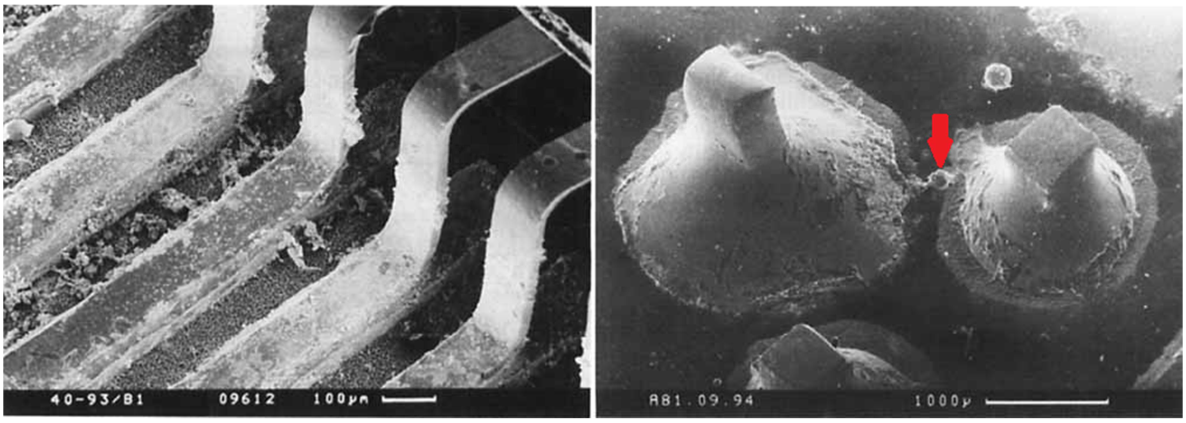

Figure 2.11: Contact failures after CAF formation between Cu wire bonds (left) and Sn joints (right) [2.62]

Regarding corrosion induced failures a model for the calculation of the mean time to failure (MTTF or τ_{50}) is given in [2.70]. The equation is based on an Arrhenius relation including the energy for temperature activation (E_A) and a term for the relative humidity (β). The geometry is relevant too; for example the life time of test structures is reduced when the space between the lines becomes shorter [2.71]. The pre exponential constant (B_0) in (2.13) is related to the geometry.

$$MTTF = B_0 \cdot exp\left(\frac{E_A}{k_B T} + \frac{\beta_M}{rh}\right) \qquad (2.13)$$

By (2.13) it becomes clear that corrosion is a relevant reliability issue at high operation temperatures, for interconnects made of mobile materials like Cu or Ag and at a high relative humidity. Furthermore EMC is reinforced by electrolytes in the moisture [2.62].

Regarding corrosion induced reliability problems, Cu-Sn IMC µ-bumps seem to be promising. Investigations on IMCs have shown that the resistance of Cu_6Sn_5 against corrosion is as high as the resistance of bare Cu, while Cu_3Sn is even more stable against corrosion [2.67] than Cu. When the Cu_6Sn_5 part of a Cu-Sn IMC joint is covered with organic material the whole joint is very resistant against corrosion [2.67]. Sn covers for Cu metals lines increase their lifetime by a factor of 50 due to Cu-Sn IMC formation at the interfaces [2.71].

2.5.2 Thermal Mismatch

Electronic devices are exposed to variations in temperature due to the difference between operation, reflow and storage temperature. Unlike construction materials like armored concrete, packaging materials differ in their thermal expansion.

The Coefficient of Thermal Expansion (CTE) is a parameter to describe the linear thermal expansion of a material in one dimension (2.14).

$$CTE = \frac{1}{l} \cdot \frac{dl}{dT} \qquad (2.14)$$

In table 2.1 the Coefficient of Thermal Expansion (CTE) of different materials being found in IC packages are given. The thermal expansion of the Si dies is relatively small while the epoxy resins being used to cover the die have a relatively high thermal expansion.

Material	CTE [ppm]	Material	CTE [ppm]	Material	CTE [ppm]	Material	CTE [ppm]
Si	6.7	SnAgCu	20	Epoxies	60-80	Cu-Sn-IMC	14-16

Table 2.1: The CTEs of the Si die, a lead free solder and the range of CTEs for different epoxies [2.26].

Furthermore a big difference between the soldering temperature (T>200°C) and the storage (room) temperature leads to a high pre stress on the mounted microelectronic devices. The thermal deformation of the different layers in the IC package leads to a temperature dependent warpage (Fig. 2.12) [2.73]. Tensile stress leads to crack formation and finally to a failure of the solder joint while compressive stress can lead to whisker formation resulting in a short cut [2.72].

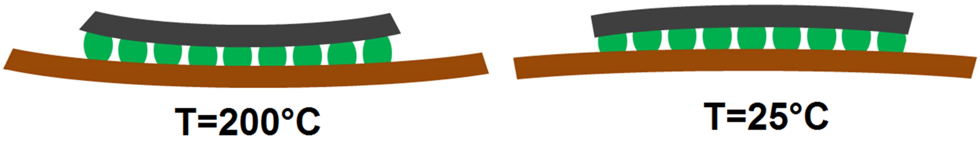

Figure 2.12: Concave (left) and convex (right) warpage profile during and after reflow

The thermal stress (σ_{th}) depends on the Young's modulus of the affected materials, the CTE and the difference to the stress free temperature (2.15). The stress free temperature (T_0) is defined as the temperature where the thermal deformation of the different materials does not lead to a measurable warpage. Often packages do have more than one stress free temperature [2.65].

$$\sigma_{th} = E \cdot CTE \cdot (T - T_0) \qquad (2.15)$$

The execution of Temperature Cycle Tests (TCT) is a common procedure to evaluate the resistivity of solder joints against thermomechanical stress. Eleven different test conditions are mentioned in the TCT related JEDEC standard [2.75]. Two typical temperature ranges are -55°C to 125°C for consumer electronics and -65°C to 150°C for special applications [2.26]. The period of on temperature cycle is often more than one hour, e.g. in [2.65] Amkor PoP devices passed a temperature range of -65°C to 125°C in 84 minutes. Hence temperature cycle includes a long period of constant conditions and the thermomechanical stress during TCT is related to Low-Cycle-Fatigue (f<<1Hz) [2.74]. The relation between strain and the maximum number cycles [N_C] is often approximated by the Coffin Manson relation (2.16) [2.76]. In case of Low-Cycle-Fatigue the plastic strain is most relevant and the Coffin Manson relation is often simplified to the Basquin equation (2.17) [2.26].

$$\varepsilon = \varepsilon_E + \varepsilon_p = K_{C1} N_C^{-c} + K_{C2} N_C^{-m_C} \qquad (2.16)$$

$$N_C = H_C \cdot \sigma^{-m_C} \qquad (2.17)$$

K_C, H_C = pre exponential constants; c, m_C = exponential constants

For the use of the Basquin equation the stress amplitude (σ) has to be known. In case of solders the strain rate and the resulting stress due to plastic deformation depends on the test temperature and deformation rate [2.77-78]. The calculation of stress amplitude is often done with FEM [2.65, 2.79].

During TCTs a growth of the IMC layers at the contact surfaces of the solder joints appears [2.80]. Furthermore the appearance of micro voids at the interface between the solder and the IMCs was observed [2.80-81]. The presence of the micro voids reduces the mechanical rigidity of the solder joints [2.81]. The CTE mismatch between the IMCs and the solder [2.81] or their different diffusivity in combination with impurities [2.54, 2.82] can be responsible for the void formation (Kirkendall effect). Furthermore non wetting leads to crack formation at the solder to PCB interfaces and is one reason for early fails of solder joints during TCT [2.81]. It is possible to increase the elastic stiffness of Cu_6Sn_5 by adding Ni, which happens automatically when the contact pads of the PCB are covered with an Electroless Nickel Immersion Gold (ENIG) surface as a diffusion barrier [2.83].

TCT often leads to crack formation in the solder close to the Die side contact surface [2.65]. FEM simulations have shown that the crack formation appears as a consequence of the warpage induced stress (Fig. 2.13).

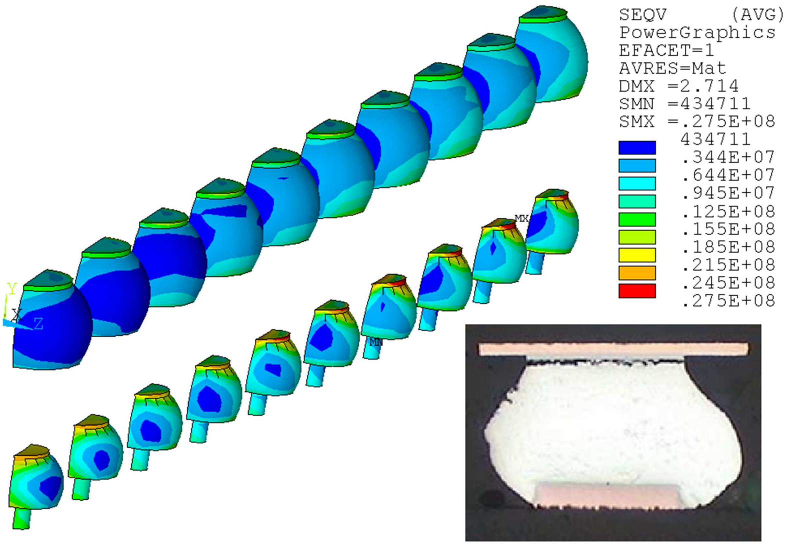

Figure 2.13: Stress distribution in a PoP BGA [2.105] and crack formation in a solder joint after temperature cycling [2.84]

Regarding to pure IMC µ-bumps even 1000 temperature cycles between -65°C and 150°C did not change the morphology of the joints [2.67]. In [2.85] even a growing number of micro voids did not lead to a failure of the stressed Cu-Sn IMC µ-bumps. Hence the performance of IMC µ-bumps during TCTs is as promising as their resistance against corrosion.

2.5.3 External Stress Loads

In addition to the thermal stress, external forces can be applied to a package and its solder joints. The reasons can be planned events like a soldering process which requires a specific pressure on the contact surfaces or there can be accidental events. A typical accidental stress load is the drop of mobile electronic devices. Under harsh environment condition also vibration induced stress can become a reliability issue.

2.5.3.1 Bending and vibration tests

To avoid failures of the package to PCB connections during assembly or in consequence of vibrations, which appear e.g. in a car engine, the stress resistivity of solder joints has to be verified under controlled conditions. Against this background vibration [2.86-87] and bending tests [2.88] were performed. In Fig. 2.14 the principal concepts of both tests are visualized.
Unlike the thermomechanical stress an external force on the test structure mainly leads to a warpage of the PCB and not of the package [2.86]. In this case a changing relative position of the PCB to the package leads to a deformation of the solder joints [2.87].

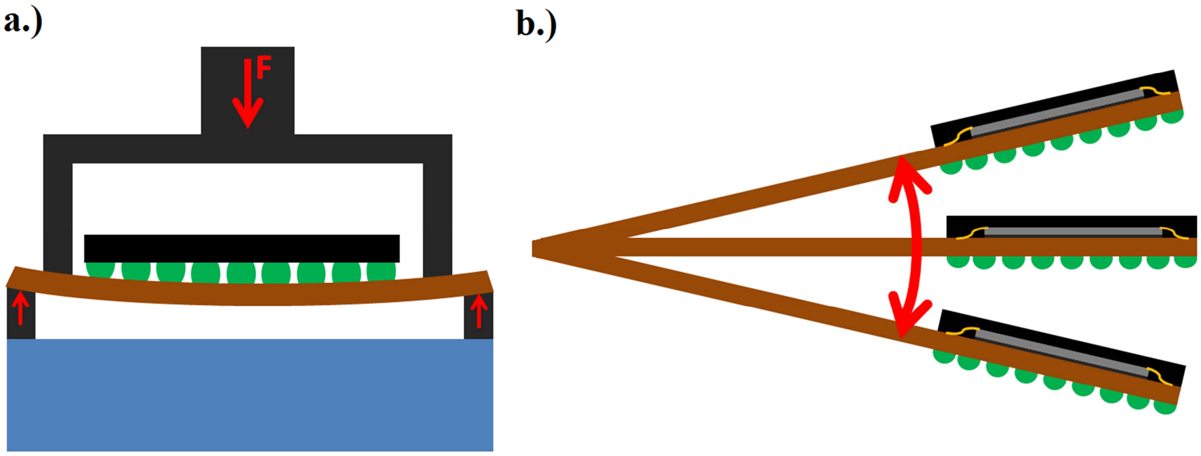

Figure 2.14: Principal experimental setup of bending (a) and vibration tests (b) in [2.86] and [2.87]

In [2.86] vibration tests were performed at cycling frequencies between 10Hz and 27Hz, afterwards finite element simulations were made to extend the frequency range (0.001-3450Hz). Independent from the chosen frequency the crack formation mainly appeared in the bulk solder [2.86-87]. Curve fitting showed a good correlation between the test results and the Basquin equation (2.17) [2.86]. Hence plastic deformation is the main reason for the fatigue of the solder joints during vibration testing.

While the thermal stress was coupled with the CTE, the stress amplitude during the vibration test depends on the angular acceleration ($\ddot{\omega}$), the mass of the test structure (“M” e.g. package + PCB + additional weight), the distance from the package to the tester (L) and the contact surface (A) [2.86]:

$$\sigma = Ml\ddot{\omega}/A \qquad (2.18)$$

Bending tests being performed with a 3Hz cycle rate show a similar correlation between the strain amplitude and the cycle lifetime as the vibration test results [2.87-88].

2.5.3.2 Drop tests

A drop test means that a PCB with one or several packages is mounted on a metal weight which will be dropped on a target (Fig 2.15). Drop tests are necessary to evaluate the influence of mechanical shocks on the package reliability. When the metal weight smashes on the target an impulse goes through the PCB and the packages [2.89]. First the breaking force bends the PCB and afterwards a stress wave is going through the devices (e.g. with 245Hz) [2.89]. Because of the fact that the PCB is much more deformed than the package, the PCB has to be standardized to get reproducible and comparable test results [2.89]. A typical break force for consumer products is F~1500g_n*M [2.90], while reliability tests for harsh environment applications go up to F~10000g_n*M. For future harsh environment applications and military application also F~100000g_n*M will be required.

From the first point of view a drop test is a combination of a bending and a vibration test, but due to the huge brake force during the impact of the tested device, high strain rates appear at the solder joints [2.89].

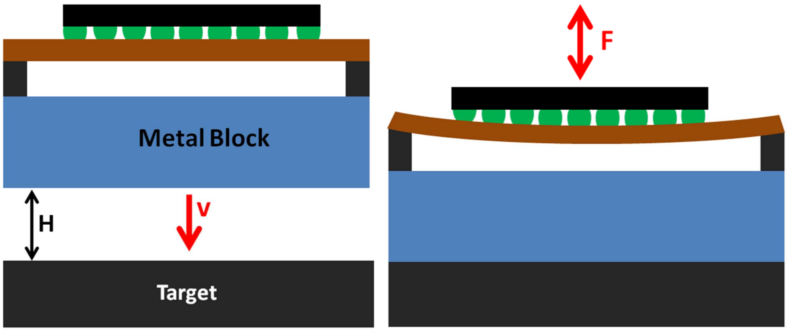

Figure 2.15: Principal procedure for a drop test

Two typical failure pictures after TCT and drop tests on lead free solder bumps are shown in Fig. 2.16 [2.88]. Failure analysis has shown that the crack formation during drop tests often appears at the interface between solder and IMC or in the IMC [2.88-92].

Figure 2.16: Crack formation in the solder during TCT (left), and crack formation in the IMC layer during drop tests (right) [2.88]

In principal the deformation profile of the solder joints during the drop tests is similar to vibration or bending test results, but drop tests show a different strain to cycle lifetime correlation (Fig. 2.17) [2.87]. This is a clear indicator that a new failure mechanism appeared during the drop tests.

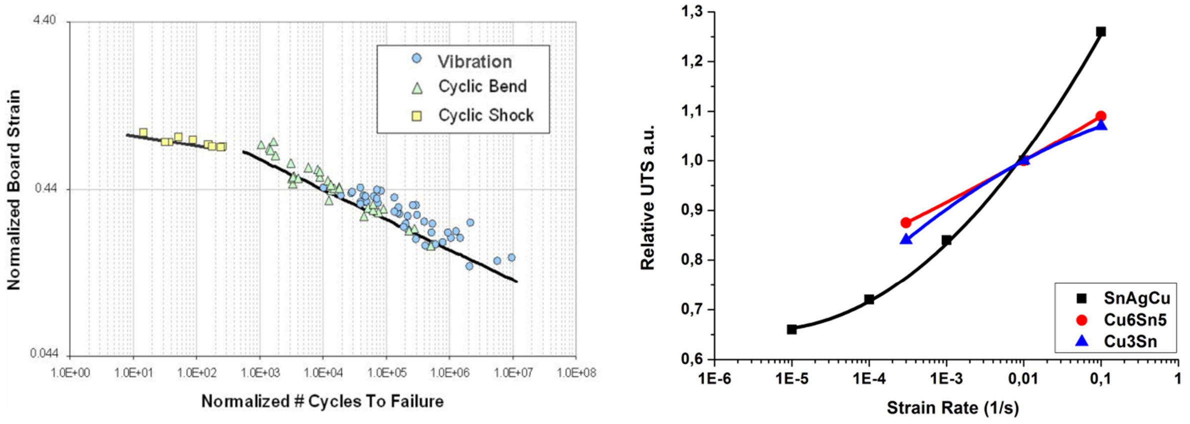

Figure 2.17: Cycles to failure vs. Board strain for vibration, bending and shock tests (left) [2.87], relative UTS of SnAgCu and Cu-Sn IMCs at different strain rates (right) [Data: 2.93-94]

The different failures after low cycling fatigue tests (bending, vibration) or drop tests are due to the different strain rate sensibilities of solders and IMCs [2.92]. In the case of low strain rates the ultimate tensile strength (UTS) of solders is lower than the UTS of IMCs, but the solders are more strain rate sensitive than the IMCs. Hence at a high strain rate, which appears during drop tests, the UTS of the solders is greater than the UTS of the IMCs (Fig. 2.17). That means if the strain rate is high enough the IMC becomes more fragile than the solder and the crack formation appears in the IMC. In [2.95] it was also clarified that the crack formation often appears at the interface between the two Cu-Sn IMCs Cu_6Sn_5 and Cu_3Sn. Hence a weak interface between the IMCs may be more important for the drop test reliability than the UTS of the IMCs [2.95].

The main failure mechanism during drop tests as well as for bending or vibration tests is the warpage of the PCB [2.90]. The bending wave going through the PCB is described by (2.19) [2.89] and the maximum deformation (u_{max}) of the board is given by (2.20). The maximum deformation of the board depends on the fall velocity (v) which can be calculated with (2.21) when the aerodynamic resistance is negligible.

$$\frac{E h_B^2}{12\rho} \cdot \frac{\partial u^4}{\partial x^4}(x,t) + \frac{\partial u^2}{\partial t^2}(x,t) = 0 \qquad (2.19)$$

$$u_{max} = \sqrt{24\rho/E} \cdot \left({}^{l}/_{\pi}\right)^2 \cdot {}^{v}/_{h_B} \qquad (2.20) \qquad v = \sqrt{2gH} \qquad (2.21)$$

ρ= mass density; l_B= board length; g= acceleration; H= drop height

In general the performance of the test structure depends on the test conditions like the drop height (velocity) or the direction of fall [2.96], the test device (board dimensions) and the shape and number of the solder joints. It was shown that a higher number of solder joints increase the drop test performance asymptotically to an upper limit while a decreasing contact surface adulterates the drop test performance [2.89]. The influence of the board thickness is more complex, a thin board increases the maximum warpage of the PCB, but a too thick PCB can also lead to a high stiffness of the test structure, which would increase the break force [2.89]. Investigations by T. Matilla [2.97] have shown that TCT before the drop testing improves the drop test performance of solder joints due to annealing, but diffusion processes during temperature cycling also lead to the formation of Kirkendall voids in the IMCs, which reduces the robustness of the solder joints when their number becomes too high [2.97-98].

In difference to corrosion or electromigration induced reliability issues, solder bumps on Ni pads have a reduced drop test performance compared to solder joints being directly connected to the metal lines [2.90, 2.98]. The reduced performance is due to the Ni content in the Cu_6Sn_5 IMC layer, because Ni increases the stiffness of Cu_6Sn_5 [2.83, 2.99].

2.5.4 Electromigration

Electromigration (EM) is a thermally activated diffusion process with a preferred direction being defined by the momentum exchange between an electron flux and the diffusing lattice ions [2.10]. In a few cases the electrical field defines the direction of the mass flux instead of the electron flux. More details about electromigration and other diffusion processes in solids will be given in chapter 3 as the theoretical basis of the experimental procedure. Furthermore excellent overviews of migration processes in general is given by Paul Shewmon [2.39] and Hans Wever [2.100].

After a period of time an electromigration induced mass flux leads to material degradation on one side of the interconnect (anode/cathode) and a materials accumulation at the opposite side (cathode/anode). Material accumulation can lead to hillock formation and finally to short circuits, especially when two EM stressed structures are placed close to each other. Material degradation leads to EM driven void formation and a disruption of the electrical contact. In general void formation is the main failure mode.

The void formation has to be in an advanced state before a resistance increase appears [2.10, 2.101], furthermore the accumulation of material on the opposite side of the stress can motivate a back flux due to an increasing hydrostatic pressure (stressmigration) [2.102]. Hence the guaranteed lifetime and the stressmigration induced back flux, also called “Blech Effect”, define a minimum current density ($\vec{J}_{min}$) where EM induced failures of electrical contacts are a relevant reliability issue. The Blech effect depends on the length of the tested structure [2.102] and the maximum tensile stress of the surrounding materials [2.103]. Electrical contacts also fail when void formation leads to disruption before the volume of the displaced material is enough to establish a back flux being as strong as the EM induced material transport [2.104].

On the IC level current densities in a range MA/cm² appear and the failure of Al or Cu interconnects due to EM are a well-known problem since the 1960s [2.10]. Even under consideration of the rapid down scaling due to three dimension packaging, the current density in solder bumps is several orders of magnitude smaller than the current densities in IC interconnects (e.g. 1.1kA/cm² in [2.101] and 1.8kA/cm² in [2.65, 2.105]), but the low activation energies (melting point) of Sn solders compared to Al or Cu lead to a high diffusivity of its lattice ions. In addition the relatively low melting point of Sn means that the use condition of the chips (T<100°C) is much closer to the critical value, being 80% of the material melting point, than for high melting metals like Cu or Al. Furthermore the big difference between the metal layer and the solder bump contact surface leads to local peaks of the current density (51kA/cm² in [2.101] and 3.6kA/cm² in [2.105]). The effect is called "current crowding" and it is visualized in Fig 2.18 (left).

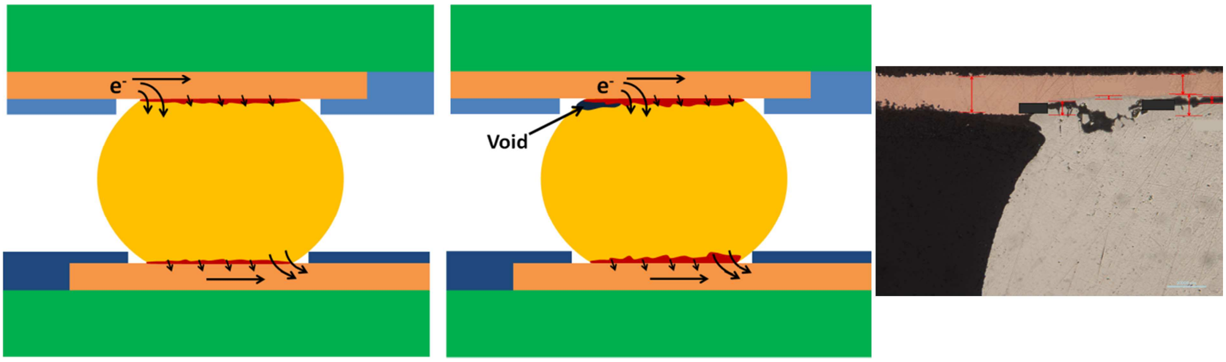

Figure 2.18: Formation of a pancake void and IMC growth as a consequence of electromigration and current crowding (left), void in an electromigration stressed SnAgCu bump (right)

Following the JEDEC standard [2.106] the mean lifetime of solder joints under EM stress can be approximated with the Black equation (2.22) [2.107], which is also used for interconnects.

$$TTF \sim j^{-n_B} exp(E_A/k_B T) \quad (2.22)$$

j= current density; n_B= exponential constant

EM induced void or hillock formation is the consequence of a local difference of the mass flux density. Using (2.23), being a more detailed model for the calculation of the EM induced mass flux ($\vec{J}_{EM}$), it is possible to describe the EM influence on the material density by the divergence of the resulting vector field [2.108]. Eq. (2.24) describes the mass flux divergence as a consequence of an inhomogeneous temperature distribution.

$$\vec{J}_{EM} = \frac{N}{k_B T} eZ^* (\vec{J} - \vec{J}_{min}) \rho_{el} D_0 exp(-E_A/k_B T) \quad (2.23)$$

N= atomic density; e= elementary charge; D_0= diffusion constant; ρ_{el} = specific resistance;
Z*= effective charge of the moving ion

$$div(\vec{J}_{EM}) = \left(\frac{E_A}{k_B T^2} + \frac{TCR \cdot \rho_0}{\rho} - \frac{1}{T}\right) \cdot \vec{J}_{EM} \cdot grad(T) \quad (2.24)$$

Based on (2.24) an alternative interpolation of the expected TTF under EM stress is possible (2.25).

$$TTF \sim 1/div(\vec{J}_{EM}) \qquad (2.25)$$

Comparing (2.22) and (2.25) and taking into account that the temperature gradient, leading to a mass flux divergence, can be the consequence of Joule heating (gradT~j^2), the relation between "n_B" in and "j" in (2.22) becomes clear. In summary a mass flux divergence and the related void formation have two possible reasons:

1. Void formation as a consequence of Joule heating being indicated by n_B=3 in the Black equation: n_B=1 for $\vec{J}_{EM}$ and n_B=2 for gradT due to Joule heating (~j^2).
2. Material degradation at a diffusion barrier. In this case a "diffusion barrier" can be every material with quite lower diffusivity than its neighbors (e.g. Cu next to Sn). This failure case is indicated by n_B=1 in the Black equation.

In solder joints both mechanisms are relevant for void formation. Hence the constant "n" is between one and three [2.109-110]. If n_B>3, the applied current changed one of the boundary conditions, e.g. Joule heating significantly increased the test temperature (T), which would reduce the TTF exponentially.

The weak point of (2.22) is that it only considers temperature gradients being the consequence of Joule heating. This assumption is sufficient for interconnects. In case of IC packaging, and especially for three dimensional packaging, the ICs act as hot spots leading to external temperature gradients not being considered by the Black equation. As consequence the Black equation overestimates the lifetime of solder joints for three dimensional packaging [2.31, 2.105]. The weak point of (2.24) is the fact that it does not consider mass flux divergences due to local differences of the diffusivity.

In lead free solder bumps the EM induced void formation appears at the interface between the less mobile IMC components and the more mobile solder (Fig. 2.19, right). As a consequence of current crowding and the resulting temperature gradients an initial void is formed at one of the corners of the contact surface (Fig 2.19, left) [2.65, 2.101]. The void formation moves the edge of the solder joints and by the way the point where current crowding and the further void formation appears. The result is a pancake void which finally leads to a failure of the solder bump (Fig. 2.18 right). The dominance of current crowding induced void formation enables the determination of weak points in the design of solder bumps and a comparison of different designs and technologies with (2.24) and FEM analysis [2.105, 2.111-113].

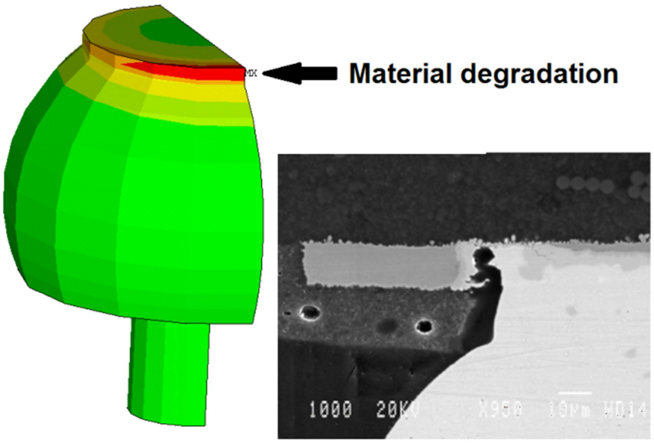

Figure 2.19: Calculation of the mass flux divergence [2.105] with ANSYS® and a user developed routine [2.108] (left), a failure picture of the related EM test (right) [2.65]

The presence of IMCs in solder joints has an influence on the EM induced failure mechanisms in solder joints. The reason for the void formation at the interface between the IMCs and the solder is due to the low mobility of atoms in the IMCs compared to the solder [2.114]. Furthermore the presence of an EM induced mass flux accelerates the IMC formation [2.65, 2.115-117]. Pure Cu-Sn or Ni-Sn IMC solder joints are not affected by EM induced failures. Even under harsh test conditions being far beyond the CSP bump test conditions no EM induced failures were observable [2.118-120]. The main reason for the high EM performance of IMC solder joints is their relatively high activation energy compared to Sn based solders [2.114].

2.6 Transient Liquid Phase Soldering

The growing importance of IMCs due to the downscaling of solder joints and the use of microelectronic devices under harsh environment conditions as well as the promising results of IMC micro bumps in many aspects of microelectronic packing reliability show the great importance of TLPS for future packaging techniques. Consequently the existing models for the design of a TLPS process step will be explained and the required material parameters will be mentioned. Afterwards the unavailability of valid material parameters will be shown.

2.6.1 Process Design

TLPS is a diffusion driven soldering process which forms an IMC solder joint out of a low and a high melting material. The TLPS process can be performed by melting the interlayer (SLID) or by solid diffusion only (SMB). Furthermore a combination of both TLPS techniques is possible (SLID+SMB). Based on [2.53, 2.121-122] the four principal process steps of TLPS are shown in Fig. 2.20:

1. **Interlayer Widening:** Melting of the interlayer. For a Cu-Sn IMC joint the interlayer would be Sn. Due to high concentration gradients and the low activation energy of Cu in molten Sn (0.18-0.29eV) [2.123] a fast dissolution of Cu in the interlayer appears.
2. **Homogenization of the interlayer:** Cu flows into the growing interlayer and the Cu content is balanced on a low level.
3. **Solidification:** When the Cu concentration reaches a critical limit (m_{int}) the melting point of the interlayer is above the process temperature and a preliminarily IMC is formed. After the formation of an IMC the further process flow depends on the solid state diffusivity of Sn and Cu in this IMC.
4. **Homogenization of the bond region:** Cu and Sn still diffuse through the solid preliminary IMC layer and form the favored IMCs with a higher Cu content (Cu_6Sn_5 or Cu_3Sn). The solid state diffusivity of Cu and Sn is three orders of magnitude lower than their diffusivity in liquid materials [2.124]. As a consequence the fourth process steps needs more than 90% of the process time.

In dependence of the chosen process temperature for step (4) the interlayer stays liquid (pure SLID) or the process temperature is reduced and the IMC formation is driven by solid state diffusion (SLID+SMB).

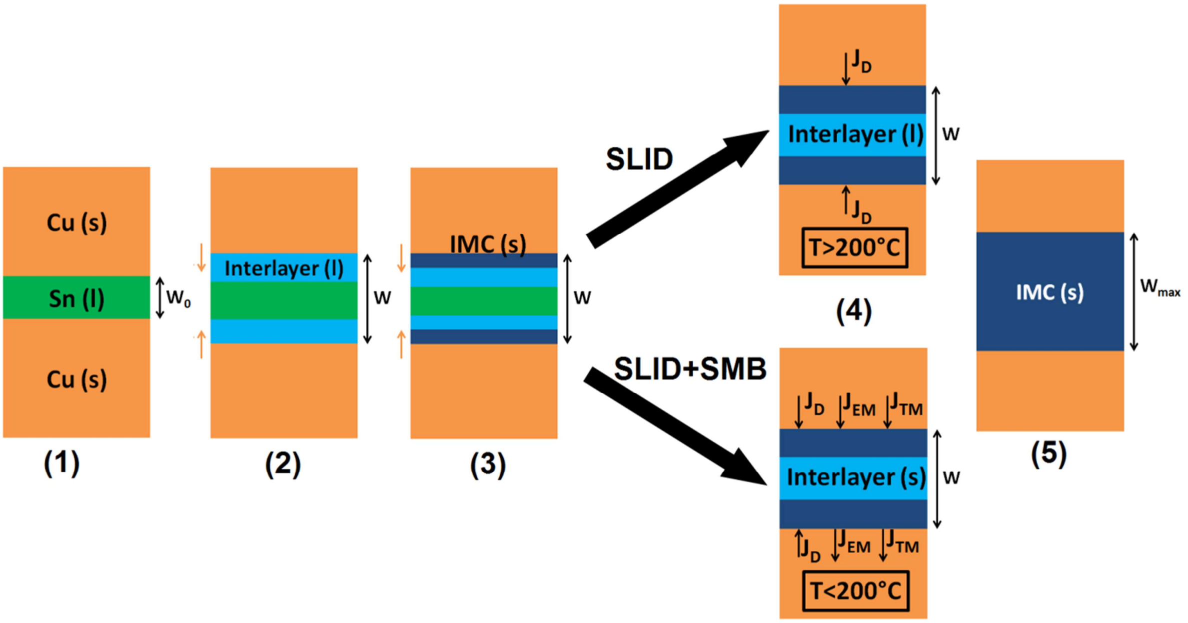

Figure 2.20: The principal process steps of Transient Liquid Phase Soldering (s): solid; (l): liquid

The first two steps of TLPS only need a few minutes and their relatively high process temperatures, being critical for many microelectronic devices, are also necessary for the realization of three dimensional packaging solutions based the reflow of conventional tin solder BGAs. In [2.125] it is shown that the Cu_6Sn_5 grows in scallops form on a flat surface of Cu_3Sn. Over time the size of the scallops increases, but their growing surface area is unfavorable and as consequence their number decreases (Fig. 2.21). If the scallops get contact before the complete interlayer is molten void formation appears and the final solder joints are brittle [2.126]. This defines the minimum thickness of the Sn interlayer.

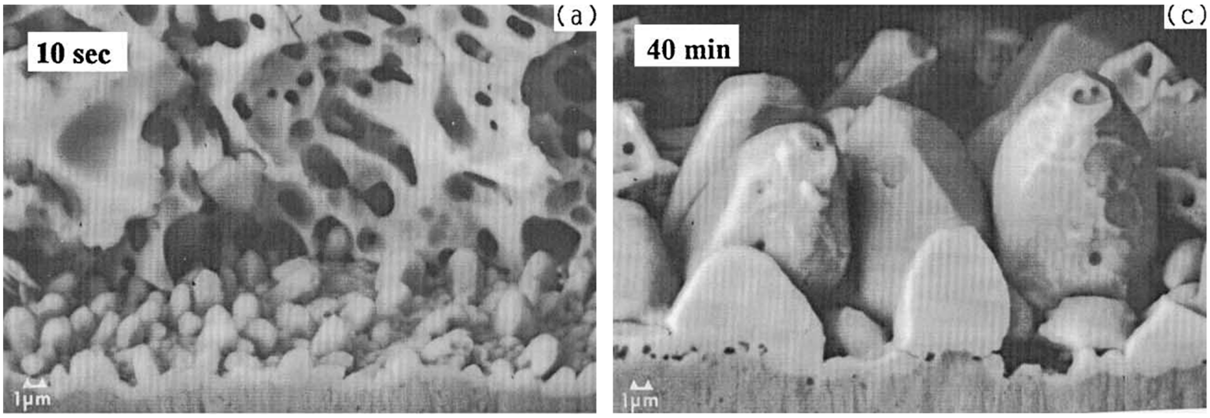

Figure 2.21: Formation of IMC scallops in SnPb at 200°C for 10s (a), 40 min (b) [2.125]

The third and the fourth steps are more critical because the following IMC formation is driven by solid state diffusion and the mass flux is dramatically reduced compared to the first two steps. A too high process temperature could destroy the microelectronic devices and consequently several hours are needed to form the final IMC connection [2.53, 2.115]. Against this background it can be reasonable to reduce the process temperature of the fourth step and change from SLID to SMB. Taken into account that the bottleneck during SLID is given by the solid IMC layer, the pure solid state diffusion during SMB does not affect the total process time too much. Furthermore the SMB process can be accelerated with a mass flux due to electromigration ($\vec{J}_{EM}$) and thermomigration ($\vec{J}_{TM}$). This can be done by combining the temperature storage step with a high applied current directly leading to EM and indirectly leading to TM as consequence of Joule heating. Hence the benefits of "SLID+SMB" are a lower process temperature and the possibility to accelerate the process with EM and TM. In fact reflow soldering being combined with the down scaling of the solder joints is nothing else than SLID, so the conventional process flow does not have to be changed (low operation barrier).

In [2.53, 2.121] a mathematical model for the process design of a SLID process is given: The first process step is driven by diffusion and only needs a few seconds, like for moisture diffusion, Fick's law (2.10) can be used to describe the mass flux over time. The following three steps of the SLID process are too complex for a theoretical description and consequently the power law (2.26) is used to approximate the IMC thickness over time.

$$h_{(t)} = a_P \cdot t^{n_P} \quad (2.26)$$

a_P= pre exponential constant, n_P= exponential constant.

The power law is only empirical and significant failures during the calculation of the process time can appear. Taking into account that the IMC formation is driven by diffusion only and that the involved materials have to pass the IMC layer the Deal-Grove model [2.127] can be used to describe the IMC growth (Eq. 2.27). This model includes a linear part and a root function. For short process time a linear growth of the IMC can be expected and for a long process times the square root curve becomes more relevant. Comparing (2.26) and (2.27) leads to the conclusion that "n" depends on the process time and should be 0.5<n<1.

$$h_{(t)} = -\frac{Y}{2} + \frac{\sqrt{Y^2 + 4Z_G \cdot t}}{2} \qquad (t > 0) \wedge (h > 0) \quad (2.27)$$

Y, Z_G = constants

While the first two process steps only need a few minutes, the following process steps need several hours, so they are most relevant for calculation of the total process time. In [2.53] a growth approximation of the required process time in dependence of the diffusivity and the interlayer thickness is given (2.28). Due to the difficulties to describe the third process step the calculated process duration is several times longer than really required [2.53].

$$t = \frac{h_{max}^2 \pi}{16 D_o} \cdot \left(\frac{1 - m_{int}}{1 - m_{IMC}}\right)^2 \cdot exp(E_A / k_B T) \qquad (2.28)$$

m= mass fraction

The Eq. (2.28) is not exact enough for the calculation of the process time but it allows an interpretation of the expected IMC formation speed:

1. The final dimension (h_{max}) of the IMC solder joint has a strong influence on the process time. This is relevant for high power or harsh environment applications with thick bonding layers.
   If the solder joints are scaled down for high performance electronics it is more relevant that the thickness of the interlayer has to be above a critical minimum. It is dictated by the used temperature ramp [2.126].

2. A high maximum Cu concentration of the liquid interlayer (m_{int}) reduces the process time. Regarding to the phase diagram (Fig. 2.22) the maximum Cu concentration in the interlayer can be increased with the process temperature, but this also means a higher stress load on the microelectronic devices.

3. The minimum Cu concentration of the final IMC (m_{IMC}) is also relevant. Hence the fabrication of a Cu_3Sn or even a $Cu_{41}Sn_{11}$ IMC joint needs more time than the fabrication of Cu_6Sn_5 solder joints [2.126]. Nevertheless Cu_3Sn is more resistant against corrosion and electromigration than Cu_6Sn_5 and the relation between the process and the maximum operation temperature is better for Cu_3Sn than for Cu_6Sn_5 joints (Fig. 2.8).

4. The mobility of Cu and Sn in the IMCs has a very strong (exponential) influence on the process time. Hence the process temperature and the activation energy of the materials have to be well known before the process design is possible.

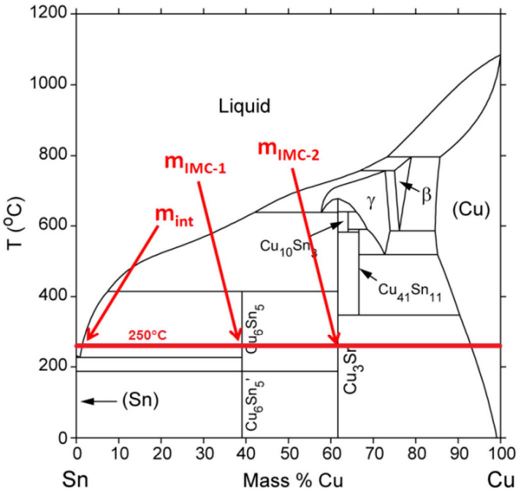

Figure 2.22: Cu-Sn phase diagram, the red line denotes a possible process temperature of 250°C [2.151]

In the case of an additional SMB step the process design has to take into account that the further IMC growth appears due to solid state diffusion. The IMC growth due to solid state diffusion is described by the Deal Grove model (2.27) or approximated by a square root curve as special case of the power law [2.53, 2.115]: (2.26) with n=0.5. The IMC growth due to electro- or thermomigration appears due to a drift of the diffusion induced mass flux and the IMC growth speed is linear time dependent: (2.26) with n=1 [2.115].

In [2.115-117] investigations of the IMC growth during temperature storage and under the influence of electromigration were made. In [2.115] also an illustration of the IMC formation process is given (Fig. 2.23).

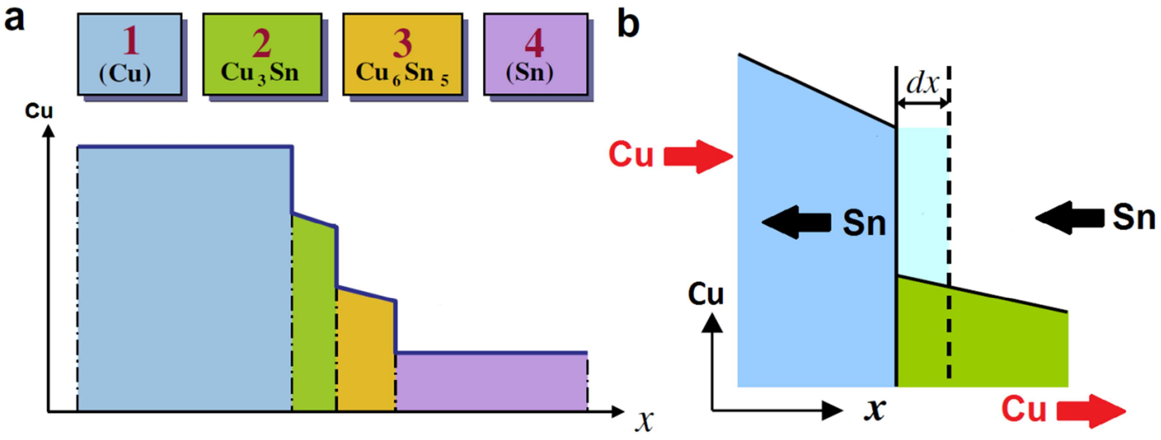

Figure 2.23: Concentration profile of a Cu on Sn contact with IMCs (a), the principal direction of the Cu and Sn mass flux in the IMCs (b) [2.115]

Before a mass flux can lead the formation of new IMC material its minimum concentration of Cu has to be reached, hence the concentration difference between the previous and the new IMC ($N_{Cu3Sn,min}$-$N_{Cu6Sn5,max}$ or $N_{Cu6Sn5,min}$-N_{SAC}) has to be overcome by the mass flux. In addition the driving forces, like the concentration gradients, which transport material into the IMC, also transport material out of the IMC (Fig. 2.23, right). Taken into account the presence of diffusion, electro- and thermomigration, the general expression for the IMC growth speed in solids is be given by (2.29a-b)

$$\vec{v}_{Cu3Sn} = \frac{\left(\vec{J}_{EM} + \vec{J}_{TM} + \vec{J}_D\right)_{Cu} - \left(\vec{J}_{EM} + \vec{J}_{TM} + \vec{J}_D\right)_{Cu6Sn5}}{\left(N_{Cu,min} - N_{Cu3Sn,max}\right)} \qquad (2.29a)$$

$$\vec{v}_{Cu6Sn5} = \frac{\left(\vec{J}_{EM} + \vec{J}_{TM} + \vec{J}_D\right)_{Cu3Sn} - \left(\vec{J}_{EM} + \vec{J}_{TM} + \vec{J}_D\right)_{SAC}}{\left(N_{Cu3Sn,min} - N_{Cu6Sn5,max}\right)} \qquad (2.29b)$$

The required material parameters for a TLPS process design can be identified with (2.29a) and (2.29b). The mass flux due to electromigration is described by (2.23), the mass flux due to thermomigration can be calculated with (2.30) and the mass flux due to diffusion is given by (2.31).

$$\vec{J}_{TM} = -\frac{Q^* D_0 N}{k_B T^2} \cdot exp(-E_A/k_B T) \cdot gradT \qquad (2.30)$$

$$\vec{J}_D = -D_0 \cdot exp(-E_A/k_B T) \cdot gradN \qquad (2.31)$$

Hence the following parameters will be needed for calculation of the migration induced movement of Cu and Sn in Cu_3Sn and Cu_6Sn_5.

Parameter	Class	Principal Sources
Specific resistance (**ρ_{el}**)	Material Parameter	Literature
Activation Energy (**E_A**)	Material Parameter, Diffusion	Literature, Experimental*
Diffusion Constant (**D_0**)	Material Parameter, Diffusion	Literature, Experimental*
Effective Charge (**Z***)	Material Parameter, Drift	Literature, Experimental*
Heat of transport (**Q***)	Material Parameter ,Drift	Experimental*
Concentration (**N**)	Material Parameter	Experimental*
Concentration Gradient	Boundary Condition	Experimental*
Temperature (**T**)	Boundary Condition	Experimental*, FEM**
Current Density (**$\vec{j}$**)	Boundary Condition	Experimental*, FEM**

Table 2.2: Material parameter and boundary conditions for the assumption of the TLPS process time.
*** Experimental means own experimental results being presented in this work.**
****FEM means results of ANSYS® simulations being performed during this work.**

2.6.2 Available Material Parameters

During the last years several investigations on the IMC formation in different solders like SnPb or in pure Sn were made. In general two different kinds of interconnects were used for the experimental studies: direct solder to Cu connections without any interlayer and solder connects with a Ni interlayer as diffusion barrier. Both are affected by IMC formation, but the migration mechanisms and the composition of the IMCs are different (Fig. 2.24). Against this background the available results of previous investigations will be given in two separate sections.

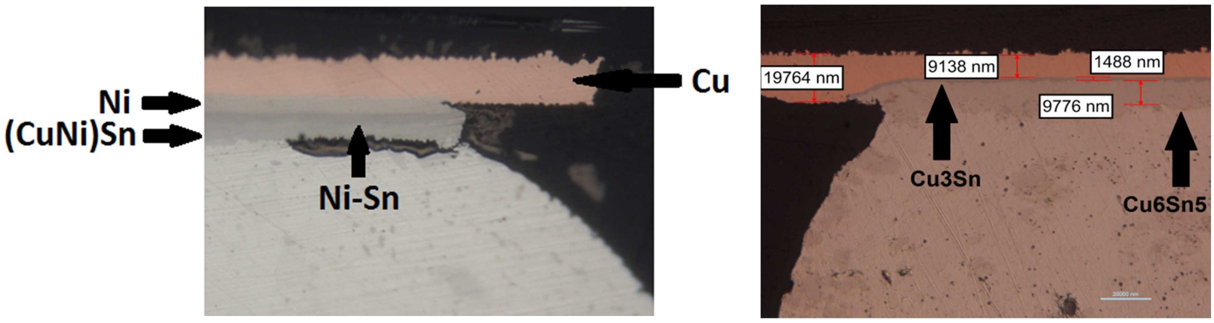

Figure 2.24: IMC formation in solder joints on Ni pads (left) [2.128], and with a direct contact to the Cu metal layer (right)

2.6.2.1 Direct contact between solder joint and Cu pad

When the diffusion of Cu into the solder is not blocked by a Ni layer Cu_6Sn_5 and Cu_3Sn IMCs are formed in every solder (Fig. 2.22). Several experiments based on reflow [e.g. 2.129] and temperature storage tests [e.g. 2.130] were made. In [2.130] the authors come to the conclusion that a nucleation barrier exists for the formation of Cu_3Sn, because in [2.131] the formation of Cu_3Sn was only observed at temperatures above 150°C, and in [2.132] no Cu_3Sn formation was observable at room temperature [2.130].

In [2.130] TiO_2 markers were used to observe the material movement in Cu_6Sn_5 and Cu_3Sn, based on this investigations the material parameters for the diffusion of Cu and Sn in both IMCs are available. In addition simulation-based parameters for the mobility of Cu and Sn in both IMCs are given in [2.133]. Often the temperature dependence of the IMC formation speed was investigated [2.130, 2.134-139] and the results are generalized parameters for the whole IMC. In [2.138] and [2.139] the activation energies for the formation of Cu_6Sn_5 and Cu_3Sn in SnAg, SnCu and SnAgCu solders were determined and clear differences in the activation energies were found. The mass flux in Cu_6Sn_5 and Cu_3Sn differs and the difference has to be compensated by vacancy sinks or sources at the IMC interfaces [2.136].

While the diffusion of Cu and Sn is addressed in many investigations the IMC growth due to EM is only part of a few investigations. In [2.135] the EM driven formation of Cu_6Sn_5 was investigated and an effective charge value (Z*) for the IMC is given. The test structure being used for the determination of Z* was designed to find a quasi-stable state of the IMC thickness by adjusting the EM induced mass flux and a back flux due to stressmigration. To get a hydrostatic pressure as a consequence of EM induced material accumulation the Cu wires and their solder contacts were surrounded with Si. The one dimensional expression for the EM induced mass flux under consideration of the Blech effect is by (2.32) [2.137].

$$J_{EM} = -\frac{N\Omega \mathrm{D}_0}{k_B T}\cdot\frac{d\sigma_H}{dx} + \frac{N D_0 Z^* e\rho_{el} j}{k_B T} \qquad (2.32)$$

Ω= atomic volume, σ_H= hydrostatic stress

Setting J_{EM}=0 leads to the formula for Z* (2.33).

$$Z^* = \frac{J_{EM} k_B T + N D_o \Omega \cdot \mathrm{d}\sigma_\mathrm{H}/\mathrm{dx}}{e\rho_{el} j N D_0} \qquad (2.33)$$

In [2.115] the effective charge of the moving ions is given for Cu and Sn in Cu_6Sn_5 and Cu_3Sn. The thermomigration in Cu-Sn IMCs was investigated in [2.100] and the heat of transport (Q*) for Cu in

Cu_3Sn was determined. Except for this value, the Q* for Cu and Sn is not available in the literature. All material parameters are given in the tables 2.4 and 2.5.

Cu_3Sn	**Cu**	**Sn**	**Cu_3Sn**	**Solder**
E_A [eV]	0.816 [2.133]	0.894 [2.133]	0.95 [2.138], 0.72 [2.139]	SnAg
	0.818 [2.130]	0.827 [2.130]	0.76 [2.130]	Sn
	-	-	1.05 [2.138], 0.72 [2.139],	SnAgCu
			1.08 [2.138], 0.61 [2.139]	SnCu
			0.73 [2.138]	SnPb
D_0 [m^2/s]	$2.21x10^{-6}$ [2.133]	$2.49x10^{-6}$ [2.133]	$5.63x10^{-7}$ [2.138]	SnAg
	$1.8x10^{-8}$ [2.130]	$7.9x10^{-10}$ [2.130]	$2.7x10^{-9}$ [2.130]	Sn
			$5.95x10^{-6}$ [2.138]	SnAgCu
			$1.09x10^{-5}$ [2.138]	SnCu
			$1.85x10^{-9}$ [2.138]	SnPb
Z*	26.6 [2.115]	23.6 [2.115]	n.a.	Sn
Q* [eV]	-0.09 [2.100]	n.a.	n.a.	Sn

Table 2.3: Literature-available migration related material parameters for Cu_3Sn. n.a.: not available

Cu_6Sn_5	**Cu**	**Sn**	**Cu_6Sn_5**	**Solder**
E_A [eV]	0.835 [2.130]	0.88 [2.130]	0.84 [2.130]	Sn
			0.75 [2.139]	SnCu/SnAgCu
			0.93 [2.139]	SnAg
D_0 [m^2/s]	$6.2x10^{-8}$ [2.130]	$5.88x10^{-7}$ [2.130]	$5.6x10^{-8}$ [2.130]	Sn
Z*	26 [2.115]	36 [2.115]		Sn
			68-87 [2.135]	SnAgCu
Q* [eV]	n.a.	n.a.	n.a.	

Table 2.4: Literature-available migration related material parameters for Cu_6Sn_5. n.a.: not available

The separate activation energies (E_A) for the diffusion of Cu and Sn in Cu_6Sn_5 and Cu_3Sn were found to be 0.8eV, but the melting temperature of Cu_6Sn_5 (415°C) is lower than the melting temperature of Cu_3Sn (676°C). The melting temperature is directly related to E_A [2.100]. Consequently the E_A for the motion of Cu and Sn in Cu_6Sn_5 should be lower than the E_A of both elements in Cu_3Sn, but previous experiments do not show a difference (E_A tables 2.4 and 2.5). Furthermore the given diffusion constants (D_0) of Cu and Sn in Cu_3Sn differ by several orders of magnitude.

Especially for Cu the given Z* values are close to the nuclear charge. The values of Z* are the result of the interaction between the atom nucleus and the electrical field and the interaction between the surrounding electron gas and the electron wind due to the current flow. Therefore the given values for Z* are relatively high. These high values are given without an explanation of transport mechanisms in the Cu-Sn IMCs and it becomes clear that the mechanisms of migration in Cu-Sn IMCs are not well understood to day.

This has the consequence that the $E_{A,}$ the D_0 and the Z* of the moving ions have to be clarified for both Cu-Sn IMCs. Furthermore the thermomigration in the Cu-Sn IMCs has to be investigated and Q* values have to be extracted.

2.6.2.2 Solder joints on ENIG pads

When the Cu pads are covered with Ni the diffusion of Cu into solder joints is blocked and replaced by the diffusion of Ni. The presence of Ni in the solder can lead to the formation Ni_3Sn_4 [2.137], but this depends on the Cu content of the solder. Often the Ni layer is protected with a thin Au film that leads to the formation of Au_4Sn during reflow [2.137].

In [2.140] it is shown that the presence of the Cu suppresses the formation of Ni-Sn IMCs during temperature storage by reducing the consumption rate of Ni. In [2.141] a SnAg solder joint without Cu content was temperature stressed and the formation of Ni_3Sn_4 was observed. In the following EM tests the growth speed of Ni_3Sn_4 was reduced by electromigration without any difference between up- and downstream cases. The missing influence of the current direction was explained by an opposite direction of the material exchange between Ni and Sn at the cathode and anode sides . A thermomigration induced formation of Ni_3Sn_4 in SnAg micro-bumps was proven in [2.142]. It was also shown that the Ni_3Sn_4 formation is suppressed below a critical temperature gradient. This critical temperature gradient decreases rapidly for smaller bump heights.

In [2.143] EM tests with SnAgCu solders were performed: if temperature storage is combined with an applied current Ni_3Sn_4 is formed in SnAgCu. In contrast with [2.141] a clear difference of the IMC thickness was found for up- and downstream tests, this is a clear indication for an EM induced mass flux. The only visible difference between both investigations is the use of SnAgCu in [2.143] instead of SnAg while the current density was similar and the test temperature was even a little bit lower than in [2.141]. Hence the presence of a current flow is necessary to form Ni_3Sn_4 in SnAgCu, but the presence of a relevant EM induced mass flux or its influence on the IMC formation is not clear.

Overall only a few material parameters for the migration induced Ni_3Sn_4 formation are available (Table 2.5). There is a wide range of possible activation energies and no values for SnAgCu are available. The effective charge values in [2.144] decrease with a rising test temperature which indicates that the used activation energy of 1.2eV is too high. Furthermore stress tests with alternating current are necessary to suppress a directed mass flux due to EM and to show a possible electrochemical reaction between SAC and Ni as a consequence of an electron flow. A possible Q* value of Ni_3Sn_4 is mentioned in [2.142] without further explanation.

	Ni	**Sn**	**Ni_3Sn_4**	**Solder**
E_A [eV]	n.a.	n.a.	0.75 [2.145]	SnAg
			0.56 [2.147]	SnAg
			0.94 [2.148]	SnAg
			0.99 [2.146]	Sn
			1.14 [2.149]	SnAg
			1.21 [2.144]	SnAg
D_0 [m^2/s]	n.a.	n.a.	n.a.	
Z*	n.a.	n.a.	-160 to (-60) [2.144]	SnAg
Q* [eV]	n.a.	n.a.	0.08? [2.142]	SnAg

Table 2.5 Literature-available migration related material parameters for the Ni_3Sn_4 in SnAg. n.a.: not available

2.7 Conclusion

On the permanently changing market for microelectronic products the creation of innovations is a must. The performance of a new product being related to concepts like “More Moore” or “Beyond Moore” is important, but not the only relevant factor. In addition the costs and the risks of development on the company’s side, as well as the benefits and the financial risks on the customer’s side have to be taken into account. The realization of “More Moore” or “Beyond Moore”, by downscaling on transistor level or by the creation of new transistor technologies, is coupled with exponentially increasing costs for the equipment and increasing development risks due to quantum mechanical effects and the growing relevance of the signal transit time for the final clock rate.

Against the background of limited financial resources, alternative concepts like “More than Moore” were developed to drive innovations on the microelectronic market. One idea of “More than Moore” is to replace the downscaling on transistor level by the three dimensional packing of ICs. Furthermore the use of existing microelectronic devices under harsh environment conditions develops new markets for the semiconductor industry. By that way the “More than Moore” concept enables the manufacturers to be in touch with their customers’ needs and it keeps the costs and development risks under control.

A critical consequence of three dimensional packaging is a growing number of electrical contacts per package. A growing number of solder joints in a BGA becomes possible by downscaling of the bump diameter. Unfortunately the reduced dimension of the solder joints means that the current density is increased. As a consequence low melting solders like SnAgCu or SnPb are affected by EM induced reliability issues. In addition the melting point of Sn based solders is too low for harsh environment applications. Hence alternatives to the conventional reflow soldering with low melting materials have to be developed.

Compared to different alternatives to reflow soldering the transformation of conventional solder joints into IMC joints is a promising concept. IMCs like Cu_6Sn_5 and Cu_3Sn have a higher melting point than Sn based solders and a lower melting point than Cu. Hence the transformation of Sn based solder joints into IMC joints can be performed at relatively low process temperatures, while the maximum operation temperature of the final IMC joints is relatively high. In addition Cu-Sn IMC bumps have shown very promising results in all aspects of IC packaging reliability.

The diffusion and migration driven transformation of Sn based solder joints into IMC joints is called Transient Liquid Phase Soldering (TLPS). The process times of TLPS depend on the solid state diffusion of Cu and Sn. A high process temperature clearly increases the IMC formation speed, but it also induces high thermal stress values in the ICs. The presence of a current flow also accelerates the IMC formation by inducing additional mass fluxes due to EM and TM. The benefit of an EM and TM accelerated IMC formation is that the process temperature does not have to be increased. Nevertheless for a prediction of the TLPS process time a general model of the diffusion and migration driven IMC formation is needed.

Unfortunately the availability of valid material parameters for the modeling of diffusion and migration driven IMC formation is in a stark contrast with the relevance of TLPS. Hence for the required prediction of the IMC formation speed the diffusion, EM and TM related material parameters have to be determined by our own experiments.

3 Theory of Diffusion and the Experimental Setup

The material parameters for the characterization of the solid state diffusion in IMCs have to be determined by exploration of the Cu-Sn IMC formation during aging tests.

At the beginning of this chapter the theoretical background of the different migration phenomena in the IMC layers will be explained (sections 3.1.-3.2). Based on this an experimental procedure for the characterization of the migration phenomena and the extraction of the related material parameters can be given (section 3.3). In the following details about the chosen experimental equipment and the preparation of the samples will be stated. In section 3.4 a mathematical model for the quantification of the migration induced mass flux out of the test results will be derived.

The simulation based analysis of the aging tests will be explained in section 3.5. At least an algorithm for the dynamic simulation of the IMC growth will be developed.

3.1 Theory of Solid State Diffusion

The atomic theory of diffusion describes the movement of atoms (ions) or molecules in gases, liquids or solids. After the first few minutes of the TLPS process the material movement in solid IMCs becomes the bottle neck for the total mass flux. As consequence the diffusion mechanisms in solid IMCs [3.1-2] dictate the total process time, being in range of a few hours. Hence the characteristics of solid state diffusion are relevant for the development of TLPS processes.

The following explanation and derivation of the atomic theory of diffusion in solids are mainly based on [3.3] and [3.4]. Both books present idealized crystalline metals, but if necessary the available models are adjusted to the material transport in the more complex Cu-Sn IMCs.

3.1.1 Transport Mechanisms

Diffusion in solids appears due to randomly jumping atoms moving through the material via different diffusion mechanisms. The two main diffusion mechanisms in the solder joints and in the IMC layers are the interstitial mechanism and the vacancy mechanism [3.3].

3.1.1.1 Interstitial mechanism

In case of interstitial diffusion the atoms move from interstitial points in the crystal lattice to neighboring ones without displacing atoms in the crystal lattice itself (Fig. 3.1).

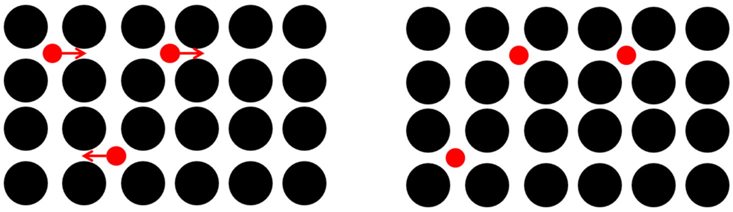

Figure 3.1: Interstitial diffusion of point defects (red) in a crystal lattice

Interstitial diffusion is only possible when the channels in the crystal lattice are big enough to let the impurities pass without a deformation of the crystal lattice. In [3.5] it was clarified that the radius of the crystal ions in the metal grid, and not the atomic radius, defines the minimum size of the channels in a metal grid.

So called “fast diffusers”, like Ni, Cu, Au or Ag in pure Sn, are able to move as interstitial point defects via diffusion channels because their atomic radius is smaller than the diffusion channels between the Sn crystal ions [3.6-9]. The main characteristics of “fast diffusers” are low activation energies (E_A=0.08-0.19eV [3.7-9]) and a low solubility of the moving species in the material, e.g. 0.05 wt. ppm for Ni in Sn [3.9].

Interstitial diffusion enables the fast transport of Cu, Ni or Au from one IMC layer, through the solder joint, to another one without changing the solder composition in a measurable scale. Hence the diffusion of interstitial point defects is an important transport mechanism between IMC layers when they are separated by the solder joints.

3.1.1.2 Vacancy mechanism

The presence of vacancies as point defects in the crystal lattice allows metal ions to jump from one lattice site to another one without displacing other atoms (Fig. 3.2). The related transport mechanism is called the vacancy mechanism and it is the main transport mechanism for the self-diffusion of pure metals like Cu or Al and it is the main transport mechanism for Cu and Sn in Cu-Sn IMCs. In contrast with the interstitial transport mechanism the vacancy mechanism requires the deformation of the crystal lattice and consequently the activation energies for diffusion via the vacancy mechanism is higher than for interstitial diffusion and the related materials do not act as “fast diffusers”.

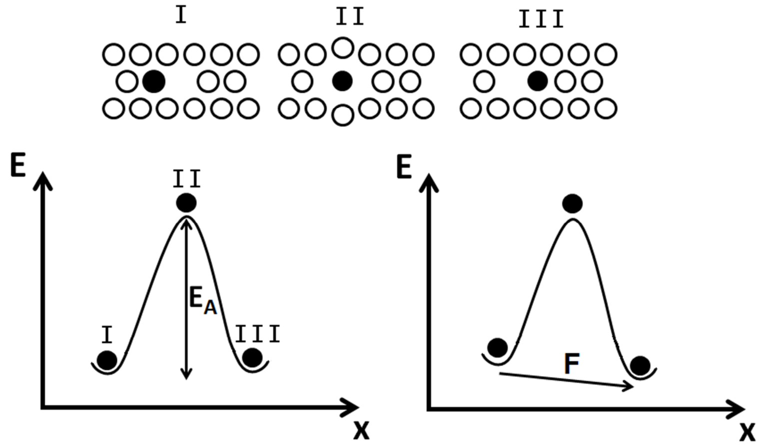

Figure 3.2: Sequence of configurations for the vacancy mechanism with (right) and without (left) a drift due to an external driving force (F) on the moving ion

For the material transport by vacancy diffusion the presence of unoccupied lattice sites is necessary. The increase in the entropy (S) in dependence of the vacancy density (N_V) is given by (3.1) [3.3].

$$\frac{\delta S}{\delta N_V} = -k_B \cdot ln\left(\frac{N_V}{1-N_V}\right) \qquad (3.1)$$

Taking the limiting behavior of (3.1) into account it becomes clear that for (N_V→0) the increase in the entropy is infinitive when a few vacancies are added to crystal lattice [3.3]. Hence a certain number of vacancies can always be expected in the crystal lattice. Furthermore the Kirkendall effect leads to the creation of vacancies at the IMC interfaces [3.10] and the existence of grain boundaries in the IMC layers [3.11] goes together with a high defect density too.

3.1.2 The Random Walk Problem and the Diffusion Coefficient

For the interstitial and for the vacancy mechanism the effective motion of the atoms can be defined as a “Random Walk Problem”. This is due to the fact that the atoms in a crystal lattice are jumping randomly from one lattice site to a neighboring one. Random walk means: even when no preferred direction is given a certain number of atoms passes an average distance over time (Fig. 3.3)

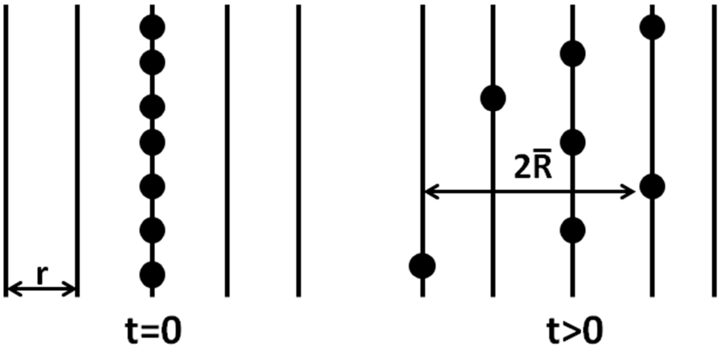

Figure 3.3: Initial distribution of atoms (left), and distribution of atoms after a few jumps (right)

This phenomenon was observed in macroscopic particles in 1827 by Robert Brown and was later called “Brownian Motion”. Based on the “Random Walk Problem”, which was firstly described by Karl Pearson in 1865 [3.12], Albert Einstein developed an atomistic theory of Brownian motion in 1905 [3.13]. The following description of the model is based on the root-mean–square displacement ($\overline{R}$) of many atoms after many possible jumps (n) and the following assumptions:

1. The passed distance per jump ($\vec{r}$) will always be the same, which would be correct for a face centered cubic (fcc) crystal structure.
2. For every lattice site an atom could jump to, there will be another free lattice site in the opposite direction. The jumping probability in both directions will be the same ($\vec{r_i} = -\vec{r_j}$).
3. The process is completely randomized, hence it has no a preferred direction. This is correct when no driving force leads to drift of the atomic movement (Fig. 3.2).

The average distance being passed by the atoms over time (t) can be described as a sum of “n” vectors (3.2). The number “n” is the jumping frequency of the atoms (f) multiplied with the time (3.3).

$$\vec{R}_n = \vec{r}_1 + \vec{r}_2 + \vec{r}_3 \ldots \vec{r}_n = \sum_{i=1}^{n} \vec{r}_i \quad (3.2) \qquad\qquad n = f \cdot t \quad (3.3)$$

The value of the vector $\vec{R}_n$ is given by (3.4) [3.3 p. 62]:

$$\vec{R}_n \cdot \vec{R}_n = R_n^2 = \sum_{i=1}^{n} \vec{r}_i \cdot \vec{r}_i + 2 \cdot \sum_{j=1}^{n-1} \sum_{i=1}^{n-j} \vec{r}_i \cdot \vec{r}_{i+j} = \sum_{i=1}^{n} r_i^2 + 2 \cdot \sum_{j=1}^{n-1} \sum_{i=1}^{n-j} |\vec{r}_i| \cdot |\vec{r}_{i+j}| \cdot cos(\theta_{i,i+j}) \quad (3.4)$$

Based on the assumption (1-3), with assumption (2) leading to cos (θ_{i+j})=cos(θ_i)+/-180°, and taking into account many jumps of many atoms (n>>1) Eq. 3.4 can be simplified to (3.5). In this case the double summation becomes zero.

$$\overline{R_n^2} = n \cdot r^2 + 2r^2 \cdot \sum_{j=1}^{n-1} \sum_{i=1}^{n-j} cos(\theta_{i,i+j}) = n \cdot r^2 \quad (3.5)$$

The diffusion coefficient (D) can now be defined by the root-mean–square displacement in on direction (3.6). The diffusion coefficient depends on the jumping frequency of the atom and the jumping distance. The factor 1/6 is due to the fact that the diffusion process appears in a three dimensional system and two directions per dimension are available.

$$\overline{R_n^2} = n \cdot r^2 = 6Dt \rightarrow \ D = 1/6 \cdot f \cdot r^2 \quad (3.6)$$

Material degradation due to diffusion is a reliability issue of IC interconnects being made of Cu or Al. Both metals have a fcc crystal structure (Fig. 3.4) and assumptions (1-3) are sufficient. Nevertheless even in this case the jumping frequency of the atoms is orders of magnitude smaller than their vibration frequency (Debye frequency) [3.3]. Hence (3.6) cannot be used for the calculation of D with common material parameters or the other way around. For the vacancy mechanism a reason for the difference between the jumping and the Debye frequency is the fact that a vacancy has to be created before the jump of a crystal ion is possible.

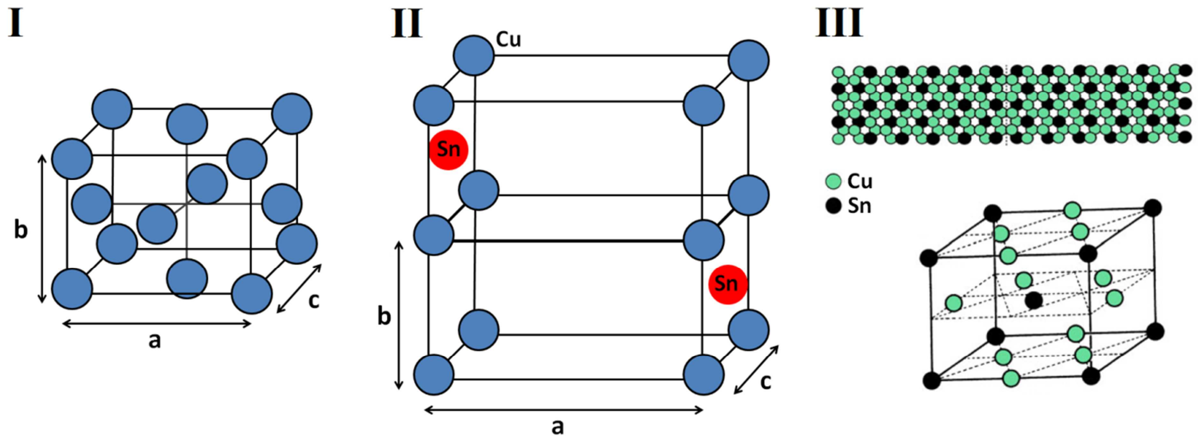

Figure 3.4: A unit cell with a face centered cubic -fcc- structure a=b=c (I), the unit cell of Cu_6Sn_5 (II) and the superstructure of Cu_3Sn (III) based on the $CuTi_3$ unit cell [3.14]

The investigated Cu-Sn IMCs Cu_6Sn_5 and Cu_3Sn have a more complex crystal structure than pure Cu or Al (Fig. 3.4):

- The unit cell of Cu_6Sn_5 is based on two orthorhombic cells (a≠b≠c) with 12 Cu atoms at the regular lattice sites and two base-centered Sn atoms with an alternating position ($oB8_2$) [3.14-15].
- The unit cell of Cu_3Sn is a superstructure of 80 atoms being formed by a body-centered orthorhombic structure of Sn atoms and Cu atoms with alternating positions on the structure surfaces (oC80) [3.16-17].

In fcc crystals the distance between two lattice sites is always the same (r=a/2 in Eq. 3.6), but the relatively complex crystal structure of IMCs leads to different jump distances in every direction and as a consequence the diffusion coefficients of the IMCs are anisotropic. Furthermore the distance between two neighboring lattice sites is different for Cu and Sn and the diffusion coefficients could also be different.

On the other hand, if the motions of both elements seen as an interaction between two separate crystal structures which form the IMC, the material exchange from one crystal structure to the other should be equal. In this case the resulting diffusion constants of both elements in the IMCs would be similar [3.18]. Nevertheless this would require a vacancy mechanism leading to the replacement of Cu sites by Sn, or the other way around, which would lead to a permanent deformation of the crystal structure. Under these conditions the moving atoms should immediately jump back to their original position to reduce configuration energy. Huntington mentioned the possibility of jumping cycles for vacancies which would enable material transport as well as the rearrangement of the crystal structure. Based on this assumption he described a vacancy mechanism based on a six jumps cycle which described the material transport in binary alloys at low temperatures [3.18]. In the literature similar [3.19] and very different diffusion coefficients [3.14] for Cu and Sn in Cu_6Sn_5 and Cu_3Sn are given, so it is not clear if a six jumps cycle or a simple vacancy mechanism is relevant for the material transport in Cu-Sn IMCs.

Another problem which prevents the calculation of the diffusion constants for Cu-Sn IMCs with (3.6) is the presence of grain boundaries as diffusion paths as shown in Fig. 3.5 [3.11], because their amorphous structure disables the determination of a constant jumping distance. Overall the diffusion coefficients of Cu and Sn in Cu_6Sn_5 and Cu_3Sn have to be determined experimentally and the results are empirical values being influenced by the anisotropy of the IMCs and the presence of grain boundaries as diffusion paths.

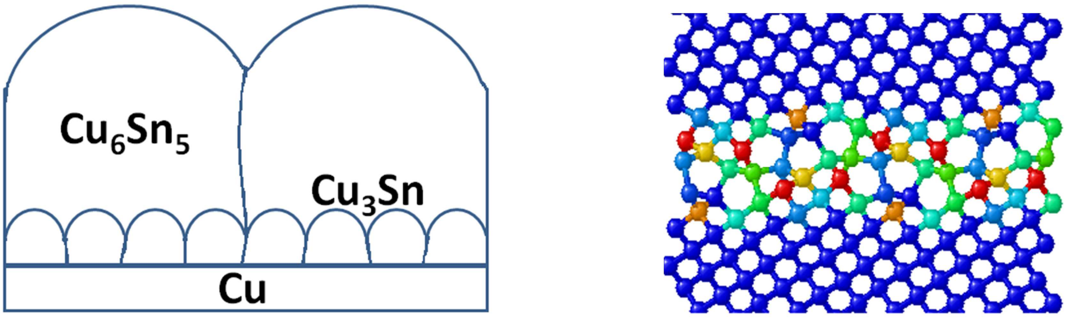

Figure 3.5: Grain structure of Cu_3Sn and Cu_6Sn_5 (left) and the amorphization of the crystal structure at the grain boundaries (right) [3.11]

3.1.3 Derivation of the General Mass Flux Equation

Based on the solution of the random walk problem a general description of the migration induced mass flux is possible. For the following description of the diffusion induced mass flux two planes in the crystal will be defined (Fig. 3.6) and a vacancy transport mechanism will be supposed [3.3]. At both planes a certain number of atoms will be present (n_A [1/m²]). Every atom has a jumping frequency “w” and for a successful jump to a neighboring lattice site a vacancy has to be created. Hence the probability of a vacancy creation also has to be taken into account (p_v). Finally the mass flux at both surfaces is given by (3.7a-b).

$$\vec{J}_1 = n_{A1} \cdot p_{V1} \cdot w_1 \cdot d\vec{A}_1 \quad (3.7a) \qquad\qquad \vec{J}_2 = n_{A2} \cdot p_{V2} \cdot w_2 \cdot d\vec{A}_2 \quad (3.7b)$$

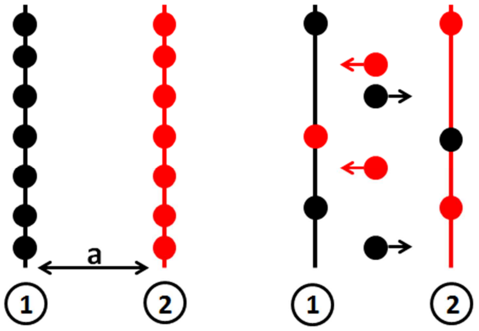

Figure 3.6: Mass flux between two planes in a crystal lattice

For the further steps the following assumptions will be made:

1. The effective mass flux is defined by the difference between the mass flux from plane one to plane two and the mass flux in the opposite direction: $\vec{J} = \vec{J}_{12} - \vec{J}_{21}$.
2. The jumping frequency at both planes is the same $w_1=w_2=w$.
3. The vacancy formation probability at both planes is the same $p_{V1}=p_{V2}=p_V$.
4. The planes are parallel to each other. The distance between both planes is $\vec{a} \perp \left(d\vec{A}_1 \wedge d\vec{A}_2\right)$.
5. The activity coefficient "K" is the probability that an atom jumps into the direction of +/- $\vec{a}$. That leads to $w_{12} = K_{12}w$ and $w_{21} = K_{21}w$.
6. If an external force (F) is present a drift of the diffusion induced mass flux appears because $K_{12} \neq K_{21}$, otherwise $K_{12}=K_{21}$.

Based on previous assumptions the resulting mass flux is now given by (3.8).

$$\vec{J} = p_V \cdot w \cdot (K_{12}n_1 - K_{21}n_2) \cdot \frac{\vec{a}}{|\vec{a}|} \quad (3.8)$$

With the volume density of the atoms ($N_1[1/m^3] = n_1/|\vec{a}|$), Eq. (3.8) can be transformed to (3.9).

$$\vec{J} = p_V \cdot w \cdot (K_{12}N_1 - K_{21}N_2) \cdot \vec{a} \quad (3.9)$$

With (3.10) the Eq. (3.9) can be transformed to (3.11), and additional theorems lead to (3.12).

$$(K_{12}N_1 - K_{21}N_2) = -\vec{a} \cdot grad(K \cdot N) \quad (3.10)$$

$$\vec{J} = -\, p_V \cdot w \cdot a^2 \cdot grad(K \cdot N) \quad (3.11)$$

$$\vec{J} = -\, p_V \cdot w \cdot a^2 \cdot [K \cdot grad(N) + N \cdot grad(K)] \quad (3.12)$$

Expecting a thermodynamic equilibrium, the Van`t Hoff equation [3.20] (3.13) with the thermodynamic activity (G) (3.14) can be used to describe the chemical potential "µ" (change of internal energy per atom). As solution the chemical potential (µ) is given in dependence of the atomic density and the jumping probability "K" (3.15).

$$\Delta\mu = \mu - \mu_0 = k_B \cdot T \cdot \ln(G) \quad (3.13) \qquad G = \frac{KN}{K_0 N_0} \quad (3.14)$$

$$\mu = \mu_0 + k_B T \cdot ln\left(\frac{KN}{K_0 N_0}\right) \quad (3.15)$$

Taking into account the principals of thermodynamics, the mass flux should reduce the intrinsic energy of the system. Hence the atoms have to follow the inverse direction of the chemical potential gradients. The gradient of μ can be calculated out of (3.12) and algebraic functions lead to (3.16).

$$\frac{N \cdot K}{k_B T} \cdot grad(\mu) = K \cdot grad(N) + N \cdot grad(K) \quad (3.16)$$

Inserting (3.15) into (3.12) leads to the Nernst-Einstein equation (3.17). This step proves that the Nernst-Einstein equation can be used for the calculation of the diffusion induced (F=0) as well as for the calculation of the drift induced mass flux (F≠0). Hence the Nernst-Einstein equation enables the physical interpretation of the test results in all possible cases.

$$\vec{J} = -\frac{NKp_V wa^2}{k_B T} \cdot grad(\mu) \quad (3.17)$$

With $|\vec{a}| = |\vec{r}|$ and $f = Fp_V w$ (3.18) can be used to define D for the given system:

$$D = K \cdot p_V \cdot w \cdot a^2 \quad (3.18)$$

At the moment (3.17) and (3.18) seem to be temperature independent, while (2.23), (2.30) and (2.31) are exponentially temperature dependent. Furthermore (3.17-18) include parameters which are difficult to measure, like the void formation probability or the jumping frequency of the atoms. Hence it is necessary to describe a relation between these values and more basic material parameters.

Expecting a thermodynamic equilibrium and referring to the Van`t Hoff equation the temperature dependency of the void formation probability follows an Arrhenius relation [3.3] (3.19). In the same manner the probability that an atom vibration leads to a jump from one lattice side to another one is exponentially temperature dependent [3.3] (3.20).

$$p_V = \exp\left(\frac{-H_V}{k_B T}\right) \quad (3.19) \qquad\qquad w = v_D \cdot \exp\left(\frac{-H_m}{k_B T}\right) \quad (3.20)$$

H_V= Enthalpy change per vacancy added to an infinite crystal.
H_m= Enthalpy change per activated complex (intermediate state of an atomic interaction) added to an infinite crystal.
v_D= Debye frequency

Finally the activation energy (E_A) needed for the movement of a crystal ion by the vacancy mechanism is: E_A=H_V+H_m. Now D can be described by (3.21):

$$D = K \cdot v_D \cdot a^2 \cdot exp\left(-\frac{E_A}{k_B T}\right) \quad (3.21)$$

In addition to the E_A the diffusion constant (D_0) will be defined as the second temperature independent material parameter to describe a migration induced mass flux. The D_0 of a material depends on the jumping distance, being related the lattice constant in the most simple cases, the Debye frequency, and the probability that an atom jumps in the considered direction (3.22).

$$D_0 = K \cdot v_D \cdot a^2 \quad (3.22)$$

The final equations (3.23-24) describe the mass flux due to diffusion as well as due to the drift of atoms as a function of the chemical potential gradient, the temperature and the generalized material parameters E_A and D_0:

$$D = D_0 \cdot exp\left(-\frac{E_A}{k_B T}\right) \quad (3.23)$$

$$\vec{J} = -\frac{N D_0}{k_B T} \cdot grad(\mu) \cdot exp\left(-\frac{E_A}{k_B T}\right) \quad (3.24)$$

Due to the complex crystal structure of the IMCs and the influence of diffusion paths, E_A and D_0 have to be determined empirically. Nevertheless the given equations help to find experimental procedures for the characterization of the migration processes and they enable the evaluation of the test results. If the temperature difference between the two observed planes becomes relevant the void formation probability (3.19) and the jumping frequency (3.20) of the atoms will not be equal anymore. In this case the assumptions (2) and (3), which this derivation is based on, are not true anymore. Under these conditions local mass flux divergences appear which change the material density over time (2.24-25). The mass flux divergences are more relevant for reliability problems due to the migration induced void formation than for the IMC formation. A detailed description of the related mathematics is given in [3.21].

3.2 Specific Mass Flux Equations and Parameters

The interpretation of the Nernst Einstein Equation leads to the following fact: if a gradient of the chemical potential is present, the diffusion process has a preferred direction and a migration induced mass flux appears. The mass flux goes in the reverse direction of the chemical potential gradient. The identification of possible reasons for local differences of the chemical potential leads to the different migration phenomena. The relevant reasons for a migration induced mass flux during the IMC growth are:

1. concentration (N) gradients leading to the dissolution of an element in the solder joints,
2. an electric field/ an electron flux leading to electromigration,
3. temperature gradients leading to thermomigration,
4. and a difference in solubility of an element (e.g. the solubility of Cu in Cu-Sn IMCs and SnAgCu) leading to local accumulation of this element.

Furthermore a gradient of the hydrostatic pressure can lead to stress migration, but this effect was not found to be relevant for the IMC formation. Nevertheless the formation of Cu-Sn IMCs can lead to high hydrostatic pressure in the solder joints [3.22-23].

The influence of the four relevant driving forces on the chemical potential leads to the mathematical description of the related migration phenomena.

3.2.1 Diffusion

Expecting a concentration gradient without any additional influence on the jumping behavior of the atoms (K=1) Eq. (3.15) can simplified to (3.25).

$$\mu = \mu_0 + k_B T \cdot ln\left(\frac{N}{N_0}\right) \quad (3.25)$$

The gradient of the chemical potential is than given by (3.26):

$$grad(\mu) = \frac{k_B T}{N} \cdot grad(N) \quad (3.26)$$

Inserting (3.26) into (3.24) leads to the mathematical description of the mass flux due to diffusion:

$$\vec{J} = -D_0 \cdot grad(N) \cdot exp\left(-\frac{E_A}{k_B T}\right) \quad (3.27)$$

Concentration gradients and the related diffusion processes will always be present in the IMC layers. Hence in all experiments there will be an influence by diffusion and its characterization will be an important step to prepare the following investigations of the other migration mechanisms.

3.2.2 Electro- and Stressmigration

Electromigration (EM) is a thermally activated motion of atoms under the influence of a current flow. EM is a well-known phenomenon in IC interconnects and often appears in combination with a back flux by stressmigration. As a consequence of miniaturization EM has also appeared in solder joints.

3.2.2.1 Derivation of the mass flux equation

Under the influence of an electric field the movement of ions changes their chemical potential if their movement is directed with or against the field vectors. The chemical potential of a crystal ion in an electrical field is given by the “effective charge of the moving ion” (eZ*) and the electrical potential (Φ):

$$\mu = e \cdot Z^* \Phi \quad (3.28)$$

The gradient of the chemical potential is proportional to the gradient of the electrical potential. The gradient of the electrical potential describes the electric field ($\vec{E}$) and Ohms Law leads to a relation between the current density and gradient of the chemical potential (3.29).

$$grad(\mu) = e \cdot Z^* grad(\Phi) = -e \cdot Z^* \cdot \vec{E} = -e \cdot Z^* \cdot \rho_{el} \cdot \vec{j} \quad (3.29)$$

The mass flux due to electromigration is given by (3.30/2.32).

$$\vec{J}_{EM} = D_0 \cdot \frac{NeZ^* \vec{j} \rho_{el}}{k_B T} \cdot exp\left(-\frac{E_A}{k_B T}\right) \quad (2.32/3.30)$$

EM is often described by the statement that *"electrons push the ions away from their lattice sites*". Those statements are false because electromigration is a thermally activated mechanism because of two reasons:

1. Respecting the fact that the maximum current density in a solid material is limited by Joule heating, respectively its melting point, the gradient of the chemical potential of the moving ion is much smaller than the activation energy ($\mu << E_A$). In addition there is a big difference between the mass and the resulting impulse of electrons and atoms.
2. A vacancy has to be created before diffusion is possible and the vacancy creation is thermally activated (3.19).

In (2.23) the variable j_{min} is given as the minimum current density to cause electromigration. In (3.30) this term is missing because it is related to a back flux due to stress migration called the Blech effect [3.26]. A back flux appears when the mass flux due to EM leads to material accumulation at one side of the test structure while the material density becomes lower at another one. The resulting difference in the hydrostatic pressure (σ_H) leads to local stress gradients and a back flux due to the stressmigration. The mass flux due to stressmigration can be described in the same way like the mass flux due to EM.

The chemical potential of a single ion is given by its atomic volume (Ω) and the hydrostatic pressure (3.31). The gradient of the chemical potential is than inserted into the Nernst-Einstein equation which leads to the formula for the calculation of the back flux due stress migration (3.32).

$$\mu = \Omega \cdot \sigma_H \qquad (3.31)$$

$$\vec{J}_{SM} = -D_0 \cdot \frac{N\Omega}{k_B T} \cdot grad(\sigma_H) \cdot exp\left(-\frac{E_A}{k_B T}\right) \qquad (3.32)$$

In the following the minimum current density to cause EM is given by the equalization of (3.30) and (3.32) ($\vec{j} = \vec{j}_{min}$):

$$\vec{j}_{min} = \frac{\Omega}{eZ^* \rho_{el}} \cdot grad(\sigma_H) \qquad (3.33)$$

For the interpretation of (3.33) it is important to mention, that an EM induced elastic deformation of the test structure is necessary to build up the hydrostatic pressure and the related stress gradients. In case of interconnects for integrated circuits the deformation of the dielectrics and diffusion barriers due to EM induced material accumulation leads to hydrostatic pressure and the related back flux. As consequence the consideration of the Blech effect is a must for EM investigation on interconnects. Nevertheless solder joints are often freestanding and no hydrostatic pressure and no stress gradients can be created by EM. As result no Blech effect can appear in such solder joints ($|\vec{j}_{min}| = 0$).

3.2.2.2 Interpretation of the effective charge of the moving ion (Z*)

The determination of the effective charge of the moving ion (Z*) is one of the difficulties that have to be overcome to describe the effect of EM on the IMC formation speed. In general the value of Z* depends on the interaction between the electron flow (e^-) and the electron shell of the metal ions ($\vec{F_e}$). Furthermore the interaction between the electric field ($\vec{E}$) and the atomic core (p^+) has to be taken into account ($\vec{F_p}$). As shown in Fig 3.7 the resulting driving forces have opposite directions. Hence the difference of both driving forces leads to the effective driving force of the EM ($\vec{F}$) and the value of Z*. EM can follow the electron flux (Z*<0, e.g. Z^*_{Cu}=-5.5 [3.4]) or it can go into the direction of the electric field (Z*>0 e.g. Z^*_{Fe}= 5.4 [3.4]).

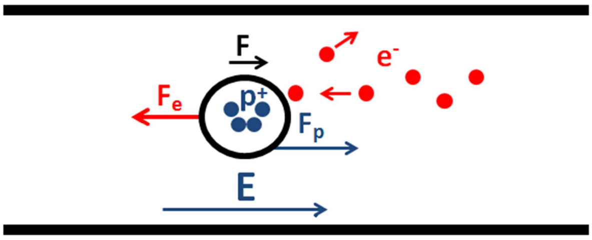

Figure 3.7: Driving force (F) for electromigration, resulting from the difference between the electric field force (F_p) and the momentum transfer due the electron flow (F_e), Z*>0

In pure metals the value of Z* should be bigger than the valence (Z) and smaller than the atomic number. A mathematical definition of Z* based on physical parameters, like the effective electron mass (m_e*), the defect density (N_D) and the specific resistance of defects (ρ_D) is given by Huntington [3.24].

$$Z^* = Z \cdot \left(\frac{1}{2} \cdot \frac{m_e}{m_e^*} \cdot \frac{\rho_{el,D,max} N}{N_D \rho_{el}} - 1\right) \qquad (3.34)$$

m_e= electron mass

In metals without a high defect density the effective charge is temperature independent [3.25]. In IMCs the Kirkendall effect and the high number of grain boundaries lead to a strong influence of vacancies on the electric field distribution. In the model of Bosvieux and Friedel [3.27] (3.35) the vacancies are seen as an additive negative charge (–Ze) and the scattering of electrons at the crystal defects is described by two Bessel functions (J_0, J_2). The resulting temperature dependent effective charge value $Z^{**}_{(T)}$ is the effective charge of a moving ion in a defective crystal lattice.

$$Z^{**}{}_{(T)} = \frac{1}{2} \cdot Z \cdot \left(1 - \frac{N \cdot \rho_D}{N_D \cdot \rho}\right) + \frac{2\tau_{(T)}}{3\pi} Z^2 \cdot \left(J_0\left(\frac{a}{r_H}\right) - 2J_2\left(\frac{a}{r_H}\right)\right) \qquad (3.35)$$

$\tau_{(T)}$ = lifetime of the electrons, a = lattice constant, r_H= Bohr radius

The temperature dependent effective charge value $Z^{**}_{(T)}$ can be higher than the atomic number. Often the $Z^{**}_{(T)}$ values for EM in grain boundaries are higher than the bulk values (Z*) and the direction of the mass flux changes: $Z^{**}_{Ag,GB}$=168, Z^*_{Ag}=-29 [3.4]. Hence the high defect density in the IMCs could explain the relatively high Z* values in the literature (tables 2.3 and 2.4).

3.2.3 Thermomigration

A visual description of thermomigration (TM) is its definition as an alternative form of a heat flux which is based on moving particles (e.g. atoms) instead of radiation (photons) or crystal vibrations (phonons). Hence the mass flux due to TM should depend on the temperature gradients and the moved thermal energy per atom.

3.2.3.1 Derivation of the mass flux equation

The relation between the temperature and the chemical potential is relatively complex, because the temperature has an influence on many other physical properties of the crystal lattice, like the lattice vibration or the relation between volume and pressure.
The Euler equation describes the internal energy of a closed system (U) as the sum of energies (E_i) being added to system by heat (Q) and work (W). The terms are given by the product of the volume and the pressure (E=-W=-VP) and the product of the temperature and the entropy (Q=TS) (3.36). The chemical potential is defined as the change of the internal energy per atom (3.37). The change of the internal energy of a closed system can be described with the fundamental thermodynamic equation (3.38).

$$U = \sum_i E_i = Q - W = T \cdot S - P \cdot V \quad (3.36)$$

$$\mu = \frac{dU}{dN} \quad (3.37) \qquad \mu \cdot dN = dU = TdS - PdV \quad (3.38)$$

For the following step the term PdV will be supposed to be zero, because the volume change of solid materials is negligible [3.28]. Furthermore many solder joints are free standing (P=0), and if a local increase of the pressure (P → σ_H<0) would appear, it would be removed by stressmigration:

$$dU = -PdV \rightarrow \mu = \frac{dV}{dN} \cdot \sigma_H = \Omega \cdot \sigma_H \quad (3.39) \rightarrow (3.31)$$

To determine the change of the chemical potential in dependence of the temperature change the remaining terms of the fundamental thermodynamic equation are differentiated with respect to the temperature (3.40).

$$d\mu \cdot dN = dS \cdot dT \quad (3.40)$$

Taking into account the relation between the entropy change and the change of the thermal energy (3.41), the chemical potential can be described by (3.42). TM is an alternative way to transport thermal energy by the motion of crystal ions. Hence the material parameter to describe this effect should be the thermal energy per ion. This parameter is called heat of transport (Q*=dQ/dN).

$$dS = \frac{dQ}{T} \quad (3.41) \qquad d\mu = \frac{dQ \cdot dT}{dN \cdot T} = Q^* \cdot \frac{dT}{T} \quad (3.42)$$

The chemical potential at one lattice side, in dependence of the temperature, is that given by the integration of (3.42) leading to (3.43). The gradient of the chemical potential as a consequence of a temperature gradient is that given by (3.44).

$$\mu = \mu_0 + Q^* ln(T) \quad (3.43)$$

$$grad(\mu) = \frac{Q^*}{T} \cdot gradT \quad (3.44)$$

Inserting (3.44) into the Nernst Einstein equation (3.24) leads to the description of the mass flux due to TM (3.45).

$$\vec{J}_{TM} = -D_0 \cdot \frac{NQ^*}{k_B T^2} \cdot grad(T) \cdot exp\left(-\frac{E_A}{k_B T}\right) \quad (3.45)$$

3.2.3.2 Interpretation of the heat of transport Q*

The characteristic parameter of the TM induced mass flux is the heat of transport Q*. An interpretation of Q* is given by Wirtz (3.46) [3.3-4]: The value of Q* is given by the transport energy of the moving ion H^M, being multiplied with a factor β_{TM} and subtracted by the vacancy formation at the neighboring lattice side. The factor β_{TM} is related to the interaction between the moving ion and the crystal lattice during TM. The term H_V can be interpreted as a thermal back flux of vacancies.
An illustration of the energy transmissions during the TM is given in Fig 3.8: to get the value of Q*, the total amount of energy being transported per crystal ion (H_α), has to be reduced by the required energy for the vacancy formation at the neighboring crystal site (H_V). Furthermore the placement of the ion at new lattice site needs a specific amount of energy too (H_γ). H_γ also has to be subtracted from H_α. Often the difference between H_α and H_γ divided by H^M can be interpreted as the factor β_{TM} (3.47).

$$Q^* = \beta_{TM} \cdot H^M - H_V \quad (3.46) \qquad \beta_{TM} = \left(H_\alpha - H_\gamma\right)/H^M \approx 0.8 \quad (3.47)$$

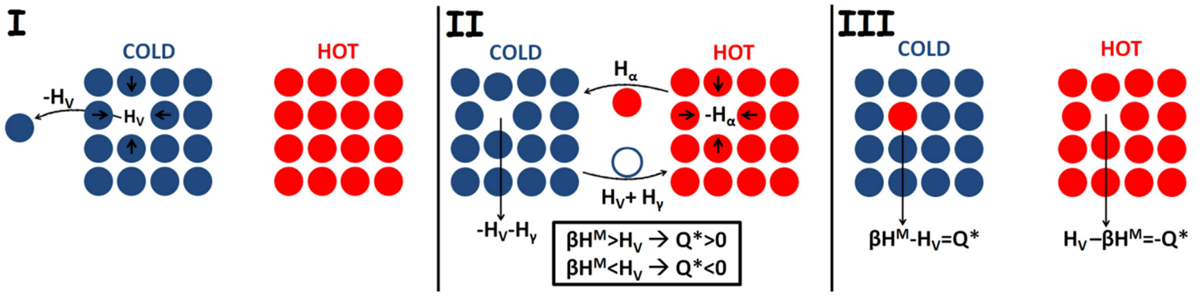

Figure 3.8: Thermomigration by a vacancy mechanism; I: vacancy creation, II: mass flux, III: energy balance

Often the transported energy per crystal ion is close to the void formation energy, and the Q* values are relatively small (e.g. Q^*_{Cu}=0.22eV [3.4]). Furthermore a material flux from the cold to the hot side can appear if the void formation energy is bigger than the transported energy per crystal ion (e.g. Q^*_{Au}= -0.22eV [3.4]).

In a solid compound like the investigated Cu-Sn IMCs the solubility of the elements is temperature dependent. Hence the temperature gradients causing TM automatically lead to local differences in the solubility. In this case the mass flux due to TM and a possible mass flux due to a temperature induced difference in solubility have the same driving force and they cannot be separated experimentally. Under these conditions a combined description of both effects is necessary. It was given for binary alloys by Wever [3.4]. The model of Wever includes a term named the heat of solution (H_S). It describes the thermal energy being needed to solve or segregate an element of a solid compound. With H_S and an Arrhenius relation the temperature dependent maximum concentration can be calculated (3.48). H_S can be defined as an additional portion of transported thermal energy per ion. The resulting equation for the TM induced mass flux in a binary alloy is that given by (3.49).

$$N_{max} = N_0 \cdot exp\left(-\frac{H_S}{k_B T}\right) \qquad (3.48)$$

$$\vec{J}_{TM} = -D_0 \cdot \frac{N \cdot (\mathrm{Q}^* + \mathrm{H_S})}{k_B T^2} \cdot grad(T) \cdot exp\left(-\frac{E_A + H_S}{k_B T}\right) \qquad (3.49)$$

For the interpretation of Q* through physical parameters Gerl divided it into two parts (3.50) [3.29]. One part describes the influence of lattice vibrations represented by phonons (Q^*_p) and one part describes the influence of the electron gas (Q^*_e). The phonon’s influence on Q* was described by Adolf Eugen Fick [3.4] (3.51). Nevertheless in metals the thermal transport is mainly done by the electron gas.

$$Q^* = Q^*_p + Q^*_e \qquad (3.50) \qquad\qquad Q^*_p = \frac{\sigma_p}{v_p}\kappa T \quad (3.51)$$

σ_P= cross section for phonon scattering, v_p= speed of sound, κ= thermal conductivity

The importance of the electron gas for the TM in metals indicates a relation between the effective charge Z* and the heat of transport Q*. Gerl and Brebec [3.30] found a relation between Z* and Q* for pure, fcc structured metals like Cu or Ag by ignoring the thermal electrical field and the electron scattering at crystal defects (3.52).

$$Q^*_{e(Z^*,T)} = -\frac{\pi^2}{6} \cdot \frac{(k_B T)^2}{\varepsilon_F} \cdot \left(1 + \left[\frac{\partial ln\sigma_{e(Z)}}{\partial \varepsilon}\right]_{\varepsilon=\varepsilon F}\right) \cdot Z^* \quad (3.52)$$

ε_F= Fermi energy, σ_e= cross section for electron scattering

In the IMC layers the high defect density has to be taken into account. Based on the work of Bosvieux and Friedel [3.27], Gerl developed a formula for the calculation of Q* under consideration of the thermal electrical field (3.53) [3.29].

$$Q^*_{e(Z^*,T)} = -\frac{m_e e^4 \sqrt{m_e^*}\sqrt{2}}{16\pi\varepsilon_0^2 {h_P}^3} \cdot \frac{\kappa_e T}{\sqrt{\varepsilon_F}} \cdot \sigma_{e(Z^*)} \cdot \left(1 + 2\left[\frac{\partial ln\sigma_{e(Z^*)}}{\partial \varepsilon}\right]_{\varepsilon=\varepsilon F}\right) \quad (3.53)$$

h_P=Planck’s constant, ε_0= vacuum permittivity, κ_e= thermal conductivity by the electron gas

Like the model of Bosvieux and Friedel (3.35) the equation of Gerl can also be used for the calculation of Q* under consideration of electron scattering at vacant crystal sites Q** (3.54) [3.29].

$$Q^{**}_{e(Z^*,T)} = \frac{1}{2} \cdot \left[-Z^* e s_T T + \left(1 + \frac{2J_2(a/r_H) - J_0(a/r_H)}{J_0(0)}\right) \cdot \; Q^*_{e(Z^*,T)}\right] \quad (3.54)$$

s_T= thermoelectric voltage

The Eqs. (3.52) and (3.54) are not the easiest way to get Q* of Cu and Sn in Cu_3Sn and Cu_6Sn_5, but the relation between Q*and Z* enables the interpretation of the test results based on the following statements:

1. Unlike the effective charge the heat of transport is temperature dependent (3.52), even when no electron scattering at crystal defects is taken into account.

2. When $Z^{**}_{(T)}$ is increased due electron scattering, $Q^{**}_{(T)}$ should also be increased. Investigations on the thermomigration in Pb have shown an increased heat of transport for grain boundary diffusion: $Q^{**}_{Pb,GB}$=0.25eV [3.31], Q^{*}_{Pb}=0.09eV [3.4]

3.2.4 Mass Fluxes due to Differences in Solubility

During the IMC growth in solder joints the copper content in the in SnAgCu solder decreases with increasing test time, while copper is accumulated in the IMCs [3.32]. In case of solder joints with Ni pads as diffusion barriers no diffusion of Cu from the metal lines into the solder joints can appear and the accumulation of Cu from the SnAgCu reservoir becomes important for the $(CuNi)_6Sn_5$ formation [3.33]. Furthermore it was shown that an increasing Ni content in the Cu-Sn IMCs leads to a higher formation speed of $(CuNi)_6Sn_5$ and to the dissolution of $(CuNi)_3Sn$ [3.34].

In contrast with TM in binary alloys, those intrinsic differences in solubility are not the result of local temperature gradients. Hence the related diffusion process has to be described with a separate model. For the modeling of the diffusion induced material accumulation a more general interpretation of the Van`t Hoff equation will be necessary than for the previous migration phenomena. In (3.55) the concentration with the lowest chemical potential (N_0) and the thermodynamic activity (G) are given as functions of the position.

$$\mu_{(x,y,z)} = \mu_0 + k_B T \cdot ln\left(\frac{N}{N_{0(x,y,z)}}\right) = \quad \mu_0 - k_B T \cdot ln\left(G_{(x,y,z)}\right) \quad (3.55)$$

The differentiation of (3.55) leads to a standard case of differential equations (3.56).

$$grad\left(\mu_{(x,yz)}\right) = k_B T \cdot \left[\frac{G_{(x)}{}'}{G_{(x)}} \hat{e}_{(x)} + \frac{G_{(y)}{}'}{G_{(y)}} \hat{e}_{(y)} + \frac{G_{(z)}{}'}{G_{(z)}} \hat{e}_{(z)}\right] \quad (3.56)$$

For the following steps the driving force for the diffusion driven material accumulation ($\vec{\beta}$) will assumed to be constant:

$$G_{(x,y,z)} = G_0 \cdot exp\left(\frac{\vec{\beta} \cdot \vec{r}_{(x,y,z)}}{k_B T}\right) \quad \vec{r}_{(x,y,z)} = \begin{pmatrix} x - x_0 \\ y - y_0 \\ z - z_0 \end{pmatrix} \quad (3.57a - c)$$

When (3.57a-c) are inserted in (3.55), the accumulation process can be described by inserting (3.55) into the Nernst Einstein equation (3.24):

$$\vec{J} = -\frac{N D_0}{k_B T} \cdot \vec{\beta} \cdot exp\left(-\frac{E_A}{k_B T}\right) \quad (3.58)$$

3.3 Experiments and Analysis

The main task of the experiments is the characterization of the migration induced Cu-Sn IMC growth in solid SnAgCu. Based on the known theoretical models an experimental procedure for the analysis of the different migration phenomena has to be developed and a sufficient test equipment has to be chosen. After the experiments an analysis of the IMC geometry and the IMC composition will be necessary. Furthermore a non-stressed package has to be analyzed to define the IMC thickness and composition after reflow as a starting point for the IMC formation during the aging tests.

3.3.1 Experimental Procedure

Independent of the chosen test conditions a mass flux due to diffusion will always be present in the solder joints. As consequence the mass flux due to diffusion has to be characterized first. Afterwards the influence of diffusion has to be considered for the interpretation of the following stress tests. Overall four different experiments are necessary to characterize the migration phenomena in the IMCs:

1. Long term and short term temperature storage tests at 150°C

Cu and Sn have to pass the IMC layer to form new IMC material. As a consequence the IMC formation speed is reduced with increasing layer thickness. The time dependence of the IMC layer thickness is described by the Deal Grove model (3.59a). For a short period of time the IMC growth speed can be assumed to be constant (3.59b), but for a long period of the time the IMC thickness over time is described by a square root curve (3.59c).

$$h_{(t)} = -\frac{Y}{2} + \frac{\sqrt{Y^2 + 4Z_G \cdot t}}{2} \qquad (t > 0) \wedge (h > 0) \quad (3.59a)$$

$$\lim_{t \to 0} h_{(t)} = \frac{Z_G}{Y} \cdot t \ (3.59b) \qquad \lim_{t \to \infty} h_{(t)} = \sqrt{Z_G \cdot t} \ (3.59c)$$

For a correct calculation of the ICM growth speed and the related mass flux values the influence of possible nonlinearities has to be known. Against this background the diffusion driven IMC formation was investigated at a constant oven temperature of 150°C for one, two, four, six and eight weeks. Based on the test results a time limit for the non-observance of a possible nonlinearity of the IMC growth over time was defined.

2. Temperature storage tests at different temperatures

Due to the Arrhenius relation, the mass flux values and the related IMC formation speed are exponentially temperature dependent. Hence the time limit to an observable nonlinearity of IMC growth has to be temperature dependent too.

For the extrapolation of the diffusion induced mass flux at different temperatures the activation energy (E_A) and the diffusion constant (D_0) have to be known. If the driving force of the mass flux is temperature independent, E_A can be determined by measuring the mass flux in the IMCs at two different test temperatures. During temperature storage tests only the mass flux due to diffusion (3.27) is relevant and the temperature gradient can be assumed to be temperature independent. By calculating the factor of temperature acceleration (AFT) with (3.60), E_A can be given by (3.61).

$$AFT = \frac{\left|\vec{J}_{D,T1}\right|}{\left|\vec{J}_{D,T2}\right|} = \frac{-D_0 \cdot |grad(N)| \cdot exp(-E_A/k_B T_1)}{-D_0 \cdot |grad(N)| \cdot exp(-E_A/k_B T_2)} = exp\left(\frac{E_A}{k_B} \cdot \left(\frac{1}{T_2} - \frac{1}{T_1}\right)\right) \quad (3.60)$$

$$E_A = \frac{ln(AFT) \cdot k_B \cdot T_1 \cdot T_2}{(T_1 - T_2)} \quad (3.61)$$

For the determination of D_0 the concentration gradients have to be known (3.62). The material composition of the IMCs was investigated with Energy-Dispersive X-Ray Spectroscopy (EDS). The compositional range of both IMCs is one mass percent [3.2] which is close to the accuracy of the EDS investigation. Furthermore the skittering effect of the incident electron beam limits the lateral resolution of the EDS in a range of 1µm. Especially the limited lateral solution of EDS complicates the investigation of the relatively thin (h<1µm) Cu_3Sn layers. Hence the known compositional ranges of the IMCs and their dimensions have to be used to estimate the concentration gradients (3.63).

$$D_0 = \frac{\left|\vec{J}_{D1,2}\right| \cdot exp\left(E_A/k_B\, T_{1,2}\right)}{|grad(N)|} \quad (3.62)$$

$$grad(N) \approx \frac{\Delta N}{(h + h_0)/2} \quad (3.63)$$

For the determination of E_A and D_0 three additional temperature storage tests will be performed at 100°C (t=2798h), 120°C (t=784h), and 140°C (t=163h). Finally four data points between 100°C and 150°C will be available for the investigation of the diffusion induced mass flux.

3. A stress test with alternating current (AC)

An applied current always leads to Joule heating, so an EM test will always be combined with TM. An alternating direction of the applied current suppresses a directed mass flux due to EM, while Joule heating and TM are still present. Furthermore it is not clear why an applied current is needed to form Ni_3Sn_4 in Cu containing solders joints on Ni pads. Against this background an AC test with SnAgCu bumps on Ni pads is necessary. It will show if an electron flux leads to an electro-chemical reaction between SnAgCu and Ni, or if a directed mass flux of Ni into the SnAgCu is necessary to form Ni_3Sn_4.

The AC test will be performed at an oven temperature of 120°C with an applied current of 0.8A (j=14µA/µm²) and the chosen test time is 790h. Previous experiments on IC interconnects have shown that a frequency of a few Hz is high enough to suppress an effective mass flux due to EM [3.35]. The suppression of EM induced effects appears because positive mass flux divergences, indicating EM induced material degradation, and negative mass flux divergences, indicating EM induced material accumulation/annealing, alternate at the same sites. The required frequency to suppress EM induced material degradation by annealing decreases with the current density [3.35]. The current density in solder joints is orders of magnitude smaller than the current densities in interconnects, while a frequency of few Hz was enough to suppress EM induced effects in interconnects. Hence the frequency of the normal line voltage (50Hz), being clearly higher than the critical frequencies in [3.35],should be high enough to suppress an effective mass flux due to EM.

For the calculation of the TM induced mass flux out of the test results, the mass flux due to diffusion has to be subtracted from the total mass flux in the IMCs (3.64). Due to Joule heating the test temperature is higher than the oven temperature and the mass flux due to diffusion has to be extrapolated. This was done with the results from step two (D_0, E_A) and (3.60).

$$\vec{J}_{TM} = \vec{J}_T - \vec{J}_D \quad (3.64)$$

For the calculation of Q**$_{(T)}$ through the TM induced mass flux, the temperature and the temperature gradients of the IMC layers have to be determined (3.65). Against this background thermo couples were placed on the top side of the stressed packages. The measured temperatures as well as the oven temperature were used as boundary conditions for a Finite Element Analysis (FEA) of the test structure (more details are given in section 3.5).

$$|Q^{**}_{(T)}| = \frac{|\vec{J}_{TM}| \cdot k_B \cdot T^2 \cdot exp(E_A/k_B\,T)}{D_0 \cdot N \cdot |grad(T)|} \quad (3.65)$$

4. Stress tests with direct current (DC)

Finally three DC tests were performed. The three tests simulate the case of all migration phenomena (EM, TM and diffusion) together. The principal directions of the three possible mass flux components are shown in Fig. 3.9. Two DC tests were performed as lifetime test by W. Feng at 100°C (t=2369h) and 120°C (t=192h) [3.36]. Afterwards a third aging test at 140°C (t=144h) was performed. In all cases the applied current was 1A (j_{avg}=18µA/µm^2).

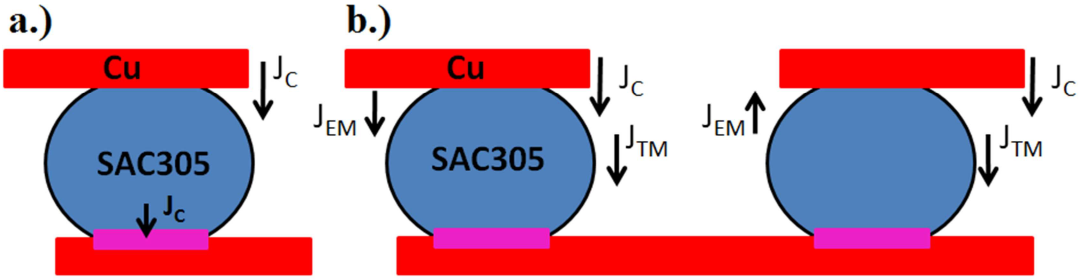

Figure 3.9: Scheme of the mass flux during temperature storage (a) and during DC stress tests (b)

To enable a direct comparison of up- and downstream EM stress, the tested solder joints are connected to daisy chains. Under this condition the mass flux due to EM and TM can be calculated through mass flux values for the up- and the downstream case (3.66-67).

$$\vec{J}_{EM} = \frac{\vec{J}_{T,Down} - \vec{J}_{T,Up}}{2} \quad (3.66) \qquad \vec{J}_{TM} = \frac{(\vec{J}_{T,Down} + \vec{J}_{T,Up})}{2} - \vec{J}_D \quad (3.67)$$

Like for the AC test, for the interpretation of the DC tests Joule heating has to be taken into account and for the calculation of Q** the temperature gradients are necessary. A FEA was performed to calculate the local test temperature and the temperature gradients at the IMC layers. For the calculation of the TM induced mass flux the diffusion induced mass flux has to be extrapolated (3.67). For the calculation of Z** with (3.68), the test temperature and the specific resistance of the IMCs are needed.

$$|Z^{**}_{(T)}| = \frac{|\vec{J}_{EM}| \cdot k_B \cdot T \cdot exp(E_A/k_B\,T)}{D_0 \cdot N \cdot |\vec{j}| \cdot e \cdot \rho_{el}} \quad (3.68)$$

The specific resistance of the IMCs will be taken from the literature (table 3.1). The specific resistance is temperature dependent (3.69) and the different test conditions cover a relatively wide range of temperatures, so the temperature coefficient of resistance (TCR) will be needed for the correct calculation of Z*. In the literature a TCR is only available for Cu_6Sn_5.

$$\rho_{el} = \rho_{T0} \cdot [1 + TCR_{T0} \cdot (T - T_0)] \quad (3.69)$$

	Cu_6Sn_5	Cu_3Sn
ρ_{el} [Ωμm]	0.175 [3.37]	$89.3x10^{-3}$ [3.37]
TCR [1/K]	$3.5x10^{-3}$ [3.38]	n.a.

Table 3.1: Specific resistance and TCR of the IMC layers.

3.3.2 Experimental Setup

For all tests Amkor® Package-on-Package (PoP) structures with a size of 12x12mm were used. The PoP structures include two packages being connected with two different Ball Grid Arrays (BGAs). An illustration of the PoP structure is given in Fig 3.10.

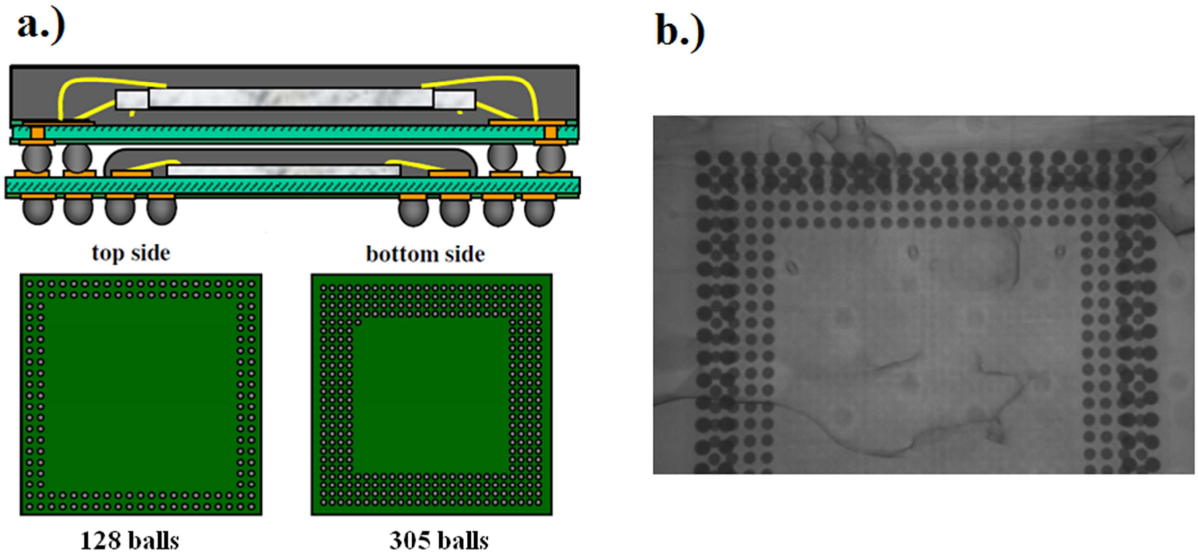

Figure 3.10: An Illustration (a) [3.39] and a X-Ray picture (b) [3.36] of the PoP test structure

The BGA of the top package is formed out of 128 $SnAg_{3.0}Cu_{0.5}$ (SAC305) solder joints. Their contact pads on the die and the board side are covered with an Electroless Nickel Gold (ENIG) layer as diffusion barrier for Cu atoms coming from the metal lines ("closed system").

The BGA of the bottom package includes 305 $SnAg_{3.0}Cu_{0.5}$ solder joints. Their die side contact surfaces are directly connected to the Cu pads, while the board side contact pads are covered with NiP (Fig. 3.11). Due to the missing diffusion barrier at the die side Cu atoms can flow from the die side contact pads into the bottom bumps ("open system").

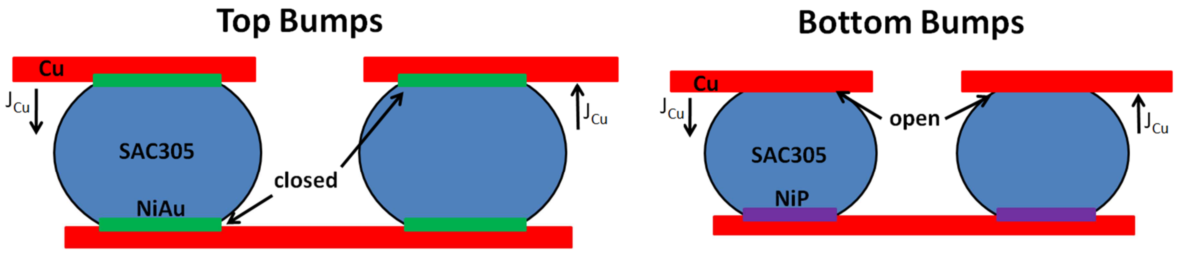

Figure 3.11: Illustration of a closed system with Ni diffusion barriers (left) and an open system without Ni barrier at the die side (right)

The long term temperature storage tests were performed with single packages. For the DC-EM and the AC-TM tests FR-4 boards with 24 packages per board were used (Fig. 3.12, left). For the thermal aging tests as well as for the DC-EM and AC-TM tests the single packages and the test boards were placed in ovens. The test boards were designed to compare EM reliability tests with temperature storage tests [3.36], so the contact pins in the middle of the cards allow the application of a current on single packages. During the AC-TM and the DC-EM tests one half of the packages were current stressed while the other packages were temperature stressed only. Afterwards the influence of a TM or EM induced mass flux on the IMC formation was clarified by comparing the AC-TM and the DC-EM test results with the IMCs in the temperature stressed packages.

As shown in Fig 3.12 the solder joints are connected to daisy chains. The daisy chains are divided into sub chains: "a1" to "a4", "b1" to "b4", "c1" to "c4" and "d1" to "d4" for the bottom packages, and "A" and "B" for the top packages. The daisy chains are accessible over contact pads on the FR-4 board which enables resistance measurements on single sub chains.

During the DC-EM tests a constant current source (Sodilec 60V 5A) guaranteed a constant driving force, even if the resistance of the daisy chains increases due to material degradation. That means the performed EM tests were "constant current tests". For the AC tests normal line voltage (230V/50Hz) was transformed (24V/50Hz) and the applied current was limited with a manual potentiometer. For the documentation of the tests a multimeter (Keithley 2000) and a LabView® program were used.

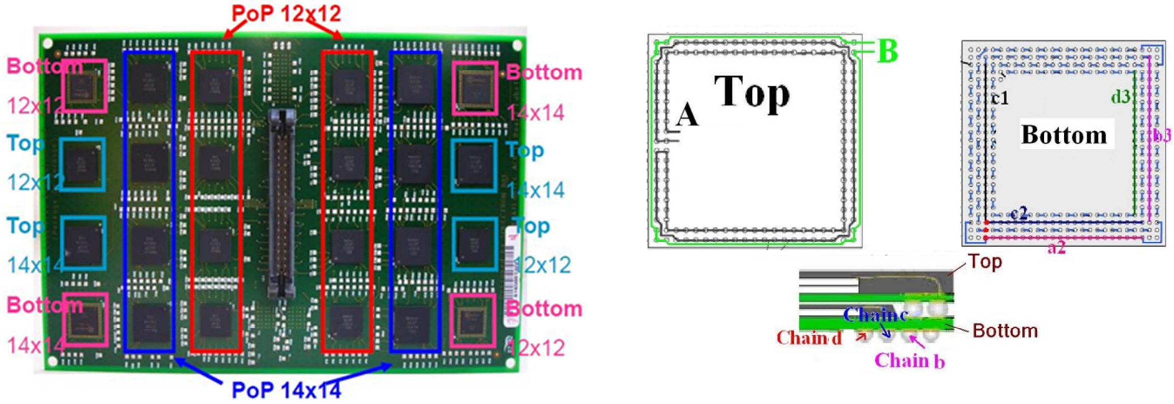

Figure 3.12: Test card used for electromigration tests (left), order of the daisy chains in the top and bottom packages and position of the sub chains (right) [3.36]

3.3.3 Sample Preparation and Analysis

After the stress tests the PoP structures were prepared for the following analysis steps. The short term temperature stressed and the current stressed packages were sawn out of the FR-4 test boards (Fig. 3.13 right). As shown in Fig 3.13 (middle) the single packages from the long term temperature storage tests and the packages being separated from the FR-4 boards were embedded into an epoxy resin (Struers EpoFix: see data sheet for more details). To verify the starting point of the IMC growth during the aging tests, non-stressed packages were embedded into resin too. Afterwards the samples were polished with sandpaper (SiC) until the cross section surface reached the BGAs. For the SiC foils grit sizes (ISO 6344) between 220 (average particle diameter: d_{avg}= 68µm) and 2000 (d_{avg}= 10.3µm) were chosen. Afterwards the cross section surfaces were diamond polished (d_{avg}= 3µm-0.25µm) until the IMC layers in the solder joints were clearly visible.

Figure 3.13: Different steps of the sample preparation: single package (left), embedded package prepared for optical microscopy (middle), and for SEM+EDS (right)

The identification of the IMC layers as well as most of the geometrical measurements were made through light microscopy. For the geometrical measurements and the documentation of the results a microscope camera and the Nikon Imaging System were used. The maximum magnification of the light microscope was 1000x and its maximum resolution was in the range of 250nm.

With respect to the limited resolution of the light microscope a scanning electron microscope (SEM) was used (JEOL: JSM-6100, Fig. 3.14) for the investigation of relatively thin IMC layers (h<1µm). Due to the electrically nonconductive resin, the probes had to be coated with a silver paste and the areas of interest had to be covered with a 10-15nm thick carbon layer (Fig 3.13, right). For the geometrical measurements the secondary electron (SE-SEM) detector and for the identification of different IMC layers the back scattered electron (BSE-SEM) detector were used. In addition to the electron detection the spectrum of the X-Ray radiation was analyzed through EDS (Oxford Instruments: INCA x-act). Taking into account the presence of the carbon layer the EDS enables the determination of IMC composition with a precision of +/-1 mass percent.

Figure 3.14: Scanning Electron Microscope (left) and X-Ray spectrometer (right) at the IMS of the Université Bordeaux I

The measured IMC thickness will show relatively strong variations being caused by different influences on the final test results:

- Variations in the microstructure of the SnAgCu solder and the presence of grain boundaries as diffusion paths. Especially during the DC and AC stress tests annealing in different degrees of intensity can lead to a more or less intensive coarsening of the grain structure [3.40].
- Variations in the Cu content of the SnAgCu solder, being mainly relevant for the closed system of the top bumps.
- Different starting points for the IMC growth due to variations of the process temperature and the process time during the reflow.
- Temperature variations in the oven, in the packages and on the test boards.

As consequence of possible variations of the IMC thickness, for every data point at least 24 solder joints will be investigated. This finally leads to several hundred light microscopy pictures and dozens of SE-SEM and BSE-SEM investigations. Furthermore several hundred EDS measurements were made to verify the composition of the relevant materials. For the analysis of the data statistical methods were used; mainly performed with Origin 8.5.

3.4 Migration Induced Intermetallic Compound Growth

For the determination of the migration related material parameters the mass flux values have to be extracted from the experimental results. In this section equation for the calculation of migration induced mass flux from the IMC growth speed will be derived. In the following this equation will be transformed for the use on Cu-Sn and Cu-Ni-Sn IMCs.

3.4.1 General Model of Migration Induced IMC Formation

The first step of the derivation is the calculation of the atomic density (N) of every element in the IMC. This was done through the mass fraction “m” being determined with EDS before.

With the mass fractions of the single elements in the IMCs (e.g. Cu or Sn) and their mass density (ρ) it is possible to estimate the mass density of the IMCs through (3.70). The equation ignores lattice stacking effects.

$$\rho_{IMC} = \sum_{i=1} \left[\frac{m_i}{\rho_i}\right]^{-1} \qquad (3.70)$$

i = components, e.g. for $(CuNi)_6Sn_5$: i=4 for Cu, Sn, Ni and Au

With the mass density and the IMC volume (V) the mass of the IMC layer (M) can be calculated (3.71) and with the mass fraction the partial mass of the single components (3.72).

$$M = \rho_{IMC} \cdot V_{IMC} \quad (3.71) \qquad\qquad M_i = M \cdot m_i \quad (3.72)$$

With the atomic mass ($M_\circ$) of a component and its partial mass, the total number of its atoms in the IMC layer (n) can be calculated (3.73). The atomic number divided by the IMC volume finally leads to atomic density of the component (3.74).

$$n_i = \frac{M \cdot m_i}{M_{i\circ}} \quad (3.73) \qquad\qquad N_i = \frac{n_i}{V_{IMC}} = \frac{M \cdot m_i}{M_{i\circ} \cdot V_{IMC}} = \frac{\rho_{IMC} \cdot m_i}{M_{i\circ}} \quad (3.74)$$

The change of the atom number over time defines the effective mass flux into the IMC layer (3.75). At the contact pads the shape of the solder joints is nearly cylindrical and as a consequence only the vertical IMC growth will be taken into account. For the calculation of the mass flux, the IMC thickness before (h_0) and after the aging tests (h) has to be known. The starting point for the IMC growth is the IMC thickness after the reflow process. Based on these assumptions (3.76) describes the mass flux of a chosen element (i). For the use of (3.76), the test time (t_{test}) is needed and the mass fraction and the material density of the IMC have to be known as functions of time.

$$\left|\vec{J}_i\right|_{(t)} = \frac{1}{A} \iiint \dot{\left(N_{\imath(x,y,z,t)}\right)} dV = \frac{1}{AM_{i\circ}} \cdot \iiint \dot{\left(m_{\imath(x,y,z,t)} p_{IMC(x,y,z,t)}\right)} dV \qquad (3.75)$$

$$J_{xi(t)} = \frac{1}{M_{i\circ}} \cdot \int_{h_0}^{h} \left(m_{\iota(x,t)} \dot{p}_{IMC(x,t)}\right) dx \qquad (3.76)$$

For the following steps the mass flux will be assumed to be constant over the test time (t_{test}). Before an accurate mass flux calculation is possible this assumption has to be checked for the chosen test times with long term temperature tests (see section 3.3.1). In case of a nearly constant IMC growth speed the average mass flux is given by (3.77).

$$\frac{\Delta n_i}{A} = J_{i,Avg} \cdot t_{test} = \frac{1}{M_{i\circ}} \cdot \iint\limits_{0\,h_0}^{t_{test}\,h} \left(m_{\iota(x,t)} \dot{p}_{IMC(x,t)}\right) dx\, dt \qquad (3.77)$$

For the following step it will be assumed that:

1. *an average atomic density of every component can be used for the resulting IMC. This means, that next to the source for the inflow of the relevant component into the investigated IMC layer, the concentration of this component has to be as high as possible (Fig. 3.15). At the opposite interface the minimum concentration of the element in the investigated IMC layer should be found.*
2. *If a critical concentration of this element is reached, the formation of a new IMC begins. This process needs much less time than the aging tests themselves. The second point is not critical because the Debye frequency enables hundreds of billions of reactions per second while the aging tests go over dozens of hours.*

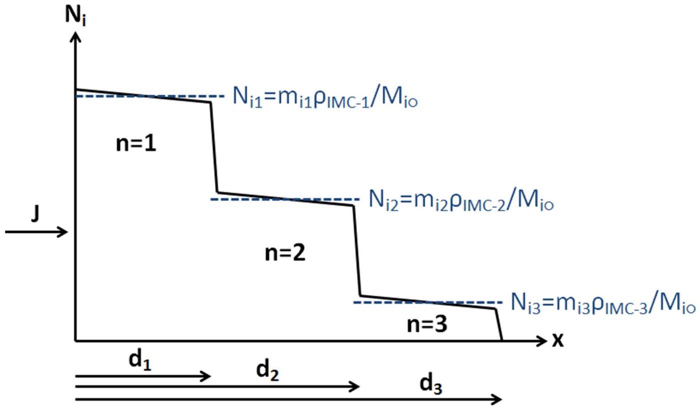

Figure 3.15: Simplified configuration for the migration induced growth of three different IMCs with a shrinking atomic density (N) of the element "i" e.g. i=Cu

As a consequence of these assumptions the integral over time can be replaced by a sum of the atomic densities of the chosen element in the relevant layers (3.78). The value of Z is the number of the relevant layers minus one. For example: if Cu flows from the contact pads (first layer) into Cu_3Sn (second layer) and the growing Cu_3Sn layer replaces Cu_6Sn_5 (third layer) → Z=2.

$$J_{i,Avg} = \frac{1}{M_{i\circ} \cdot t_{test}} \cdot \sum_{n=0}^{Z} \int_{h_n}^{h_{n+1}} m_{i,n+1(x)} p_{IMC,n+1(x)} dx \qquad h_{Z-1} = h \quad h_Z = h_0 \qquad (3.78)$$

Z+1 = Number of the relevant layers.

Taking into account that the concentration gradients in the IMCs are small compared to the atomic density ($\mathrm{grad}(N_i)d_n \ll N$) [3.2] the atomic density in the IMC will be defined to be isotropic. Under this condition the mass flux in the IMC can be calculated with an additive formula (3.79a-b):

$$J_{i,Avg} = \frac{1}{M_{i\circ} \cdot t_{test}} \cdot \sum_{n=0}^{Z} m_{i,n+1} p_{IMC,n+1} \cdot (h_{n+1} - h_n) \qquad (3.79a)$$

$$J_{i,Avg} = \frac{1}{t_{test}} \cdot \sum_{n=0}^{Z} N_{i,n+1} \cdot (h_{n+1} - h_n) \qquad (3.79b)$$

During the previous steps the geometrical values “h_n” were related to specific IMC layers, this was done for more clarity but it is not a must. Hence if a relevant concentration gradient is present in the IMC layers, they can be divided into several parts without changing (3.79) in principle. Due to this fact Z is related to “layers” and not to materials. Hence the use of (3.79) is possible for anisotropic IMCs, but the value “Z” and the resulting computing time will be higher than for isotropic IMCs.

As described by the Deal-Grove model the IMC formation speed slows done over time. Hence for a long testing time the assumption of a constant mass flux over time is not sufficient. Nevertheless the accuracy of the calculation can be improved by a linear approximation of the resulting square root curve. In this case the test time has to be divided into intermediate steps (t_n) and the resulting mass flux is described by a double sum (3.80). The time steps used have to be chosen through long term temperature storage tests.

$$J_{i,Avg} = \frac{1}{M_{i\circ}} \cdot \sum_{r=1}^{R} \left[\frac{1}{(t_r - t_{r-1})} \cdot \sum_{n=0}^{Z} m_{i,n+1} p_{IMC,n+1} \cdot (h_{n+1} - h_n) \right] \qquad (3.80)$$

$$t_{test} = t_R \quad t_0 = 0 \quad h_0 = h_{(t=t_h)}$$

3.4.2 Adaptation of the IMC Growth Model for the Cu-Ni-Sn and Cu-Sn Formation

For this study Amkor® Package-on-Package (PoP) structures were used. The PoP structures are based on two different BGAs. For the top package the contact pads are covered with a NiAu layer. As consequence no Cu migration from the Cu Pads into the solder joints was possible: “closed system” (Fig. 3.11).

The solder joints of the bottom package were directly connected to the Cu pads on the die side, while the board side contact pads are covered with NiP. Hence Cu can flow from the die side contacts into the solder joints: “open system”.

Hence the investigation of the migration induced IMC formation has to be done for two principal cases: the “open system” with a direct contact between Cu and $SnAg_{3.0}Cu_{0.5}$ and the “closed system” with two diffusion barriers between Cu and $SnAg_{3.0}Cu_{0.5}$. For both cases different adaptations of the mass flux equation (3.78) will be necessary.

3.4.2.1 Open System

In an open system the formation of Cu_3Sn and Cu_6Sn_5 can be expected. Both IMCs grow in two directions: in case of Cu_3Sn the IMC growth into two directions appears because the inclusion of Sn at the Cu pads transforms Cu into the Cu_3Sn, while the inflow of Cu at the Cu_3Sn/Cu_6Sn_5 interfaces leads to Cu_3Sn formation too (Fig 3.16). During the Cu_6Sn_5 growth the inclusion of Sn transforms Cu_3Sn to Cu_6Sn_5 and at the Cu_6Sn_5/SnAgCu interface additional Cu_6Sn_5 is formed by the inflow of Cu into SnAgCu.

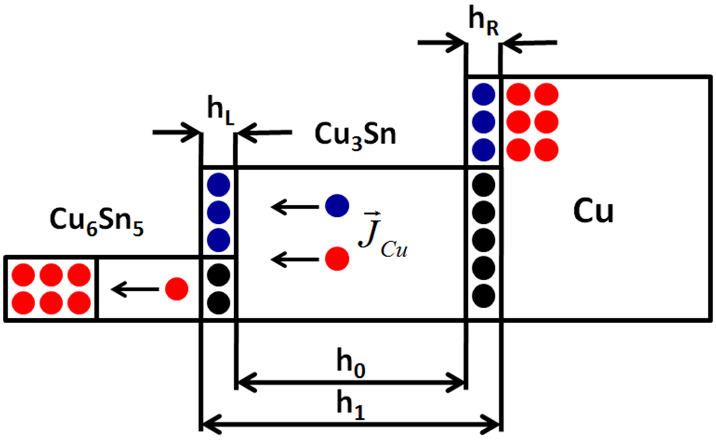

Figure 3.16: Principal Cu migration during the IMC growth on an open system

The formation of IMCs in both directions leads to the measurable increase of the IMC layer thickness during the aging tests (3.81). The mobility of Cu and Sn in Cu_3Sn and Cu_6Sn_5 is different and the interfaces between the IMCs act as vacancy sinks or sources [3.10]. As a consequence the mass fluxes in Cu_3Sn and Cu_6Sn_5 have to be calculated independent from each other. Furthermore the IMC growth mechanism is simplified by the assumption that the IMC composition stays the same during the aging tests. (3.82).

$$h - h_0 = h_r + h_l \quad (3.81) \qquad J_{i,Avg} = J_{ir} = J_{il} \quad (3.82)$$

For the calculation of the mass flux values at both interfaces (3.79b) can be used with Z=0:

$$J_{ir} = \frac{h_r}{t_{test}} \cdot \left(N_{i,I} - N_{i,II}\right) \quad (3.83a) \qquad J_{il} = \frac{h_l}{t_{test}} \cdot \left(N_{i,II} - N_{i,III}\right) \quad (3.83b)$$

I, II, III = the meaning of these indices is given in table 3.2

Phase	II=Cu_3Sn		II=Cu_6Sn_5	
Indices	I=Cu	III=Cu_6Sn_5	I=Cu_3Sn	III=SnAgCu

Table 3.2: Indices for the Eqs. 3.82-3.85 with $N_{Cu,SnAgCu}$=0 and $N_{Sn,Cu}$=0.

The values d_r and d_l cannot be measured separately, but they become available by inserting (3.83a-b) into (3.82) and the resulting (3.84) into (3.81). The final results are Eqs. (3.85a-b).

$$h_r = \frac{\left(N_{i,II} - N_{i,III}\right)}{\left(N_{i,I} - N_{i,II}\right)} \cdot h_l \quad (3.84)$$

$$h_r = (h - h_0) \cdot \frac{\left(N_{i,II} - N_{i,III}\right)}{\left(N_{i,I} - N_{i,III}\right)} \quad (3.85a) \qquad h_l = (h - h_0) \cdot \frac{\left(N_{i,I} - N_{i,II}\right)}{\left(N_{i,I} - N_{i,III}\right)} \quad (3.85b)$$

Using (3.79b) with Z=1 and inserting (3.85a-b) into (3.79b) leads to mass flux of Cu and Sn in Cu_3Sn and Cu_6Sn_5 (3.86a-b). It was taken into account that the growth of the IMC layers into the solder joint ($\Delta h=h_l$) is related to the inflow of Cu from the contact pads, while the IMC growth into the opposite direction ($\Delta h=h_r$) is related to the inclusion of Sn.

$$J_{Cu,II} = J_l = \frac{(h-h_0)}{t_{test}} \cdot \frac{(N_{Cu,I} - N_{Cu,II})}{(N_{Cu,I} - N_{Cu,III})} \cdot (N_{Cu,II} - N_{Cu,III}) \qquad (3.86a)$$

$$J_{Sn,II} = J_r = \frac{(h-h_0)}{t_{test}} \cdot \frac{(N_{Sn,II} - N_{Sn,III})}{(N_{Sn,I} - N_{Sn,III})} \cdot (N_{Sn,II} - N_{Sn,III}) \qquad (3.86b)$$

3.4.2.2 Closed System

The pending question about the closed system is: if Ni_3Sn_4 is formed in SnAgCu during the stress test or not and if it is formed, what are the conditions? Meanwhile the formation of $(CuNi)_6Sn_5$ is certain for all test conditions. For the analysis of the test results two principal equations will be used. The first describes the migration of Cu, Au and Ni when $(CuNi)_6Sn_5$ is formed. The second describes the motion of Ni if $(CuNi)_6Sn_5$ and Ni_3Sn_4 are formed. For the second case an additional interpretation of the Cu or Au flux is not necessary, because the related accumulation process (section 3.2) appears at the SnAgCu to $(CuNi)_6Sn_5$ interface and is not affected by the Ni_3Sn_4 formation.

For the derivation of (3.87), describing the Ni flux from the Pad into $(CuNi)_6Sn_5$, the same principals as for the description of the Cu flux from the contact pads into an open system can be used (3.85a). With $N_{Ni,SAC}=0$ the resulting equation for the mass flux is (3.87):

$$J_{Ni,CuNiSn} = J_l = \frac{(h-h_0)}{t_{test}} \cdot \left(1 - \frac{N_{Ni,CuNiSn}}{N_{Ni,Ni}}\right) \cdot (N_{Ni,CuNiSn}) \qquad (3.87)$$

The accumulation of Cu and Au in $(CuNi)_6Sn_5$ does not go along with an observable dissolution of the Ni pad. Hence the mass flux equations for Cu and Au are given through (3.78b) with Z=1 (3.88):

$$J_{i,Avg} = \frac{(h-h_0)}{t_{test}} \cdot (N_{i,CuNiSn} - N_{i,SAC}) \qquad (3.88)$$

i = Cu or Au

If Ni_3Sn_4 and $(CuNi)_6Sn_5$ are formed, the equation for the calculation of the Ni flux has to cover both IMCs. In this case the growth of $(CuNi)_6Sn_5$ does not lead to a consumption of the Ni pad, but the formation of Ni_3Sn_4 does. So the final equation is a sum of (3.87) and (3.88) with $N_{Ni,SAC}=0$ (3.89a-b):

$$J_{Ni} = J_{Ni,NiSn} + J_{Ni,CuNiSn} \qquad (3.89a)$$

$$J_{Ni} = \frac{h_{NiSn}}{t_{test}} \cdot \left(1 - \frac{N_{Ni,NiSn}}{N_{Ni,Ni}}\right) \cdot (N_{Ni,NiSn} - N_{Ni,CuNiSn}) + \frac{(h-h_0)_{CuNiSn}}{t_{test}} \cdot (N_{Ni,CuNiSn}) \qquad (3.89b)$$

The Au concentration in Ni_3Sn_4 is very low. Hence (3.88) is also sufficient for the analysis of the Au mass flux if the formation of Ni_3Sn_4 appears. For the mass flux of Cu the same approach as for Ni can be used, but the consumption of the Ni pad is not relevant (3.90a-b):

$$J_{Cu} = J_{Cu,NiSn} + J_{Cu,CuNiSn} \qquad (3.90a)$$

$$J_{Cu} = \frac{h_{NiSn}}{t_{test}} \cdot \left(N_{Cu,NiSn}\right) + \frac{(h-h_0)_{CuNiSn}}{t_{test}} \cdot \left(N_{Cu,CuNiSn} - N_{Cu,SAC}\right) \quad (3.90b)$$

3.5 Preparation of the Finite Element Analysis

A Finite Element Analysis (FEA) of the test structure was performed with ANSYS® to get the exact test temperatures under consideration of Joule heating. Furthermore the temperature gradients in the IMC layers were needed. For the creation of the model the geometrical data of the solder joints and the surrounding package were measured through light microscopy and implemented by the parameter design language of ANSYS® (APDL). Afterwards the relevant material parameters for every component were defined by literature values.

After the analysis of aging tests the resulting material parameters of the migration induced mass flux in the IMC layers will be used for a dynamic simulation of the IMC growth. For this task a user routine was developed.

3.5.1 Model Geometry

For the FEA, two top bumps, two bottom bumps, a part of the package and a part the FR-4 test board were modeled. A detailed illustration of the model is given by Fig. 3.17. The top and the bottom solder joints are connected with Cu metal layers (M1-M4). For all geometrical parameters being relevant for current crowding, like the contact pad diameters or the metal layer height, the mean values of several dozen measurements and their standards deviations (sd) are available [3.42].

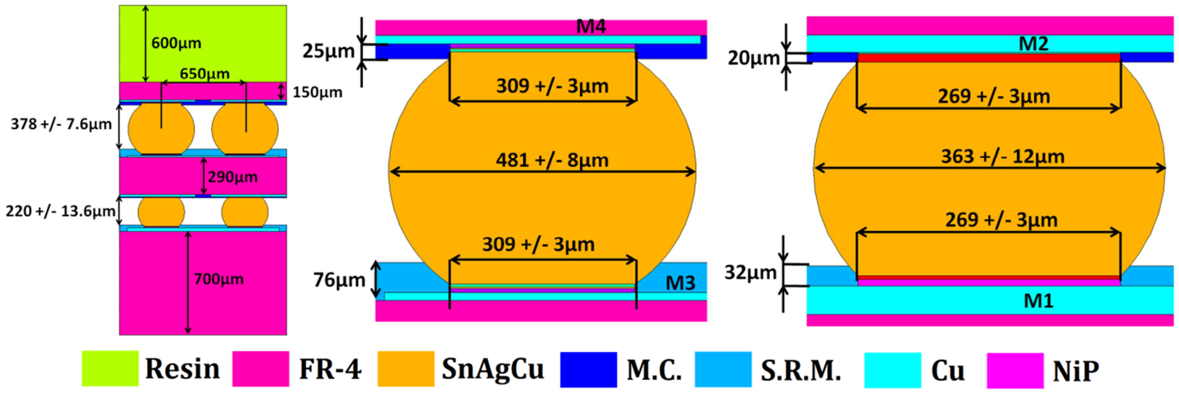

Figure 3.17: Finite Element model of the PoP (left) structure, the top (middle) and the bottom (right) bumps M.C.: Mold Compound, S.R.M.: Solder Resist Mask

For the determination of the bump height or the metal layer thickness (table 3.3) the light microscopy data could be used without an additional interpretation, but in case of the contact pad diameters and the bump diameters further investigations were necessary.

M1	M2	M3	M4
29 +/- 3µm	17.8 +/- 2.5µm	13.3 +/- 2.1µm	14 +/- 1.4µm

Table 3.3: Thickness of the four relevant metallization layers.

The contact pad diameters were determined through light microcopy measurements of the top side of non-soldered bottom packages (Fig. 3.18, left). In the data sheets the principle solder bump diameters can be found (Top: 450µm, Bottom: 300µm [3.41 p.5]), but unlike the contact pad diameters the final bump diameters depend on the pressure used during the reflow process and the viscosity of the solder. Hence the bump diameter values in the data sheets have to be verified for the actual test structures. A direct measurement of the diameter is impossible because the measured diameter values on a two dimensional cross section surface do not have to be the real diameters of the three dimensional solder bumps (Fig. 3.18, right). Nevertheless, knowing the contact diameter, it is possible to reconstruct the bump diameters with (3.91). Furthermore the profile of the cross section surface can be visualized by calculating its distance to the center of the bumps (3.92).

$$D_{B,max} = \sqrt{D_B^2 + D_{C,max}^2 - D_C^2} \qquad (3.91)$$

$D_{B,max}$= real bump diameter; D_B= measured bump diameter at the cross section surface;
$D_{C,max}$= real contact pad diameter; D_C= measured contact pad diameter at the cross section surface

$$S_D = \frac{1}{2} \cdot \left(\sqrt{D_{B,max}^2 - D_B^2} \right) = \frac{1}{2} \cdot \left(\sqrt{D_{C,max}^2 - D_C^2} \right) \qquad (3.92)$$

S_D= Distance between the cross section surface and the center of the bump.

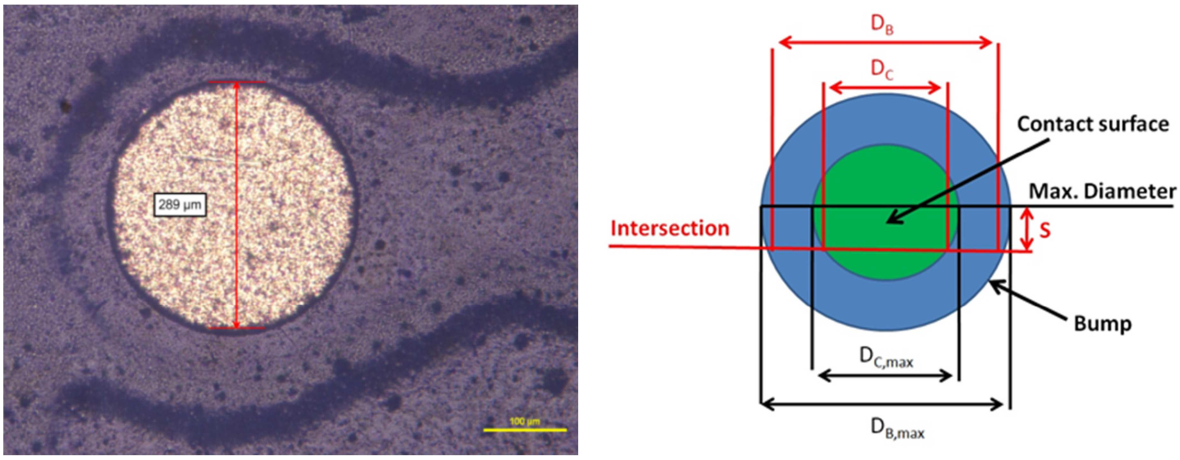

Figure 3.18: Contact pad on the top of a non-soldered bottom package (left), and the principal relation between the real bump diameter and the measured diameter at the cross section surface (right)

In Fig 3.19 the measured diameters on the cross section surface of five different samples are shown. Furthermore the related surface profiles as results of (3.92) are given. The combination of both pictures shows the relation between the measured diameters and the cross section surface profile:

- the measured diameters strongly depend on the distance between the bump center and the cross section surface. So the measured diameter for the samples “120°C”, “120°C/1A” and “100°C/1A” clearly differ from the measured diameters of the samples “100°C” and “ref”.
- a warpage of the cross section surface as result of over polishing increases the standard deviation of the diameter (sample "120°C").
- a decline of the cross section surface (sample “120°C/1A”), which appears as consequence of a torque being created by the friction force between the rotating grinding disc and the polished sample, leads to a distorted distribution of the bump diameter values.

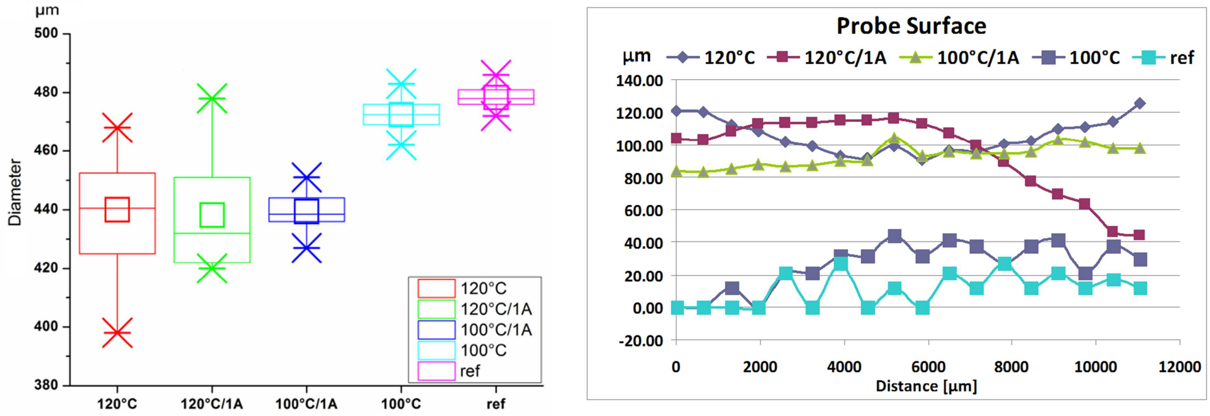

Figure 3.19: Box plots of the measured top bump diameters separated by the stress test conditions (left) and the surface profile of the related samples (right) [3.42]

In addition (3.90) can be used to calculate the correct bump diameters out of the measured diameter values. The visualization of the measured diameters (Fig. 3.20) before and after correction with (3.90) shows better correlation of the corrected values to the expected normal distribution of the bump diameters.

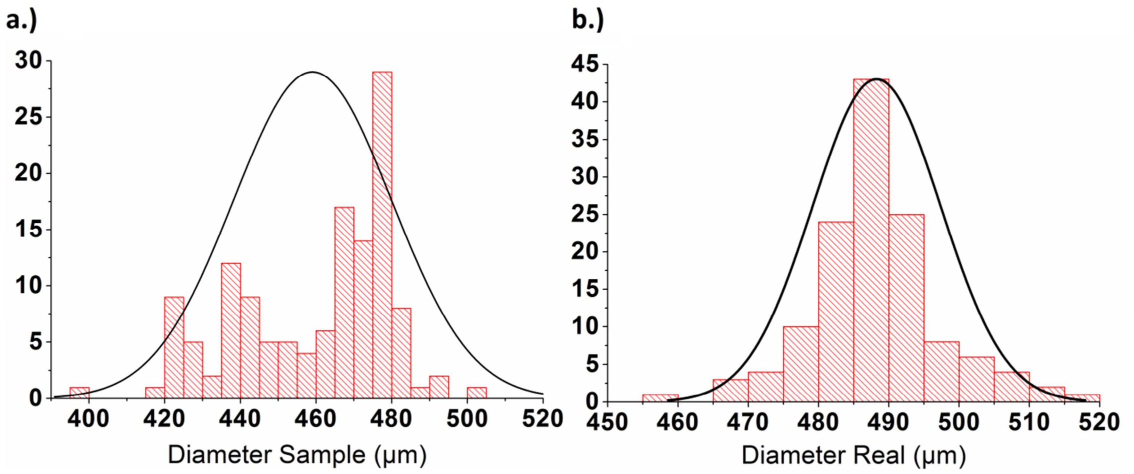

Figure 3.20: Distribution of the top bump diameters before (a) and after the adjustment (b) [3.42]

An alternative way to measure the bump diameters after the reflow process are X-Ray pictures of the PoP structures. Nevertheless the accuracy of the X-ray measurements was limited and their relative standard deviation was 10%, so the resulting diameters are approximate values only. Finally the bump diameter values from four different sources can be compared (table 3.4) and the influence of the reflow process and the package warpage on the bump diameters can be described. In general the deformation of the solder joints appears due to the pressure being applied during the soldering and due to the package warpage. Both effects increased the diameter bump diameters compared to data sheet values. For the smaller bottom bumps the effect is more relevant, because the process influences are combined with smaller bump diameters. The variation of the bump geometry has an influence on the current crowding effect and the expected lifetime of the solder joints under EM stress. More details about the relation between lifetime and geometry variations are given in [3.42]

Source:	Data sheet	Microscope	X-ray	Real
Top	450µm	459 +/- 21µm	470µm	481 +/- 8µm
Bottom	300µm	348 +/- 36µm	376µm	363 +/- 11µm

Table 3.4: Diameter of the top and bottom bumps.

3.5.2 Material Parameters and the Boundary Conditions

For the thermal electrical simulation the different packaging materials have to be defined by their specific resistance and their thermal conductivity. This was done for a temperature range from 200K (-73.16°C) to 600K (326.84°C).

3.5.2.1 Specific resistance (ρ_{el})

All electrical conductive materials in the package are metals. Their temperature dependent specific resistance was defined by a linear model (3.69) with a TCR (table 3.5). The TCR of the IMCs was only available for Cu_6Sn_5. For $(CuNi)_6Sn_5$ the same value as for Cu_6Sn_5 was used. The TCR, of Cu_3Sn and Ni_3Sn_4 have to be extracted from the experimental results.

Material	**Cu**	**Ni**	**SnAgCu**	**Cu_6Sn_5/$(CuNi)_6Sn_5$**
TCR [1/K]	$3.85x10^{-3}$ [3.43]	$6.44x10^{-3}$ [3.44]	$2.8x10^{-3}$ [3.43]	$3.5x10^{-3}$ [3.38]

Table 3.5: TCR of the metals and IMCs in the PoP structure.

The specific resistances of all other materials were assumed to be temperature-independent:

Material/Temperature	**200K**	**300K**	**400K**	**500K**	**600K**
Copper [3.43]	$10.6x10^{-3}$	$17.4x10^{-3}$	$23.1\ x10^{-3}$	$30.7x10^{-3}$	$37.3x10^{-3}$
Nickel [3.44]	$23.7x10^{-3}$	$66.9x10^{-3}$	0.11	0.153	0.196
NiP [3.45-46]	0.669	0.7	0.732	0.763	0.795
Cu_6Sn_5/$(CuNi)_6Sn_5$ [3.37]	$93.6x10^{-3}$	0.175	0.254	0.333	0.411
S.R.M. [3.47]	$0.2x10^{18}$				
FR-4 [3.48]	$0.5x10^{15}$				
SnAgCu [3.43]	$96x10^{-3}$	0.132	0.169	0.207	0.244
Resin [3.49]	$1x10^{18}$				
M.C.[3.50]	$10x10^{15}$				
Cu_3Sn* [3.37]	$61.9x10^{-3}$	$89.3x10^{-3}$	0.117	0.144	0.172
Ni_3Sn_4 [3.37]	$87.2x10^{-3}$	0.285	0.483	0.681	0.878

Table 3.6: Specific resistances of the used materials [Ωµm].

3.5.2.2 Thermal conductivity (κ)

In metals the thermal transport is mainly done by the electron gas and as a consequence the thermal conductivity is proportional to the electrical conductivity. The relation between the thermal and the electrical conductivity is described by the Wiedemann Franz law (3.93):

$$\kappa = \frac{\pi^2 \cdot k_B^2}{3 \cdot e^2} \cdot \frac{T}{\rho_0 \cdot [1 + TCR \cdot (T - T_0)]} \quad (3.93)$$

For the nonmetals temperature independent values were implemented. Due to the fiberglass content the thermal conductivity of the FR-4 board is anisotropic. For $(CuNi)_6Sn_5$ the same value as for Cu_6Sn_5 were used.

Material/Temperature	200K	300K	400K	500K	600K
Copper [3.43]	$460x10^{-6}$	$421x10^{-6}$	$405x10^{-6}$	$398x10^{-6}$	$393x10^{-6}$
Nickel [3.44]	$0.206x10^{-3}$	$0.11x10^{-3}$	$88.8x10^{-6}$	$79.8x10^{-6}$	$73.8x10^{-6}$
Cu_6Sn_5/$(CuNi)_6Sn_5$ [3.37]	$62x10^{-6}$	$33.1x10^{-6}$	$23.5x10^{-6}$	$17.9x10^{-6}$	$13.5x10^{-6}$
S.R.M. [3.47]	$0.21x10^{-6}$				
FR-4 [3.48]					
x	$1.05x10^{-6}$				
y	$0.34x10^{-6}$				
z	$1.05x10^{-6}$				
SnAgCu [3.43]	$50.83x10^{-6}$	$55.52x10^{-6}$	$57.82x10^{-6}$	$59x10^{-6}$	$60.07x10^{-6}$
NiP [3.45-46]	$8.83x10^{-6}$	$8.0x10^{-6}$	$7.66x10^{-6}$	$7.34x10^{-6}$	$7.05x10^{-6}$
Resin [3.49]	$0.2x10^{-6}$				
M.C.[3.50]	$0.167x10^{-6}$				
Cu_3Sn [3.37]	$0.1x10^{-3}$	$70.4x10^{-6}$	$53.9x10^{-6}$	$43.6x10^{-6}$	$36.6x10^{-6}$
Ni_3Sn_4 [3.37]	$63.1x10^{-6}$	$19.6x10^{-6}$	$11.6x10^{-6}$	$8.21x10^{-6}$	$6.36x10^{-6}$

Table 3.7: Thermal conductivity of the used materials [W/(µmK)].

3.5.2.3 Implementation of the Boundary Conditions

The main task of the simulation is the calculation of the test temperature at the IMC layers and the determination of temperature distribution under consideration of Joule heating. Against this background thermocouples were placed on the PoP structures and the package temperature was recorded during the AC and the DC stress tests. Later the measured temperatures were used to define the thermal boundary conditions for the FEA.

At upper ends of the metal layers the input currents and the grounds were placed (Fig. 3.21, left). The arrangement of the metal lines represents the bump chains in the real packages and enables the simulation of the up- and the downstream case. To ensure a correct calculation of the local temperature gradients at the contact surfaces, the model also includes IMC layers (Fig. 3.21, middle, right).

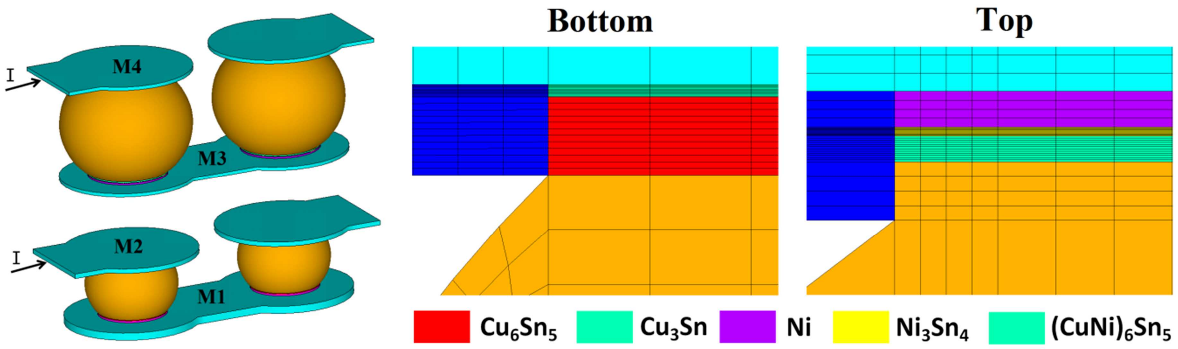

Figure 3.21: FE Model of the bump chain (left) and a detailed view on the implemented IMC layers (right)

On the free standing surfaces of the Finite Element (FE) model a temperature dependent heat transmission coefficient (HTC) has to be defined. The HTC represents the heat loss due to convection and radiation. A model of four solder joints represents only a small part of the package or the whole test board surface. Hence a variable HTC was set up at the top and the bottom surface of the FE model, while the oven temperature was set as ambient temperature. Afterwards an optimization algorithm of ANSYS® was used to determine an HTC which represents the heat flux over the total package or test board surface. The target values of the optimization algorithm are the recorded package temperatures of the experimental part. The results of the temperature measurements and the simulations as well as the final HTC are given in table 3.8. Based on previous investigations [3.51] the HTC at the bump surfaces was chosen between 11-13W/m²K.

T_{Oven} [°C]	I [A]	$T_{Measured}$ [°C]	$T_{Simulation}$ [°C]	T_{IMC} [°C]	HTC [W/m²K]
100	1	132	133	139	60.15
120	0.8	141	141	145	59.5
120	1	154	155	162	56.05
140	1	178	179	186	58.5

Table 3.8: Chosen oven temperature, applied current, measurement results, simulation results for the top side of the PoP and the IMC layers, estimated HTC.

3.5.3 Dynamic Simulation of the IMC Growth

The last step of the investigation will be the dynamic simulations of the IMC growth under consideration of the chosen ambient temperature and the presence of a current flow. The developed program will use the results of the FEA as well as the experimental results from the different aging tests. The experimental results will be included as general material parameters E_A, D_0, Z*, Q* and β which describe the mobility of the different materials in the IMCs.

A flowchart of the dynamic IMC growth simulation is shown by Fig. 3.22: the first step is the creation of the three dimensional model of the solder joint, afterwards a thermal electrical (TE) simulation is performed. Based on the results of the thermal electrical simulations and Z* the temperature dependent effective charge of Cu ($Z^{**}_{(T)}$) was calculated [3.52]. Then Z** and the other migration related material parameters as well as the results from the TE simulation were used to calculate the mass flux due to EM and TM ("MF") with an user routine [3.21]. Afterwards the mass flux due to concentration gradients was implemented with an user routine and the total mass flux in the IMCs ("MFG") was calculated. With the total Cu mass flux the growth speed ($\vec{v}$) of Cu_6Sn_5 and Cu_3Sn (3.94a-b) can be calculated by using the inverse function of (3.86a):

$$\vec{v}_{Cu3Sn} = \vec{J}_{Cu,Cu3Sn} \cdot \frac{\left(N_{Cu,Cu} - N_{Cu,Cu6Sn5}\right)}{\left(N_{Cu,Cu} - N_{Cu,Cu3Sn}\right) \cdot \left(N_{Cu,Cu3Sn} - N_{Cu,Cu6Sn5}\right)} \quad (3.94a)$$

$$\vec{v}_{Cu6Sn5} = \vec{J}_{Cu,Cu6Sn5} \cdot \frac{\left(N_{Cu,Cu3Sn} - N_{Cu,SnAgCu}\right)}{\left(N_{Cu,Cu3Sn} - N_{Cu,Cu6Sn5}\right) \cdot \left(N_{Cu,Cu6Sn5} - N_{Cu,SnAgCu}\right)} \quad (3.94b)$$

The dynamic simulation is split into a variable number of time steps (n_{max}) and for every time step the thermal and electrical conditions and the actual mass flux can be calculated. In addition the ANSYS® simulations enable the investigations of geometrical influences, like current crowding, on the IMC formation speed. In that way the ANSYS® simulation restores information which was lost by the use of averaged values for the mathematical interpretation of the experimental results.

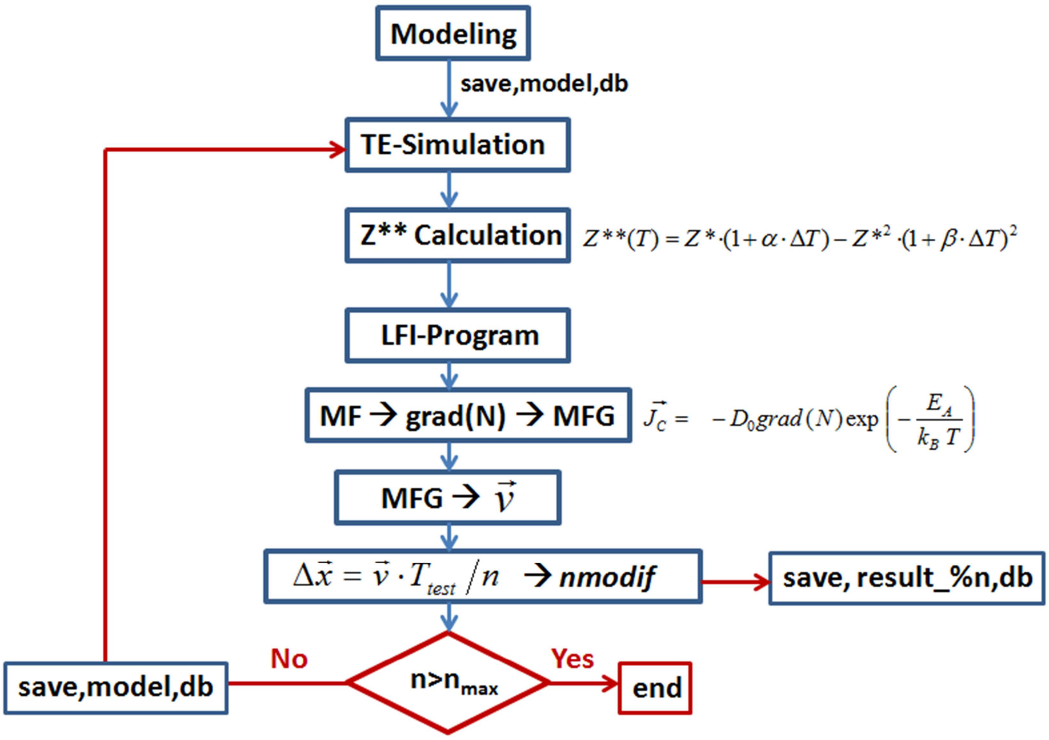

Figure 3.22: Flowchart for the dynamic simulation of the IMC growth

3.6 Conclusion

For the IMC formation in solder joints different migration phenomena are relevant. Based on different aging tests these phenomena have to be described separately and a general model of the IMC growth has to be developed.

During the aging tests two transport mechanisms are relevant: the interstitial diffusion of noble metals in the tin solder and the vacancy mechanism for the material transport in the IMCs. Based on the solution of the random walk problem and the resulting Nernst-Einstein equation the physical interpretation of the diffusion related material parameters like the activation energy (E_A), the diffusion coefficient (D) and the diffusion constant (D_0) is possible. Nevertheless the complex crystal structure of the IMCs and the presence of grain boundaries do not allow a direct calculation of these parameters from known material values. Nevertheless the Nernst-Einstein equation can be used to describe migration phenomena due to external driving forces, like an applied current (EM), temperature gradients (TM) or local differences in the solubility of an element in the investigated binary compounds. Furthermore the definition of independent material parameters for the different migration phenomena is possible: like the effective charge of the moving ion (Z*) in case of EM, the heat of transport (Q*) for TM, as well as an driving force “β” for the migration due to differences in the solubility. As for E_A and D_0 the complex crystal structure of the IMCs and the high defect density due to grain boundaries disables the direct calculation of the migration related material parameters. Hence an experimental determination is needed. Overall four different experiments have to be performed to characterize the IMC formation in the solder joints (table 3.9).

Test	Migration mechanism	IMC features	Parameter extracted
Temperature storage long term	Diffusion Accumulation	Time dependency of the IMC formation speed	Time limit for a constant IMC formation speed.
Temperature storage short term	Diffusion Accumulation	Temperature dependency of the IMC formation speed	Activation Energy (E_A) Diffusion Constant (D_0) Driving force (β)
Temperature storage + AC current load	Diffusion + Accumulation + Thermomigration	Increased/Decreased IMC formation speed at the die/board side → TM downstream	Heat of transport (Q*)
Temperature storage + DC current load (use case)	Diffusion + Accumulation + Thermomigration + Electromigration	Downstream case → Increased/Decreased IMC formation speed at the die/board side Upstream case → Decreased/Increased IMC formation speed at the die/board side	Effective charge (Z*) Heat of transport (Q*) Heat of solution (H)

Table 3.9.Summary of the test procedures and the extracted material parameters.

For the experiments single packages and test boards with 24 packages will be used. After the aging tests cross sections of the packages will be made. Afterwards the dimensions of the IMCs will be measured with light microscopy and SEM and their material composition has to be determined with EDS.

The main result of the aging tests should be an increased IMC layer thickness compared to the starting point. The starting point was defined by the IMC layer thickness after the reflow soldering. Against this background a mathematical model for the calculation of the average mass flux in the IMCs was developed from their growth speed during the aging test.

The applied current, which is needed for the EM and TM tests, leads to Joule heating. Hence a FEA will be needed to get the exact test temperature at the IMC layers and the temperature gradients. The temperature gradients were used for the analysis of the TM induced mass flux and for the determination of Q*.

When all migration related material parameters are available, the FEM will also be used to perform a dynamic simulation of the IMC growth. The simulations will be done under the consideration of the ambient temperature, the applied current and the three dimensional shape of the investigated solder joints.

4 Migration Induced IMC Growth in SnAgCu Solder Bumps

In this chapter the results of the temperature storage (TS) tests, the TM-AC tests and the EM-DC tests will be given for the bottom bumps (“open system”) and the top bumps (“closed system”).

By comparing the IMC formation speed at different test conditions the mass flux values due diffusion, material accumulation, TM and EM will be extracted. Based on these values the experimental material parameters will be calculated. If necessary a further interpretation of these values will be given. In this case especially the difference between the crystal structure of fcc metals and the IMCs will be taken into account. The final results will be the activation energies (E_A), the diffusion constants (D_0), the driving forces for material accumulation (β), the heat of transport (Q^*) and the effective charge of the moving ions (Z^*) for all relevant materials (Cu, Sn, Ni, Au) in the IMCs Cu_3Sn, Cu_6Sn_5, $(CuNi)_6Sn_5$ and Ni_3Sn_4.

4.1 Long- and Short Term Behavior of IMC Formation During Temperature Storage

All aging or stress tests on solder joints go along with TS, leading to diffusion along concentration gradients. Hence the characterization of the diffusion driven IMC formation is the first step of the investigation. Afterwards other migration phenomena like EM or TM will be investigated. Against this background the long- and the short-term behavior of the IMC growth in the top and bottom bumps will be investigated. The long term tests were performed with single packages being stored in an oven at 150°C. Afterwards three additional short term TS tests at 100°C, 120°C, 140°C were performed to extrapolate the E_A and the D_0 of the material movement in the IMCs. For the short term tests the packages were placed on test cards.

4.1.1 Bottom Bumps “Open System”

The die side contacts of the bottom bumps are directly connected to the Cu pads. As a consequence the Cu migrated from the pads into the solder joints and Cu_6Sn_5 and Cu_3Sn IMC layers were formed. The IMC formation begins during the reflow soldering. During the TS the inflow of Cu leads to a further growth of the two different Cu-Sn IMCs (Fig. 4.1).

The Cu content of Cu_3Sn is higher than the Cu content of Cu_6Sn_5. In general the Cu_3Sn IMC layer is several times thinner than the neighboring Cu_6Sn_5 layer, and it grows more slowly. The board pads are covered with NiP. The NiP layer is a diffusion barrier for Cu coming from the metal lines. Furthermore the diffusion of Ni into the IMCs suppresses the formation of $(CuNi)_3Sn$ [4.1]. Hence the only observable IMC layer at the board side contacts was $(CuNi)_6Sn_5$.

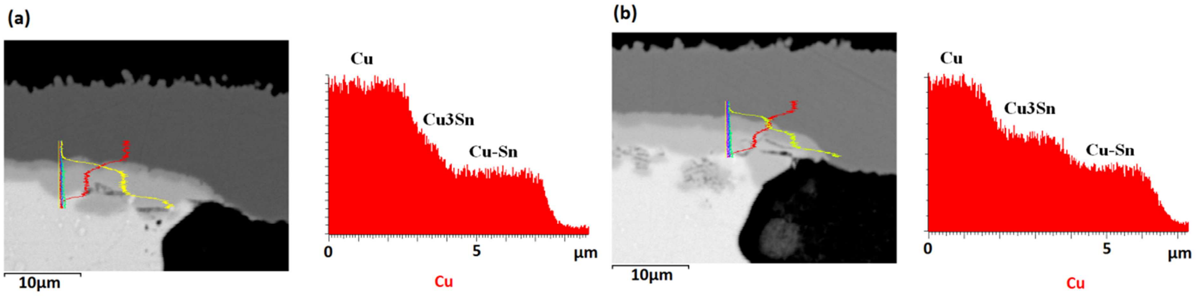

Figure 4.1: SEM pictures and Cu concentration profiles of Cu_6Sn_5 and Cu_3Sn after 168h (a) and 672h (b) TS at 150°C

4.1.1.1 Long term temperature storage

During the IMC formation Cu and Sn have to flow through the IMC layers to form new material. As a consequence the IMC growth speed is reduced with the growing layer thickness (Fig. 4.2a). This indicates a limited mobility of Cu and Sn in the IMCs. The resulting IMC formation can be described with the Deal Grove model. The curves of the IMC growth profiles were fitted with the power law (4.1).

$$h_{(t)} = a_P \cdot t^{n_P} \quad (4.1)$$

For the Deal-Grove model the exponential factor “n” should be one for the beginning IMC formation, and 0.5 for a long term test with saturation effects on the IMC growth. The exponent of the Cu_6Sn_5 growth profile is n=0.6, while the exponent of the Cu_3Sn profile is n=0.72. The different exponents indicate that the formation of Cu_6Sn_5 was driven into saturation earlier than the Cu_3Sn formation. A possible reason is the higher growth speed of Cu_6Sn_5, leading to the earlier appearance of saturation effects.

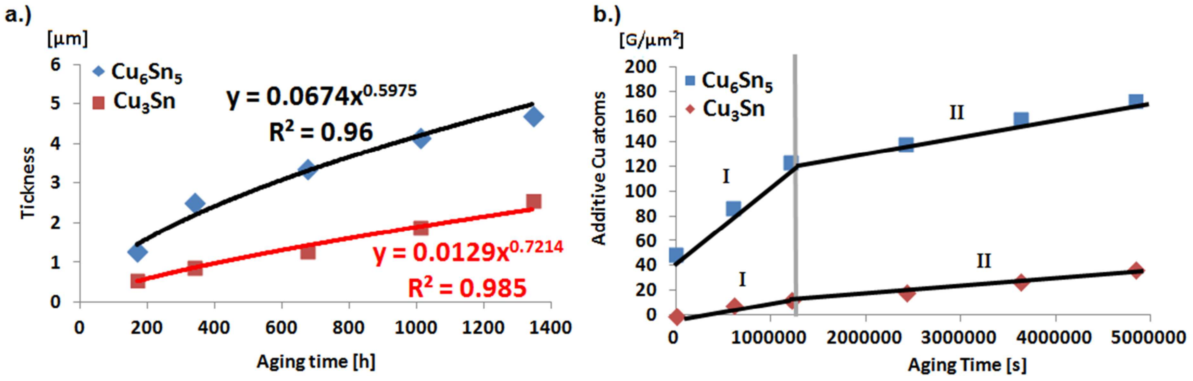

Figure 4.2: Cu_3Sn and Cu_6Sn_5 growth for TS at 150°C. Layer thickness a) and cumulative Cu atoms b). Mass flux (b) changes between mode I (linear) and mode II (saturation). G= 10^9

For the determination of the Cu and Sn mass flux during the stress tests, the atomic density (N) of the single components and the mass density (ρ) of the IMC layers have to be known. The mass fractions (m) of the IMCs were determined with EDS. Afterward the mass density of the related IMCs was calculated with (4.2). Finally the atomic density of the components was determined with (4.3).

$$\rho_{IMC} = \sum_{i=1}\left[\frac{m_i}{\rho_i}\right]^{-1} \quad (4.2)$$

i = components, e.g. for $(CuNi)_6Sn_5$: i=4 for Cu, Sn, Ni and Au

$$N_i = \frac{\rho_{IMC} \cdot m_i}{M_{i\circ}} \quad (4.3)$$

M = atomic mass of the component

The material composition of the IMCs, their mass density and the resulting atomic density of the components are given in the tables 4.1-2. The mass fractions given are the mean values of several dozen measurements and their standard deviations (SD). The relatively high SD of Cu_3Sn compared to Cu_6Sn_5 is due to its thin layer thickness and the limited resolution of EDS. Despite their differences in composition Cu_6Sn_5 and $(CuNi)_6Sn_5$ have similar mass densities. Ag could not be found in the IMC layers because Ag forms stable Ag_3Sn grains in the solder and remains there during the stress tests.

	Cu_3Sn		Cu_6Sn_5			
Element	**Cu**	**Sn**	**Cu**	**Sn**	**Ni**	**Au**
m [%]	63.5 ± 8.3	36.5 ± 8.3	33.6 ± 2.1	62.1 ± 1.4	1.6 ± 1.1	1.7 ± 0.9
ρ_{IMC} [g/cm³]	8.2		7.9			
N [1/m³]	3.9×10^{28}	1.55×10^{28}	2.6×10^{28}	2.5×10^{28}	1.6×10^{27}	3.8×10^{26}

Table 4.1: Material composition of Cu_3Sn and Cu_6Sn_5 at the die side contact surfaces.

	Cu	Sn	Ni	Au
Mass [%]	27.2 ± 1.9	62.1 ± 1.4	8.8 ± 1.1	1.9 ± 0.9
ρ_{IMC} [g/cm³]	7.9			

Table 4.2: Material composition of $(CuNi)_6Sn_5$ at the board side contacts of the bottom bumps.

Based on the material composition of the IMCs and the difference in the IMC layer thickness before and after TS (table 4.3), the average mass flux over time can be calculated with (4.4a-b).

Test time [h]	Reflow (0)	168	336	672	1008	1344
Cu_3Sn [µm]	0.6 ± 0.06	1.1 ± 0.1	1.4 ± 0.14	1.9 ± 0.15	2.5 ± 0.13	3.1 ± 0.28
Cu_6Sn_5 [µm]	2.0 ± 0.2	3.2 ± 0.3	3.5 ± 0.7	5.3 ± 0.3	6.1 ± 0.37	6.7 ± 0.65

Table 4.3: IMC dimensions after reflow and after the TS tests.

$$J_{Cu,II} = \frac{(h-h_0)}{t_{test}} \cdot \frac{\left(N_{Cu,I}-N_{Cu,II}\right)}{\left(N_{Cu,I}-N_{Cu,III}\right)} \cdot \left(N_{Cu,II}-N_{Cu,III}\right) \qquad (4.4a)$$

$$J_{Sn,II} = \frac{(h-h_0)}{t_{test}} \cdot \frac{\left(N_{Sn,II}-N_{Sn,III}\right)}{\left(N_{Sn,I}-N_{Sn,III}\right)} \cdot \left(N_{Sn,II}-N_{Sn,III}\right) \qquad (4.4b)$$

Phase	II=Cu_3Sn		II=Cu_6Sn_5	
Indices	I=Cu	III=Cu_6Sn_5	I=Cu_3Sn	III=SnAgCu

Table 4.4: Indices for the Eqs. 4.4a-b with $N_{Cu,SnAgCu}$=0 and $N_{Sn,Cu}$=0.

After 336h of TS the decelerated IMC formation speed led to a reduction of average mass flux in both IMCs (Fig. 4.2b). Against this background a test time of 336h at 150°C was defined as an empirical limit for the consideration of saturation effects. The IMC formation speed and the related average mass flux values for Cu and Sn in Cu_6Sn_5 and Cu_3Sn at 150°C are given in table 4.5.

		Cu_3Sn			Cu_6Sn_5		
	Test time [h]	**v[nm/h]**	**J_{Cu}[1/µm²s]**	**J_{Sn}[1/µm²s]**	**v[nm/h]**	**J_{Cu}[1/µm²s]**	**J_{Sn}[1/µm²s]**
I	**<336h**	2.54	1.1×10^4	-3.6×10^3	7.53	6.1×10^4	-2.3×10^4
II	**>336h**	1.77	7.2×10^3	-3.5×10^3	2.17	1.4×10^4	-7.2×10^3

Table 4.5: IMC growth speed and the related mass flux during TS tests at 150°C.

4.1.1.2 Short term temperature storage

Based on the long term TS tests a time limit for saturation is known. Nevertheless for the characterization of the diffusion driven IMC formation and the extrapolation of the time limit to other test temperatures D_0 and E_A will be needed.

For the determination of the E_A TS tests were performed at three additional temperatures between 100°C and 140°C. The resulting IMC layer dimensions are given in table 4.6. For the long term tests single packages were used, while the short term tests were performed on test boards. As a consequence the IMC dimension after reflow, being the starting point for the investigated IMC growth, differ by nearly one micrometer.

	Reflow	100°C-2798h	120°C-784h	140°C-164h
Cu_3Sn [µm]	0.57 ± 0.08	0.93 ± 0.14	0.97 ± 0.2	0.74 ± 0.15
v[nm/h]	-	0.13	0.51	1.04
Cu_6Sn_5 [µm]	2.8 ± 0.4	5.8 ± 1.19	5.5 ± 1.3	3.3 ± 0.87
v[nm/h]	-	1.07	3.4	9.1

Table 4.6: IMC dimensions at the die side contacts of the bottom bumps after reflow and after the TS tests.

If the driving force for the migration process (in this case it’s the concentration gradient) stays the same, the IMC growth speeds at two different temperatures enable the calculation of the factor of temperature acceleration (AFT). The Arrhenius equation of the AFT includes E_A and the test temperature. Hence the IMC growth speeds at different temperatures and the inverted function of the AFT enable the calculation of E_A with (4.5):

$$E_A = \frac{ln(AFT) \cdot k_B \cdot T_1 \cdot T_2}{(T_1 - T_2)} \qquad (4.5)$$

For the determination of the E_A through the four given data points a curve fitting procedure, based on (4.5), was used. The average mass flux values for Cu and Sn in Cu_6Sn_5 and Cu_3Sn are given in Fig. 4.3 and 4.4. The y-axis is the mass flux in logarithmic scale. The x-axis is the exponential term of the Arrhenius function. For every data point the mean and standard deviation of several measurements are given. The fitted curves in the Figures show the E_A of Cu and Sn as exponential constants. The linear constants are the products of D_0 and the concentration gradients.

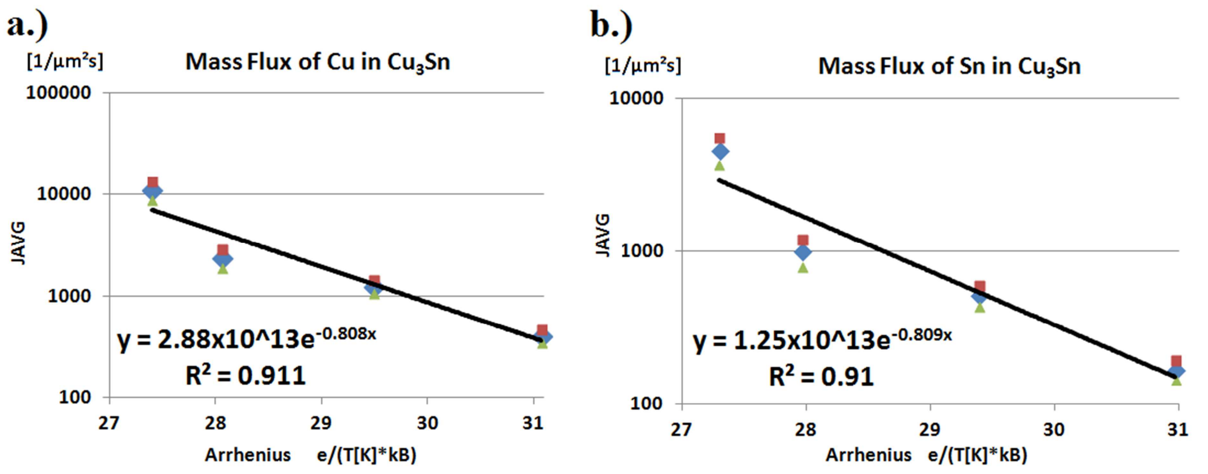

Figure 4.3: Mass flux of Cu (a) and Sn (b) in Cu_3Sn at different TS temperatures (mean ± SD)

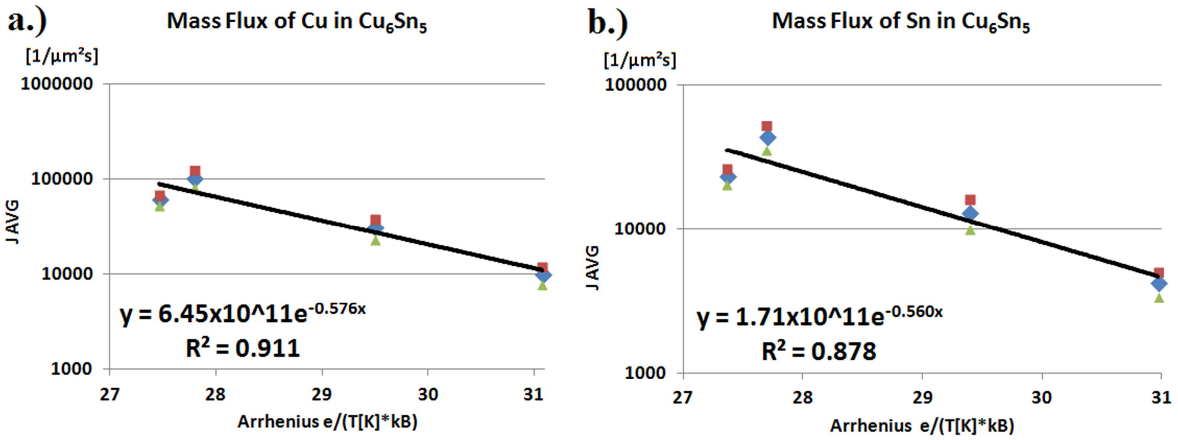

Figure 4.4: Mass flux of Cu (a) and Sn (b) in Cu_6Sn_5 at different TS temperatures (mean ± SD)

The compositional range of the IMCs cannot be expected to be bigger than one mass percent [4.2]. Due to the limited accuracy and the limited resolution of the EDS the concentration gradient in the IMCs cannot be measured directly. Nevertheless the expected range in the material composition can be transformed into the expected range of the atomic density (4.3). The range of the atomic density and the mean thickness of the IMC layers lead to the mean concentration gradients (4.6).

$$|grad(N)| \approx \frac{\Delta N}{(h+h_0)/2} \quad (4.6)$$

Knowing the concentration gradients, D_0 can be calculated with the linear constants of the fitted curves. In table 4.7 the expected concentration gradients in Cu_6Sn_5 and Cu_3Sn and the resulting material parameters for the characterization of diffusion processes in both IMCs are given.

	Cu_3Sn		Cu_6Sn_5	
	Cu	Sn	Cu	Sn
E_A[eV]	0.808 ± 0.05	0.809 ± 0.05	0.58 ± 0.07	0.56 ± 0.07
grad(N) [1/m^4]	$1.7x10^{33}$	$5.3x10^{32}$	$2.1x10^{32}$	$1.0x10^{32}$
D_0 [m²/s]	$1.3x10^{-8}$	$1.2x10^{-8}$	$2.9x10^{-9}$	$1.7x10^{-9}$

Table 4.7: E_A, concentration gradients and D_0 of Cu and Sn in Cu_6Sn_5 and Cu_3Sn.

4.1.1.3 Discussion

E_A for the diffusion of Cu and Sn were 0.81eV in Cu_3Sn and nearly 0.6eV in Cu_6Sn_5. The E_A values of Cu_3Sn are close to the available literature values (table 4.8). The E_A values of Cu_6Sn_5 are lower than the values for Cu_3Sn and the available literature values.

	Cu_3Sn		Cu_6Sn_5	
	Cu	Sn	Cu	Sn
E_A [eV]	0.816 [4.3] 0.818 [4.4] **0.808**	0.894 [4.3] 0.827 [4.4] **0.809**	- 0.835 [4.4] **0.58**	- 0.88 [4.4] **0.56**
D_0 [m^2/s]	$2.21x10^{-6}$ [4.3] $1.8x10^{-8}$ [4.4] **$1.3x10^{-8}$**	$2.49x10^{-6}$ [4.3] $7.9x10^{-10}$ [4.4] **$1.2x10^{-8}$**	- $6.2x10^{-8}$ [4.4] **$2.9x10^{-9}$**	- $5.88x10^{-7}$ [4.4] **$1.7x10^{-9}$**

Table 4.8: Comparison between experimental results and literature values.

The main transport mechanism in the IMCs is a vacancy mechanism. The E_A of the vacancy mechanism is related to the melting temperature of the material [4.5]. The melting temperature of Cu_6Sn_5 (415°C) is lower than the melting temperature of Cu_3Sn (676°C) [4.6]. Hence a higher E_A for material transport in Cu_3Sn can be expected. Independent of the lower E_A the formation speed of Cu_6Sn_5 during this investigation was not significantly faster than in previous investigations. Compared to the literature the lower E_A of this investigation is compensated by relatively low diffusion constants.

In this investigation the D_0 of Cu and Sn were found to be similar for Cu_6Sn_5 as well as for Cu_3Sn. The D_0 of Cu and Sn in Cu_6Sn_5 were one order of magnitude smaller than the D_0 for Cu_3Sn. The D_0 of Cu in Cu_3Sn was in the range of [4.4]. In this investigation the D_0 of Sn in Cu_3Sn was close to the Cu value, while in [4.4] a reduced mobility of Sn in Cu_3Sn was found. In [4.3] the D_0 of Cu and Sn in Cu_3Sn were also similar, but both D_0 values were two orders of magnitude higher than in this investigation.

In [4.4] the difference in the mobilities of Sn and Cu in Cu_3Sn was explained by the difference in the related mass fractions. Due to the relatively high Cu content in Cu_3Sn the number of regular lattice sides for Cu is higher than for Sn. Consequently a motion of Sn, without crystal deformation, would require jumps over larger distances than for Cu. As a consequence the motion of Sn atoms would be less probable than the motion of Cu atoms and the D_0 of Sn would be lower. Nevertheless in [4.4] the diffusion constant of Sn in Cu_6Sn_5 is also lower than for Cu, while their material fraction is similar.

Based on a theory of Huntington a diffusion mechanism, including crystal deformation, is given for binary alloys [4.7]. In this case the material motion is based on a six jump motion cycle of vacancies that allows Cu atoms to jump on to Sn lattice sides, or the other way around. In this case the effective jump distance for Sn and Cu is the same and the D_0 of Cu and Sn would be similar in Cu_6Sn_5 and in Cu_3Sn.

Overall the similarities of D_0 in [4.3] and in this investigation indicate the presence of a six jump vacancy mechanism in the Cu-Sn IMCs. As in [4.4], also in this investigation a smaller mass flux of Sn in Cu_3Sn was found, but this is due to the lower atomic density and the smaller concentration gradient of Sn compared to Cu.

E_A can be used to define time limits for the consideration of saturation effects during the IMC formation. Furthermore E_A will be used to extrapolate the diffusion induced mass flux in the solder joints during the TM and EM stress tests. In table 4.9 the time limits for the relevant TS test temperatures are given. If the test time is below the calculated limit for the given test temperature and the related IMC, the value in the table is marked green. If the test time is above the limit the value in the table is marked red and saturation effects have to be taken into account when the average mass flus is calculated.

Temperature:	**100°C**	**120°C**	**140°C**	**150°C**
Cu_3Sn (0.8eV)	6108h	1753h	568h	336h
Cu_6Sn_5 (0.56eV)	2674h	1095h	487h	336h
Test time:	2798h	784h	163h	336h

Table 4.9: Time limits for the consideration of saturation effects during the IMC growth.

4.1.2 Top Bumps “Closed System”

During the reflow process $(CuNi)_6Sn_5$ was formed at the contact surfaces of the top bumps (Fig. 4.5, top). During the TS tests the layer thickness of $(CuNi)_6Sn_5$ was increased (Fig. 4.5, below). EDS investigations did not show any Cu in the Ni pads. Hence the Ni layer is an effective diffusion barrier for Cu coming from the metal lines. Under these conditions the Cu content of $SnAg_{3.0}Cu_{0.5}$ is the only available source for Cu. The $(CuNi)_6Sn_5$ layers are formed by the accumulation of Cu and Au at the contact surfaces, and the diffusion of Ni from the pad into the solder joint. From the Ni pad, through the $(CuNi)_6Sn_5$ layer, to the $SnAg_{3.0}Cu_{0.5}$ joint a continuously shrinking amount of Ni is observable. Beyond the $(CuNi)_6Sn_5$ to $SnAg_{3.0}Cu_{0.5}$ interface the Ni content immediately drops to very low values, that cannot be measured with EDS. The disappearance of Ni at the borderlines to $SnAg_{3.0}Cu_{0.5}$ is in compliance with the assumption that Ni is a “fast diffuser” in Sn. Due to the main characteristics of “fast diffusion” via an interstitial mechanism it can be expected that Ni easily migrates through the solder joints from one IMC layer to another one, without being detectable by EDS.

While TS tests on SnAg samples lead to the formation of Ni_3Sn_4 [4.8], no Ni_3Sn_4 could be found in TS stressed SnAgCu samples.

In the following the diffusion of Ni in the IMCs as well as the driving forces for the Cu and Au accumulation have to be characterized, furthermore possible saturation mechanisms during long term tests have to be identified.

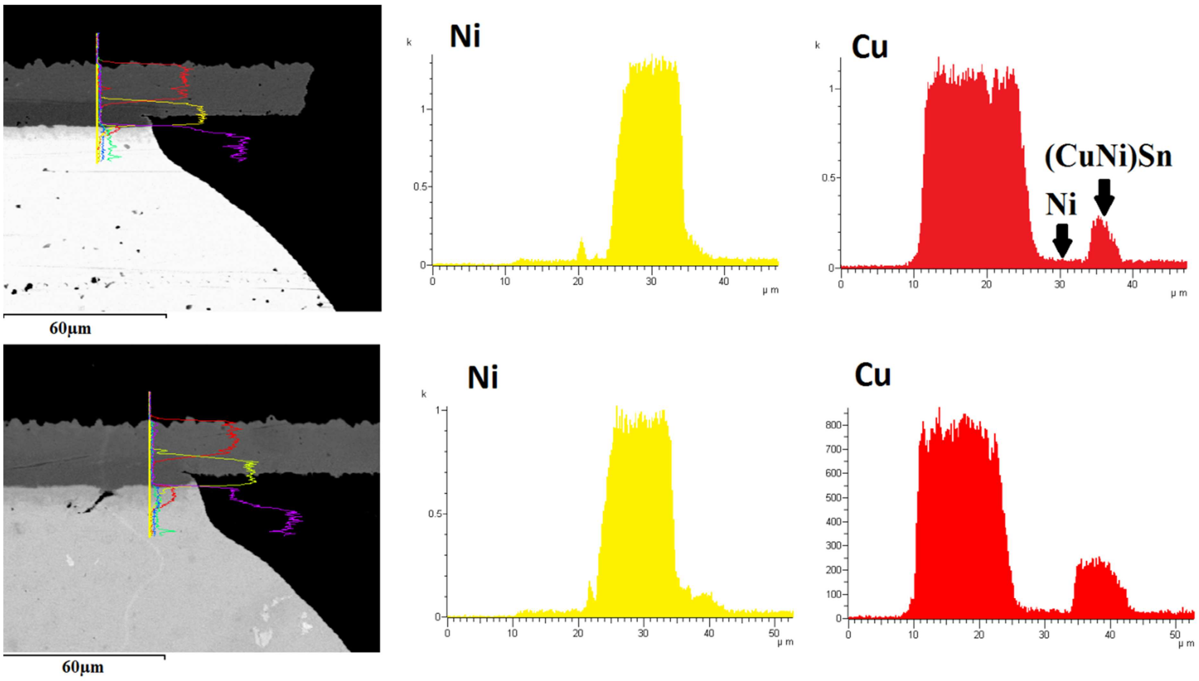

Figure 4.5: EDS results at the die side contact surfaces of the top bumps after reflow (top), and after eight weeks TS at 150°C (below), Red: Cu; Yellow: Ni

4.1.2.1 Long term temperature storage

During the $(CuNi)_6Sn_5$ formation Ni has to cover a growing distance before it can add to the IMC. In addition the consumption of Cu and Au during the IMC formation reduces their concentration in the solder joint [4.9]. As for the open system the required motion of Ni through the IMC layer leads to a saturation effect on the $(CuNi)_6Sn_5$ formation during long term TS tests (Fig. 4.6, left). For the $(CuNi)_6Sn_5$ formation Cu is also required and in difference to the open system the amount of available Cu is shrinking during the IMC growth. As a consequence the fitted curve of the $(CuNi)_6Sn_5$ profile (4.1) has a "n" value below 0.5 for the long term case. Finally the limitation of available Cu should limit the maximum thickness of $(CuNi)_6Sn_5$ ($t \rightarrow \infty$, $n \rightarrow 0$) .

As for the open system the mass flux of Cu, Au and Ni in the closed system can be calculated through the IMC growth speed, when IMC dimensions and the composition are known (4.7-8).

$$J_{Ni} = \frac{(h - h_0)}{t_{test}} \cdot \left(1 - \frac{N_{Ni,CuNiSn}}{N_{Ni,Ni}}\right) \cdot \left(N_{Ni,CuNiSn}\right) \qquad (4.7)$$

$$J_{Cu,Au} = \frac{(h - h_0)}{t_{test}} \cdot \left(N_{Cu,Au;CuNiSn} - N_{Cu,Au;SAC}\right) \qquad (4.8)$$

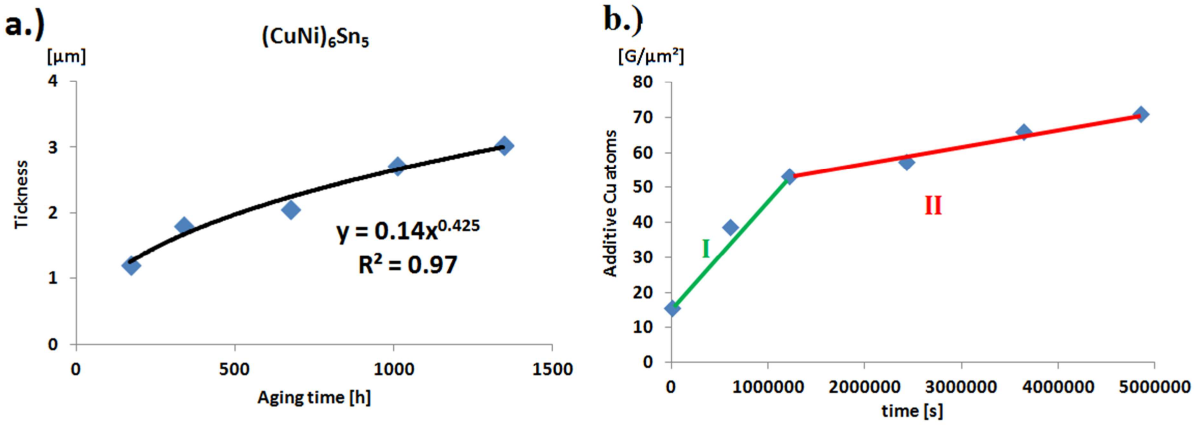

Figure 4.6: TS induced $(CuNi)_6Sn_5$ growth at 150°C (a), Cu accumulation (b) [4.10]: the mass flux changes between mode I (linear) and mode II (saturation) $G=10^9$

The composition of $(CuNi)_6Sn_5$ in the top bumps differs from the composition of the Cu-Ni-Sn IMCs on the board side of the bottom bumps. This is due to the fact that the test board contact pads are covered with NiP, while the contact pads in the PoP structure are covered with NiAu. The thin (~50nm) Au layers on the Ni pads were dissolved during the reflow process and afterwards Au accumulates in the $(CuNi)_6Sn_5$ layers. The phosphorus prevents Ni from moving into the IMC layers. Hence the Ni content of Cu-Ni-Sn IMCs on NiAu contact pads is higher than the Ni content of IMCs on NiP pads. Due to the presence of Cu diffusion barriers on both sides of the top bumps the Cu content in the Cu-Ni-Sn IMCs is lower than in the bottom bumps. While the composition of the IMCs in the bottom bumps remains the same, the TS changed the composition of the $(CuNi)_6Sn_5$ layers. The amount of Cu and especially Au is clearly increased, while the mass fraction of Ni is reduced (table 4.10).The formation of Ni_3Sn_4 requires a relatively high Ni content, so taking into account the shrinking mass fraction of Ni during TS, the missing Ni_3Sn_4 formation in SnAgCu solders is not surprising anymore. As for the bottom bumps, the Ag in the top bumps forms Ag_3Sn grains with the solder. The Ag_3Sn grains remain in the solder during the stress tests. Consequently no Ag was found in the IMC layers of the top bumps.

		Cu	**Sn**	**Ni**	**Au**
Reflow	**Mass [%]**	17 ± 2.0	70 ± 3.0	12.0 ± 2.4	1.0 ± 0.1
	ρ_{IMC} [g/cm³]	7.8			
	N [1/m³]	1.25×10^{28}	2.7×10^{28}	9.9×10^{27}	2.4×10^{26}
TS	**Mass [%]**	19 ± 1.3	68 ± 2.0	9 ± 0.8	3.0 ± 0.7
	ρ_{IMC} [g/cm³]	7.9			
	N [1/m³]	1.4×10^{28}	2.7×10^{28}	7.1×10^{27}	9.6×10^{26}

Table 4.10: Material composition of $(CuNi)_6Sn_5$ after reflow, and after the TS tests.

Test time [h]	**Reflow (0)**	**168**	**336**	**672**	**1008**	**1344**
$(CuNi)_6Sn_5$ [µm]	1.3 ± 0.2	2.5 ± 0.4	3.0 ± 0.3	3.3 ± 0.3	3.9 ± 0.37	3.3 ± 0.65

Table 4.11: $(CuNi)_6Sn_5$ dimensions after reflow and after the TS tests.

The IMC dimensions after the short- and the long term TS tests are given in table 4.11. The saturation effects on the $(CuNi)_6Sn_5$ lead to clear reduction of the mass flux of all three components. As a consequence, for a test time of more than 336h, the mass flux in the IMC layers is reduced to 36% of the starting values (table 4.12).

	$(CuNi)_6Sn_5$			
Test time [h]	**v[nm/h]**	**J_{Cu}[1/µm²s]**	**J_{Ni}[1/µm²s]**	**J_{Au}[1/µm²s]**
<336h	5.4	3.9×10^4	1.9×10^4	3.5×10^3
>336h	1.2	1.4×10^4	7.2×10^3	1.0×10^3

Table 4.12: $(CuNi)_6Sn_5$ growth speed and the related mass flux during the TS tests at 150°C.

4.1.2.2 Short term temperature storage

As for the open system, three short term TS test between 100°C and 140°C were performed in addition to the TS tests at 150°C. The resulting IMC dimensions are given in table 4.13. In contrast with to the long term TS tests the packages were soldered on a test board and two contact surfaces per solder joint can be investigated. Compared to the results of the open system, the SDs of the closed system are higher, because the intrinsic characteristics of the test devices (e.g. the compositional range of SnAgCu) have a stronger influence on the IMC formation speed. The IMC formation speed at the die side contacts was higher than at the board side contacts. The board side results fit better to the long term results. A possible reason for the increased IMC formations speed at the Die side contacts is a higher concentration of Cu and Au at the upper part of the solder joints.

		Reflow	**100°C-2798h**	**120°C-784h**	**140°C-164h**
Die side	**$(CuNi)_6Sn_5$ [µm]**	1.3 ± 0.2	2.8 ± 0.4	2.4 ± 0.3	2.8 ± 0.4
	v[nm/h]	-	0.54	1.4	9.1
Board side	**$(CuNi)_6Sn_5$ [µm]**	1.25 ± 0.14	2.3 ± 0.4	1.6 ± 0.25	2.2 ± 0.3
	v[nm/h]	-	0.36	0.51	5.8

Table 4.13: IMC dimensions at both contact surfaces after reflow and after the TS tests.

Based on the different TS results the E_A for the motion of Ni, Cu and Au were determined with a curve fitting procedure (Fig. 4.7).

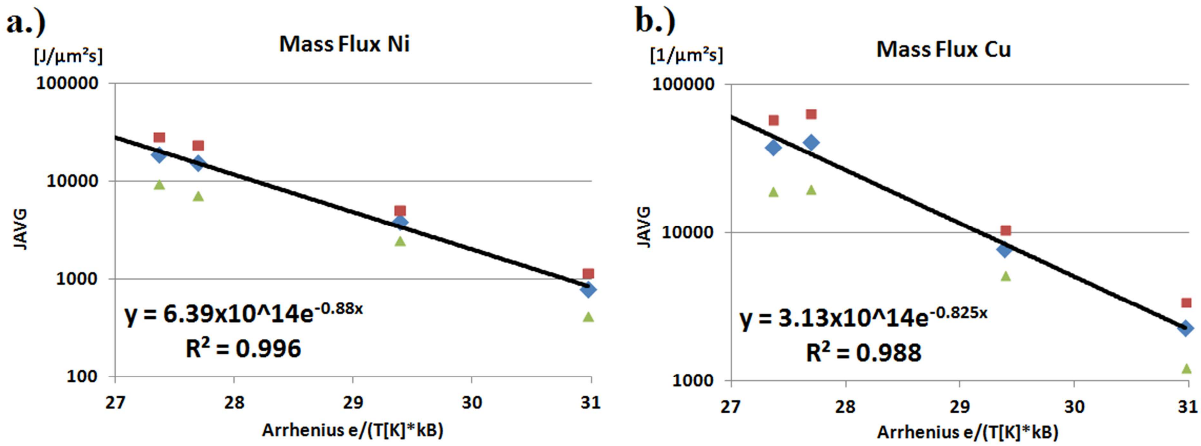

Figure 4.7 Mass flux of Ni (a) [4.10] and Cu (b) in $(CuNi)_6Sn_5$ at different TS temperatures (mean ± 3*SD)

As for the bottom bumps the linear constant of the fitted Ni curve is the product of the concentration gradient and the diffusion constant (Fig. 4.7, left). In contrast with the 1% compositional range of the Cu-Sn IMCs in the bottom bumps, the compositional range of Ni in Cu-Ni-Sn is 100%: $m_{Ni}\approx100\%$ in the pad, and $m_{Ni}\approx0\%$ in SnAgCu. This enables the direct measurement of the Ni concentration gradient in $(CuNi)_6Sn_5$ with EDS. Afterwards D_0 was calculated with (4.7).

The linear constant of the fitted Cu curve (Fig. 4.7, right) and the Au curve include the D_0 of both elements in SnAgCu and the driving forces for accumulation (β). The driving force "β" cannot be measured directly and the extraction of D_0 and β from of one experiment is impossible. Hence for Cu and Au, literature values of D_0 were used and β was extracted from the experimental results [4.11-12]. The material parameters for the diffusion of Ni and the accumulation of Cu and Au are given in table 4.14.

	Ni	Cu	Au
E_A[eV]	0.814-0.88	0.825-0.85	0.80-0.81
D_0 [m²/s]	0.5-9.3 x 10^{-7}	2.4 x 10^{-7} [4.11]	1.6 x 10^{-5} [4.12]
grad(N) [1/m⁴]	6.9x10^{32}	-	-
β [N]	-	3.6-7.8 x 10^{-16}	0.6-2.6 x 10^{-18}

Table 4.14 Activation energies, concentration gradients, diffusion constants and β of Cu and Ni and Au.

4.1.2.3 Discussion

During the TS tests on the closed system the Ni pads prevent the motion of Cu from the metal lines into the solder joints. Instead the diffusion of Ni into the solder, and the accumulation of Cu and Au, coming from the solder led to the formation of a $(CuNi)_6Sn_5$ layer. The formation of $(CuNi)_3Sn$ was suppressed by the relatively high Ni content [4.1]. In contrast with previous stress tests on SnAg solders the TS did not lead to the formation of Ni_3Sn_4. The presence of 0.5% Cu in the SnAgCu solder reduced the Ni consumption. As a consequence the Ni content in the IMC layers was too low for a Ni_3Sn_4 formation [4.13]. The IMC growth speed in the closed system is more dependent on the intrinsic conditions in the solder joints, than for the open system. Hence the SD of the IMC dimensions is higher for the closed than for the open system. Against this background the extraction of exact material parameters is more difficult than for the closed system.

E_A for the motion of Cu, Ni and Au in the Cu-Ni-Sn IMCs was a round 0.8eV. The D_0 of Ni in the IMCs was relatively high compared to the mobility of Cu and Sn in the Cu-Sn IMCs of the open system.

Nevertheless the required motion of Ni through the growing IMC layer and the limited availability of Cu and Au led to a saturation of the $(CuNi)_6Sn_5$ growth during the long term TS tests. The saturation effect was even clearer than for the Cu-Sn IMCs in the open system. The time limits for the different intensities of saturation show that all TS stress tests were in the short term range, and no adjustments of the mass flux calculation were necessary (table 4.15). As for table 4.9 the related time limits are marked green. For the EM and TM stress tests the situation will be more critical, because the test times remain the same while the test temperatures are increased by Joule heating.

Saturation states at 150°C (0.8eV)		**Remaining mass flux in percent**			**Time limits for the TS tests**		
		J_{Sat}/J_0 -Ni-	**J_{Sat}/J_0 -Cu-**	**J_{Sat}/J_0 -Au-**	**T=100°C t=2798h**	**T=120°C t=784h**	**T=140°C t=168h**
Sat=I	**t>168h**	76%	81%	64%	3,168h	895h	286h
II	**t>336h**	48%	50%	38%	6,336h	1,790h	572h
III	**t>672h**	40%	38%	29%	12,672h	3,580h	1,144h
IV	**t>1008h**	32%	30%	23%	19,008h	5,190h	1,716h

Table 4.15: Time limits for different intensities of saturation during the $(CuNi)_6Sn_5$ formation, the remaining mass flux compared to the starting values, and the extrapolated time limits for the TS test conditions.

4.2 Thermomigration Induced IMC Formation

For the AC tests 24 PoP structures were placed on a test card. One half of the packages were TS stressed only and AC was applied to the other ones. Based on the knowledge of the diffusion driven IMC formation, the investigation of the migration induced IMC formation is possible. An applied current always leads to Joule heating. The Joule heating has to be added to the oven temperature and increases the total test temperature. Furthermore it leads to local hot spots due current crowding. Hence the diffusion driven IMC formation has to be extrapolated for the increased test temperature.

The inhomogeneous temperature distribution goes along with temperature gradients, being the driving force for TM. For the TM stress tests AC (0.8A, 50Hz) was applied to the TS stressed PoP structures. The alternating driving force for EM will suppress an effective mass flux, while Joule heating is still present. Hence the influence of TM can be investigated without an influence of EM.

In the case of the open system the test will show the direction of the TM induced mass flux and its influence on the IMC formation speed. Regarding the closed system, the test will also show if the presence of an electron flux causes the formation of Ni_3Sn_4 in a Cu containing solder.

4.2.1 General Test Results

The most relevant consequence of EM is the formation of voids at the contact surfaces of the solder joints [4.14-15]. Over a long period of time the EM induced void formation does not change the resistance of the test structure, but at the end the void formation leads to an increased current density and accelerates the void formation itself. As a consequence the final increase of the solder joint resistance appears very fast. In Fig. 4.8b an exemplary resistance measurement during an EM test with DC current is shown. After initialization the resistance kept constant for 30min. During the next 30min the resistance grew by 1.0Ω and a few seconds later an early failure due to EM appeared (resistance out of range, >50Ω).

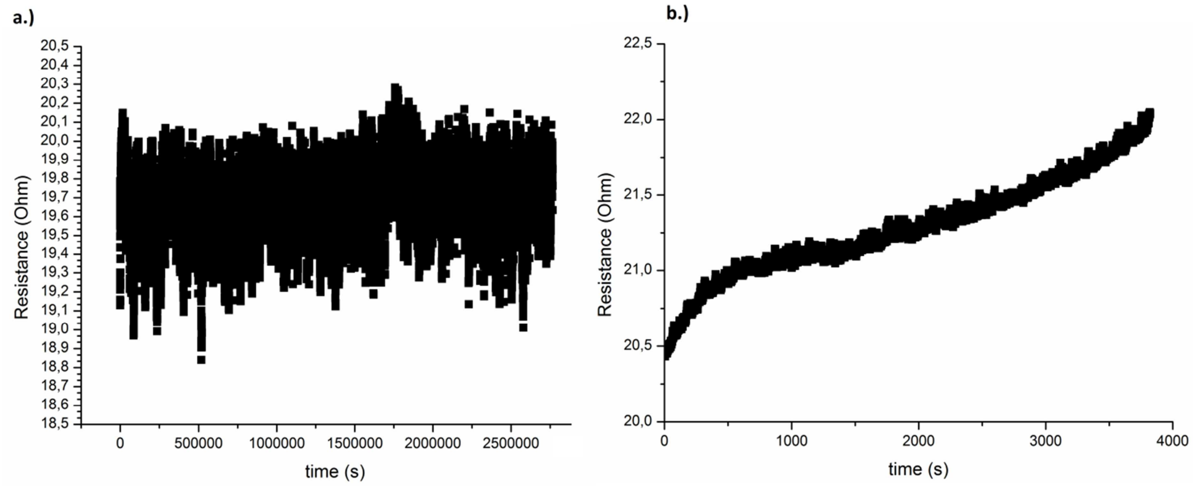

Figure 4.8: Resistance measurements during 790h AC-TM stress at 141°C (a), and one hour DC-EM stress at 178°C (b)

Even after 790h of testing the AC load did not show a significant increase of the solder joints resistance, and no voids were found at the contact surface of the solder joints. The related resistance measurement is shown in Fig 4.8a. The mean resistance was 19.7Ω. The noise (±0.4Ω) is due to the test equipment, including non-shielded cables, connectors and potentiometers.

During the AC tests a thermocouple was placed on the top side of the PoP structures. The oven temperature was 120°C and the temperature measurements show a package temperature of 141°C. This information was used to calculate the temperature of IMC layers and their local temperature gradients with the FEM. The simulation results show a further heating in the center of the PoP. The IMC temperature is 145°C, so the applied current of 0.8A led to 25°C Joule heating in the IMC layers (Fig. 4.9, left).

As a consequence of current crowding, being a well-known effect in our test structure [4.14], the temperature gradients in the IMC layers are not homogenous.

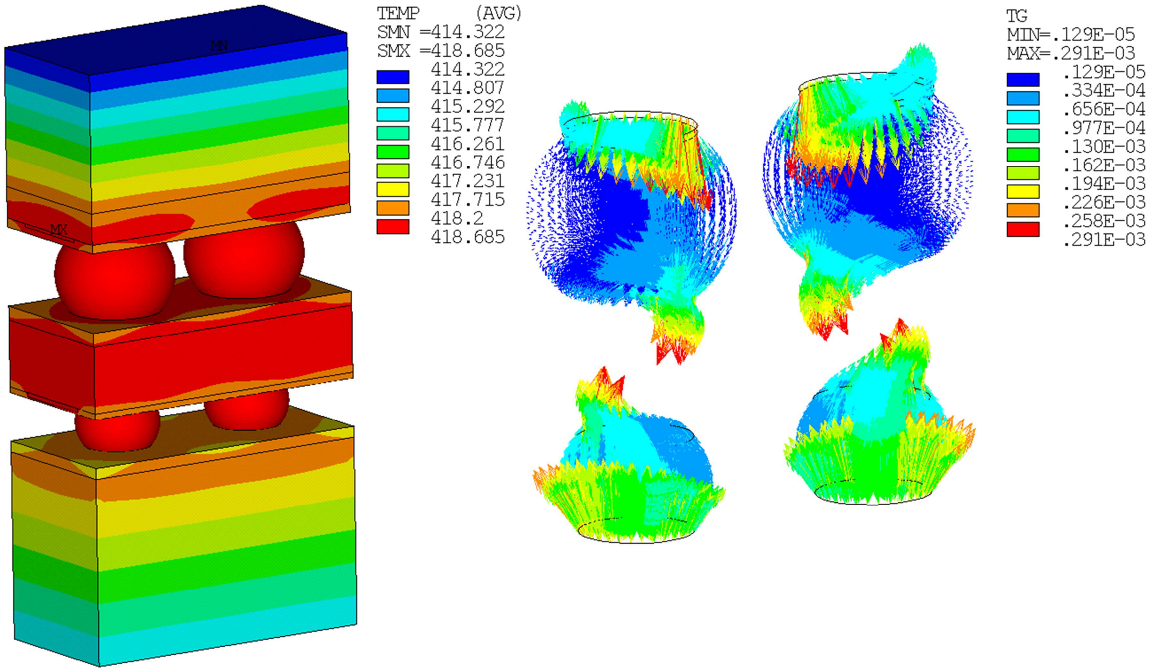

Figure 4.9: Temperature [K] distribution in the PoP structure (left), and the temperature gradients [K/µm] in the solder joints (right)

For the further interpretation of the experimental results an average temperature gradient will be used (4.9).

$$grad(T)_{Avg} = \frac{1}{A_{Sum}} \cdot \sum_{n=1}^{N} grad(T_n) \cdot A_n \quad (4.9)$$

A_{Sum}= contact surface, N= number of finite elements, A_n= partial contact surface of a finite element, grad(T_n)= local temperature gradient

Previous infrared observations of solder joints have shown temperature gradients in an order of 10,000 K/m [4.16]. The maximum temperature gradients in the PoP structure appeared in the NiP layers; they were of the order of 3000 K/m. The temperature gradients in the good thermally conducting IMC layers are lower. The average gradients in the three relevant IMC layers are given in table 4.16. The high thermal conductivity of Cu_3Sn compared to Cu_6Sn_5 and $(CuNi)_6Sn_5$ leads to smaller temperature gradients. The relatively low average temperature gradient in $(CuNi)_6Sn_5$ is a consequence of a smaller current density, due to the larger contact surfaces of the top bumps. The averaged gradients will be used for calculation of the Q** values. In table 4.16 also the maximum temperature gradients are given. Due to current crowding their values are above 1000 K/m for Cu_6Sn_5 and $(CuNi)_6Sn_5$.

IMC	Cu_3Sn	Cu_6Sn_5	$(CuNi)_6Sn_5$
$grad(T)_{Avg}$ [K/m]	125	302	203
$grad(T)_{max}$[K/m]	473	1049	1392

Table 4.16: Average temperature gradients in the IMC layers during the AC test.

4.2.2 Bottom Bumps “Open System”

A comparison between the AC stressed and the TS stressed packages shows the influence of TM on the IMC formation. The mean IMC dimensions of the temperature stressed and the AC stressed packages are given in table 4.17. The test results show an accelerated IMC formation speed in the AC stressed solder joints. Furthermore no difference between the formal upstream and the downstream case was observable. The absence of a significant difference between the IMC growth speed for the up- and downstream cases indicates the suppression of an EM induced IMC formation.

Test	Downstream		Upstream	
	Cu_3Sn [µm]	Cu_6Sn_5 [µm]	Cu_3Sn [µm]	Cu_6Sn_5 [µm]
120°C/0 A	0.79 ± 0.1	3.52 ± 0.49		
v[nm/h]	0.28	0.91		
145°C/0.8 A	1.33 ± 0.13	5.6 ± 0.68	1.35 ± 0.14	5.5 ± 0.6
v[nm/h]	0.96	3.54	0.99	3.41

Table 4.17: IMC dimensions in the bottom bumps after 790h TM stress at 145°C.

Before an investigation of the TM induced mass flux is possible the diffusion due to the TS stress has to be estimated and subtracted from the total mass flux (4.10). The diffusion induced mass flux at 120°C is known from the short term TS results. The acceleration due to Joule heating (AFT) can be calculated with the E_A taken from section 4.1.1.

$$\left|\vec{J}_{TM}\right| = \left|\vec{J}_{Sum}\right| - AF \cdot \left|\vec{J}_{D,120}\right| \quad (4.10)$$

AF= acceleration factor

A 790h TS test at 145° drives the IMC formation into saturation and the reduction of mass flux has to be taken into account. The final acceleration factor (AF) for the diffusion driven IMC formation during the AC test is then given by (4.11).

$$AF = AFT \cdot \left[\frac{TL/AFT + |\vec{J}_I| / |\vec{J}_0| \cdot (t_{test} - TL/AFT)}{t_{test}} \right] \quad (4.11)$$

TL= time limit to saturation

Knowing the mass flux due to TM and the average temperature gradients in the IMC layers, the experimental heat of transport (Q**) can be calculated (4.12). The Q** includes the intrinsic heat of transport of the of the material (Q*) and the external influences by crystal defects and the temperature dependence of the solubility of the single element in the IMC .

$$|Q^{**}_{(T)}| = \frac{|\vec{J}_{TM}| \cdot k_B \cdot T^2 \cdot exp(E_A / k_B\, T)}{D_0 \cdot N \cdot |grad(T)|} \quad (4.12)$$

Compared to Cu_6Sn_5 the Q**of Cu_3Sn is relatively high (tables 4.18-19). In Cu_3Sn more grain boundaries as in Cu_6Sn_5 can be found. The higher density of grain boundaries leads to increased density of crystal defects. As expected by Gerl [4.17] this may be lead to increased Q** values as a consequence of electron scattering. The positive Q** indicate that the Cu and Sn ions in Cu_3Sn move from the hot to the cold crystal sites. While the negative Q** values for Cu_6Sn_5 indicate a motion from cold to the hot crystal sites.

Cu	**J_{Sum} [1/µm²s]**	**$J_{Dif,120}$ [1/µm²s]**	**AFT**	**TL-120°C [h]**	**AF**	**$J_{Dif,145}$ [1/µm²s]**	**J_{TM} [1/µm²s]**	**Q^{**}_{Cu} [eV]**
Cu_3Sn	3.5 x10^3	7.9 x10^2	3.2	1753	3.6	2.8 x10^3	0.6 x10^3	754
Cu_6Sn_5	32 x10^3	19 x10^3	2.8	1095	1.8	35 x10^3	-3.0 x10^3	-50

Table 4.18: TM induced mass flux of Cu in Cu_3Sn and Cu_6Sn_5, and the Q.**

Sn	**J_{Sum} [1/µm²s]**	**$J_{Dif,120}$ [1/µm²s]**	**AFT**	**TL-120°C [h]**	**AF**	**$J_{Dif,145}$ [1/µm²s]**	**J_{TM} [1/µm²s]**	**Q^{**}_{Sn} [eV]**
Cu_3Sn	1.7 x10^3	0.3 x10^3	3.2	1753	3.7	1.2 x10^3	0.5 x10^3	1088
Cu_6Sn_5	14 x10^3	10 x10^3	2.7	1095	1.8	18 x10^3	-3.1 x10^3	-27

Table 4.19: TM induced mass flux of Sn in Cu_3Sn and Cu_6Sn_5, and the Q.**

Taken into account that Q**describes the thermal energy being transported per atom, the measured values for both IMCs are too high. It can be expected that the thermal transport in binary alloys differs from pure elements, but for a further interpretation of the Q** values more results at different test temperatures will be needed. The experimental results required for a further interpretation of the TM induced mass flux will be given in section 4.3.

4.2.3 Top Bumps "Closed System"

The main point of the AC stress tests on the closed system is the clarification, if the presence of an electron flux is able to induce a Ni_3Sn_4 formation in Cu containing solders or not. Even after 790h AC stress at 145°C no Ni_3Sn_4 was observable. Hence, neither the additional Ni transport due TM, nor the presences of an electron flux are able to induce Ni_3Sn_4 formation in $SnAg_{3.0}Cu_{0.5}$. Nevertheless the AC stress changed the composition of $(CuNi)_6Sn_5$ by increasing the Cu and the Au content, while the relative amount of Sn is shrinking (table 4.20).

		Cu	Sn	Ni	Au
AC	**Mass [%]**	20 ± 2.0	62 ± 3.0	11.0 ± 2.4	7.0 ± 0.1
	ρ_{IMC} [g/cm³]	8.1			
	N [1/m³]	1.5×10^{28}	2.6×10^{28}	9.1×10^{27}	1.7×10^{27}

Table 4.20: Composition $(CuNi)_6Sn_5$ of after 790h AC stress at 145°C.

The AC stress test is combined with TS, so the formation of $(CuNi)_6Sn_5$ was certain. Compared to the TS tests the IMC formation speed was accelerated during the AC stress tests (table 4.21). As for the bottom bumps, one important reason for the accelerated IMC formation speed was the higher test temperature due to Joule heating. Comparing the TS and the AC test results and taking into account the additional mass flux due to diffusion, a TM induced mass flux from the die to the board side contacts was observable. Due to TM, the IMC formation speed at the die side contacts is reduced, while the IMC formation at the board side contacts is increased. A comparison between the formal upstream and downstream cases did not show a relevant difference in the IMC formation speed. Hence the presence of an EM induced mass flux cannot be expected.

4.2.3.1.1	**Die Side [µm]**		**Board Side [µm]**	
	Downstream	**Upstream**	**Downstream**	**Upstream**
Reference	1.26	1.26	1.25	1.25
120°C/0A	2.12	2.12	1.44	1.46
v [nm/h]	1.1	1.1	0.24	0.27
145°C/0.8A	2.77	2.68	2.11	2.2
v [nm/h]	1.9	1.8	1.1	1.2

Table 4.21: $(CuNi)_6Sn_5$ dimensions after reflow, TS and AC stress tests.

Knowing E_A for the transport mechanisms of Cu, Au and Ni in $(CuNi)_6Sn_5$ it is possible to extrapolated the expected mass flux due to diffusion and accumulation. Afterwards the mass flux due to TM and the related Q** values were extracted from the experimental results by subtracting TS induced mass flux values from the total mass flux during the AC test (4.10), (4.12). During the 790h test time at 145°C, the $(CuNi)_6Sn_5$ growth passes two saturation limits (table 4.15) and the reduction of the mass flux has to be taken into account (4.13).

$$AF = AFT \cdot \left[\frac{TL + |\vec{J}_I| / |\vec{J}_0| \cdot TL + |\vec{J}_{II}| / |\vec{J}_0| \cdot (t_{test} - 2 \cdot TL)}{t_{test}} \right] \quad (4.13)$$

The resulting Q** values of Cu, Ni and Au are given in tables 4.22-23. The Q** values are relatively large. Hence additional TM investigations at other test temperatures will be needed for a further interpretation of the TM driven material transport in $(CuNi)_6Sn_5$.

Die side	**J_{Sum} [1/µm²s]**	**$J_{Dif,120}$ [1/µm²s]**	**AFT**	**TL [h]**	**AF**	**$J_{Dif,145}$ [1/µm²s]**	**J_{TM} [1/µm²s]**	**Q** [eV]**
Cu	8.8×10^3	3.9×10^3	3.3	236	3.2	1.55×10^4	-6.7×10^3	-1479
Ni	5.8×10^3	2.1×10^3	3.7	224	3.3	7.0×10^3	-1.3×10^3	-430
Au	1.6×10^3	5.1×10^2	3.1	218	2.6	1.32×10^3	2.8×10^2	3.8

Table 4.22: TM induced mass flux of Cu, Ni and Au in the upper $(CuNi)_6Sn_5$ layer.

Board side	J_{Sum} [1/µm²s]	$J_{Dif,120}$ [1/µm²s]	AFT	TL-1 [h]	AF	$J_{Dif,145}$ [1/µm²s]	J_{TM} [1/µm²s]	Q** [eV]
Cu	6.3 x10^3	1.6 x10^3	3.5	221	3.2	5.1 x10^3	1.3 x10^3	-519
Ni	2.7 x10^3	7.9 x10^2	3.2	218	2.9	2.3 x10^3	3.3 x10^2	-299
Au	1.22 x10^3	3.97 x10^2	3.2	218	2.59	1.28 x10^3	-0.6 x10^2	3.3

Table 4.23: TM induced mass flux of Cu, Ni and Au in the lower $(CuNi)_6Sn_5$ layer.

4.2.4 Conclusion

During the AC stress tests no void formation and no migration induced failure of the bump chains were observable. In the top- or bottom bumps no difference in the IMC formation speed was observable for the formal up- or downstream case. Hence it can be assumed that the chosen frequency of 50Hz was high enough to suppress an effective mass flux due to EM.

The applied current of 0.8A led to 25°C Joule heating and current crowding appeared at the corners of the solder joints. The combination of Joule heating and current crowding led to an inhomogeneous temperature distribution in the solder joints. The resulting temperature gradients are a driving force for TM.

The presence of TM in the IMCs had a clear influence on the IMC formation speed in the top and the bottom bumps. Nevertheless the influence of TM was not strong enough to induce a Ni_3Sn_4 formation in $SnAg_{3.0}Cu_{0.5}$. As a consequence only a directed mass flux due to EM can expected to be a possible driving force for the Ni_3Sn_4 formation in Cu containing solders.

With the E_A of the different transport mechanism for Cu, Sn, Ni and Au in the IMC layers it was possible to predict the influence of diffusion and material accumulation on the AC test results. Afterwards the extraction of the TM induced mass flux was possible. Knowing the TM induced mass flux and the temperature gradients the Q** values were extracted.

The single Q** values of Cu and Sn in Cu_3Sn and Cu_6Sn_5 and of Cu, Ni and Au in $(CuNi)_6Sn_5$ were calculated. Nevertheless one data point does not allow a further interpretation of the TM driven material transport in binary or even more complex alloys. Hence the presence of TM during the DC tests will be used for an extraction of three additional Q** values at different test temperatures.

4.3 Electromigration Induced IMC Formation

The EM tests were performed at three different oven temperatures: 100°C, 120°C and 140°C. For the EM tests the TS is combined with a DC of 1A. During the DC tests, diffusion, material accumulation, TM and EM appeared. The DC tests are close to the use case of BGAs and they can be used to simulate a migration accelerated TLPS process. For the interpretation of the DC test results, the previous test results from the TS and the AC stress tests are relevant. Furthermore EM is able to induce Ni_3Sn_4 formation in Cu containing solders.

4.3.1 General Test Results

The applied current of 1A leads to Joule heating. Hence the test temperature is higher than the chosen oven temperature. As for the AC tests thermocouples were used for temperature measurements, being the boundary conditions for a FEA. The test temperatures at the IMC layers are: 138°C, 161°C and 185°C. Hence Joule heating increased the test temperature by +38°C from 100°C, and by +45°C from 140°C. The reason for more Joule heating at higher oven temperatures is a higher specific resistance of the metal lines and the solder joints. While the resistance of the bump chain was increased due to the rising temperature a LabView® program increased the voltage to keep a constant current of 1A. By that way the applied electrical power was also increased.

As for AC tests the DC tests are also influenced by current crowding (Fig. 4.10). The consequences are temperature gradients in the solder joints and in the IMC layers (table 4.24), as well as mass flux divergences of the EM (3.24).

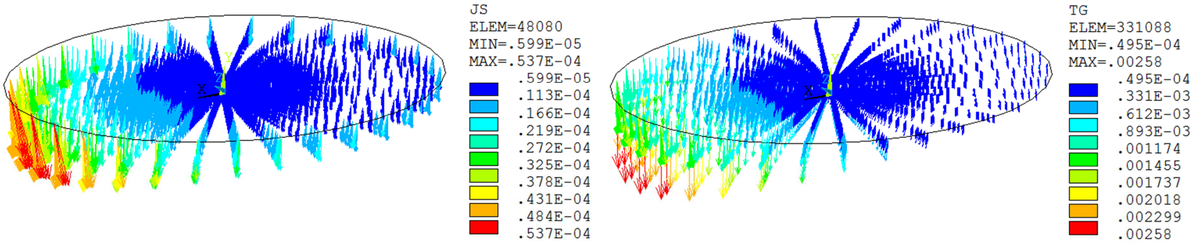

Figure 4.10: Current density [A/µm²] (left) and temperature gradient distribution [K/µm] at the die side contact surfaces of the top solder joints (right) [4.10]

T_{test} [°C]	Cu_3Sn [K/m]		Cu_6Sn_5 [K/m]		$(CuNi)_6Sn_5$ [K/m]		Ni_3Sn_4 [K/m]	
	avg	**max**	**avg**	**max**	**avg**	**max**	**avg**	**max**
138	195	601	509	1435	293	1627	297	2520
161	220	663	575	1605	313	1576	313	2377
185	247	659	636	1599	344	1739	344	2655

Table 4.24: Averaged and maximum temperature gradients in the IMC layers.

In contrast with the AC tests, the DC tests led to an effective mass flux by EM. The divergences of the EM induced mass flux led to migration induced void formation (Fig. 4.11). Hence the EM DC tests can lead to failures of the bump chain, while the TS or AC tests cannot.

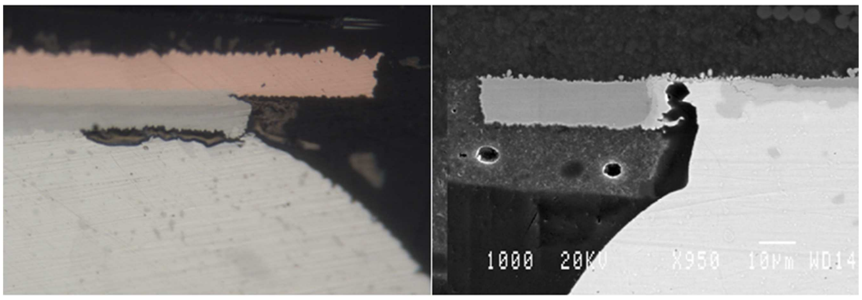

Figure 4.11: EM induced void formation as consequence of current crowding at the top bump (left) and the bottom bump contact surfaces (right) [4.18]

4.3.2 Bottom Bumps "Open System"

For both the AC and the DC experiments, test cards with 24 PoP structures were used. One half of the packages were TS stressed only, the others were TS and DC stressed. Afterwards the IMC dimensions of the DC stressed and TS stressed packages were compared.

4.3.2.1 Parameter extraction

Compared to the TS tests the formation speeds of Cu_6Sn_5 and Cu_3Sn were increased (table 4.25). One reason for the accelerated IMC formation is Joule heating and the resulting difference in the test temperatures for the TS and the EM tests.

In contrast with the AC tests, DC stress led to different results for the up- and the downstream cases. The IMC formation speeds of Cu_6Sn_5 and Cu_3Sn were accelerated for the upstream and decelerated for the downstream case. In all cases at the board side contact surfaces only a thin $(CuNi)_6Sn_5$ layer was observable. Hence the presence of phosphorus in the Ni pad suppressed the Ni_3Sn_4 formation, even under DC stress at 185°C.

		Upstream		Downstream	
Test	**Surface**	**Cu_3Sn [µm]**	**Cu_6Sn_5 [µm]**	**Cu_3Sn [µm]**	**Cu_6Sn_5 [µm]**
138°C/1 A 2369 h	**Upper**	1.15 ± 0.1	6.4 ± 1.0	1.34 ± 0.17	8.7 ± 0.73
	Lower	-	3.2 ± 0.6	-	2.9 ± 0.5
161°C/1 A 192 h	**Upper**	1.5 ± 0.34	6.9 ± 1.1	1.6 ± 0.24	8.8 ± 1.25
	Lower	-	3.5 ± 1.14	-	3.1 ± 0.8
185°C/1 A 144 h	**Upper**	1.6 ± 0.4	9.67 ± 1.87	2.0 ± 0.32	11.4 ± 2.4
	Lower	-	7.4 ± 1.4	-	6.6 ± 1.7

Table 4.25: Cu_3Sn and Cu_6Sn_5 dimensions after the EM stress tests.

As a consequence of current crowding the IMC formation speed at the corners of the solder joints should differ from the IMC formation speed at the center of the solder joints. The direct observation of EM by current crowding was difficult: the upstream case led to relatively homogenous IMC layers (Fig. 4.12, left), while the current crowding induced degradation of the IMC layer (Fig 4.12, right) became visible for the upstream case. The reason why the IMC formation in the bottom bumps was not clearly affected by current crowding has to be clarified with FEA (chapter 5).

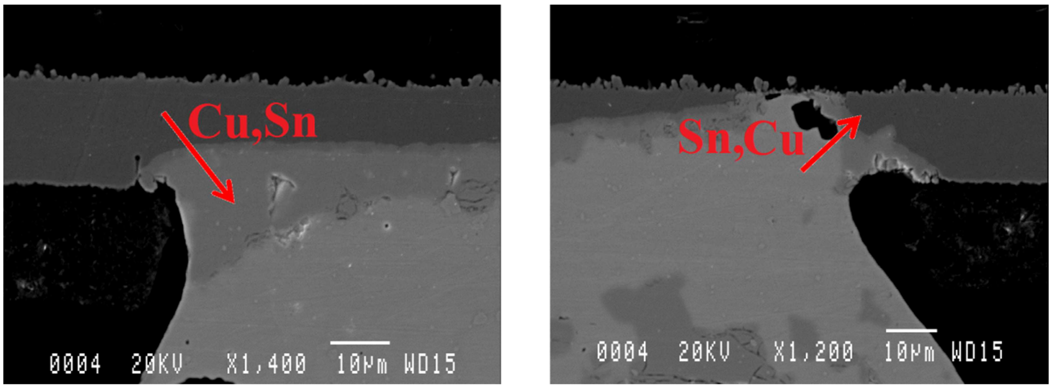

Figure 4.12: IMC layers at the die sided contact surfaces of a downstream (left) and an upstream stressed (right) bump after 2769h EM at 138°C

As a consequence of the missing current crowding effect on the IMC formation, statistics were used to clarify the influence of EM on the IMC formation speed for the up- and downstream cases (Fig. 4.13).

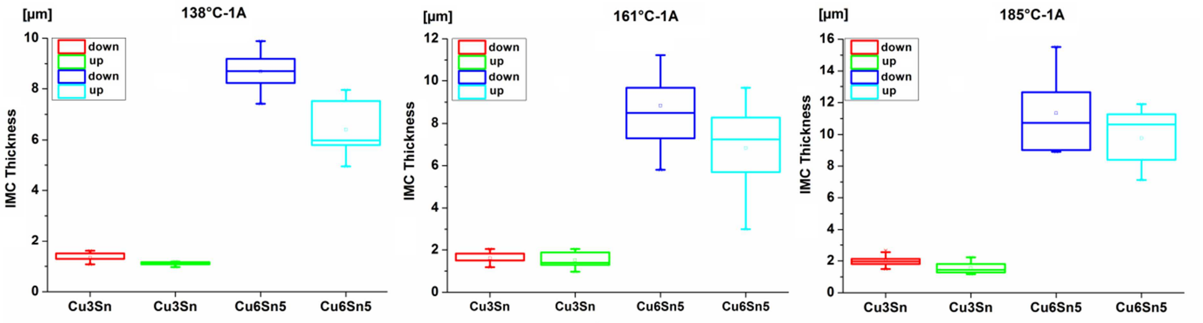

Figure 4.13: Box plots of the IMC dimensions after the up- and downstream EM stress tests for three different test temperatures

The extraction of the EM induced mass flux was done by comparing the up- and downstream cases (4.14). The benefit of this method is the fact that no extrapolation of the diffusion induced mass flux is necessary. Due to Joule heating, an extrapolation of the diffusion induced mass flux was necessary for the extraction of the TM induced mass flux (4.15).

$$\vec{J}_{EM} = \frac{\vec{J}_{T,Down} - \vec{J}_{T,Up}}{2} \quad (4.14) \qquad \vec{J}_{TM} = \frac{(\vec{J}_{T,Down} + \vec{J}_{T,Up})}{2} - \vec{J}_{D,TS} - \vec{J}_{D,DC} \quad (4.15)$$

The EM DC tests are life time tests and downtimes without Joule heating appeared, because bump chains failed due to void formation. Afterwards the system had to be reset. During the resulting downtimes only a diffusion driven mass flux at the oven temperature appeared in the formally DC stressed solder joints. The mass flux during the downtimes was taken into account by transforming the AF (4.11) to AF* (4.16).

$$AF^{*} = AF \cdot \left[1 + \left(\frac{t_{TS} - t_{DC}}{AF \cdot t_{DC}}\right)\right] \quad (4.16)$$

t_{TS}= total test time including all downtimes, t_{DC}= test time without downtimes

The resulting mass flux values of Sn and Cu in Cu_3Sn and Cu_6Sn_5 are given in the tables 4.26-29. In Cu_3Sn the TM induced mass flux is higher than the EM induced mass flux. In the Cu_6Sn_5 layer both kinds of migration lead to similar math flux values. The relatively high TM values in both IMCs have to be explained by a further analysis of the test results.

Cu_3Sn -Cu-	J_{Down} [1/µm²s]	J_{Up} [1/µm²s]	$J_{EM,Cu}$ [1/µm²s]	$J_{Dif,TS}$ [1/µm²s]	AFT	TL [h]	AF	AF*	$J_{Dif,DC-EM}$ [1/µm²s]	$J_{TM,Cu}$ [1/µm²s]
138°C	1.2 x10^3	0.75 x10^3	**0.24 x10^3**	0.1 x10^3	10	646	8.0	8.2	0.8 x10^3	**0.2 x10^3**
161°C	22 x10^3	20 x10^3	**1.0 x10^3**	1.3 x10^3	9.5	192	9.5	12	16 x10^3	**3.9 x10^3**
185°C	34 x10^3	26 x10^3	**3.0 x10^3**	2.4 x10^3	9.3	62	7.7	7.8	19 x10^3	**11 x10^3**

Table 4.26: Total mass flux during the up- and downstream tests, the mass flux due to EM, the diffusion induced mass flux, the AFs and the TM induced mass flux. All values for Cu in Cu_3Sn.

Cu_3Sn -Sn-	J_{Down} [1/µm²s]	J_{Up} [1/µm²s]	$J_{EM,Sn}$ [1/µm²s]	$J_{Dif,TS}$ [1/µm²s]	AFT	TL [h]	AF	AF*	$J_{Dif,DC-EM}$ [1/µm²s]	$J_{TM,Sn}$ [1/µm²s]
138°C	0.5 x10^3	0.3 x10^3	**0.1 x10^3**	0.4 x10^2	10	646	8.0	8.2	0.3 x10^3	**0.1 x10^3**
161°C	8.9 x10^3	8.1 x10^3	**0.4 x10^3**	0.5 x10^3	9.5	192	9.5	12	6.2 x10^3	**2.0 x10^3**
185°C	14 x10^3	11 x10^3	**1.7 x10^3**	1.0 x10^3	9.3	62	7.7	7.8	7.8 x10^3	**3.4 x10^3**

Table 4.27: Total mass flux during the up- and downstream tests, the mass flux due to EM, the diffusion induced mass flux, the AFs and the TM induced mass flux. All values for Sn in Cu_3Sn.

Cu_6Sn_5 -Cu-	J_{Down} [1/µm²s]	J_{Up} [1/µm²s]	$J_{EM,Cu}$ [1/µm²s]	$J_{Dif,TS}$ [1/µm²s]	AFT	TL [h]	AF	AF*	$J_{Dif,DC-EM}$ [1/µm²s]	$J_{TM,Cu}$ [1/µm²s]
138°C	21 x10^3	13 x10^3	**3.7 x 10^3**	10 x10^3	5.2	533	2.0	2.2	22 x10^3	**-5.2 x10^3**
161°C	2.6 x10^5	1.9 x10^5	**37 x10^3**	31 x10^3	5.0	225	5.0	8.1	2.5 x10^5	**-25 x10^3**
185°C	5.5 x10^5	3.4 x10^5	**1.1 x10^5**	1.2 x10^5	3.9	100	3.7	3.0	5.0 x10^5	**-53 x10^3**

Table 4.28: Total mass flux during the up- and downstream tests, the mass flux due to EM, the diffusion induced mass flux, the AFs and the TM induced mass flux. All values for Cu in Cu_6Sn_5.

Cu_6Sn_5 -Sn-	J_{Down} [1/µm²s]	J_{Up} [1/µm²s]	$J_{EM,Sn}$ [1/µm²s]	$J_{Dif,TS}$ [1/µm²s]	AFT	TL [h]	AF	AF*	$J_{Dif,DC-EM}$ [1/µm²s]	$J_{TM,Sn}$ [1/µm²s]
138°C	8.8 x10^3	5.8x10^3	**1.4 x10^3**	3.2 x10^3	5.0	525	2.3	2.5	10 x10^3	**-2.0 x10^3**
161°C	1.1 x10^5	0.8 x10^5	**16 x10^3**	13 x10^3	3.8	227	3.8	7.9	1.0 x10^5	**-5.9 x10^3**
185°C	2.4 x10^5	1.5 x10^5	**37 x10^3**	54 x10^3	3.7	104	3.8	3.9	2.1 x10^5	**-11 x10^3**

Table 4.29: Total mass flux during the up- and downstream tests, the mass flux due to EM, the diffusion induced mass flux, the AFs and the TM induced mass flux. All values for Sn in Cu_6Sn_5.

The extracted mass flux values of the EM and TM during the DC tests enabled the calculation of the related Z** (4.17) and Q** (4.12) values. The results are given in table 4.30. For the calculation of Z** the specific resistances of the IMCs and their TCRs have to be known. The specific resistances of Cu_3Sn and Cu_6Sn_5 are available in the literature, but a TCR is only available for Cu_6Sn_5 (table 3.1). Hence the Z** values were calculated with a temperature independent specific resistance. The consequence is a temperature dependency of the Z** values. The Q** values are regularly temperature dependent.

$$\left|Z^{**}_{(T)}\right| = \frac{\left|\vec{J}_{EM}\right| \cdot k_B \cdot T \cdot exp(E_A/k_B\,T)}{D_0 \cdot N \cdot \left|\vec{j}\right| \cdot e \cdot \rho_{el}} \qquad (4.17)$$

	Cu_3Sn				**Cu_6Sn_5**			
	Cu		**Sn**		**Cu**		**Sn**	
T_{test} [°C]	**Z****	**Q**[eV]**	**Z****	**Q**[eV]**	**Z****	**Q**[eV]**	**Z****	**Q**[eV]**
138	29	908	56	1115	14	-50	6	-20
161	45	645	71	665	28	-43	15	-13
185	61	491	84	68	37	-38	16	-11

Table 4.30: Z and Q** values of Cu and Sn in Cu_3Sn and Cu_6Sn_5.**

4.3.2.2 Discussion

The DC tests reproduced the Q** values of the AC test. Nevertheless all Q** and Z** values are too high for single ions, and they are strongly temperature dependent. The equations being used for the calculation of Z** and Q** are appropriate for metals with a fcc crystal structure. The main difference between the IMCs and an idealized fcc structure is the presence of grain boundaries. The presence of grain boundaries leads to a high defect density. Hence the interpretation of the extracted Z** values has to be done under consideration of electron scattering at crystal defects.

In metals, heat transmission is mainly influenced by the electron gas. Hence electron scattering in the IMC does not only lead to increased Z** values, it also leads to high Q** values. As a consequence of smaller grains and a higher density of grain boundaries the Q** values of Cu_3Sn were relatively large compared to Cu_6Sn_5.

A model for the determination of temperature independent Z* under consideration of crystal defects is given by Bosvieux and Friedel (4.18). More details are available in section 3.2.2.

$$Z^{**}{}_{(T)} = \frac{1}{2} \cdot Z \cdot \left(1 - \frac{N \cdot \rho_D}{N_D \cdot \rho}\right) + \frac{2\tau_{(T)}}{3\pi} Z^2 \cdot \left(J_0\left(\frac{a}{r_H}\right) - 2J_2\left(\frac{a}{r_H}\right)\right) \qquad (3.35/4.18)$$

The Bohr radius (r_H) of the elements, the lattice constants of the IMCs (a) and the results of the Bessel functions are given table 4.31. All results of the Bessel functions are negative.

	b [nm]	**$r_{H\text{-}Cu}$ [nm]**	**$r_{H\text{-}Sn}$ [nm]**	**(J_0-$2J_2$) -Cu-**	**(J_0-$2J_2$) -Sn-**
Cu_3Sn	0.56	0.128	0.145	-0.86	-1,2
Cu_6Sn_5	0.5	0.128	0.145	-1.17	-1.3

Table 4.31: Result of the Bessel functions for Cu and Sn in Cu_3Sn and Cu_6Sn_5.

The Z** values depend on the average lifetime of the moving electrons (τ). Furthermore the TCRs of the IMCs were not taken into account. The result is a nonlinear temperature dependence of Z**.
In the following most of the material parameters in (4.18) will be summarized in Z*. The nonlinear part of (4.19) is related the to influence of the electron's lifetime, also being the main part of the TCR. The linear part (α) of (4.19) is related to the temperature dependence of the relative defect density ($1-N\rho_D/N_D\rho$). Due to the negative results of the Bessel functions the nonlinear part of (4.19) is negative too.

$$Z^{**}_{(T)} = Z^* \cdot [1 + \alpha \cdot (T - 300K)] - Z^{*2} \cdot [1 + TCR \cdot (T - 300K)]^2 \qquad (4.19)$$

By curve fitting the data points of Z** (Fig. 4.14) the TCR, α and Z* can be approximated through the linear terms (A, B, C) of the trend line (4.20).

$$Z^{**}_{(T)} = -C\Delta T^2 + B\Delta T + A \qquad (4.20)$$

The term A, includes Z* (4.21). The terms C and B include the TCR (4.22) and α (4.23).

$$Z^*_{(1,2)} = 0.5 \pm \sqrt{(0.25)^2 - A} \quad (4.21) \qquad TCR = \sqrt{-C/Z^{*2}} \quad (4.22)$$

$$\alpha = \frac{B + 2 \cdot Z^{*2} \cdot TCR}{Z^*} \qquad (4.23)$$

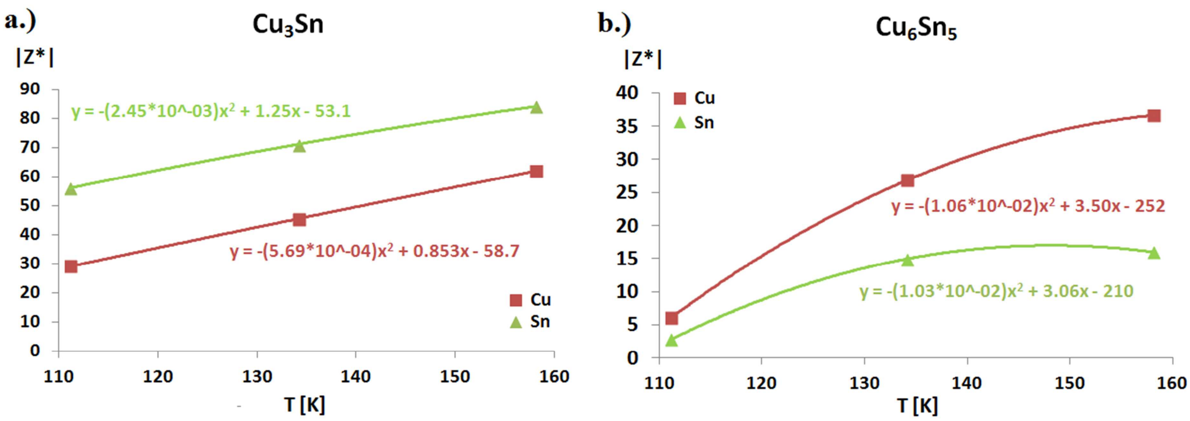

Figure 4.14: Trend lines on the temperature dependent Z values of Cu and Sn in Cu_3Sn (a) and Cu_6Sn_5 (b)**

Compared to Cu_6Sn_5 the higher density of grain boundaries in Cu_3Sn leads to a higher defect density and increased Z** values. The Z* values do not include the environmental influences anymore. As a consequence the results for Cu_6Sn_5 and Cu_3Sn become more similar (table 4.32). The calculated TCRs are not very accurate, because an EM test is not a very effective way to determine basic material parameters. In the case of Cu_6Sn_5 the literature TCR ($3.5\text{x}10^{-3}$) and the measured TCRs differ by 23%. For Cu_3Sn no comparison with literature values was possible.

IMC	Element	A	B	C	α [K^{-1}]	TCR [K^{-1}]	Z*
Cu_3Sn	**Cu**	-58.7	0.85	$-5.7\text{x}10^{-4}$	0.06	**$2.91\text{x}10^{-3}$**	**8.2**
	Sn	-53.1	1.25	$-2.45\text{x}10^{-3}$	0.13	**$1.90\text{x}10^{-3}$**	**7.8**
Cu_6Sn_5	**Cu**	-252	3.5	$-1.06\text{x}10^{-2}$	0.13	**$2.62\text{x}10^{-3}$**	**16.4**
	Sn	-210	3.1	$-1.03\text{x}10^{-2}$	0.12	**$2.83\text{x}10^{-3}$**	**15**

Table 4.32: The TCR and Z* of Cu and Sn in Cu_3Sn and Cu_6Sn_5.

Unlike Z** values, Q** values are exponentially temperature dependent. The reason is the temperature dependent maximum concentration (N_{max}) of the single components in Cu_6Sn_5 and Cu_3Sn (4.24).

$$\vec{J}_{TM} = -D_0 \cdot \frac{N \cdot (Q^* + H_S)}{k_B T^2} \cdot grad(T) \cdot exp\left(-\frac{E_A + H_S}{k_B T}\right) \qquad (4.24)$$

By curve fitting the resulting Q** values from the AC and the DC tests, the heat of solution (H_S), and the temperature independent Q* can be extracted (Fig. 4.15).

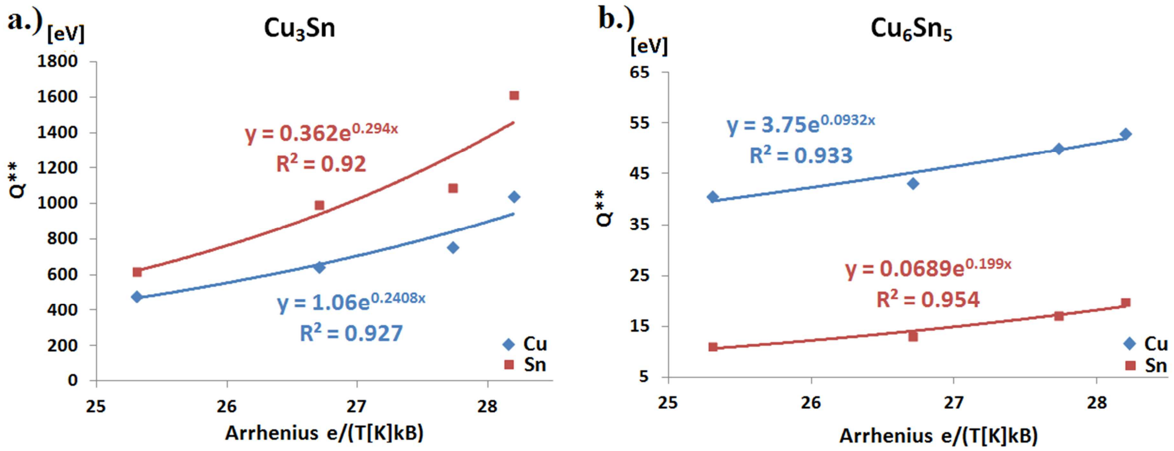

Figure 4.15: Trend lines of the Q values of Cu and Sn in Cu_3Sn (a) and Cu_6Sn_5 (b)**

Taking into account the temperature dependent solubility of single components in the binary IMCs, the resulting Q* values for Cu and Sn are closer to the expected range, being defined by the physical model of thermomigration (table 4.33). Furthermore the results for Cu_3Sn and Cu_6Sn_5 do not differ by two orders anymore. Compared to the Q* values of Cu, the Q* values of Sn in both IMCs are relatively small.

IMC	**Element**	**$E_{A,Dif}$ [eV]**	**H [eV]**	**$E_{A,TM} = (E_A + H_S)$ [eV]**	**Q* + H_S [eV]**	**Q* [eV]**
Cu_3Sn	**Cu**	0.81	-0.24	0.57	1.1	**1.34**
	Sn	0.81	-0.29	0.52	0.36	**0.65**
Cu_6Sn_5	**Cu**	0.58	-0.09	0.49	-3.75	**-3.7**
	Sn	0.56	-0.2	0.36	-0.07	**0.13**

Table 4.33: The H_S and the Q* values of Cu and Sn in Cu_3Sn and Cu_6Sn_5.

4.3.3 Top Bumps “Closed System”

As for the open system, the results of the DC stress tests of the closed system were extracted by comparing the DC and the TS test results. Afterwards the Q** and Z** values were calculated through the related mass flux values of TM and EM. Finally a physical interpretation of the material values is needed.

4.3.3.1 Parameter extraction

The presence of a non-alternating current flow leads to the formation of Ni_3Sn_4 in the SnAgCu solder joints. Furthermore a $(CuNi)_6Sn_5$ layer is formed. The resulting IMC layer dimensions at the die and the board side contact surfaces are given in the tables 4.34-35. The influence of the current flow on the two different IMC layers is different. As in [4.8], and in contrast with [4.9], the direction of the current flow had no significant influence on the Ni_3Sn_4 formation speed. Following the interpretation of [4.8] a possible reason for the missing influence of the current direction is an equal exchange of Ni and Sn at the Ni_3Sn_4 to Ni interface.

	$(CuNi)_6Sn_5$ [µm]		**Ni_3Sn_4 [µm]**	
	Down	**Up**	**Down**	**Up**
138°C/1A	3.85±0.44	3.98±0.8	1.14±0.36	1.33±0.37
161°C/1A	3.84±1.25	6.47±0.9	2.94±0.58	2.64±0.48
185°C/1A	3.86±1.17	6.08±0.65	3.02±0.18	3.5±1.1

Table 4.34: IMC dimensions and the SD at the die side contacts after the EM stress tests.

	$(CuNi)_6Sn_5$ [µm]		**Ni_3Sn_4 [µm]**	
	Down	**Up**	**Down**	**Up**
138°C/1A	3.39±0.87	3.9±0.8	1.26±0.5	1.74±0.9
161°C/1A	5.0±0.53	3.29±0.73	3.93±0.92	3.83±1.0
185°C/1A	5.28±0.74	3.57±0.89	5.17±0.71	5.0±0.46

Table 4.35: IMC dimensions and the SD at the board side contacts after the EM stress tests.

The direction of the current flow has a clear influence on the $(CuNi)_6Sn_5$ growth speed. The main reason is the NiAu diffusion barrier: e.g. for the downstream case Cu is moving, via interstitial diffusion, from the die side contact surfaces to the board side ones. The missing Cu from the die side accumulates at the board side and cannot be replaced by Cu from the metal lines. In the upstream case the same effect appears in an opposite direction. In combination with current crowding the disappearance of Cu did not only reduce the $(CuNi)_6Sn_5$ formation speed, it led to a complete dissolution of the $(CuNi)_6Sn_5$ layer (Fig. 4.16). This also led to a relatively high SD of the $(CuNi)_6Sn_5$ dimensions for the downstream case on the die side, or for the upstream case at the board side.

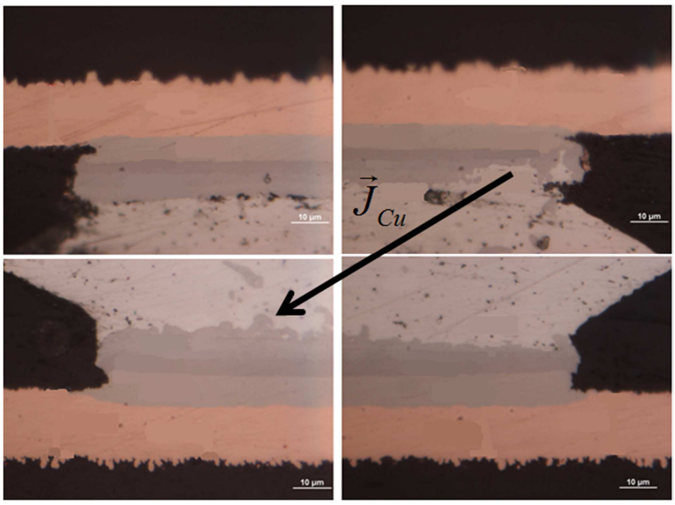

Figure 4.16: IMCs at the contact surfaces of a top bump after 144h DC stress at 185°C [4.10]

As the AC test the DC tests also changed the composition of $(CuNi)_6Sn_5$ (table 4.36). In addition the composition of Ni_3Sn_4 had to be investigated (table 4.37). Compared to the TS or the AC tests the amount of Ni in $(CuNi)_6Sn_5$ was increased. The mass fractions of Au and Cu are nearly the same.

		Cu	Sn	Ni	Au
$(CuNi)_6Sn_5$	**Mass [%]**	19 ± 1.3	60 ± 2.0	12.5 ± 0.8	7.5 ± 0.7
	ρ_{IMC} [g/cm³]	8.2			
	N [1/m³]	1.4×10^{28}	2.5×10^{28}	1.1×10^{28}	2.1×10^{27}

Table 4.36: Material composition of $(CuNi)_6Sn_5$ after the EM stress tests.

		Cu	Sn	Ni	Au
Ni_3Sn_4	**Mass [%]**	5 ± 0.8	73 ± 1.0	22 ± 1.4	0
	ρ_{IMC} [g/cm³]	7.7			
	N [1/m³]	3.6×10^{27}	2.8×10^{28}	1.7×10^{28}	0

Table 4.37: Material composition of Ni_3Sn_4 after the EM stress tests.

The EM induced mass flux leads to an increasing amount of Ni in $(CuNi)_6Sn_5$. If an atomic concentration of 25% is reached, the $(CuNi)_6Sn_5$ in transformed into Ni_3Sn_4 (Fig. 4.17). During this process the Au vanishes and the Cu content is reduced to a few mass percent.

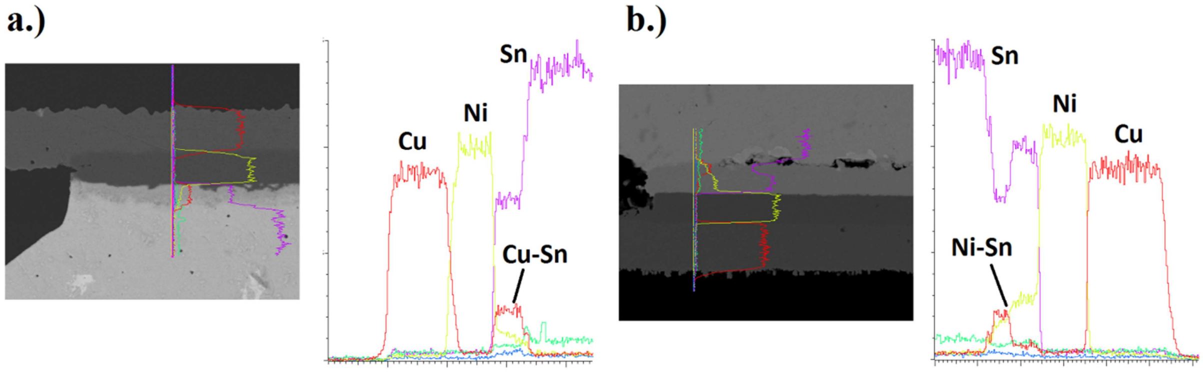

Figure 4.17: Material composition of the die side contact surface of a TS top bump (a) and the board side of a EM stressed top bump (b) [4.20]

As for the bottom bumps the difference in the IMC layer dimensions for the up- and the downstream cases can be used to extract the TM and EM induced mass flux values (4.14-16). In the cases of Cu and Au the mass fluxes will be mainly related to the $(CuNi)_6Sn_5$ layer, because the portion of both elements in Ni_3Sn_4 is negligible. The Ni values will be related to both IMCs, because Ni has a continuous diffusion profile through both IMC layers (Fig 4.17). The resulting mass fluxes of Cu, Ni and Au at the die and the board side contacts are given in tables 4.38-40. As for the bottom bumps the TM induced mass flux values are relatively high compared to the EM induced mass flux.

-Cu- Die	**J_{Down} [1/µm²s]**	**J_{Up} [1/µm²s]**	**$J_{EM,Cu}$ [1/µm²s]**	**$J_{Dif,TS}$ [1/µm²s]**	**AFT**	**TL [h]**	**AF**	**AF***	**$J_{Dif,DC-EM}$ [1/µm²s]**	**$J_{TM,Cu}$ [1/µm²s]**
138°C	3.5x10^3	6.4x10^3	**0.9x10^3**	2.3x10^3	11	323	5.9	6.1	14x10^3	**-8.8x10^3**
161°C	0.9x10^5	1.2x10^5	**16x10^3**	10x10^3	10	95	9.0	12	1.2x10^5	**-14x10^3**
185°C	1.0x10^5	1.6x10^5	**29x10^3**	42x10^3	9.7	30	6.5	6.6	2.8x10^5	**-1.5x10^5**
Board										
138°C	5.3x10^3	3.2x10^3	**0.5x10^3**	1.8x10^3	11	329	6.5	6.7	12x10^3	**-7.1x10^3**
161°C	93x10^3	60x10^3	**17x10^3**	8.6x10^3	11	93	9.5	13	1.1x10^5	**-35x10^3**
185°C	1.5x10^5	95x10^3	**24x10^3**	29x10^3	10	29	6.8	6.9	2.0x10^5	**-85x10^3**

Table 4.38: Total mass flux of the up- and downstream cases, the mass flux due to EM, the diffusion induced mass flux, the AFs and the TM induced mass flux. All values for Cu in $(CuNi)_6Sn_5$.

-Ni- Die	**J_{Down} [1/µm²s]**	**J_{Up} [1/µm²s]**	**$J_{EM, Ni}$ [1/µm²s]**	**$J_{Dif,TS}$ [1/µm²s]**	**AFT**	**TL [h]**	**AF**	**AF***	**$J_{Dif,DC-EM}$ [1/µm²s]**	**$J_{TM, Ni}$ [1/µm²s]**
138°C	5.3x10^3	7.1x10^3	**0.9x10^3**	0.8x10^3	13	342	7.0	7.2	5.7x10^3	**0.5x10^3**
161°C	1.2x10^5	1.3x10^5	**3.3x10^3**	3.9x10^3	12	91	10	13	51x10^3	**78x10^3**
185°C	1.7x10^5	2.0x10^5	**14x10^3**	13x10^3	11	27	7.1	7.2	94x10^3	**94x10^3**
Board										
138°C	6.6x10^3	3.9x10^3	**0.9x10^3**	0.4x10^3	10	323	5.6	6.6	2.7x10^3	**3.3x10^3**
161°C	1.5x10^5	1.3x10^5	**11x10^3**	1.1x10^3	9.7	95	8.5	9.2	10x10^3	**1.2x10^5**
185°C	2.5x10^5	2.2x10^5	**18x10^3**	6.6x10^3	9.4	31	6.2	6.3	42x10^3	**1.9x10^5**

Table 4.39: Total mass flux of the up- and downstream case, the mass flux due to EM, the diffusion induced mass flux, the AFs and the TM induced mass flux. All values for Ni in $(CuNi)_6Sn_5$.

-Au- Die	**J_{Down} [1/µm²s]**	**J_{Up} [1/µm²s]**	**$J_{EM,Au}$ [1/µm²s]**	**$J_{Dif,TS}$ [1/µm²s]**	**AFT**	**TL [h]**	**AF**	**AF***	**$J_{Dif,DC-EM}$ [1/µm²s]**	**$J_{TM,Au}$ [1/µm²s]**
138°C	1.1x10^3	0.9x10^3	**0.1x10^3**	0.2x10^3	10	317	3.6	3.7	0.9x10^3	**0.1x10^3**
161°C	13x10^3	18x10^3	**2.3x10^3**	0.7x10^3	9.3	97	7.7	11	7.7x10^3	**8.1x10^3**
185°C	16x10^3	26x10^3	**3.8x10^3**	1.8x10^3	9.1	31	5.2	5.3	9.5x10^3	**12x10^3**
Board										
138°C	0.9x10^3	0.7x10^3	**0.1x10^3**	0.1x10^3	10	323	3.7	3.9	0.6x10^3	**0.2x10^3**
161°C	14x10^3	10x10^3	**1.9x10^3**	0.4x10^3	9.5	96	6.4	9.5	3.2x10^3	**7.4x10^3**
185°C	20x10^3	13x10^3	**3.3x10^3**	1.4x10^3	9.3	31	5.3	5.4	7.6x10^3	**8.9x10^3**

Table 4.40: Total mass flux of the up- and downstream case, the mass flux due to EM, the diffusion induced mass flux, the AFs and the TM induced mass flux. All values for Au in $(CuNi)_6Sn_5$.

The extraction of the TM and EM induced mass flux values enabled the calculation of the Q** and Z** values for Cu, Ni and Au in $(CuNi)_6Sn_5$ (4.12), (4.17). The Z** and Q**values of Cu and Ni were too high to be compatible with the physical model of the related migration phenomena (table 4.41-4.42). Unlike Z** values of Cu and Ni the values of Au are relatively low. The experimental results indicate that the Ni and Au ions move from hot to cold crystal sites, while Cu ions move from cold to hot sites. All values are temperature dependent. Hence a further discussion of the values and their physical background is necessary.

Die Side	**Cu**		**Ni**		**Au**	
T_{test} [°C]	**Z****	**Q**[eV]**	**Z****	**Q**[eV]**	**Z****	**Q**[eV]**
138	63	-1577	96	253	0.3	2.5
145	-	-1479	-	430	-	3.8
161	193	-856	79	389	1.5	24
185	171	-2559	71	227	1.6	10

Table 4.41: Z and Q** values of Cu, Ni and Au in $(CuNi)_6Sn_5$, die side contact surface.**

Board Side	**Cu**		**Ni**		**Au**	
T_{test} [°C]	**Z****	**Q**[eV]**	**Z****	**Q**[eV]**	**Z****	**Q**[eV]**
138	68	-2538	279	740	0.5	8.6
145	-	-519	-	300	-	3.4
161	312	-3706	603	109	1.2	55
185	256	-2765	446	84	1.2	21

Table 4.42: Z and Q** values of Cu, Ni and Au in $(CuNi)_6Sn_5$, board side contact surface.**

4.3.3.2 Discussion

The Q** and Z** values in the tables 4.41-42 are temperature dependent and do not fit to the physical background of the related EM and TM phenomena. The equations being used for extraction of Q** and Z** were derived for pure fcc metals. Hence for the interpretation of migration phenomena in an IMC layer with three components an adaptation of the equation used will be needed.

An important fact is an exponential temperature dependence of Z**. The Z** values of Ni and Cu decrease with increasing test temperatures, while the Au values are growing. This behavior indicates a difference in the E_A values between the TS tests, as the source of E_A, and the DC tests. Taking into account the shift "ΔE" (4.25), reasonable Z* values for all three materials are available (table 4.43).

$$D = D_0 \cdot exp\left(-\frac{(E_A - \Delta E)}{k_B T}\right) \quad (4.25)$$

A possible reason for the shift of E_A during the DC tests is the formation of a Ni_3Sn_4 layer. It leads to a new Ni to Ni_3Sn_4 interface that could influence the Ni migration. Another possible reason for the E_A shift is the influence of the current flow on the crystal structure of the SnAgCu bumps (current driven annealing) [4.21]. A changing crystal structure would explain the influence of the DC tests on Cu and Au migration and the E_A shift during the AC test, without the presence of the Ni_3Sn_4 layer.

As for the binary IMCs Cu_3Sn and Cu_6Sn_5, a temperature dependent solubility of the single components should exist in the three component system $(CuNi)_6Sn_5$ too. In case of Ni the heat of solution (H_S) could be extracted (table 4.43), but for Cu and Au the variance between the Q** values was not regular enough. One reason for the irregular variation of the Cu and Au values is the fact that a material accumulation and not a diffusion process takes place. The driving force β of the accumulation process has its own range of variation and that covers a possible regularity in the Q** values. In addition literature values for the diffusion constants of Cu and Au had to be used. These values were chosen with the assumption of an interstitial transport mechanism of Cu and Au in Sn, but differences between the experimental setup in the literature and the PoP devices could not be taken into account. The consequences are relatively large Q* values for Cu and Au in $(CuNi)_6Sn_5$.

	E_A [eV]	**ΔE [eV]**	**$E_{A\text{-}EM}$ [eV]**	**Z***	**H_S [eV]**	**$E_{A\text{-}TM}$ [eV]**	**Q* [eV]**
Cu	0.825-0.85	0.11-0.14	0.71-0.72	**7.0-11**	-	0.71-0.72	**(-54)-(-96)**
Ni	0.81-0.88	0.11-0.21	0.6-0.77	**2.0-3.6**	(-0.25)-(-0.27)	0.56-0.61	**0.35-0.52**
Au	0.80-0.81	-0.03	0.84	**3.6-3.7**	-	0.84	**22-26**

Table 4.43: EM and TM related material parameters for Cu, Au, and Ni in $(CuNi)_6Sn_5$ and Ni_3Sn_3.

4.4 Conclusion

The IMC formation in SnAgCu solder joints during TS, AC and DC tests was investigated. The tests were performed on direct solder to Cu contacts (“open system”) and on solder joints with NiAu pads (“closed system”). In the open system Cu could flow from the metal lines into the solder joints. As a consequence in all solder joints, including the non-stressed ones, Cu_3Sn and Cu_6Sn_5 IMC layers could be found. In the closed system Cu and Au were accumulated at the contact surfaces and Ni was diffusing into the solder joint. As a consequence the formation of a three component $(CuNi)_6Sn_5$ IMC layer took place.

TS tests lead to an ongoing IMC formation. While the composition of Cu_3Sn and Cu_6Sn_5 stayed the same the material composition of $(CuNi)_6Sn_5$ changed. During the TS tests the Cu and the Au portion in $(CuNi)_6Sn_5$ increased, while the relative Ni content decreased. In contrast with the TS tests on SnAg bumps, the TS of SnAgCu bumps did not lead to a Ni_3Sn_4 formation at the interfaces between the Ni pads and the solder joints.

The IMC formation in the closed and open systems can be described by the Deal-Grove model, because single components like Cu or Ni have to move through the IMC layers before new IMC material can be formed. The consequence is a reduced IMC formation speed during long term TS tests. The time limits for the appearance of a relevant saturation effect were 336h for the open, and 168h for the closed system.

Based on this knowledge, short term TS tests at different temperatures were performed and the activation energies (E_A) and diffusion constants (D_0) for the motion of Cu and Sn in Cu_3Sn and Cu_6Sn_5 and the diffusion of Ni in $(CuNi)_6Sn_5$ were extracted. In the case of the Cu and Au accumulation in $(CuNi)_6Sn_5$ the E_A and the driving force for the accumulation process (β) were extracted. For D_0, literature values were used.

In the following, the SnAgCu bumps were AC and DC stressed. The TS and the current driven stress tests were performed on the same test cards. A comparison between the TS and AC test results enabled the identification of possible effects of the AC on the IMC formation. During the AC test Joule heating was observed. Against this background simulations were performed to calculate the test temperature and the temperature gradients in the IMC layers. The investigation of the closed and the open system has shown an accelerated IMC growth due to TM. The heat of transport (Q*) of Cu and Sn in Cu_3Sn and Cu_6Sn_5, and the Q* of Cu, Ni and Au in $(CuNi)_6Sn_5$ could be extracted. The AC stress did not lead to a Ni_3Sn_4 formation at the Ni contact pads of the top bumps.

The last steps of the experimental procedure were three DC tests. DC leads to an effective mass flux due to EM, and to Joule heating. As a consequence of Joule heating, temperature gradients appeared as a driving force of TM. That means, during the DC tests all relevant forms of migration appeared. In the closed and in the open system diffusion, EM and TM lead to an increased IMC formation speed.

In addition a Ni_3Sn_4 layer was formed at the Ni contact pads of the top bumps.

The presence of EM leads to different IMC formation speeds during the upstream and the downstream tests. Based on the resulting IMC growth speeds the TM and the EM induced mass flux values of the open and closed systems could be extracted. Through the mass flux values the effective charge (Z*) and Q* of Cu and Sn in Cu_3Sn and Cu_6Sn_5 could be extracted, and Z* and Q* of Cu, Ni and Au in $(CuNi)_6Sn_5$ and Ni_3Sn_4.

A good compliance between the Q* values of the AC tests and DC tests was found. The knowledge of Z* and Q* values at different test temperature enabled the interpretation of the EM and TM driven migration in the IMCs. In the case of the EM and TM induced material transport in Cu_3Sn and Cu_6Sn_5 a strong influence of crystal defects was found. The TM was also influenced by the temperature dependent solubility of the single components. Taking into account these special conditions in the IMC layers, temperature independent Q* and Z*, being compatible to existing physical models, could be extracted.

In the closed system the presence of the Ni_3Sn_4 changed the E_A for the Ni diffusion. Due to annealing the current flow changed the crystal structure of the solder. The accumulation of Cu and Au is influenced by the crystal structure of the SnAgCu solder. Hence the E_A of the Cu and Au accumulation was changed too. By considering the resulting shift of the E_A, it was possible to extract promising Z* values for the EM driven motion of Ni, Cu and Au in Ni_3Sn_4 and $(CuNi)_6Sn_5$.

For the extraction of Q* through the TM driven motion of Ni the temperature dependency of its solubility in the IMCs was taken into account. For Cu and Au no conclusion like that was found. One reason for the missing regularity of the Q** values of Cu and Au, is the temperature dependency of the accumulation process and the resulting variation of the related driving force β. Furthermore the use of literature D_0 values for the given test devices does not have to lead to correct results for the following migration parameters. Finally a complete characterization of the TM driven migration process in the closed system was only possible for Ni.

Based on the material parameters a general description of the migration driven IMC growth in SnAgCu solder joints under consideration of TM and EM is possible. Against this background the available material parameters will be used to simulate the migration driven IMC formation in solder joints.

5 Simulation of the Material Transport in IMCs

Based on experimental results, migration related material parameters were extracted. In this chapter the available parameters will be used to calculate the mass flux values of Cu, Sn, Au and Ni in the IMC layers of the top and the bottom bumps. For the calculations user developed routines will be used. First the resulting mass flux values will be compared with experimental results to validate the used material parameters. Afterwards the simulation results will enable a further interpretation of IMC formation during the stress tests.

The extraction of the general material parameters led to the loss of all local information. FEA enables the reconstruction of geometrical effects on the IMC formation. Especially the influence of current crowding during the DC tests has to be clarified, because the resulting IMC profiles did not always fit the expected results.

5.1 Bottom Bumps "Open System"

During the TS tests different migration phenomena appeared in the open and closed systems. Hence two different simulation procedures will be needed for the investigation of the migration induced IMC growth. Following the diffusion, the EM and the TM induced mass flux of Cu in the open system will be simulated. Afterward a dynamic simulation of the IMC growth will be performed.

5.1.1 Simulation of the Diffusion Induced Mass Flux

The mass flux due to diffusion is a relevant driving force of the IMC formation. Diffusion appeared during all stress tests (TS, DC and AC). Hence eight data points for the verification of the diffusion related material parameter are available. The material values being used for the simulation are given in table 5.1.

	E_A[eV]	N [1/m³]	grad(N) [1/m⁴]	D_0 [m²/s]
Cu_3Sn	0.808	3.9×10^{28}	1.7×10^{33}	1.3×10^{-8}
Cu_6Sn_5	0.58	2.6×10^{28}	2.1×10^{32}	2.9×10^{-9}

Table 5.1: Material parameters for the calculation of the Cu mass flux in Cu_3Sn and Cu_6Sn_5.

The equation of the diffusion induced mass flux (5.1) was implemented with the "ANSYS Parametric Design Language" (APDL). The diffusion induced mass flux values in all finite elements were calculated separately. The required temperature values became available by the thermal electrical (TE) simulations. The mean concentration gradient over time (5.2) was used as the thermoelectric driving force. Hence the influence of diffusion on the IMC formation is only correct when the total test time was observed. For a shorter duration its influence on the resulting IMC dimensions would be too weak, and for a longer duration it would be too strong.

$$\vec{J} = -D_0 \cdot grad(N) \cdot exp\left(-\frac{E_A}{k_B T}\right) \quad (5.1)$$

$$|grad(N)| \approx \frac{\Delta N}{(h + h_0)/2} \quad (5.2)$$

The Cu mass flux values from the experimental results and the simulation result for Cu_3Sn are given in table 5.2.

	100°C	120°C	138°C	140°C	145°C	150°C	161°C	185°C
Exp.	0.41x10^{3}	1.26x10^{3}	3.4x10^{3}	2.42x10^{3}	2.8x10^{3}	11x10^{3}	16x10^{3}	19 x10^{3}
Sim.	0.36x10^{3}	1.28x10^{3}	3.9x10^{3}	3.0x10^{3}	6.15x10^{3}	6.9 x10^{3}	13x10^{3}	40 x10^{3}

Table 5.2: Experimental and simulation results for the diffusion induced mass of Cu in Cu_3Sn.

In the main the simulation results fit to the experimental results (Fig. 5.1, right). Differences between the simulation and the test results were found for 140°C, 150°C and 185°C. The reason for this differences is the fact, that the E_A used is based on the trend line of the diffusion induced mass flux values during the TS at 100°C, 120°C ,140°C and 150°C (Fig. 5.2, left). While the values for 100°C and 120°C were close to the trend line, the mass flux value at 140°C was below, and the value at 150°C was above the trend line. The mass flux values at 185°C were extrapolated from the test results at 140°C.

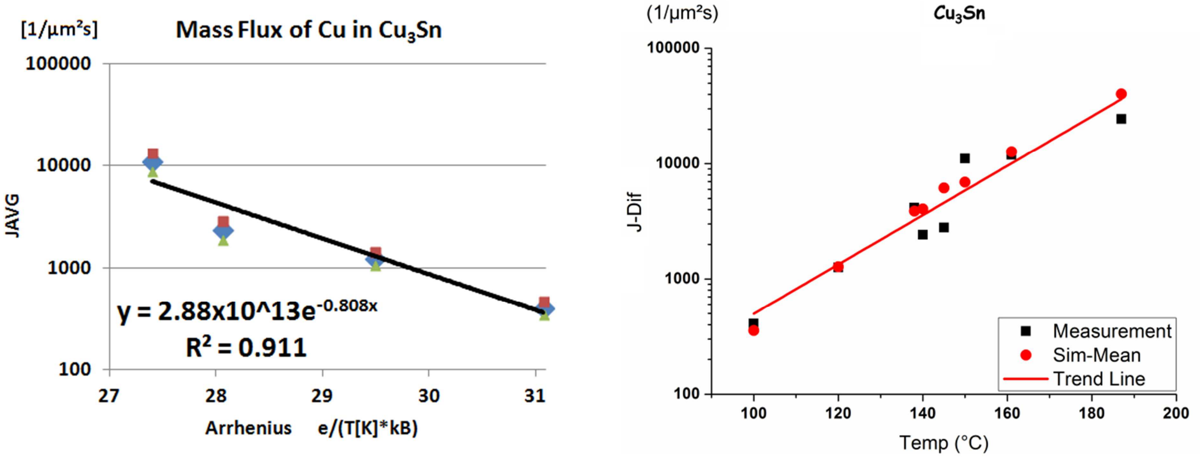

Figure 5.1: Interpolation of E_A from experimental results (left), mass flux values being calculated with E_A (right)

The experimental and the calculated Cu mass flux values for Cu_6Sn_5 are given in table 5.3. The simulation does not take into account saturation effects. As a result the estimated mass flux at 138°C was too high (Fig. 5.2, right). Like for Cu_3Sn, a difference between the simulation and the test results appeared for 140°C and 150°C. This is due to the mismatch between the trend line of the diffusion induced mass flux and the test results for 140°C and 150°C (Fig. 5.2, left).

	100°C	120°C	138°C	140°C	145°C	150°C	161°C	185°C
Exp.	10x10^{3}	31 x10^{3}	22 x10^{3}	1.0 x10^{5}	30x10^{3}	57x10^{3}	2.5x10^{5}	3.0x10^{5}
Sim.	12x10^{3}	29x10^{3}	64x10^{3}	66x10^{3}	81x10^{3}	97x10^{3}	1.5x10^{5}	3.7x10^{5}

Table 5.3: Experimental results for the diffusion induced mass of Cu in Cu_6Sn_5 and the related simulation results.

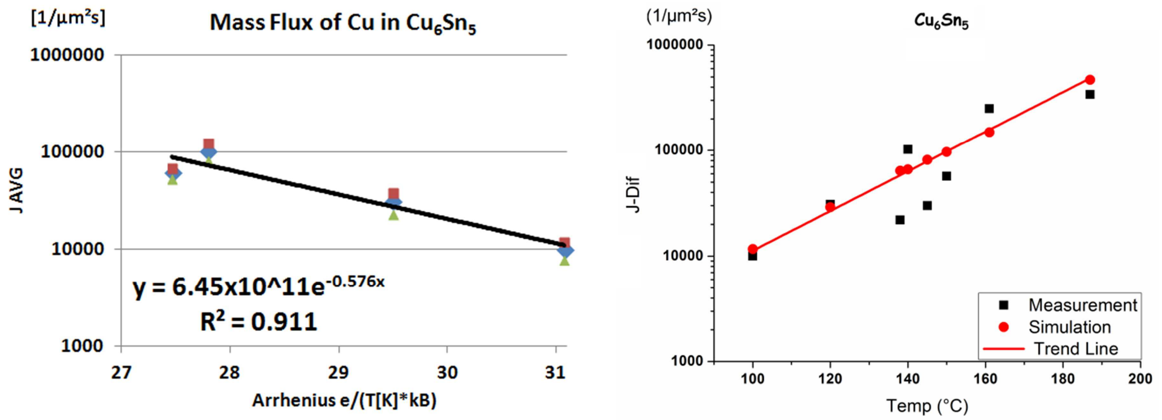

Figure 5.2: Interpolation of E_A from experimental results (left), mass flux values being calculated with E_A (right).

5.1.2 Simulation of the Electro- and Thermomigration Induced Mass Flux

The calculations of the TM and EM induced mass flux values were performed with a user developed routine [5.1]. The values in table 5.1 were also used as D_0 and E_A for the EM (5.3). The heat of solution (H_S) was also required for the calculation of the TM (5.4).

$$\vec{J}_{EM} = D_0 \cdot \frac{NeZ^{**}\vec{j}\rho_{el}}{k_B T} \cdot exp\left(-\frac{E_A}{k_B T}\right) \qquad (5.3)$$

$$\vec{J}_{TM} = -D_0 \cdot \frac{N \cdot (Q^* + H_S)}{k_B T^2} \cdot grad(T) \cdot exp\left(-\frac{E_A + H_S}{k_B T}\right) \qquad (5.4)$$

In addition the Z* and the Q* of Cu in Cu_3Sn and Cu_6Sn_5 are needed. Due to electron scattering at crystal defects in the IMC layers Z* is temperature dependent. An additional user routine [5.2] was used to calculate Z* (5.5) forthe test temperature, being a result of the previous TE simulations. The used temperature coefficients, Z* and Q* values are given in table 5.4.

$$Z^{**}_{(T)} = Z^* \cdot [1 + \alpha \cdot (T - 300K)] - Z^{*2} \cdot [1 + TCR \cdot (T - 300K)]^2 \qquad (5.5)$$

	α [1/K]	**TCR [1/K]**	**Z***	**$E_{A,TM}$ [eV]**	**Q* [eV]**
Cu_3Sn	0.06	2.91×10^{-3}	8.2	0.57	-0.86
Cu_6Sn_5	0.13	2.62×10^{-3}	16.4	0.49	3.8

Table 5.4: Temperature coefficients of Z, the effective charge Z*, the E_A for TM and the Q* of Cu.**

The current driven migration phenomena are clearly affected by current crowding (Fig. 5.3), but for the extraction of material parameters from the experimental results, averaged values were used. Hence information about the influence of current crowding on the IMC formation was lost. A three dimensional FEA allows the reconstruction of the current crowding effect by combining the general migration parameters (Z*, Q*) with the influence of the solder joint geometry on the driving forces of the EM and TM.

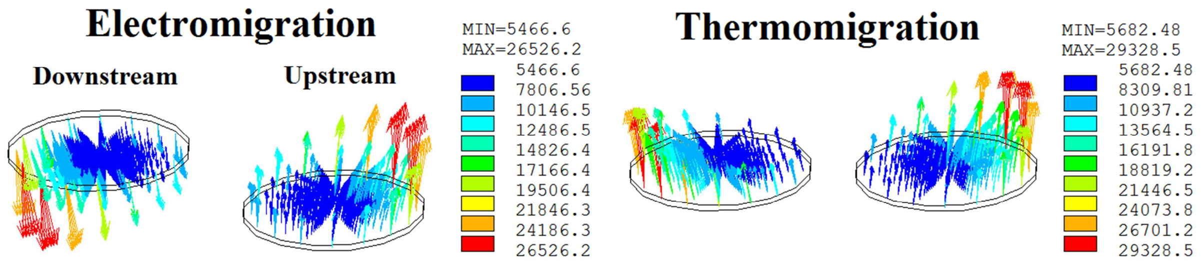

Figure 5.3: EM and TM induced mass flux of Cu in Cu_6Sn_5 at 138°C/1A [1/µm²s]

For a verification of the simulation results their mean values (5.6) have to be compared with the test results.

$$X_{mean} = \frac{1}{A_{Sum}} \cdot \sum_{n=1}^{N} X_n \cdot A_n \quad (5.6)$$

A_{Sum}= contact surface, N= number of finite elements, A_n= partial contact surface of a finite element, X_n= optional simulations results

In Figs. 5.4-5 the maximum and minimum simulation results for the EM and TM induced mass fluxes in Cu_3Sn and Cu_6Sn_5 are shown. Furthermore the mean values of the simulation results were compared with the test results.

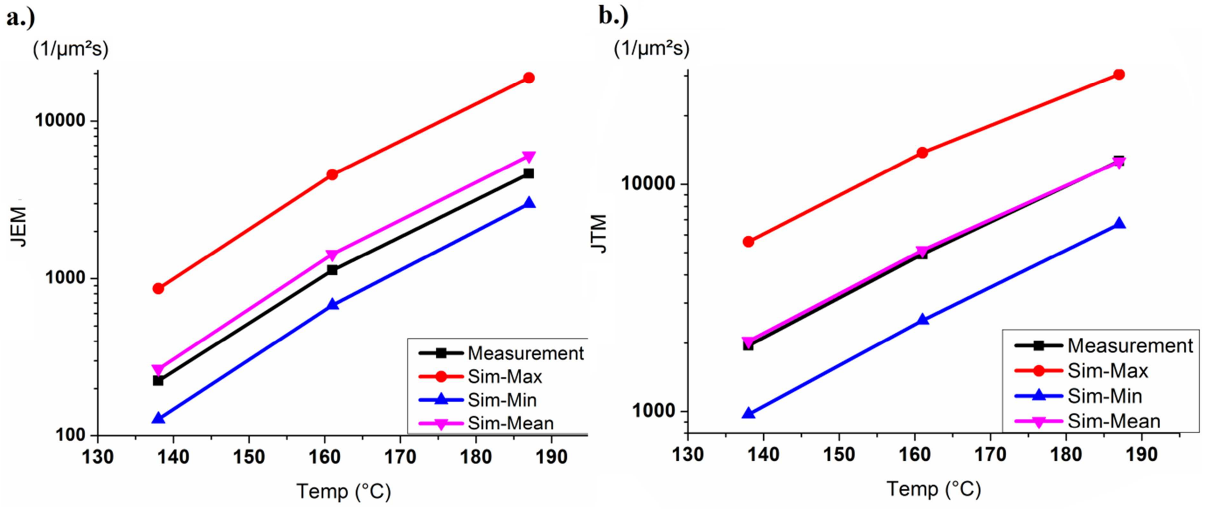

Figure 5.4: Comparison of the simulated and the measured EM (a) and TM (b) induced Cu fluxes in Cu_3Sn

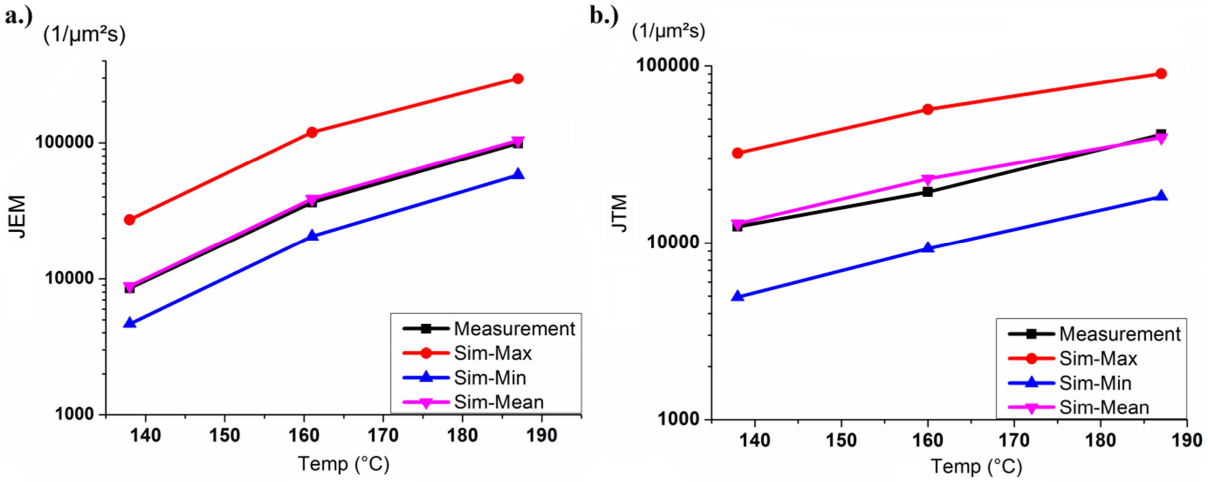

Figure 5.5: Comparison of the simulated and the measured EM (a) and TM (b) induced Cu fluxes in Cu_6Sn_5

The mean values of the simulation results are in good compliance with the test results. Hence the simulation programs are able to reconstruct the mass flux in the IMCs during the TS, the AC and the DC tests. Furthermore they are able to calculate local mass flux values under conditions of current crowding.

Based on these results it can be assumed that the simulation algorithm is sufficient to calculate the total mass flux in Cu_3Sn and Cu_6Sn_5. With the total mass flux it is possible to calculate the migration induced IMC growth under consideration of the chosen boundary condition (test temperature, Joule heating, current density) and current crowding. Against this background FEA can be used for a further interpretation of the IMC formation during the stress tests.

5.1.3 Visualization of the IMC growth

Regarding to bottom bumps, the analysis of the DC test results has shown that the current crowding effect was more relevant for the upstream case than for the downstream (Fig. 5.6).

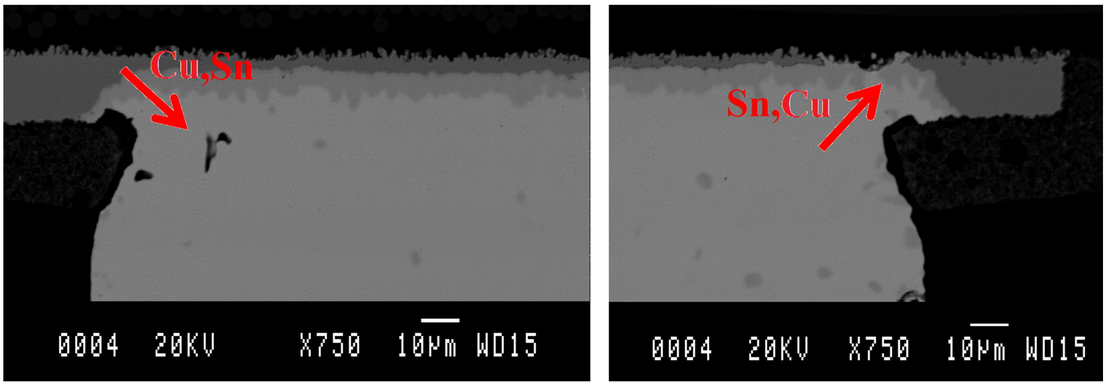

Figure 5.6: The effect of current crowding on the IMC formation in the bottom bumps for the up- (right) and the downstream cases (left). The bump was stressed at 161°C/1A for 192h, the red arrows show the principle direction of the mass flux in the IMCs

In Fig 5.7 the calculated mass flux values in Cu_6Sn_5 at 138°C are shown by cross sections of the FE model. The left column in Fig 5.7 shows the downstream case. In this case the TM induced mass flux in Cu_6Sn_5 compensates the EM induced mass flux. Especially the current effect increases the mass flux due TM as well as the mass flux due to EM. As a consequence their compensation is present on the whole contact surface, including the corners of the solder joint.

For the upstream case the TM induced mass flux amplifies the current crowding effect and as shown in Fig 5.6 a relatively strong influence of current crowding on the IMC formation becomes visible.

Nevertheless in both cases the mass flux due diffusion is as strong as the sum of TM and EM. As a consequence an effective inflow of Cu into the solder joint is present for up- and the downstream case and no dissolution of IMCs can be observed.

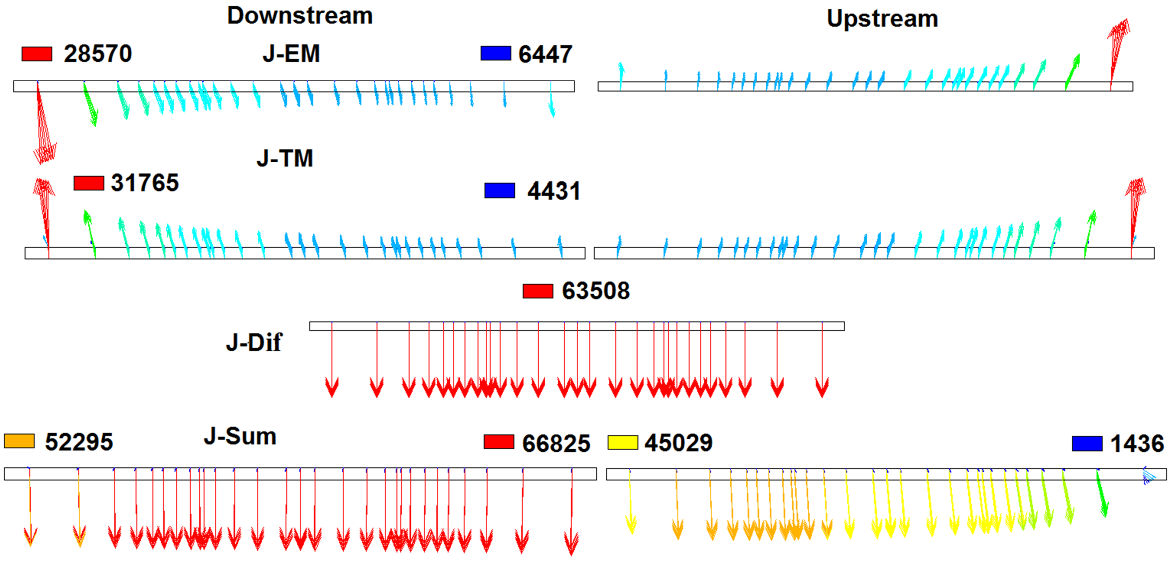

Figure 5.7: The EM (“J-EM”), TM (“J-TM”), and diffusion induced (J-Dif) mass fluxes of Cu in Cu_6Sn_5, the total mass flux (“J-Sum”) of Cu [$1/\mu m^2 s$]

With the total mass flux of Cu it is possible to calculate the momentary growth speed of Cu_3Sn and Cu_6Sn_5 (5.7-8).

$$\vec{v}_{Cu3Sn} = \vec{J}_{Cu,Cu3Sn} \cdot \frac{\left(N_{Cu,Cu} - N_{Cu,Cu6Sn5}\right)}{\left(N_{Cu,Cu} - N_{Cu,Cu3Sn}\right) \cdot \left(N_{Cu,Cu3Sn} - N_{Cu,Cu6Sn5}\right)} \qquad (5.7)$$

$$\vec{v}_{Cu6Sn5} = \vec{J}_{Cu,Cu6Sn5} \cdot \frac{\left(N_{Cu,Cu3Sn} - N_{Cu,SnAgCu}\right)}{\left(N_{Cu,Cu3Sn} - N_{Cu,Cu6Sn5}\right) \cdot \left(N_{Cu,Cu6Sn5} - N_{Cu,SnAgCu}\right)} \qquad (5.8)$$

For the dynamic simulation of the IMC formation during the stress tests, the test time was divided into 100 time steps. For every time step the IMC growth speed was calculated and the IMC layer thickness was increased by the product of the momentary IMC growth speed and the duration of the time step (for more details see section 3.5.3).

The IMC dimensions at the starting point and at the end of the test time are shown in Fig. 5.8. As for the experimental results a relatively thick and homogenous IMC layer was formed during the downstream tests, and a relatively thin IMC layer with a clear current crowding profile was formed during the upstream tests.

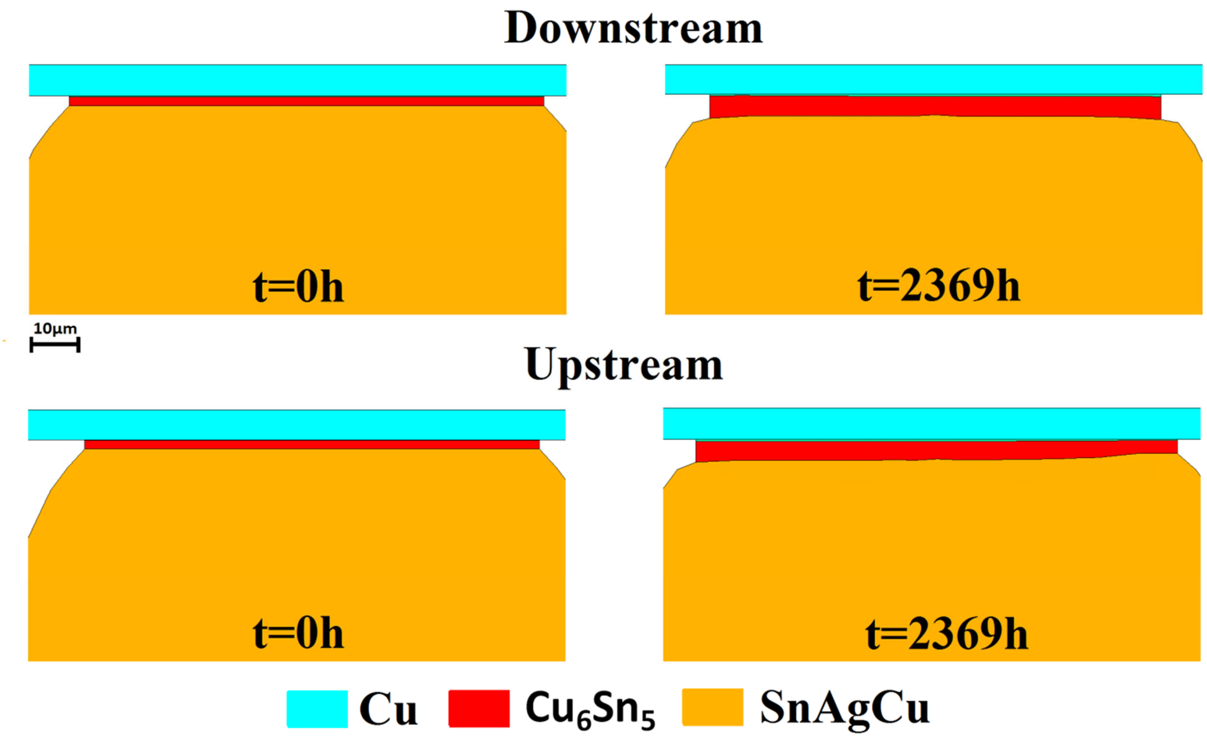

Figure 5.8: Cu_6Sn_5 profile before (left) and after (right) a DC stress test 138°C (2369h)

5.2 Top Bumps “Closed System”

The IMC formation in the top bumps is driven by the diffusion of Ni into the solder joints and the accumulation of Cu and Au at the contact surfaces. For the simulation of the accumulation process a user developed routine was used.

In the following the mass flux values during the TS test will be calculated. Afterwards the mass fluxes due to EM and TM will be calculated. Finally the sum of all mass flux values will be compared with the DC test results.

5.2.1 Simulation of the Mass Flux in a Closed System During Temperature Storage

The diffusion induced mass flux and the material accumulation in the top bumps appeared during all stress tests. Hence the related material parameters can be verified by comparing the simulation results with the experimental results for eight different test temperatures. The parameters used, are given in table 5.5, including the driving force β. The material parameters used are the averaged values of the die side and the board side test results.

	E_A[eV]	N [1/m³]	grad(N) [1/m⁴]	D_0 [m²/s]	β [N]
Cu	0.84	1.4×10^{28}	-	2.4×10^{-7} [5.3]	5.7×10^{-16}
Ni	0.85	7.1×10^{27}	6.9×10^{32}	3.9×10^{-7}	-
Au	0.80	9.6×10^{26}	-	1.6×10^{-5} [5.4]	1.6×10^{-18}

Table 5.5: Material parameters for the calculation of the mass flux in $(CuNi)_6Sn_5$.

The user routine for the calculation of the diffusion induced mass flux and the accumulation process was implemented with APDL. The simulation results and the related test results are given in table 5.6. In general the simulation results were similar to the experimental results. In the case of Cu the calculated mass flux at 140°C was too low. The reason is that the trend line of the mass flux values of Cu, leading to the E_A, was below the experimental data point at 140°C.

Cu	100°C	120°C	138°C	140°C	145°C	150°C	161°C	185°C
Exp.	$2.3x10^3$	$7.8x10^3$	$13x10^3$	$42x10^3$	$16x10^3$	$39x10^3$	$94x10^3$	$2.8x10^5$
Sim.	$1.45x10^3$	$5.5x10^3$	$18x10^3$	$18x10^3$	$25x10^3$	$32x10^3$	$62x10^3$	$2.1x10^5$
Ni								
Exp.	$0.8x10^3$	$3.9x10^3$	$5.7x10^3$	$13x10^3$	$7.0x10^3$	$19x10^3$	$51x10^3$	$94x10^3$
Sim.	$2.2x10^3$	$8.3x10^3$	$15x10^3$	$28x10^3$	$38x10^3$	$49x10^3$	$97x10^3$	$3.3x10^5$
Au								
Exp.	$0.2x10^3$	$0.7x10^3$	$0.9x10^3$	$1.8x10^3$	$1.3x10^3$	$3.5x10^3$	$7.7x10^3$	$9.5x10^3$
Sim.	$0.1x10^3$	$0.4x10^3$	$1.3x10^3$	$1.3x10^3$	$1.8x10^3$	$2.3x10^3$	$3.4x10^3$	$14x10^3$

Table 5.6: Experimental and simulation results for the mass flux of Cu, Ni and Au in $(CuNi)_6Sn_5$.

In Fig 5.9 the trend lines of the simulation and the experimental results for the Cu and Ni mass flux values in $(CuNi)_6Sn_5$ are shown. The simulation results for the Ni diffusion and the experimental result differ by a constant factor. The reason is that an average value of D_0 was used for the simulations, while the experiments have shown a relatively big difference between D_0 for the die side and the board side contacts. Hence the simulation results, being based on averaged values, do not perfectly fit to the board or the die side related mass flux values.

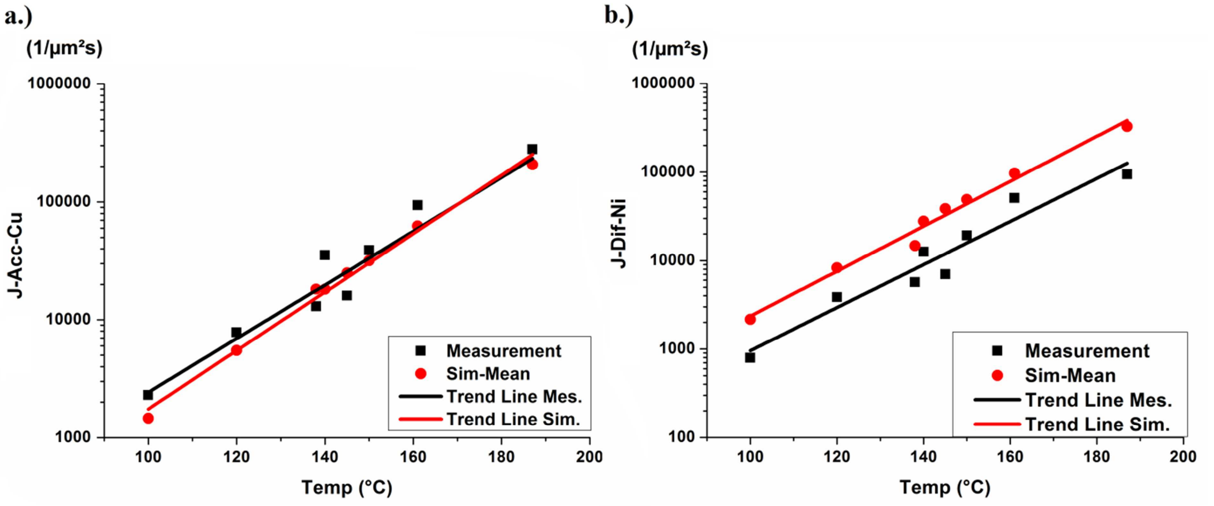

Figure 5.9: Simulated and measured mass flux values for the accumulation of Cu (a) and the diffusion of Ni (b) in $(CuNi)_6Sn_5$

5.2.2 Simulation of the Electro- and Thermomigration Induced Mass Flux

As for the open system, the calculation of the TM and EM induced mass flux values in the closed system were performed with a user developed routine [5.1]. The material parameters used for Cu, Ni and Au are given in table 5.7. For the simulations the mean values of the board and the die side parameters were used.

	E_{A-EM} [eV]	Z*	E_{A-TM} [eV]	Q* [eV]
Cu	0.715	**9.0**	0.715	**-75**
Ni	0.715	**3.3**	0.59	**0.44**
Au	0.84	**3.2**	0.84	**24**

Table 5.7: The EM and TM related material parameters of Cu, Ni and Au.

In Fig. 5.10 the EM and the TM induced mass fluxes of Cu are shown for the downstream case.

Furthermore the accumulation was taken into account. The TM and the EM are strongly affected by current crowding and the related mass fluxes densities are higher than the mass flux densities due to material accumulation. This is a clear difference to the bottom bumps, because the related mass flux values due to diffusion were as high as the sum of TM and EM.

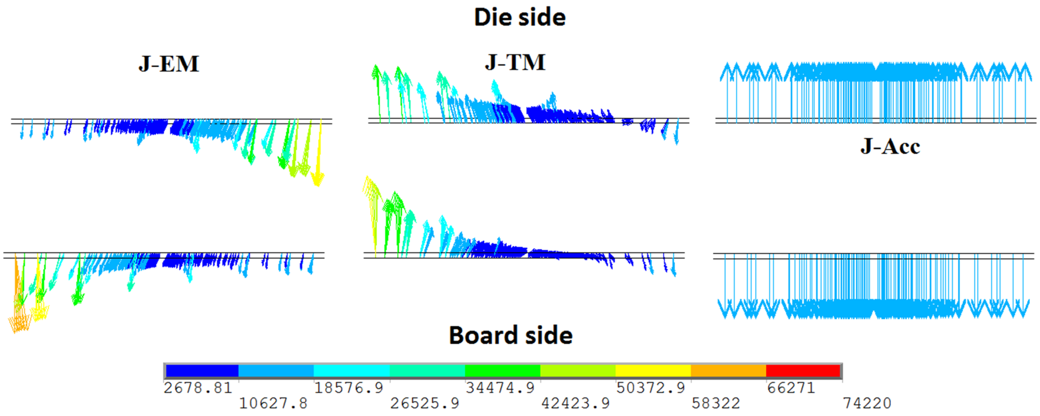

Figure 5.10: The EM (left), TM (middle) induced mass fluxes and the accumulation (right) of Cu at the die and the board side contact surfaces of a downstream stressed top bumps (138°C, 1A) [1/µm²s]

As shown in Fig. 5.11, the strong influence of EM can lead to a dissolution of the $(CuNi)_6Sn_5$ layer. The dissolution of $(CuNi)_6Sn_5$ appeared at the die side contacts during the downstream tests. For the upstream case a similar, but weaker, dissolution effect of $(CuNi)_6Sn_5$ was observed at the board side contacts.

The formation of $(CuNi)_6Sn_5$ mainly depends on the Cu mass flux. The simulation results of the total mass flux show that the reason for the dissolution of $(CuNi)_6Sn_5$ was the disappearance of Cu due the EM induced mass flux. The TM and EM have opposite directions. Hence they should compensate each other, but the current crowding led to smaller temperature gradients. As a consequence a reduced mass flux due to TM was observed. The increased Joule heating due to current crowding locally warmed up the relatively cold top bumps. Consequently the temperature of the affected regions was closer to the maximum package temperature in the package and the temperature gradients and the related mass flux due to TM become smaller. Under these conditions the EM induced mass flux was not compensated by TM. In addition the EM induced mass flux was stronger than the mass flux due to material accumulation.

At the board side contacts the TM and EM induced mass fluxes were able to compensate each other and the IMC growth profile was relatively uniform.

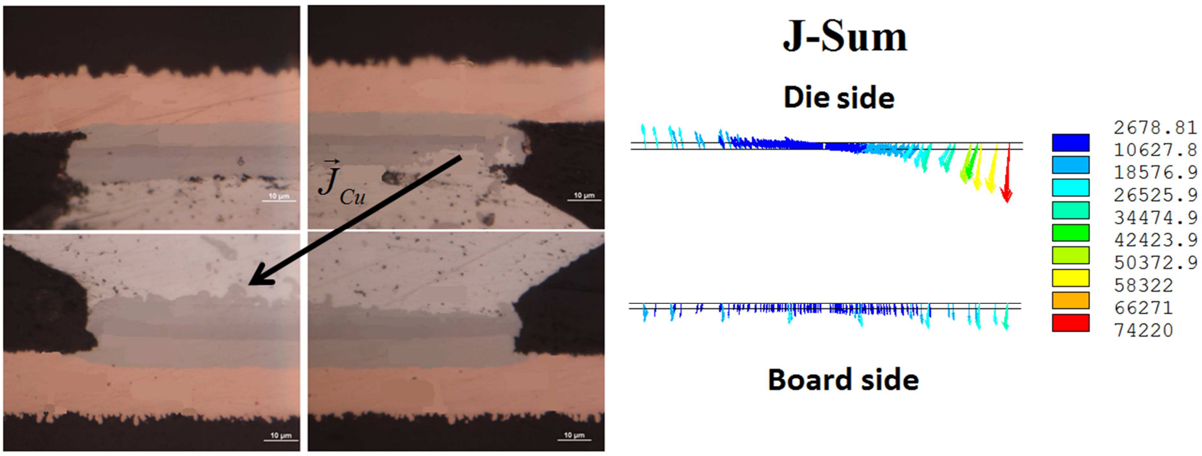

Figure 5.11: IMC dissolution after downstream DC stress (left) [5.5] and the sum of all Cu mass flux values (right). [1/µm²s]

In addition to the migration of Cu, the EM and TM induced mass fluxes of Au and Ni were calculated. The mass fluxes of Au and Ni did not have an influence on the $(CuNi)_6Sn_5$ formation speed, and the Ni_3Sn_4 formation, as a consequence of EM driven Ni motion, was independent of the direction of the current flow. Nevertheless the validation of the Z* and Q* values of Cu and Ni was possible by comparing the mean value of the simulation results with the experimental results (Fig. 5.12-13).

In the main the calculated mass flux values due to EM fit to the experimental results. Only the mass flux of Cu at 138°C was overestimated, because the simulation program does not take into account the strong saturation effect on the Cu accumulation during the long term TS tests. The simulated and the measured mass flux values due TM are similar in all cases.

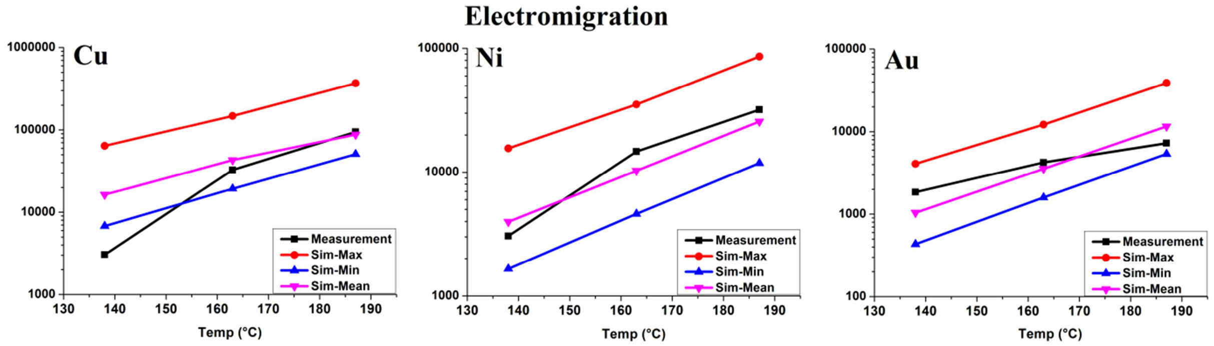

Figure 5.12: Comparison of the simulated and the measured EM induced mass flux values of Cu, Ni and Au in the top bumps [1/µm²s]

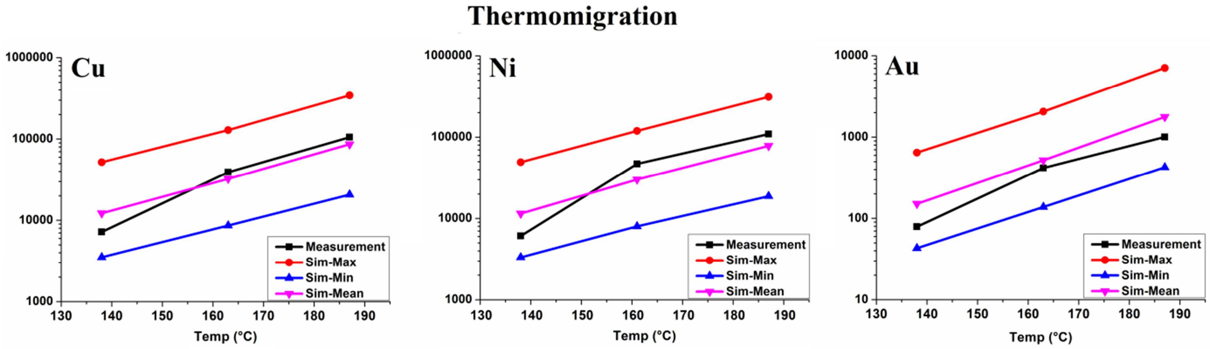

Figure 5.13: Comparison of the simulated and the measured TM induced mass flux values of Cu, Ni and Au in the top bumps [1/µm²s]

5.3 Conclusion

The diffusion and migration induced mass fluxes in the IMCs layers of the bottom and the top bump were reproduced by simulations. The diffusion of Cu and Sn in Cu_3Sn and Cu_6Sn_5 and the diffusion of Ni in $(CuNi)_6Sn_5$ were calculated by using the experimental gained E_A and D_0 values. Furthermore the accumulation of Cu and Au was calculated with an APDL routine.

In the following step the Q* and the Z* values of Cu, Sn, Ni, Au were implemented in an user routine. The mass flux values due to TM and EM in the bottom and the top bumps were calculated. A good compliance between the experimental and the simulation results were found for the IMC layers in the bottom bumps, as well as for the IMC layers in the top bumps.

The successful calculation of diffusion and migration related mass flux values enabled the simulation based interpretation of the stress tests under consideration of the solder joint geometry. The main influence of the solder joints geometry on IMC formation is due to current crowding. The parameter extraction through the mean IMC dimensions after the TS, AC and DC stress tests led to the elimination of all information being related to local effects. Based on FEA it became possible to reconstruct the local IMC formation under consideration of current crowding and the three dimensional temperature distributions in the solder joints.

Regarding to the DC tests on the bottom bumps the FEA of the interaction between TM, EM and diffusion enabled the explanation of the missing current crowding effect on the Cu_3Sn and Cu_6Sn_5 growth during the downstream DC tests. In this case the locally enhanced mass flux due EM was compensated by an opposed mass flux due TM.

Regarding to the top bumps it became clear that current crowding leads to an EM and TM induced Cu migration, being stronger than the material accumulation induced mass flux. For the downstream case no compensation of TM and EM induced migration appeared at the die sided contact surfaces. As a consequence the EM induced mass flux overwhelmed the Cu accumulation process, and a dissolution of $(CuNi)_6Sn_5$ appeared instead of the expected acceleration of the IMC growth speed.

Overall the FEA with general and migration related material parameters has proven to be a promising technique to predict the IMC formation in solder joints. Especially it allows the prediction of the IMC growth in a solder joint during an EM and TM accelerated TLPS process.

6 Conclusion & Perspectives

6.1 Conclusion

In this work the material motion, leading to the IMC formation during stress tests on SnAgCu solder joints, was characterized with temperature storage (TS) tests that were partially combined with an additional DC or AC load. The IMC growth during the TS tests appeared due to diffusion. If a current was applied to the test structure also mass fluxes due to electro- (EM) and thermomigration (TM) appeared.

All stress test were performed in ovens at a minimum temperature of 100°C. Hence the investigation of the EM or TM related IMC formation, and the extraction of related material parameters was only possible after the diffusion induced mass fluxes in the solder bumps were determined. Against this background short term and long term TS tests were performed at 150°C. Afterwards the short term tests were repeated at 100°C, 120°C and 140°C.

In case of the bottom bumps the diffusion of Cu from the metal line into the solder joints led to the formation Cu_3Sn and Cu_6Sn_5. During the long term tests the formation speed of both IMCs was reduced with increasing layer thickness. Shrinking concentration gradients and a longer distance for Cu to pass were identified as possible reasons for the long term effect. Being aware of possible long term saturation affects, the TS tests at 150°C and the three additional TS tests could be used to characterize the diffusion of Cu and Sn in Cu_3Sn and Cu_6Sn_5. As results the activation energies (E_A) and the diffusion constants (D_0) of Cu and Sn were extracted for both IMCs. The results were compared with literature values. By that way the mathematical model for the mass flux extraction could be validated and a six jump cycle, firstly described by Huntington, could be identified as the most relevant transport mechanism for the motion of Sn and Cu in the investigated Cu_3Sn and Cu_6Sn_5 layers.

In case of the top bumps the Ni pads acted as diffusion barrier for the motion of Cu coming from the metal lines. Nevertheless during the TS tests a $(CuNi)_6Sn_5$ layer was formed by the accumulation of Cu and the diffusion of Ni form the pads into the solder joints. As shown by previous experiments no Ni_3Sn_4 formation was observable after the TS tests on Cu containing solder joints. The Cu source for the $(CuNi)_6Sn_5$ formation was the 0.5% Cu content in SnAgCu. As a consequence the Cu content in the solder was reduced during $(CuNi)_6Sn_5$ formation and a clear declaration of the $(CuNi)_6Sn_5$ formation was observed during the long term TS tests. Taking into account the long term effects on the $(CuNi)_6Sn_5$ formation, it was possible to characterize the diffusion of Ni and the accumulation of Cu by extracting the mass flux values for four different storage temperatures. Like for the bottom bumps, the E_A for the motion Cu and Ni was determined. Before this step no literature values for the motion of single elements in $(CuNi)_6Sn_5$ were available. For a more general description of the accumulation related migration process the Nernst-Einstein equation was used to define a driving force "β", being responsible for the directed motion of the Cu atoms to contact surfaces. In difference to the Ni diffusion the driving force β and the D_0 of the Cu accumulation are part of one equation and only one parameter could be extracted. Hence the D_0 of Cu was taken from literature and β was calculated from the mass flux values.

AC (0.8A/50Hz) stress tests at 145°C led to Joule heating and TM, but they also suppressed an effective mass flux due to EM. The tests did not show any EM induced void formation in the solder joints. Nevertheless the IMC formation in the top and in the bottom bumps was accelerated. The IMC formation speed was independent from the direction of the current flow. Hence the presence of a

TM induced mass flux can be expected. At the contact surfaces of the top bumps no Ni_3Sn_4 was found. Hence it became clear that a directed mass flux due to EM is needed to increase the Ni portion in IMCs above the critical value for the Ni_3Sn_4 formation.

Taking into account that the applied current increases the test temperature, the expected mass flux due diffusion was extrapolated with the E_A and D_0 values from the TS tests. Afterwards an extraction of the TM induced mass flux in the top and bottom bumps was possible. Based on the TM induced mass flux values the heat of transport (Q*) values for the TM induced motion of Cu and Sn in Cu_3Sn and Cu_6Sn_5 as well as for the Cu, Ni motion in $(CuNi)_6Sn_5$ could be determined.

Unlike the TS and TM tests, the DC tests led to the formation of a Ni_3Sn_4 IMC layer at the contact surfaces of the top bumps. The EM induced mass flux increased the Ni content in $(CuNi)_6Sn_5$. EDS investigations have shown that an atomic concentration of 25% is the critical amount of Ni being needed for the Ni_3Sn_4 formation. Like for the AC tests an accelerated IMC formation speed was observable in the top and in the bottom bumps. The applied DC led to void formation in the solder joints and the IMC formation speed was influenced by the direction of the current flow. Both effects clearly indicate the presence of EM. A difference between the mean IMC dimensions at the board and the die side contact surfaces also indicate the presence of a TM induced mass flux.

By comparing the IMC dimensions for upstream and the downstream case the EM induced mass flux in bottom and in the top bumps could be extracted. After the extrapolation of the diffusion and material accumulation related mass flux values also the TM induced mass flux was available. Based on these additional results effective charge values (Z*) at three different temperatures and Q* values for four different test temperatures were extracted. These values were used to describe the temperature dependency of the EM and the TM induced mass fluxes in Cu_3Sn, Cu_6Sn_5, $(CuNi)_6Sn_5$ and Ni_3Sn_4.

The results of this analysis are temperature independent values of Z* and Q* for the calculation of the EM and TM induced mass flux in the IMCs. Combined with the influence by diffusion and the related parameters (E_A, D_0) they can be used for the prediction of the IMC growth speed in solder joints for a broad range of boundary conditions.

For the interpretation of the experimental results and the extraction of the material parameters averaged values were used. Hence localized effects like current crowding could not be investigated. Based on the three dimensional FE model the test conditions could be reconstructed and the IMC profile after the DC tests could be explained by taking into account the influence of current crowding on the IMC formation speed.

In case of the bottom bumps the EM and the TM induced mass fluxes compensate each other for the downstream case and were added for the upstream case. The sum of the mass fluxes due to TM and EM was as big as the mass flux due to diffusion. Hence the interaction between the three mass flux values could explain why the IMC profile was relatively homogenous for the downstream case, while the influence of current crowding became clearly visible for the upstream case.

Regarding to the top bumps the mass flux values due to TM and EM were added for the downstream case and they compensated each for the upstream case. In difference to the bottom bumps the TM and EM induced mass fluxes were stronger than the mass flux due material accumulation. Hence the simulations could show why the downstream case shows a complete dissolution of the $(CuNi)_6Sn_5$ layer.

6.2 Perspectives

Based on this work it is possible to predict the IMC formation speed in SnAgCu solder joints for a wide variation of process temperatures under consideration of EM and TM induced mass fluxes. A prediction of the IMC formation, being based on temperature independent material values, enables the simulation based optimization of the TLPS process parameters and the solder joint geometry. The availability of temperature independent Z* and Q* also enables the development and the optimization of EM and TM accelerated TLPS. EM and TM enhanced TLPS could enable the reduction of the process temperature or the application of TLPS on Sn layers being normally too thick to transform into an IMC joint in a reasonable time. This can be done for direct metal to solder contacts as well as for solder joints on Ni/Au contact pads.

The experimental approach of this work and the related model for the IMC formation describe a general method for the characterization of the IMC formation due to EM and TM. Hence an EM and TM accelerated TLPS could also be developed for alternatives to SnCu IMCs, like AuSn or Au_5Sn.

In addition the prediction of the IMC formation with respect to the influences by EM and TM supports the development of simulation tools for the investigation of aging effects on conventional SnAgCu solder joints.

References

Chapter 2:

[2.1] E.M Rogers, "Diffusion of Innovations 5th Edition", Free Press, New York, 2003, pp. 234, 281.

[2.2] S. Ram, J. N. Sheth, "Consumer Resistance to Innovations: The Marketing Problem and its Solutions ", The Journal of Consumer Marketing, Vol.6 No.2 (1989), pp. 5-13.

[2.3] J. N. Sheth, S. Ram, "Bringing innovation to market: how to break corporate and customer barriers", Wiley, New Jersey, 1987, pp.3-4, 64.

[2.4] S . Ram, J. N. Sheth, " Marketing Barriers to Innovations: The case of the Entrepreneur", AMA Symposium on Research Activities in Marketing Entrepreneurship, 1988, pp. 403-409.

[2.5] G. E. Moore, “Cramming more Components onto Integrated Circuits,” Electronics, Vol. 38 No. 8 (1965), reproduced in IEEE Proceedings Vol. 86 No. 1 (1998) pp. 82-85.

[2.6] R. H. Dennard, F. H. Gänßlen, H. N. Yu et al., “Design of ion-implanted MOSFETs with very small physical dimensions”, IEEE, Journal of Solid-State Circuits, Vol. 9 (1974), p.256 -268.

[2.7] M. Kawano, S. Uchiyama, Y. Egawa et al. "A 3D Packaging Technology for 4 Gbit Stacked DRAM with 3 Gbps Data Transfer", IEEE, International Electron Devices Meeting (IEDM), San Francisco, December 2006, pp. 1-3.

[2.8] Raymond A. Fournelle, „Lead-Free Solders and Processing Issues in Microelectronics“, JOM, 2003, pp. 49.

[2.9] G. Philip, "Wafer Level Chip Scale Packaging (WL-CSP): An Overview", IEEE, Transactions Advanced Packaging, Vol. 23, No. 2, MAY 2000, pp. 198-205.

[2.10] Y. Nishi, R. Doering, "Handbook of Semiconductor Manufacturing Technology ", 2nd Edition, CRC Press, Boca Raton, Florida, 2007, chapter 4, 11, 30, 35.

[2.11] C. Auth, C. Allen, A. Blattner et al., " A 22nm High Performance and Low-Power CMOS Technology Featuring Fully-Depleted Tri-Gate Transistors, Self-Aligned Contacts and High Density MIM Capacitors ", IEEE, Symposium on VLSI Technology Digest of Technical Papers, Honulu, Hawai, 2012, pp. 131-132.

[2.12] C.-H. Jan, U. Bhattacharya, R. Brain et al., "A 22nm SoC Platform Technology Featuring 3-D Tri-Gate and High-k/Metal Gate, Optimized for Ultra Low Power, High Performance and High Density SoC Applications", IEEE, International Electron Devices Meeting (IEDM), San Francisco, December 2012, pp. 44-47.

[2.13] R. H. Havemann, J. A. Hutchby, "High-Performance Interconnects: An Integration Overview", IEEE Proceedings Vol. 86 No. 5 (2001) pp. 586-601.

[2.14] S. Borkar, "Design challenges of technology scaling", IEEE, Micro, Vol. 14 No. 4 (1999), pp. 23-29.

[2.15] S. E. Thompson, S. Parthasarathy, "Moore's law: the future of Si microelctronics", materials today, Vol. 9 No. 6 (2006), pp. 20-25.

[2.16] G. Messner, "Cost-Density Analysis of Interconnections", IEEE, Components, Hybrids, and Manufacturing Technology, Vol. 10 No. 2 (1987), pp. 143-151.

[2.17] K. Rupp, S. Selberherr, "The Economic Limit to Moore’s Law", IEEE, Transactions on Semiconducter Manufactoring, Vol. 24, No. 1 (2011), pp. 1-3.

[2.18] International Monetary Fund, "World Ecomoic Outlook Update", Wshignton D.C., USA, 2012, pp. 1-8.

[2.19] R. K. Cavin, P. Lugli, V. V. Zhirnov, "Science and Engineering Beyond Moore’s Law", IEEE Proceedings Vol. 100 (2012) pp. 1720-1749.

[2.20] Semiconductor Industry Association, The International Technology Roadmap for Semiconductors, 2009.

[2.21] W. Arden, M. Brillouët, P. Cogez, et al. "Towards a Moore Than Moore Roadmap", CATRENE© Scientific Committee, 2011.

[2.22] R. W. Johnson, J. L. Evans, P. Jacobsen, The Changing Automotive Environment: High-Temperature Electronics, IEEE, Transactions Electronics Packaging Manufacturing, Vol. 27 No. 3 (2004), pp. 164-176.

[2.23] M. L. ElGizawy, "Continuous Measurement-While-Drilling Surveying System Utilizing MEMS Inertial Sensors", Dissertation, University of Calgary, Department of Geomatics Engineering, Calgary, Alberta, 2009.

[2.24] F. G. Kuper, "Automotive IC reliability: Elements of the battle towards zero defects", “, IEEE, Microelectronics Reliability, Vol. 48 (2008), pp. 1459-1463.

[2.25] R. Kisiel, Z. Szczepański, „Trends in assembling of advanced IC packages“, Journal of Telecommunication and Information technology, 2005, pp. 63-69.

[2.26] R. R. Tummala, E. J. Rymaszewski, A. G. Klopfenstein, “Microelectronics Packaging Handbook”, 2nd Edition, Springer Science and Business Media, Berlin, Germany, 1997, pp. 65, 84, 470, 476.

[2.27] K. DeHaven, J. Dietz, „Controlled Collapse Chip Connection (C4) - An Enabling Technology“, IEEE, Electronic Components and Technology Conference (ECTC), Washington D.C. , June 1994, pp. 1-6.

[2.28] Semiconductor Industry Association, The International Technology Roadmap for Semiconductors 2010 Update, 2010.

[2.29] P. Ramm, J. J. Q. Lu, M. M. V. Taklo, "Handbook of Waferbonding", Wiley-VCH Verlag, Weinheim, Germany, 2012, pp. 162-167, 181-185, 204-209, 305.

[2.30] J. Cheng Lin, J. Yu, B. Chung et. al : “Development on Ultra High Density Memory Package with PoP Structure “, IEEE, Electronic Components and Technology Conference (ECTC) 2011, Orlando, pp. 1136-1140.

[2.31] L. Meinshausen, K. Weide-Zaage, H. Frémont, „Thermal Management for Stackable Packages with Stacked ICs", IEEE, Mechanical & Multi-Physics Simulation, and Experiments in Microelectronics and Microsystems (EuroSimE), Lisbon, 2012, pp. 1-6.

[2.32] H. Gan, S.L. Wright, R. Polastre, et al., "Pb-free Micro-joints (50 µm pitch) for the Next Generation Micro-systems: the Fabrication, Assembly and Characterization", IEEE, Electronic Components and Technology Conference (ECTC), 2006, Marina, California, pp. 1210-1215.

[2.33] S. Gee, N. Kelkar, J. Huang, “Lead-Free and PbSn Bump Electromigration Testing”, ASME International Technical Conference and Exhibition on Packaging and Integration of Electronic and Photonic Microsystems (InterPACK), 2005, San Francisco, pp. 1-9.

[2.34] B. Salam, N. N. Ekere, D. Rajkumar, "Study of the Interface Microstructure of Sn-Ag-Cu Lead-Free Solders and the Effect of Solder Volume on Intermetallic Layer Formation", IEEE, Electronic Components and Technology Conference (ECTC), 2001, Orlando, Florida, pp. 1-7.

[2.35] L. Meinshausen, H. Frémont, K. Weide-Zaage, „Migration induced IMC formation in SAC305 solder joints on Cu, NiAu and NiP metal layers“, IEEE, Microelectronics Reliability, Vol. 52 No 9-10 (2012), pp. 1827-1832.

[2.36] Semiconductor Industry Association, The International Technology Roadmap for Semiconductors, 2002.

[2.37] Semiconductor Industry Association, The International Technology Roadmap for Semiconductors 2012 Update, 2012.

[2.38] M. Abtewa, G. Selvaduray, "Lead-free Solders in Microelectronics", Materials Science and Engineering, Vol. 27 (2000), pp. 95-141.

[2.39] P. G. Shewmon, "Diffusion in Solids", 2nd Edition, Wiley, New York City, 1989, pp. 37, 54-74.

[2.40] J. Philibert, “Creep and Diffusion”, Solid State Ionics, Vol. 12 (1984), pp. 321-336.

[2.41] M.D. Mathew, H. Yang, S. Movva, „Creep Deformation Characteristics of Tin and Tin-Based Electronic Solder Alloys“, Metallurgical and Materials Transactions A, Vol. 36A (2005), pp. 99-105.

[2.42] M. R. Werner, „Review on materials, microsensors, systems and devices for high-temperature and harsh-environment applications“, IEEE, Industrial Electronics, Vol. 48 No. 2 (2001), pp. 249-257.

[2.43] R. Klieber, „Evaluation of materials for high temperature IC packaging“, 15th International Workshop on Thermal Investigations of ICs and Systems (THERMINIC), Leuven, Belgium, 2009, pp. 117-120.

[2.44] R. G. Azevedo, „A SiC MEMS Resonant Strain Sensor for Harsh Environment Applications“, IEEE, Sensors Journal, Vol. 7 No. 4 (2007), pp. 568-576.

[2.45] K. N. Chen, „Microstructure examination of copper wafer bonding“, Journal of Electronic Materials, Vol. 30 No. 4 (2001), pp. 331-335.

[2.46] T. H. Kim, M. M. R. Howlader, T. Itoh, et al. "Room temperature Cu–Cu direct bonding using surface activated bonding method", Journal of Vacuum Science & Technology A: Vacuum, Surfaces, and Films, Vol. 21 No. 2, p. 449-453.

[2.47] P. Gueguen, L. Di Cioccio, P. Gergaud, "Copper Direct-Bonding Characterization and Its Interests for 3D Integration", The Electrochemical Society, Vol. 16 No. 8 (2008), pp. 31-37.

[2.48] E. Ide, S. Angata, A. Hirose, "Metal–metal bonding process using Ag metallo-organic nanoparticles", Acta Materialia, Vol. 53 (2005), pp. 2385–2393.

[2.49] G. Zou, J. Yan, F. Mu, "Low Temperature Bonding of Cu Metal through Sintering of Ag Nanoparticles for High Temperature Electronic Application", The Open Surface Science Journal, Vol. 3 (2011), pp. 70-75.

[2.50] A. Hu, J. Y. Guo, H. Alarifi, "Low temperature sintering of Ag nanoparticles for flexible electronics packaging", Applied Physics Letters , Vol. 97 (2010), pp. 1-3.

[2.51] A. Moujbani, J. Kludt, K. Weide-Zaage, “Dynamic Simulation of Migration Induced Failure Mechanism in Integrated Circuit Interconnects”, IEEE, Microelectronics Reliability, Vol. 53 (2013), pp. 1365-1369.

[2.52] N. Watanabe, T. Kojima, T. Asano, "Wafer-level Compliant Bump for Three-Dimensional LSI with High-Density Area Bump Connections", International Electron Devices Meeting (IEDM), Washington D. C., December 2005, pp. 671-673.

[2.53] I. Tuah-Poku, M. Dollar, T. B. Massalski, "A Study of the Transient Liquid Phase Bonding Process Applied at Ag/Cu/Ag Sandwich Joint", Mtallurgical Transactions A, Vol. 19A (1988), pp. 675-686.

[2.54] R. Agarwal, W. Zhang, P. Limaye, "Cu/Sn Microbumps Interconnect for 3D TSV Chip Stacking", IEEE, Electronic Components and Technology Conference (ECTC), 2010, Las Vegas, pp. 858-863.

[2.55] K. Guth, D. Siepe, J. Görlich, et al., „New assembly and interconnects beyond sintering methods“, Power Conversion and Inteligent Motion (PCIM), Nürnberg, Germany, 2010, pp. 1-6.

[2.56] K.S. Kim, S.H. Huh, K. Suganuma, "Effects of intermetallic compounds on properties of Sn–Ag–Cu lead-free soldered joints", Journal of Alloys and Compounds, Vol. 352 (2003), pp. 226–236.

[2.57] H. B. FAN, E. K. L. Chan, C. K.Y. Wong, "Moisture Diffusion Study in Electronic Packaging using Molecular Dynamic Simulation", IEEE, Electronic Components and Technology Conference (ECTC), 2006, Marina, California, pp. 1425-1428.

[2.58] M. Kitano, A. Nishimura, S. Kawai, et al. "Analysis of Package Cracking During Reflow Soldering Process", IEEE, 26th International Reliability Physics Symposium, Monterey, California, 1988, pp. 90-95.

[2.59] I.Fukuzawa, S.Ishiguro, S.Nanbu et al., "Moisture Resistance Degardation of Plastic LSIs by Reflow Soldering", IEEE, 23rd International Reliability Physics Symposium, New York, 1985, pp. 192-197.

[2.60] K. Weide-Zaage, W. Horaud, H. Frémont, "Moisture diffusion in Printed Circuit Boards : Measurements and Finite- Element- Simulations", IEEE, Microelectronics Reliability, Vol. 45 (2005), pp. 1662-1667.

[2.61] JEDEC JESD22-A101C, “Steady State Temperature Humidity Bias Life Test”, March 2009.

[2.62] Kh. G. Schmitt-Thomas, S. Wege, H. Schweigart, "Elektrochemische Migration - eine typische Korrosionserscheinung in der Mikroelektronik", Materials and Corrosion, Vol. 46 (1995), pp. 366-369, in German.

[2.63] E. H. Wong, K.C. Chan, R. Rajoo, "The Mechanics and Impact of Hygroscopic Swelling of Polymeric Materials in Electronic Packaging", IEEE, Electronic Components and Technology Conference (ECTC), 2000, Las Vegas, pp. 576-580.

[2.64] E. H. Wong, Y. C. Teo, T. B. Lim, " Moisture Diffusion and Vapour Pressure Modeling of IC Packaging", IEEE, Electronic Components and Technology Conference (ECTC), 1998, Seattle, USA, pp. 1372-1378.

[2.65] W. Feng, “Caractérisation Expérimentale et Simulation Physique des Mécanismes de dégradation de Interconnexions sans plomb dans les technologies d’assemblage a très forte densité d’intégration “”Boitier sur Boitier”, Dissertation, Université Bordeaux I, Talence, France, 2010, in French.

[2.66] J. W. Yoon, B.-I. Noh, Y.-H. Lee, "Effects of isothermal aging and temperature–humidity treatment of substrate on joint reliability of Sn–3.0Ag–0.5Cu/OSP-finished Cu CSP solder joint", Microelectronics Reliability, Vol. 48 (2008), pp. 1864–1873.

[2.67] H. Huebner, S. Penka, B. Barchmann et al., „Microcontacts with sub-30 µm pitch for 3D chip-on-chip integration, Microelectronic Engineering“, Microelectronic Engineering, Vol. 83 No. 11–12 (2006), pp. 2155-2162,

[2.68] P. J. Boddys, R. H. Delaney, J. N. Lahti, "Accelarated Life Testing of Flexible Printing Circuits", 14th Reliability Physics Symposium, Las Vegas, 1976, pp. 108-117.

[2.69] D. Q. Yu, W. Jillek , E. Schmitt, "Electrochemical migration of lead free solder joints", Journal of Materials Science: Materials in Electronics, Vol. 17 (2006), pp. 229–241.

[2.70] K. M. Striny, A. W. Schelling, "Reliability Evaluation of Aluminum-Metallized MOS Dynamic RAM's in Plastic Packages in High Humidity and Temperature Environments", IEEE, Transactions on Components Hybrids and Manufactoring, Vol. 4 No. 4 (1981), pp. 476-481.

[2.71] M. S. Jung, S. B. Lee, H. Y. Lee, " Improvement of Electrochemical Migration Resistance by Cu/Sn Inter-Metallic Compound Barrier on Cu in Printed Circuit Board ", IEEE, Transactions on Device and Materials Reliability, Vol. 99 (2012), pp. 1-8.

[2.72] C. Xu, Y. Zhang, C. Fan, “Understanding Whisker Phenomenon – Driving Force for the Whisker Formation”, IPC, Surface Mount Equipment Manufacturers Association, 2006, pp. 1-6.

[2.73] JEDEC JESD22-B112A, „Package Warpage Measurement of Surface-Mount Integrated Circuits at Elevated Temperature“, October 2009.

[2.74] W.W. Lee, L.T. Nguyen, G.S. Selvaduray et al. „Solder joint fatigue models: review and applicability to chip scale packages“, Microelectronics Reliability, Vol. 40 (2000), pp. 231–243.

[2.75] JEDEC JESD22-A104D, „Temperature Cycling“, March 2009.

[2.76] S. S. Manson, “Fatique: A Complex Subject – Some Simple Approximations”, Experimental Mechanics, 1964, pp. 193-226.

[2.77] S.B. Brown, K.H. Kim, L. Anand, “An internal variable constitutive model for hot working of metals”, International Journal of Plasticity, vol. 5 (1989), pp. 95-130.

[2.78] M. Pei and J. Qu, “Constitutive modeling of lead-free solders,” ASME: Adv. Electron. Package, pp. 1307–1311, 2005.

[2.79] Y. Liu, S. Irving, T. Luk et al., „3D Modeling of Electromigration Combined with Thermal-Mechanical Effect for IC Device and Package “, Microelectronics Reliability, Vol. 48 (2008), pp. 811–823.

[2.80] Y. L. Huang, K. L. Lin, „Microstructure evolution and micro impact performance of Sn–Ag–Cu solder joints under thermal cycle test“, Journal of Materials Research, Vol. 25 No. 7, 2010, pp. 1312-1320.

[2.81] M. Meilunas, A. Primavera, O. Steven, „Reliability and Failure Analysis of Lead-Free Solder Joints“, Proceedings of the IPC Annual Meeting, 2003, Minneapolis, USA, pp. 1-15.

[2.82] J. Y. Kim, J. Yu, „Effects of residual impurities in electroplated Cu on the Kirkendall void formation during soldering“, Applied Physics Letters , Vol, 92 No. 9 (2008), pp. 1-3.

[2.83] L. Xu, J. H.L. Pang, F. Che, „Impact of Thermal Cycling on Sn-Ag-Cu Solder Joints and Board-Level Drop Reliability“, Journal of Eelctronic Materials, Vol. 37, No. 6 (2008), pp. 880-886.

[2.84] J. Y. Lee, T. K. Hwang, J.Y. Kim: „Study on the Board Level Reliability Test of Package on Package (PoP) with 2nd Level Underfill“, IEEE, Electronic Components and Technology Conference (ECTC), 2007, pp.1905-1910.

[2.85] R. Labie, P. Limaye, K.W. Lee et al. “Reliability testing of Cu-Sn intermetallic micro-bump interconnections for 3D-device stacking”, Electronic System-Integration Technology Conference (ESTC), Berlin, 2010, pp. 1-5.

[2.86] Y. B. Kim, H. Noguchi, M. Amagai, „Vibration fatigue reliability of BGA-IC package with Pb-free solder and Pb–Sn solder“, Microelectronics Reliability, Vol. 46 (2006), pp. 459–466.

[2.87] S. F. Wong, P. Malatkar, C. Rick et al., „Vibration Testing and Analysis of Ball Grid Array Package Solder Joints“, IEEE, Electronic Components and Technology Conference (ECTC), 2007, Reno, Nevada, USA, pp. 373-380.

[2.88] T. Pringle, P. Raghavan, P. Malatkar, „Solder Joint Reliability of BGA Package under End-User Handling Test Conditions“, IEEE, Electronic Components and Technology Conference (ECTC), 2007, Reno, Nevada, USA, pp. 400-406.

[2.89] E.H. Wong, K.M. Lim, N. Lee et al., „Drop Impact Test - Mechanics & Physics of Failure“, 4th Electronics Packaging Technology Conference (EPTC), Singapore, 2002, pp. 327-333

[2.90] T.C. Chai, S. Quek, W. Y. Hnin et al., „Board Level Drop Test Reliability of IC Packages“, IEEE, Electronic Components and Technology Conference (ECTC), 2005, Lake Buena Vista, Florida, pp. 630-636.

[2.91] JEDEC JESD22-B111, „Board Level Drop Test Method of Components for Handheld Electronic Products“, July 2003.

[2.92] J. M. Song, B. R. Huang, C. Y. Liu, „Nanomechanical responses of intermetallic phase at the solder joint interface – Crystal orientation and metallurgical effects“, Materials Science and Engineering, A 534 (2012), pp. 53– 59.

[2.93] J. M. Song, Y. L. Shen, C.-W. Su et al., „Strain Rate Dependence on Nanoindentation Responses of Interfacial Intermetallic Compounds in Electronic Solder Joints with Cu and Ag Substrates“, Materials Transactions, Vol. 50 No. 5 (2009), pp. 1231-1234.

[2.94] H. John , L. Pang, B. S: Xiong et al., „Modeling Stress Strain Curves For Lead-Free 95.5Sn-3.8Ag-0.7Cu Solder“ ,IEEE, Mechanical & Multi-Physics Simulation, and Experiments in Microelectronics and Microsystems (EuroSimE), Brussels, Belgium, 2004, pp. 449-453.

[2.95] C. C. Lee, P. J. Wang, J. S. Kim, „Are Intermetallics in Solder Joints Really Brittle?“, IEEE, Electronic Components and Technology Conference (ECTC), 2007, Reno, Nevada, USA, pp. 648-652.

[2.96] S .K. W. Seah, C.T. Lim, E. H. Wong, „Mechanical Response of PCBs in Portable Electronic Products During Drop Impact“, 4th Electronics Packaging Technology Conference (EPTC), Singapore, 2002, pp. 120-125.

[2.97] T. Mattila, „ Reliability of High Density Lead-Free Solder Interconnections Under Thermal Cycling and Mechanical Shock Loading”, Dissertation, Helsinki, Helsinki University of Technology, Laboratory of Electronics Production Technology, 2005.

[2.98] X. Yanghua, L. Chuanyan, X. Xiaoming, “Effect of Interfacial Reactions on the Reliability of Lead-Free Assemblies after Board Level Drop Tests”, Journal of Electronic Materials, Vol. 36 No. 9 (2007), pp. 1129-1136.

[2.99] D. Y.R. Chong , F.X. Che, J. H.L. Pang, „Drop impact reliability testing for lead-free and lead-based soldered IC packages“, Microelectronics Reliability, Vol. 46 (2006), pp. 1160–1171.

[2.100] H. Wever, “Elektro und Thermotransport in Metallen”, Johann Ambrosius Barth, Lebzig, 1973, in German, pp. 56, 232.

[2.101] C. Chen, H.M. Tong, K.N. Tu, “Electromigration and Thermomigration in Pb-Free Flip-Chip Solder Joints”, Annual Review of Materials Research, Vol. 40 (2010), pp. 531-555.

[2.102] I. A. Blech, “Electromigration in thin aluminum films on titanium nitride“, Journal of Applied Physics, Vol. 47 (1976), pp. 1203-1208.

[2.103] Y. Hou, C. M. Tan, „Blech Effect in Cu Interconnects with Oxide and Low-k Dielectrics“, 14th International Symposium on the Physical and Failure Analysis of Integrated Circuits (IPFA), 2007, Bangalore, India, pp. 65-69.

[2.104] V.M. Dwyer, „Analysis of critical-length data from Electromigration failure studies“, Microelectronics Reliability, Vol. 51 (2011), pp. 1568–1572.

[2.105] L. Meinshausen, K. Weide-Zaage, H. Frémont, “Electro- and Thermomigration induced Failure Mechanisms in Package on Package“, IEEE, Microelectronics Reliability, Vol. 52 No 12 (2012), pp. 2889-2906.

[2.106] JEDEC JEP154, “Guideline for Characterizing Solder Bump Electromigration under Constant Current and Temperature Stress”, January 2008.

[2.107] J. R. Black, “Electromigration of Al-Si Alloy Films”, IEEE, 16th Annual International Reliability Physics Symposium (IRPS), San Diego, California, 1978, pp. 233-236.

[2.108] K. Weide-Zaage, “Untersuchungen von Stromdichte-, Temperatur- und Massenflussverteilungen in Viastrukturen integrierter Schaltungen”, Dissertation, VDI Verlag, Düsseldorf, 1994, in German.

[2.109] C. Hau-Riege, R. Zang, Y. W. Yau, et al. „Electromigration Studies of Lead-Free Solder Balls used for Wafer-Level Packaging“, IEEE, Electronic Components and Technology Conference (ECTC), 2011, Lake Buena Vista, Florida, pp. 717-721.

[2.110] K. Nakagawa, S. Baba, M. Watanabe, et al. „Thermo-Electromigration Phenomenon of Solder Bump, Leading to Flip-Chip devices with 5,000 Bumps“, IEEE, Electronic Components and Technology Conference (ECTC), 2001, Orlando, Florida, pp. 1-7.

[2.111] K. Weide-Zaage, H. Frémont, L. Wang, “Simulation of migration effects in PoP“,IEEE, Mechanical & Multi-Physics Simulation, and Experiments in Microelectronics and Microsystems (EuroSimE), Freiburg, Germany, 2008, pp. 1-7.

[2.112] K. Weide-Zaage, “Simulation of Migration Effects in Solder Bumps”, IEEE, Transactions on Device and Materials Reliability, Vol. 8 No. 3 (2008), pp. 442-448.

[2.113] L. Meinshausen, K. Weide-Zaage, M. Petzold, “Electro- and thermomigration in microbump interconnects for 3D integration”, IEEE, Electronic Components and Technology Conference (ECTC), 2011, Lake Buena Vista, Florida, pp. 1444-1451.

[2.114] L. Meinshausen, K. Weide-Zaage , H. Frémont, „Migration induced material transport in Cu-Sn IMC and SnAgCu micro bumps“, IEEE, Microelectronics Reliability, Vol. 51 No 9-11, 2011, pp. 1860-1863.

[2.115] B. H. L. Chao, X. Zhang, S. H. Chae, P. S. Ho, „Recent advances on kinetic analysis of electromigration enhanced intermetallic growth and damage formation in Pb-free solder joints“, IEEE, Microelectronics Reliability, Vol. 49 No. 9-11, 2009, pp. 253-263.

[2.116] B. Chao, S. H. Chae, Xuefeng Zhang, et al. „Electromigration enhanced intermetallic growth and void formation in Pb-free solder joints“, Journal of Applied Physics, Vol. 100 (2006), pp.1-10.

[2.117] S. H. Chae, B. Chao, X. Zhang, „ Investigation of Intermetallic Compound Growth Enhanced by Electromigration in Pb-Free Solder Joints“, IEEE, Electronic Components and Technology Conference (ECTC), 2007, Reno, Nevada, USA, pp. 1442-1449.

[2.118] A. Syeed, K. Dhandapani, R. Moody, et al. “Cu Pillar and µ-bump electromigration reliability and comparison with high pb, SnPb, and SnAg bumps”, IEEE, Electronic Components and Technology Conference (ECTC), 2011, Lake Buena Vista, Florida, pp. 332-339.

[2.119] R. Labie, P. Limaye, K. W. Lee, „Reliability testing of Cu-Sn intermetallic micro-bump interconnections for 3D-device stacking“, 3rd Electronic System-Integration Technology Conference (ESTC),Berlin, 2010, pp. 1-5.

[2.120] F. Y. Ouyang, H. Hsu, Y. P. Su, et al., „Electromigration induced failure on lead-free micro bumps in three-dimensional integrated circuits packaging“, Journal of Applied Physics, Vol. 112 (2012), pp.1-5.

[2.121] W. D. MacDonald, T.W. Eagar, “Transient Liquid Phase Bonding”, Annual Review of Materials Science, Vol. 22 (1992), pp. 23-46.

[2.122] D.Q. Yu, L. Wang, „The growth and roughness evolution of intermetallic compounds of Sn–Ag–Cu/Cu interface during soldering reaction“, Journal of Alloys and Compounds, Vol. 458 (2008), pp. 542–547.

[2.123] C. H. Ma, R. A Swalin, “A study of solute diffusion in liquid tin” Acta Metallurgica, Vol. 8, No. 6 (1960), pp. 388-395.

[2.124] K. N. Tu, T. Y. Lee, „Wetting reaction versus solid state aging of eutectic SnPb on Cu“, Journal of Applied Physics, Vol. 89 No. 9 (2001), pp. 4843-4849.

[2.125] K. N. Tu, K. Zeng, „Tin-lead (SnPb) solder reaction in flip chip technology“, Materials Science and Engineering, R 34 (2001), pp. 1-58.

[2.126] N.S. Bosco, F.W. Zok, „Critical interlayer thickness for transient liquid phase bonding in the Cu–Sn system“, Acta Materialia, Vol. 52 (2004), pp. 2965–2972.

[2.127] B. E. Deal, A. S. Grove, "General Relationship for the Thermal Oxidation of Silicon", Journal of Applied Physics, Vol. 36 (1965), pp. 3770-3778.

[2.128] L. Meinshausen, H. Frémont, K. Weide-Zaage et al., "Electro- and Thermomigration-induced IMC Formation in $SnAg_{3.0}Cu_{0.5}$ Solder Joints on Nickel Gold Pads", IEEE, Microelectronics Reliability, Vol. 53 (2013), pp. 1575-1580.

[2.129] B. Salam, N. N. Ekere, D. Rajkumar, "Study of the Interface Microstructure of Sn-Ag-Cu Lead-Free Solders and the Effect of Solder Volume on Intermetallic Layer Formation", IEEE, 51th Electronic Components and Technology Conference (ECTC), Orlando, USA, 2001, pp. 471-477.

[2.130] A. Paul, C. Ghosh, W. J. Boettinger, „Diffusion Parameters and Growth Mechanism of Phases in the Cu-Sn System“, Metallurgical and Materials Transactions A, Vol. 42A (2011), pp. 952-963.

[2.131] K.N. Tu, R.D. Thompson, „Kinetics of interfacial reaction in bimetallic Cu-Sn thin films, Acta Metallurgica, Vol. 30 No. 5 (1982), pp. 947-952.

[2.132] P. T. Vianco, D. R. Frear, „Issues in the replacement of lead-bearing solders“, JOM, Vol. 45 No. 7 (1993), pp 14-19.

[2.133] F. Gao, J. Qu, „Calculating the diffusivity of Cu and Sn in Cu_3Sn intermetallic by molecular dynamics simulations“, Materials Letters, Vol. 73 (2012), pp. 92–93.

[2.134] H. Gan H, K. N. Tu, "Polarity effect of electromigration on kinetics of intermetallic compound formation in Pb-free solder V-groove samples„ Journal of Applied Physics, Vol. 97 (2005), pp.1-10.

[2.135] S. Ou, K. N. Tu, "A Study of Electromigration in Sn3.5AG and Sn3.8Ag0.7Cu Solder Lines", IEEE, 55th Electronic Components and Technology Conference (ECTC), Orlando, USA, 2005, pp. 1445-1450.

[2.136] B. Pieraggi, R. A. Rapp, F. J. J. van Loo, "Interfacial Dynamics in Diffusion-Driven Phase Transformations", Acta Metallurgica et Materialia, Vol. 38 No. 9 (1990), p. 1781-1788.

[2.137] K. N. Tu, "Solder Joint Technology Material Properties Reliability", Springer Science and Business Media, New York, 2007, pp. 113, 198, 257.

[2.138] T.Y. Lee, W.J. Choi, K.N. Tu, „Morphology, kinetics, and thermodynamics of solid-state aging of eutectic SnPb and Pb-free solders (Sn–3.5Ag, Sn–3.8Ag–0.7Cu and Sn–0.7Cu) on Cu“, Journal of Materials Research, Vol. 17 No. 2 (2002), pp. 291-301.

[2.139] T.A. Siewert, J.C. Madeni, S. Liu, "Formation and Growth of Intermetallics at the Interface Between Lead-free Solders and Copper Substrates", NIST, 2003.

[2.140] Y. D. Jeon, K. W. PAIK, A. OSTMANN, et al. „Effects of Cu Contents in Pb-Free Solder Alloys on Interfacial Reactions and Bump Reliability of Pb-Free Solder Bumps on Electroless Ni-P Under-Bump Metallurgy“, Journal of Electronic Materials, Vol. 34 No. 1 (2005), pp. 80-90.

[2.141] A. Kumar, M. He, Z. Chen, „Effect of electromigration on interfacial reactions between electroless Ni-P and Sn–3.5% Ag solder“, Thin Solid Films, Vol. 462–463 (2004), pp. 413– 418.

[2.142] F. Y. Ouyang, W. C. Jhu, „Comparison of thermomigration behaviors between Pb-free flip chip solder joints and microbumps in three dimensional integrated circuits: Bump height effect“, Journal of Applied Physics, Vol. 113 (2013), pp. 1-8.

[2.143] M.L. Huang, S. Ye, N. Zhao, „Current-induced interfacial reactions in Ni/Sn–3Ag 0.5Cu/Au/Pd(P)/Ni–P flip chip interconnect“, Journal of Materials Research, Vol. 26 No. 24 (2011), pp. 3009-3019.

[2.144] C.-M. Chen, S.-W. Chen, „Electromigration effect upon the Sn/Ag and Sn/Ni interfacial reactions at various temperatures“, Acta Materialia, Vol. 50 (2002), pp. 2461–2469.

[2.145] C. B. Lee, J. W. Yoon, S. J. Suh, “Intermetallic compound layer formation between Sn-3.5mass% Ag BGA solder ball and (Cu, immersion Au/Electroless Ni-P/Cu) substrate”, Journal of Materials Science: Materials in Electronics, Vol. 14 (2003), pp. 487-493.

[2.146] C. Gosh, “Study on important diffusion parameters of binary Ni_3Sn_4 phase”, Journal of Materials Science: Materials in Electronics, Vol. 24 (2013), pp. 2558-2561.

[2.147] H. D. Blair, T. Y. Pan, J. M. Nicholson, „Intermetallic compound growth on Ni, Au/Ni, and Pd/Ni substrates with Sn/Pb, Sn/Ag, and Sn solders [PWBs]“, IEEE, Electronic Components and Technology Conference (ECTC), 1998, Seattle, USA, pp. 259-267.

[2.148] M. He, A. Kumar, P.T. Yeo, „Interfacial reaction between Sn-rich solders and Ni-based metallization“, Thin Solid Films, Vol. 462–463 (2004), pp. 387– 393.

[2.149] M. He, Z. Chen, G. Qi, „Solid state interfacial reaction of Sn–37Pb and Sn–3.5Ag solders with Ni–P under bump metallization“, Acta Materialia, Vol. 52 (2004), pp. 2047–2056.

[2.150] Prof. Dr. Ing. Hans Jürgen Albrecht, Siemens AG, personal communication, January, 2014.

[2.151] NIST, “Phase Diagrams & Computational Thermodynamics: Cu-Sn System”, http://www.metallurgy.nist.gov/phase/solder/cusn.html (04.05.2014).

Chapter 3:

[3.1] I. Tuah-Poku, M. Dollar, T. B. Massalski, "A Study of the Transient Liquid Phase Bonding Process Applied at Ag/Cu/Ag Sandwich Joint", Mtallurgical Transactions A, Vol. 19A (1988), pp. 675-686.

[3.2] B. H. L. Chao, X. Zhang, S. H. Chae, P. S. Ho, „Recent advances on kinetic analysis of electromigration enhanced intermetallic growth and damage formation in Pb-free solder joints“, IEEE, Microelectronics Reliability, Vol. 49 No. 9-11, 2009, pp. 253-263.

[3.3] P. G. Shewmon, "Diffusion in Solids", 2nd Edition, Wiley, New York City, 1989, pp. 54-74, 233.

[3.4] H. Wever, “Elektro und Thermotransport in Metallen”, Johann Ambrosius Barth, Lebzig, 1973, in German, pp. 45, 52-56, 104-107, 146, 216-217, 249.

[3.5] B. F. Dyson, T. Anthony, D. Turnbull, „Interstitial Diffusion of Copper and Silver in Lead“, Journal of Applied Physics, Vol. 37 No. 6 (1966), pp. 2370-2373.

[3.6] J. R. Lloyd, K.-N. Tu, J. Jaspal, “Handbook of Lead-Free Solder Technology for Microelectronic Assemblies”, CRC Press, 2004, p. 834-836.

[3.7] B. F. Dyson, „Diffusion of Gold and Silver in Tin Single Crystals, Vol. 37 No 6 (1966), pp. 2375-2377.

[3.8] B. F. Dyson, T. Anthony, D. Turnbull, „Interstitial Diffusion of Copper in Tin“, Journal of Applied Physics, Vol. 38 (1967), pp. 3408-3409.

[3.9] D. C. Yeh and H. B. Huntington, „Extreme Fast-Diffusion System: Nickel in Single-Crystal Tin“, Physical Review Letters, Vol. 53 No 15 (1984), pp. 1469-1472.

[3.10] B. Pieraggi, R. A. Rapp, F. J. J. van Loo, “Interfacial Dynamics in Diffusion-Driven Phase Transformations”, Acta Metallurgica et Materialia, Vol. 38 No. 9 (1990), p. 1781-1788

[3.11] P.J. Shang, Z.Q. Liu, X.Y. Pang et al., „Growth mechanisms of Cu_3Sn on polycrystalline and single crystalline Cu substrates“, Acta Materialia, Vol. 57 (2009), pp. 4697-4706.

[3.12] K. Pearson, “The Problem of the Random Walk”, Nature, Vol. 72 No. 1875 (1905), pp. 293.

[3.13] A. Einstein, “Über die von der molekularkinetischen Theorie der Wärme geforderte Bewegung von in ruhenden Flüssigkeiten suspendierten Teilchen”, (1905), Annalen der Physik Vol. 17, pp. 549-560, in German.

[3.14] A. Paul, C. Ghosh, W. J. Boettinger, „Diffusion Parameters and Growth Mechanism of Phases in the Cu-Sn System“, Metallurgical and Materials Transactions A, Vol. 42A (2011), pp. 952-963.

[3.15] J.O. Suh, K.N. Tu, and N. Tamura, „A Synchrotron Radiation X-Ray Microdiffraction Study on Orientation Relationships between a Cu_6Sn_5 and Cu Substrate in Solder Joints“, JOM, 2006, pp. 63-66.

[3.16] Y. Watanabe, Y. Funjinaga, H. Iwasaki, “Lattice Modulation in the long period structure of Cu_3Sn”, Acta Crystallographica Section B, Vol. 39 No. 3 (1983), pp. 306-311.

[3.17] X.Y. Pang, S.Q. Wang, L. Zhang, et al., „First principal calculation of elastic and lattice constants of orthorhombic Cu_3Sn crystal“, Journal of Alloys and Compounds, Vol. 466 (2008), pp. 517-520.

[3.18] E. W. Elcock , C. W. Mccombie, „Vacancy Diffusion in Binary Ordered Alloys“, Physical Review, Vol. 109 No. 2 (1958), pp. 605-606.

[3.19] F. Gao, J. Qu, „Calculating the diffusivity of Cu and Sn in Cu_3Sn intermetallic by molecular dynamics simulations“, Materials Letters, Vol. 73 (2012), pp. 92–93.

[3.20] J. H. Van’t Hoff, “Etudes de Dynamique Chimique”, Frederik Muller & Co., Amsterdam, 1884, p. 116, in French.

[3.21] K. Weide-Zaage, “Untersuchungen von Stromdichte-, Temperatur- und Massenflussverteilungen in Viastrukturen integrierter Schaltungen”, Dissertation, VDI Verlag, Düsseldorf, 1994, pp. 9-11, in German.

[3.22] S. H. Chae, B. Chao, X. Zhang, „ Investigation of Intermetallic Compound Growth Enhanced by Electromigration in Pb-Free Solder Joints“, IEEE, Electronic Components and Technology Conference (ECTC), 2007, Reno, Nevada, USA, pp. 1442-1449.

[3.23] K.N. Tu, Hsiang-Yao Hsiao, Chih Chen, „Transition from flip chip solder joint to 3D IC microbump: Its effect on microstructure anisotropy“, IEEE, Microelectronics Reliability, Vol. 53 (2013), pp. 2-6.

[3.24] H. B. Huntington, A. R. Crone, „Current Induced Marker Motion in Gold Wires“, Journal of Physics and Chemistry of Solids, Vol. 20 (1961), pp. 76-87.

[3.25] H. M. Gilder, D. Lazarus, „Effect of High Electronic Current Density on the Motion of Au"' and Sb"' in Gold“, Physical Review, Vol. 145 No. 2 (1966), pp. 507-518.

[3.26] I. A. Blech, “Electromigration in thin aluminum films on titanium nitride“, Journal of Applied Physics, Vol. 47 (1976), pp. 1203-1208.

[3.27] C. Bosvieux, J. Friedel, „Sur L’électrolyse des Alliages Métalliques“, Journal of Physics and Chemistry of Solids, Vol. 23 (1962), pp. 123-136, in French.

[3.28] K. Weide-Zaage, „Simulation von Ausfallmechanismen auf Package- und Chiplevel“, Hannover, Gottfried Wilhelm Leibniz Universität Hannover, Laboratorium für Informationstechnologie, Habilitation, 2010, in German.

[3.29] M. Gerl, „Contribution au Calcul des Forces Agissant sur une Impurete d’un Metal Soumis a un Gradient de Temperature“, Journal of Physics and Chemistry of Solids, Vol. 28 (1967), pp. 725-736, in French.

[3.30] G. Brebec, N. Von Doan, M. Gerl, “Relation entre chaleur de transport et valence efficace”, Scripta Metallurgica, Vol. 2 No. 6 (1968), pp. 323-326, in French.

[3.31] R. A. Johns, D. A. Blackburn, „Grain Boundaries and their Effect on Thermomigration in pure Lead at low Diffusion Temperatures“, Thin Solid Films, Vol. 25 (1975), pp. 291-300.

[3.32] M.L. Huang, S. Ye, N. Zhao, „Current-induced interfacial reactions in Ni/Sn–3Ag 0.5Cu/Au/Pd(P)/Ni–P flip chip interconnect“, Journal of Materials Research, Vol. 26 No. 24 (2011), pp. 3009-3019.

[3.33] L. Meinshausen, H. Frémont, K. Weide-Zaage et al., “Electro- and Thermomigration-induced IMC Formation in $SnAg_{3.0}Cu_{0.5}$ Solder Joints on Nickel Gold Pads”, , IEEE, Microelectronics Reliability, Vol. 53 No 9-11, 2013, pp. 1575-1580.

[3.34] H. Yu, V. Vuorinen, J. Kivilahti, „Effect of Ni on the Formation of Cu_6Sn_5 and Cu_3Sn Intermetallics, IEEE, Electronic Components and Technology Conference (ECTC), San Diego, May-June 2006, pp. 1204-1209.

[3.35] J. Tao, J. F. Chen, N. W. Cheung, "Modeling and Characterization of Electromigration Failures Under Bidirectional Current Stress", IEEE, Transactions on Electron Devices, Vol. 43 No. 5 (1996), pp. 800-808.

[3.36] W. Feng, “Caractérisation Expérimentale et Simulation Physique des Mécanismes de dégradation de Interconnexions sans plomb dans les technologies d’assemblage a très forte densité d’intégration “”Boitier sur Boitier”, Dissertation, Université Bordeaux I, Talence, France, 2010, in French.

[3.37] R. J. Fields and S. R. Low, "Physical And Mechanical Properties Of Intermetallic Compounds Commonly Found in Solder Joints", The National Institute of Standards and Technology (NIST), 1991.

[3.38] W. C. Kuan, S.W. Liang, C. Chen, " Effect of bump size on current density and temperature distributions in flip-chip solder joints", IEEE, Microelectronics Reliability , Vol. 49 (2009) , pp. 544–550.

[3.39] L. Meinshausen, K. Weide-Zaage, H. Frémont, “Electro- and Thermomigration induced Failure Mechanisms in Package on Package“, IEEE, Microelectronics Reliability, Vol. 52 No 12 (2012), pp. 2889-2906.

[3.40] N. Saud, A. Jalar, „Sn-Rich Phase Coarsening in Sn-Ag-Cu Solder Joint during Moderate Current Stressing“, Advanced Materials Research, Vols. 264-265 (2011), pp. 212-216.

[3.41] Practical Components, “Dummy Components, Test Boards, Solder Training Kits, Tools and Supplies”, Los Alamitos, California, 2008, p.5.

[3.42] L. Meinshausen, H. Frémont, K. Weide-Zaage et al., Electro- and Thermomigration-induced IMC Formation in $SnAg_{3.0}Cu_{0.5}$ Solder Joints on Nickel Gold Pads, IEEE, 14th Mechanical & Multi-Physics Simulation, and Experiments in Microelectronics and Microsystems (EuroSimE), Wroclaw, Poland, 15-17 April, 2013, pp. 1-7.

[3.43] Yi- Shao Lai, Kuo- Ming Chen, Chin-Li Kao et al., "Electromigration of Sn-37Pb and Sn-3Ag-1.5Cu/Sn-3Ag-0.5Cu composite flip-chip solder bumps with Ti/Ni(V)/Cu under bump metallurgy", Microelectronics Reliability, Vol.47 (2007), pp. 1273-1279.

[3.44] Robert C. Weast, Ed. 62 Edition - CRC Handbook of Chemistry and Physics - CRC Press, Boca Raton, FL, 1981.

[3.45] R. Parkinson, "Properties and applications of electroless nickel (10081)", Nickel Development Institute 37, 1997, p.6.

[3.46] N. Miura, Y. Fuura, A. Kazami, "Electroless Nickel Resistors Formed on IMST Substrate, IEEE, Transactions on Components; Hybrids and Manufacturing Technology, Vol. 4 No. 4 (1981), pp. 532-535.

[3.47] P. Tsotra, K. Friedrich, "Thermal, mechanical, and electrical properties of epoxy Resin /polyaniline -dodecylbenzenesulfonic acid blends", Synthetic Metals, Vol. 143 (2004), pp. 237-242.

[3.48] Hua Ye, Cemal Basaran , Douglas C. Hopkins, "Mechanical degradation of microelectronics solderjoints under current stressing", International Journal of Solids and Structures, Vol. 40 (2003), pp. 7269- 7283.

[3.49] W. Feng, H. Frémont, A. Guédon-Gracia, F. Verdier et. al: "Analytical Model for Thermally-induced Warpage of PoP", IEEE- EuroSimE, 2008.

[3.50] ESA Publications Division ESTEC: "Data for Selection of Space Materials", Paris (1994), European Space Agency.

[3.51] K. Weide-Zaage, "Simulation of Migration Effects in Solder Bumps", IEEE, Transactions on Device and Materials Reliability, Vol. 8, No. 3 (2008), pp. 442-448.

[3.52] Programming was made by Dipl. Ing. Jörg Kludt, Leibniz Universität Hannover, Laboratorium für Informationstechnologie.

[3.53] K. Weide-Zaage, "Exemplified calculation of stress migration in a 90nm node via structure", IEEE, Mechanical & Multi-Physics Simulation and Experiments in Microelectronics and Microsystems (EuroSimE), 2010.

Chapter 4:

[4.1] H. Yu, V. Vuorinen, J. Kivilahti, „Effect of Ni on the Formation of Cu_6Sn_5 and Cu_3Sn Intermetallics, IEEE, Electronic Components and Technology Conference (ECTC), San Diego, May-June 2006, pp. 1204-1209.

[4.2] B. H. L. Chao, X. Zhang, S. H. Chae, P. S. Ho, „Recent advances on kinetic analysis of electromigration enhanced intermetallic growth and damage formation in Pb-free solder joints", IEEE, Microelectronics Reliability, Vol. 49 No. 9-11, 2009, pp. 253-263.

[4.3] F. Gao, J. Qu, „Calculating the diffusivity of Cu and Sn in Cu_3Sn intermetallic by molecular dynamics simulations", Materials Letters, Vol. 73 (2012), pp. 92–93.

[4.4] A. Paul, C. Ghosh, W. J. Boettinger, „Diffusion Parameters and Growth Mechanism of Phases in the Cu-Sn System“, Metallurgical and Materials Transactions A, Vol. 42A (2011), pp. 952-963.

[4.5] H. Wever, “Elektro und Thermotransport in Metallen”, Johann Ambrosius Barth, Lebzig, 1973, in German, p. 56.

[4.6] K. Guth, D. Siepe, J. Görlich, et al., „New assembly and interconnects beyond sintering methods“, Power Conversion and Inteligent Motion (PCIM), Nürnberg, Germany, 2010, pp. 1-6.

[4.7] E. W. Elcock , C. W. Mccombie, „Vacancy Diffusion in Binary Ordered Alloys“, Physical Review, Vol. 109 No. 2 (1958), pp. 605-606.

[4.8] A. Kumar, M. He, Z. Chen, „Effect of electromigration on interfacial reactions between electroless Ni-P and Sn–3.5% Ag solder“, Thin Solid Films, Vol. 462–463 (2004), pp. 413– 418.

[4.9] M.L. Huang, S. Ye, N. Zhao, „Current-induced interfacial reactions in Ni/Sn–3Ag 0.5Cu/Au/Pd(P)/Ni–P flip chip interconnect“, Journal of Materials Research, Vol. 26 No. 24 (2011), pp. 3009-3019.

[4.10] L. Meinshausen, H. Frémont, K. Weide-Zaage et al., “Electro- and Thermomigration-induced IMC Formation in $SnAg_{3.0}Cu_{0.5}$ Solder Joints on Nickel Gold Pads”, IEEE, Microelectronics Reliability, Vol. 53 No 9-11, 2013, pp. 1575-1580.

[4.11] B. F. Dyson, T. Anthony, D. Turnbull, „Interstitial Diffusion of Copper in Tin“, Journal of Applied Physics, Vol. 38 (1967), pp. 3408-3409.

[4.12] B. F. Dyson, „Diffusion of Gold and Silver in Tin Single Crystals*,* Vol. 37 No 6 (1966), pp. 2375-2377.

[4.13] Y. D. Jeon, K. W. Paik, A. Ostmann, et al. „Effects of Cu Contents in Pb-Free Solder Alloys on Interfacial Reactions and Bump Reliability of Pb-Free Solder Bumps on Electroless Ni-P Under-Bump Metallurgy“, Journal of Electronic Materials, Vol. 34 No. 1 (2005), pp. 80-90.

[4.14] L. Meinshausen, K. Weide-Zaage, H. Frémont, “Electro- and Thermomigration induced Failure Mechanisms in Package on Package“, IEEE, Microelectronics Reliability, Vol. 52 No 12 (2012), pp. 2889-2906.

[4.15] W. Feng, “Caractérisation Expérimentale et Simulation Physique des Mécanismes de dégradation de Interconnexions sans plomb dans les technologies d’assemblage a très forte densité d’intégration “”Boitier sur Boitier”, Dissertation, Université Bordeaux I, Talence, France, 2010, in French.

[4.16] C. Chen, H.M. Tong, K.N. Tu, “Electromigration and Thermomigration in Pb-Free Flip-Chip Solder Joints”, Annual Review of Materials Research, Vol. 40 (2010), pp. 531-555.

[4.17] M. Gerl, „Contribution au Calcul des Forces Agissant sur une Impurete d’un Metal Soumis a un Gradient de Temperature“, Journal of Physics and Chemistry of Solids, Vol. 28 (1967), pp. 725-736, in French.

[4.18] L. Meinshausen, H. Frémont, K. Weide-Zaage et al., Influence of contact geometry variations on the life time distribution of IC packages during electromigration testing, IEEE, 14th Mechanical & Multi-Physics Simulation, and Experiments in Microelectronics and Microsystems (EuroSimE), Wroclaw, Poland, 15-17 April, 2013, pp. 1-7.

[4.19] M.L. Huang, S. Ye, N. Zhao, „Current-induced interfacial reactions in Ni/Sn–3Ag 0.5Cu/Au/Pd(P)/Ni–P flip chip interconnect“, Journal of Materials Research, Vol. 26 No. 24 (2011), pp. 3009-3019.

[4.20] L. Meinshausen, H. Frémont, K. Weide-Zaage, „Migration induced IMC formation in SAC305 solder joints on Cu, NiAu and NiP metal layers“, IEEE, Microelectronics Reliability, Vol. 52 No 9-10, 2012, pp. 1827-1832.

[4.21] N. Saud, A. Jalar, „Sn-Rich Phase Coarsening in Sn-Ag-Cu Solder Joint during Moderate Current Stressing“, Advanced Materials Research, Vols. 264-265 (2011), pp. 212-216.

Chapter 5:

[5.1] K. Weide-Zaage, "Exemplified calculation of stress migration in a 90nm node via structure", IEEE, Mechanical & Multi-Physics Simulation and Experiments in Microelectronics and Microsystems (EuroSimE), 2010.

[5.2] The programming was made by Dipl. Ing. Jörg Kludt, Leibniz Universität Hannover, Laboratorium für Informationstechnologie.

[5.3] B. F. Dyson, T. Anthony, D. Turnbull, „Interstitial Diffusion of Copper in Tin“, Journal of Applied Physics, Vol. 38 (1967), pp. 3408-3409.

[5.4] B. F. Dyson, „Diffusion of Gold and Silver in Tin Single Crystals, Vol. 37 No 6 (1966), pp. 2375-2377.

[5.5] L. Meinshausen, H. Frémont, K. Weide-Zaage et al., "Electro- and Thermomigration-induced IMC Formation in $SnAg_{3.0}Cu_{0.5}$ Solder Joints on Nickel Gold Pads", IEEE, Microelectronics Reliability, Vol. 53 No 9-11, 2013, pp. 1575-1580.

Attachments: Curriculum Vitae and Publications

I. Contact Information

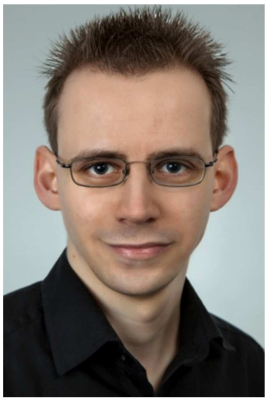

Full Name: Lutz Meinshausen
Address: Striehlstr. 4, 30159 Hanover, Germany
Home Tel.: 0049 - 511 - 1319566
Mobile: 0049 -173 - 2309788
E-Mail lmei@lfi.uni-hannover.de

II. Research

Research field: Reliability of IC interconnects and ball grid arrays, regarding migration effects, thermal expansion and intermetallic compound formation

01.01.2011-01.01.2014 Ph.D. student in France and Germany with binational doctoral advisers (“cotutelle de thèse”). Financed by a grant from the French Ministry for Higher Education & Science (MESR)

Dissertation: “Modelling the SAC microstructure evolution under thermal, thermo mechanical and electrical constraints”

01.01.2013-31.12.2013 *Ph.D. student, Information Technology Laboratory (LFI), University of Hanover (Leibniz Universitaet Hannover).*

01.09.2011-31.12.2012 *Research working at the “Laboratoire de l'Intégration du Matériau au Système“ IMS („Laboratory for the integration of materials into systems“), University of Bordeaux 1, France.*

01.01.2011-31.08.2011 *Ph.D. student, Information Technology Laboratory (LFI), University of Hanover (Leibniz Unversitaet Hannover).*

01.03.2010-31.12.2010 Member of research staff, Information Technology Laboratory (LFI), University of Hanover

- *Preparing project proposals*
- *Presenting project results at international conferences*
- *Finite element analysis of reliability issues in package on package (PoP) structures under consideration of electromigration, thermomigration and CTE mismatch*

01.01.2010-28.02.2010 Student Research Assistant, LFI, University of Hanover

- *Finite element analysis of reliability issues in package on package (PoP) structures under consideration of electromigration, thermomigration and CTE mismatch.*

III. Further professional training

01.09.2009 - 21.12.2009	Internship, Quality & Reliability Department (QRE), Global Foundries, Dresden *Improvement of an existing fast waver level electromigration test (inline measurements), to enable the reproduction of package level tests.*
02.08.2004 - 24.09.2004	Internship, Department of Professional Education, Siemens, Hanover *Construction of a power supply unit.*

IV. Education

01.10.2004 - 26.01.2010	University of Hanover Diplom-Ingenieur (Dipl. Ing.): advanced academic degree in engineering being equivalent to Master level. Specialization: Microelectronics

V. Publications

L. Meinshausen, H. Frémont, K. Weide-Zaage et al., “Electro- and Thermomigration-induced IMC Formation in $SnAg_{3.0}Cu_{0.5}$ Solder Joints on Nickel Gold Pads”, IEEE, Microelectronics Reliability, Vol. 53 No 9-11, 2013, pp. 1575-1580.

A. Moujbani, J. Kludt, K. Weide-Zaage, M. Ackermann, V. Hein, L. Meinshausen, "Dynamic Simulation of Migration Induced Failure Mechanism in Integrated Circuit Interconnects", IEEE, Microelectronics Reliability, Vol. 53 No 9-11, 2013, pp. 1365-1369.

L. Meinshausen, H. Frémont, K. Weide-Zaage et al., Influence of contact geometry variations on the life time distribution of IC packages during electromigration testing, IEEE, 14th Mechanical & Multi-Physics Simulation, and Experiments in Microelectronics and Microsystems (EuroSimE), Wroclaw, Poland, 15-17 April, 2013, pp. 1-7.

L. Meinshausen, H. Frémont, K. Weide-Zaage, „Migration induced IMC formation in SAC305 solder joints on Cu, NiAu and NiP metal layers“, IEEE, Microelectronics Reliability, Vol. 52 No 9-10, 2012, pp. 1827-1832.

L. Meinshausen, K. Weide-Zaage, H. Frémont, “Electro- and Thermomigration induced Failure Mechanisms in Package on Package“, IEEE, Microelectronics Reliability, Vol. 52 No 12, 2012, pp. 2889-2906.

L. Meinshausen, K. Weide-Zaage, H. Frémont, „Thermal Management for Stackable Packages with Stacked ICs", IEEE, Mechanical & Multi-Physics Simulation, and Experiments in Microelectronics and Microsystems (EuroSimE), April 2012, pp. 1-6.

K. Weide-Zaage, L. Meinshausen, H. Fremont, "Prediction of Electromigration Induced Void Formation in TSV and SAC Contacts", IEEE Congress on Engineering and Technology (CET), Shanghai 2011, IEEE Cat. Num.: CFP1148NCDR, ISBN: 978-1-61284-362-9, p. 376-382.

I. Bauer, K. Weide-Zaage, L. Meinshausen, „Influence of Air Gaps on the Thermal Electrical Mechanical Behavior of a Copper Metallization“, IEEE, Microelectronics Reliability, Vol. 51 No 9-11, 2011, pp. 1587-1591.

L. Meinshausen, K. Weide-Zaage, H. Frémont, „Migration induced material transport in Cu-Sn IMC and SnAgCu micro bumps“,IEEE, Microelectronics Reliability, Vol. 51 No 9-11, 2011, pp. 1860-1864.

L. Meinshausen, K. Weide-Zaage, M. Petzold, "Electro- and thermomigration in microbump interconnects for 3D integration", IEEE, Electronic Components and Technology Conference (ECTC), June 2011, pp. 1444-1451.

L. Meinshausen, K. Weide-Zaage, "Exploration of Migration and Stress Effects in PoPs Considering Inhomogeneous Temperature Distribution", International Wafer-Level Packaging Conference (IWLPC), October 2010, pp. 137-145.

K. Weide-Zaage, L. Meinshausen, H. Frémont, "Characterisation of thermal-electrical and mechanical behaviour of PoP", Surface Mount Technology Association, SMTAI Orlando, October 2010, personal invited.

L. Meinshausen, K. Weide-Zaage, H. Frémont, "Underfill and Mold Compound Influence on PoP Aging under High Current and High Temperature Stress", IEEE, Electronics System Integration Technology Conference (ESTC), September 2010.

L. Meinshausen, K. Weide-Zaage, H. Frémont, W. Feng, „PoP: 'Prototyping by determination of matter transport effect", CPMT Symposium Japan, 2010 IEEE, p. 1-4.

L. Meinshausen, K. Weide-Zaage, H. Frémont, „Underfill and mold compound influence on PoP ageing under high current and high temperature stresses", Electronic System-Integration Technology Conference (ESTC), 2010 3rd, p.1-6.

L. Meinshausen, K. Weide-Zaage, H. Frémont, W. Feng, „Virtual prototyping of PoP interconnections regarding electrically activated mechanisms", IEEE, Mechanical & Multi-Physics Simulation, and Experiments in Microelectronics and Microsystems (EuroSimE), April 2010, pp. 1-8.

VIII. Presentations

K. Weide-Zaage, J. Kludt, L. Meinshausen, A. Farajzadeh, "Synergiepotenzial von finite Elemente Simulationen bei der Optimierung des Entwurfsprozesses von Metallisierungen", GMM CfP TuZ, February 2013, Dresden, Germany.

L. Meinshausen, H. Frémont, K. Weide-Zaage, „Preparation of reliability experiments for three dimensional packaging", Smart Failure Analysis for New Materials in Electronic Devices (smart-FA), September 2012, Dresden, Germany.

L. Meinshausen, H. Frémont, „Influence of the fabrication process and the preparation on electromigration induced IMC formation in PoP", analyse de défaillance de composants électroniques (anadef), June 2012, Seignosses, France.

K. Weide-Zaage, L. Meinshausen, J. Kludt: "Simulation von Phasenbildung in Metallisierungen und Bumps", VDE-ITG Fachgruppe 8.5.6 fWLR/ Wafer Level Reliability, Zuverlässigkeits- Simulation & Qualifikation, May 2012, München, Germany.

L. Meinshausen, O. Aubel, H. Schmidt, "Ermittlung optimierter Ausfallkriterien für den Vergleich zwischen PL-EM und Isothermal Tests", VDE ITG fWLR Workshop, November 2009, Dresden, Germany.